Julius-Maximilians-Universität Würzburg
Graduate School of Science and Technology

**Doctoral thesis**

for the doctoral degree

**Doctor rerum naturalium (Dr. rer. nat.)**

# High-quality Organolead Trihalide Perovskite Crystals: Growth, Characterisation, and Photovoltaic Applications

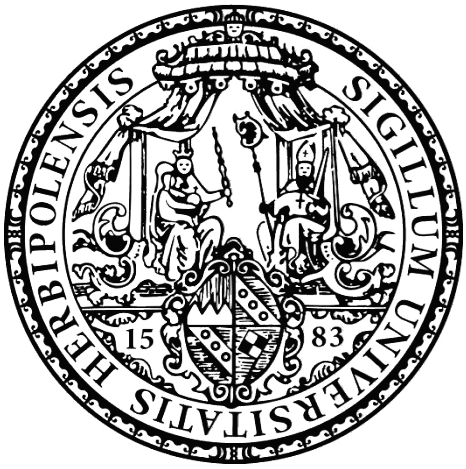


Submitted by

**Julian Harald Höcker**

from

Aschaffenburg

Würzburg, 2021

Submitted on: 20.10.2021

Stamp Graduate School

**Members of thesis committee:**

Chairperson: Prof. Dr. Bert Hecht

1. Reviewer and Examiner 1: Prof. Dr. Vladimir Dyakonov

2. Reviewer and Examiner 2*:* Prof. Dr. Jürgen Hartmann

3. Examiner: Prof. Dr. Robert Luxenhofer

Day of thesis defence: 22.02.2022

**This thesis is dedicated to my parents**
**Katharina and Harald Höcker.**

# Table of Contents

# 1 Introduction

**Figure 1.** Crystal fascination.

Crystals have fascinated people for thousands of years by their gloss, symmetry, and colour (Figure 1), but they are also the key material of the 21st century [1, 2]. The term crystal is derived from the Greek word krýstallos (κρύσταλλος) and means "ice" [3-5]. From the time of ancient Greece to the Early Middle Ages, people assumed that rock crystals were made of frozen water [4, 5]. Today, crystals are part of our daily life, as many substances are in crystalline form. Humans ingest crystals through food in the form of sugar and salts [1, 2]. In addition, crystalline materials have become indispensable in modern life due to the technical changes in the 20th century, as they are also present in household appliances and vehicles [1]. Modern communication and media technology, which includes smartphones, televisions, and computers, rely on the special physical properties of crystals [1]. The list seems endless, as medical technology as well as energy supply are also dependent on crystalline materials [1, 2].

For most modern applications and technologies, crystalline materials must be used, which are semiconductors [6-8]. Examples of these semiconductors are the compounds gallium arsenide, indium phosphide, and silicon (Si) [6, 8-10]. The semiconductors, which are primarily used in electronics, optoelectronics, and photovoltaics [6, 8, 9], must be grown synthetically on an industrial scale [1, 10]. An important industrial crystal growth process is the epitaxy [10, 11]. This method allows the growth of single crystals [12, 13] whose high quality can be confirmed by modern measurement techniques, such as X-ray diffraction (XRD) [11, 14].

Undoubtedly, production, investigation, and application of crystalline semiconductors are well known and highly industrialized processes. Nevertheless, mankind's insatiable and ever-growing demand for technical applications cannot be sustained by inorganic semiconductors, especially considering that the resources of these semiconductors are finite [15-18]. Since they are precisely used for the energy supply of humans, which will also continue to increase in this century [16], it is urgently necessary to replace inorganic semiconductors with more sustainable alternatives in the long term [18]. Alternatives to the classical semiconductors are organic semiconductors [19, 20], but also hybrid semiconductors like lead halide perovskites [21, 22]. These perovskites consist of an organic and an inorganic part, and are called organolead trihalide perovskites (OLTPs) [23]. OLTPs are already used for a wide range of optoelectronic applications [17, 18, 24-26]. The simple fabrication at comparatively low manufacturing costs may enable mass production of optoelectronic OLTP devices in the future [2, 17, 18, 25].

The OLTPs can be traced back to the inorganic perovskite calcium titanate ($CaTiO_3$) [27]. This "first" perovskite was discovered in the 19th century by the Prussian mineralogist Gustav Rose in the Urals in the druse of a rock sample [28, 29]. In honour of the Russian politician and mineralogist Lev Alekseyevich Perovskiy, Rose gave the new mineral the name perovskite [29]. The natural perovskite as well as the nowadays synthetically produced hybrid perovskites follow the chemical structure $ABX_3$ [21, 22]. This chemical structure allows a variety of different perovskites [21, 30, 31]. A well-known example of OLTPs is methylammonium lead triiodide ($MAPbI_3$) [21]. By replacing the organic cation and/or the halogen, many other lead-containing perovskites such as methylammonium lead trichloride ($MAPbCl_3$) or formamidinium lead triiodide ($FAPbI_3$) are possible [21, 32]. The lead cation in turn can be replaced by tin. Typical examples of this perovskite are then methylammonium tin triiodide

($MASnI_3$), but also methylammonium tin tribromide ($MASnBr_3$) [30]. However, many other compounds are also possible containing neither lead nor tin in their stoichiometry [33], such as the double perovskite caesium silver bismuth bromide ($Cs_2AgBiBr_6$), which has the molecular formula $A_2BB'X_6$ [34-37].

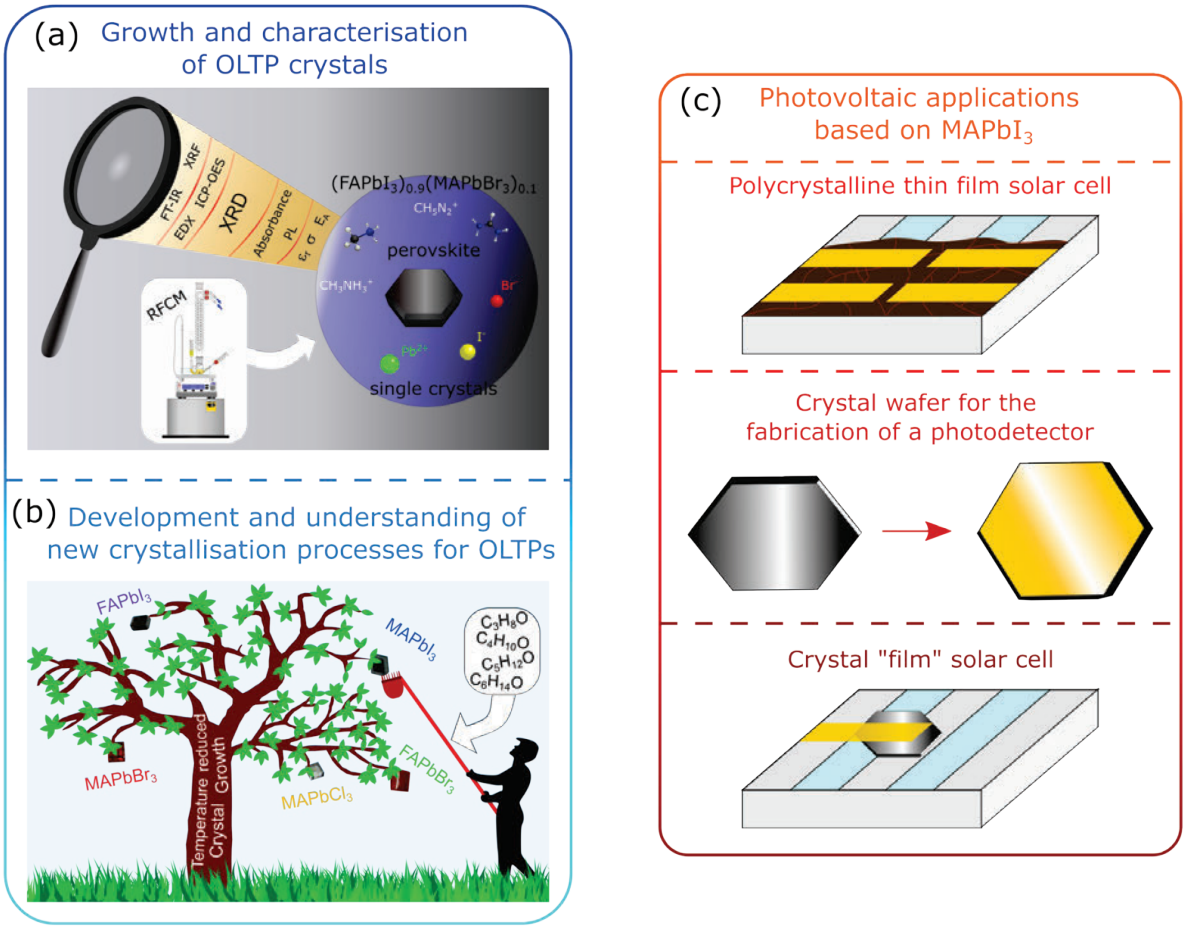


**Figure 2.** Illustration of the dissertation. (a) Growth and characterisation of organolead trihalide perovskite (OLTP) crystals. (b) Development and understanding of new crystallisation processes for OLTPs. The knowledge gained from the crystal growth, the characterisation, and the experience gained in the fabrication of polycrystalline methylammonium lead triiodide ($MAPbI_3$) thin-film solar cells (c) was indispensable for the manufacturing of a crystal wafer photodetector as well as a crystal film solar cell. (a) and (b) reproduced from Ref. [26] and Ref. [23], respectively, with permission from the Royal Society of Chemistry.

If one now studies, for example, the perovskites $MAPbI_3$, $MASnI_3$, and $Cs_2AgBiBr_6$, the advantages of the lead-containing perovskite will quickly become apparent: $MAPbI_3$ and $MASnI_3$ have small band gaps of 1.59 eV and 1.24 eV [38], respectively, making them both interesting for optoelectronic devices. However, compared to $MAPbI_3$, the tin-based perovskite is unstable and decomposes very quickly [39-41]. Compared to the iodine-containing perovskites, $Cs_2AgBiBr_6$ has an indirect band gap of about 2.1 eV [37, 42, 43], making it difficult to consider this perovskite for devices such as solar cells. These and many other physical properties make the lead-containing perovskites a sought-after field of research with amazing results [17]: With regard to the application of these perovskites as photovoltaic cells, many research groups succeed in obtaining power conversion efficiencies (PCEs) above 20 % [44-47], which indicates a very good reproducibility, and makes them competitive with silicon solar cells [17]. Nevertheless, it is not yet possible to increase the efficiency of OLTP solar cells up to the Shockley-Queisser limit [48], which is 31 % for $MAPbI_3$ solar cells [49]. One reason for this could be the polycrystalline OLTP layers themselves, which are used to

build solar cells and other optoelectronic devices [44-47]. These polycrystalline layers consist of many small single crystals separated by grain boundaries [50, 51]. The grain boundaries can contribute to charge transport losses in the active perovskite layer and thus reduce the efficiency of an OLTP based solar cell [52-54].
For this reason, the focus of many researchers is shifting towards the study of OLTP single crystals, as they have no grain boundaries and are dislocation-free, which may make them more suitable for building optoelectronic devices [55, 56]. Another advantage of single crystals in comparison to their polycrystalline counterparts is the possibility to use them to explore the physical properties of the pure perovskite in order to gain important knowledge for applications [56, 57].
However, it quickly becomes clear to every perovskite crystal researcher in everyday laboratory life that the first problem is to grow high-quality crystals and, in the best case, single crystals. The OLTP crystals are grown from solution, and although there are now many manufacturing options [56, 58], this is where the challenges arise: Some crystallisation processes require long growth times [59], others are only applicable to a few OLTPs [60, 61], and again some require high temperatures to grow the crystals [62], which can cause lattice defects in the crystals [23]. Also the background of some crystallisation processes is poorly understood, making it very difficult to improve existing techniques. Like the traditional semiconductors, the quality of the grown OLTP crystals must also be verified by X-ray measurements. However, many publications refer to OLTP single crystals without verifying their crystallinity more precisely [60, 62-65]. Problems also arise with regard to electrical measurements in order to characterise the crystals and their optoelectronic components since the crystals are small (a few mm in size) and brittle.
In the present thesis, the mentioned problems are addressed and solved with regard to OLTP crystals. Therefore, this doctoral thesis can also serve as a handbook for any OLTP crystal researcher. Figure 2 illustrates the growth, characterisation, and application of OLTP crystals for photovoltaic purposes, which represents the structure of this thesis.
An overview of the crystallographic aspects and their relation to the OLTP perovskites is shown in Chapter 2. For the systematic study of the crystals and their photovoltaic devices, the associated measurement methods are described in Chapter 3. Chapter 4 provides an overview of a systematic study of OLTP crystals of different stoichiometric ratios based on four different crystallisation methods. In Chapter 5, mostly unexplored complex perovskite crystals are introduced. A new crystallisation technique for growing large-sized crystals is also presented here in order to measure the crystals with new electrical contacting boards. Furthermore, a new chemical crystallisation process, which allowed the growth of high-quality OLTP single crystals, is provided in Chapter 6. In addition, the background of the crystallisation process was analysed. The crystal characterisation (Figure 2a) and the newly developed chemical crystallisation process (Figure 2b) were the preliminary work to focus on optoelectronic devices based on thin perovskite crystals (Chapter 7). Furthermore, in order to enable optoelectronic components based on crystals, polycrystalline $MAPbI_3$ solar cells were fabricated first (Subchapter 7.1). These findings were essential to manufacture first prototypes of a photodetector (Subchapter 7.2) and a solar cell, based on $MAPbI_3$ crystals (Subchapter 7.3) (Figure 2c). An overview of the field of OLTP crystals and the findings of the thesis are summarised in Chapter 8.

# 2 Crystallography and its Relation to Perovskites

Crystals are the central objects of crystallography [66]. Crystallography focuses on the description of crystal structures and crystal morphology, as well as the synthesis and growth processes of crystals [66]. In order to analyse hybrid organolead perovskite crystals in a meaningful way, the crystallographic aspects must be considered whose theoretical background is described in the following.

## 2.1 Definition of a Single Crystal

An ideal crystal or single crystal is considered to be an infinite repetition of identical structural elements (Figure 3) [50, 67]. Here, atoms, ions or molecules are periodically arranged in three dimensions [66]. A single crystal is further defined by a structural unit, which includes a base and a space lattice [67]:

$$crystal = base + lattice \tag{1}$$

The base can be variously complex consisting of only one, two or more atoms [67]. For example, hybrid perovskite single crystals with the molecular formula $CH_3NH_3PbBr_3$ or $CH_3NH_3PbI_3$ consist of five atoms, whereas the more complex single crystal with the stoichiometry $(CH_5N_2PbI_3)_{0.9}(CH_3NH_3PbBr_3)_{0.05}(CsPbBr_3)_{0.05}$ consists of seven different atoms.

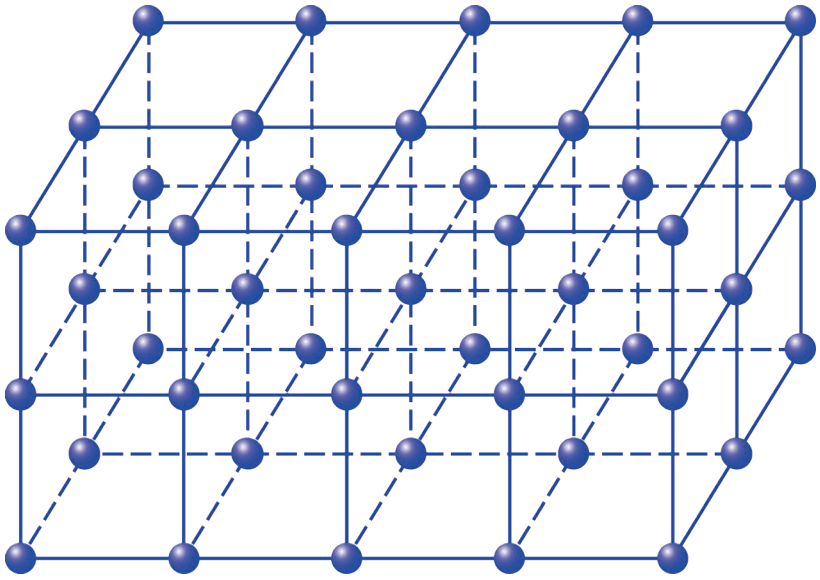

**Figure 3.** Three-dimensional periodic space lattice to illustrate a single crystal. Reproduced in a modified design from Ref. [50].

Their anisotropic and homogeneous properties distinguish ideal crystals from polycrystalline and amorphous solids. Polycrystals consist of many small single crystals. The size and orientation of the single crystals are distributed randomly. Therefore, a periodic lattice can only be assigned to each microcrystal. In contrast, amorphous solids consist of an irregular arrangement of atoms or molecules. A strict periodicity is not present here. [50]

## 2.2 The Structure of an Ideal Crystal

Single-crystalline solids are simply described by atomic crystals. Here, exactly one atom occupies one point of the space lattice (Figure 4a). To create a coordinate system, one atom is determined as the zero point. The position vectors $\vec{a}$, $\vec{b}$, and $\vec{c}$ to the three neighbouring atoms are called the base vectors of the lattice. Thereby, the vector $\vec{a}$ looks forward, $\vec{b}$ to the right, and $\vec{c}$ upwards, thus setting up a lattice. Those three basis vectors span the smallest unit of a crystal, which is called the unit cell. By stringing the unit cell together in the three directions of space, a macroscopic crystal is formed. The entire crystal lattice can then be built up by translations of the unit cell. For this reason, such a lattice is also called a translational lattice. The unit cell always has six "faces" and eight "corners" and is therefore described by six lattice parameters. The absolute values of the lattice translation $a = |\vec{a}|$, $b = |\vec{b}|$, and $c = |\vec{c}|$ represent the side lengths of the unit cell and are referred to as the lattice constants a, b, and c, respectively. The description of the unit cell is completed by the angles $\gamma = \vec{a} \wedge \vec{b}$, $\beta = \vec{a} \wedge \vec{c}$, and $\alpha = \vec{b} \wedge \vec{c}$ between the respective vectors. For each grid point it is possible to determine a location vector starting from the zero point, which is called the translation vector: [66]

$$\vec{\tau} = u \cdot \vec{a} + v \cdot \vec{b} + w \cdot \vec{c} \tag{2}$$

The integer coordinates (u, v, and w) are important here, which are summarised as the triple uvw. As an example in Figure 4b, the vector $\vec{\tau_1}$ indicates the grid point 120 and the vector $\vec{\tau_2}$ marks the grid point 023. The corresponding grid line always contains the origin coordinate 000. Accordingly, these are directional indications that are always indicated with square brackets. The specified grid lines are therefore given in the form [120] and [023]. [50, 66]

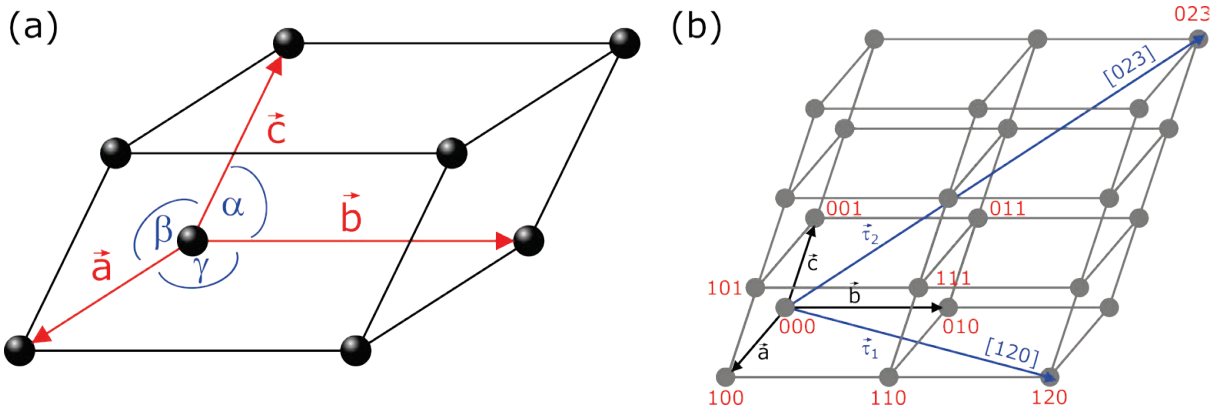


**Figure 4.** (a) Illustration of an unit cell exemplified by a parallelepiped, which is based on a space lattice with the basis vectors $\vec{a}$, $\vec{b}$, and $\vec{c}$, and their angles α, β, and γ. (b) Identification of grid points and the grid lines $\vec{\tau_1}$ and $\vec{\tau_2}$, starting from the grid origin. Reproduced in a modified design from Ref. [50] and [66].

## 2.3 Classification of the Crystal Lattices

Crystal lattices can be divided into seven crystal systems in three-dimensional space. A distinction is made between cubic, hexagonal, trigonal, tetragonal, rhombic, monoclinic, and triclinic unit cells. The crystal systems are defined by their symmetry, which differ by their base vectors $\vec{a}$, $\vec{b}$, and $\vec{c}$, as well as their respective angles α, β, and γ. Each of these systems can be assigned the symmetry operation of the point group. Such a lattice is called primitive. In addition to this, other non-primitive lattices are possible, which are called centred lattices. When all possible centrings are applied, a total of 14 lattice types can be determined, which are called

Bravais lattices. These lattices represent the crystallographic space groups. In the case of centred lattices, a further distinction is made between face-centred and base-centred lattices, which originate from several primitive lattices. Thus, the translation vector in the case of the body-centred space lattice is half a space diagonal. The centred lattice is then twofold primitive. In contrast, the all-sided face-centred lattice is fourfold primitive because all half face diagonals represent universal translation vectors. Table 1 summarises the seven crystal systems with the 14 Bravais lattices. [50, 67]

**Table 1.** The seven crystallographic systems with the 14 Bravais lattices and their corresponding lattice parameters [50, 67, 68].

| Crystal system | | Lattice parameters | | Bravais lattice |
|---|---|---|---|---|
| 1 | cubic | $a = b = c$ | $\alpha = \beta = \gamma = 90°$ | 1. primitive<br>2. body-centred<br>3. face-centred |
| 2 | hexagonal | $a = b \neq c$ | $\alpha = \beta = 90°; \gamma = 120°$ | 1. primitive |
| 3 | trigonal<br>(rhombohedral) | $a = b = c$ | $\alpha = \beta = \gamma \neq 90° < 120°$ | 1. primitive<br>2. body-centred<br>3. face-centred<br>4. base-centred |
| 4 | tetragonal | $a = b \neq c$ | $\alpha = \beta = \gamma = 90°$ | 1. primitive<br>2. body-centred |
| 5 | rhombic | $a \neq b \neq c$ | $\alpha = \beta = \gamma = 90°$ | 1. primitive |
| 6 | monoclinic | $a \neq b \neq c$ | $\alpha = \gamma = 90°; \beta \neq 90°$ | 1. primitive<br>2. base-centred |
| 7 | triclinic | $a \neq b \neq c$ | $\alpha \neq \beta \neq \gamma$ | 1. primitive |

The relevant crystal systems for OLTPs at room temperature (RT) are the cubic and tetragonal lattices. The Bravais lattices of the respective unit cells are illustrated in Figure 5 and Figure 6, respectively. The cubic lattice has the highest symmetry in comparison to the other crystallographic systems. The axes of the lattice are of equal length and interchangeable. A rectangular coordinate system is present. The cubic lattice is divided into three Bravais lattices with non-equivalent space groups, simple cubic (sc), face-centred cubic (fcc), and body-centred cubic (bcc). Each of the grids corresponds to the point group of a cube. [50, 67]

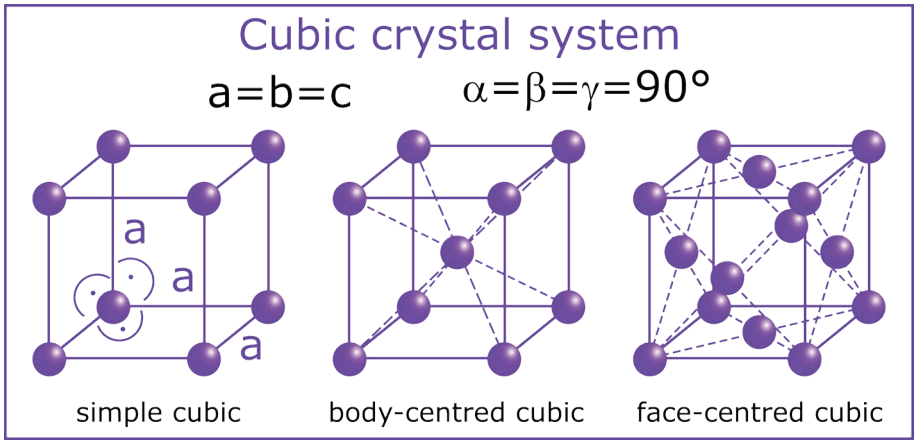


**Figure 5.** The relevant cubic Bravais lattices for OLTP crystals. Reproduced in a modified design from Ref. [66].

The tetragonal symmetry group is obtained when the cubic symmetry is reduced. To achieve the new symmetry, two opposite surfaces must be pulled apart. As a result, only two axes have the same length. As in the cubic crystal system, the angles of the tetragonal system are rectangular. The crystal system contains two Bravais lattices, the tetragonal primitive and the tetragonal space-centred which are obtained by stretching the cubic Bravais lattices. Thus, the tetragonal primitive lattice is obtained by stretching the cubic primitive lattice, and the tetragonal body-centred lattice is obtained by stretching the cubic body-centred and face-centred lattices. [50, 67]

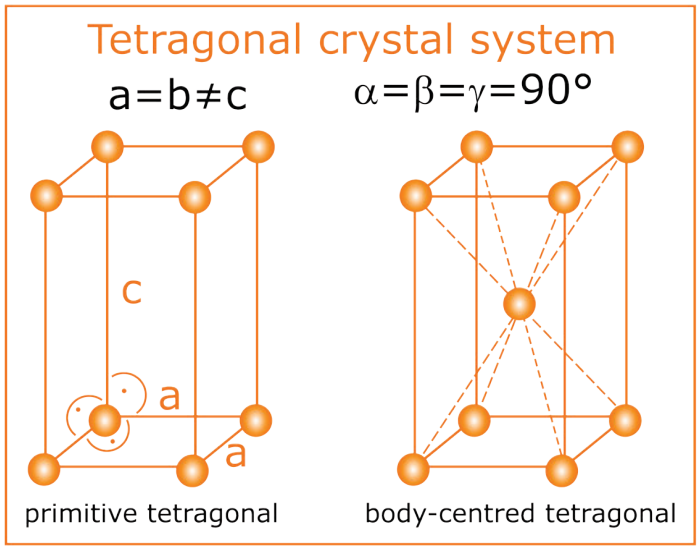


**Figure 6.** The relevant tetragonal Bravais lattices for OLTP crystals. Reproduced in a modified design from Ref. [66].

## 2.4 Lattice Planes and Miller Indices

A lattice plane is defined by at least three lattice points, which do not lie on a straight line. The lattice plane is oriented to the crystal axes (a, b, and c), and intersects the axes at the points with the coordinates m00 (x-axis), 0n0 (y-axis), and 00p (z-axis), which is shown in Figure 7a. Although the position of the lattice plane is unambiguously defined by the coordinates of these three points, the reciprocal values $\frac{1}{m}$, $\frac{1}{n}$, and, $\frac{1}{p}$ are used instead of the direct coordinates. If these values are multiplied by a smallest integer (q), one obtains: [66]

$$h = \frac{q}{n}; k = \frac{q}{m}; l = \frac{q}{p} \tag{3}$$

The triple (hkl) is the smallest integer multiple of the reciprocal axis, and is called Miller indices. The Miller indices are not only used to determine the position of a lattice plane, but also to denote an infinite set of parallel lattice planes, which have the same elementary meshes and lattice plane distances. The triple (hkl) is always indicated with round brackets. Figure 7a is further used to understand the Miller indices. The coordinates of the lattice planes (m, n, and p) are two, three, and three. The corresponding reciprocal values are then $\frac{1}{2}$, $\frac{1}{3}$, and $\frac{1}{3}$. The smallest common number is six. This results in the Miller indices (322). [66]
Figure 7b shows the Miller indices for the lattice planes (100), (110), and (010) in a cubic unit cell. It can be seen that the (100) plane is parallel to the b- and c-axes and intersects only the a-axis. For the m-coordinate the value one is obtained, and for the n- and p-coordinates the terminus infinity (∞) is applied. The reciprocal values are one, zero, and zero, thus the Miller

indices are (100). In general, it should be noted that the Miller indices are zero when the lattice plane set is parallel to the crystal axis. As another example, the (200) plane is shown. Here $m = \frac{1}{2}$, $n = \infty$, and $p = \infty$. The reciprocal values are then two, zero, and zero, which leads to the Miller indices (200). [50, 66, 67]

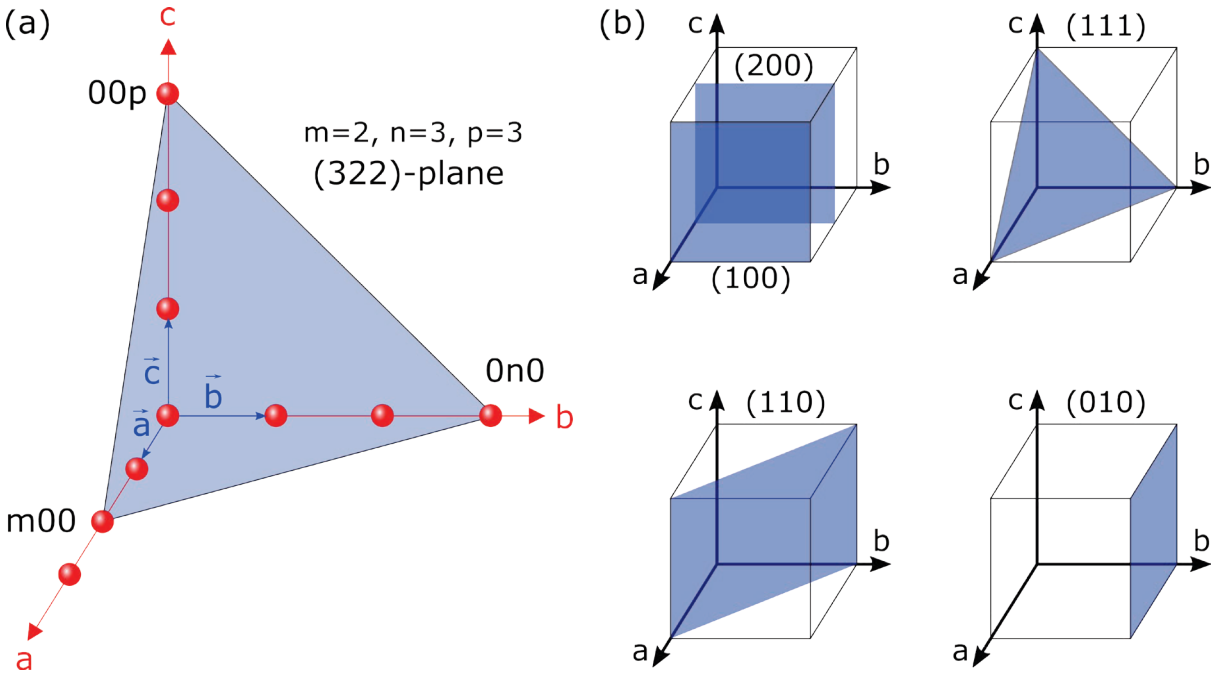


**Figure 7.** (a) Representation of a lattice plane with the Miller indices (322). (b) The Miller indices for the lattice planes (100), (200), (111), (110), and (010), presented in a cubic unit cell. Reproduced in a modified design from Ref. [50] and [66].

## 2.5 The Reciprocal Lattice and the Lattice Plane Distance

The reciprocal lattice is an important tool to illustrate the location of the lattice planes and their X-ray interferences. The reciprocal lattice vector ($\vec{G}$) is defined by the Miller indices (hkl) and the reciprocal basis vectors $\vec{g}_1$, $\vec{g}_2$, and $\vec{g}_3$, as follows: [50, 66]

$$\vec{G} = h \cdot \vec{g}_1 + k \cdot \vec{g}_2 + l \cdot \vec{g}_3 \tag{4}$$

The reciprocal lattice vector is always perpendicular to a lattice plane, which is characterised by the Miller indices. It is further valid that the absolute value $|\vec{G}|$ is inversely proportional to the lattice plane distance ($d_{hkl}$) between two neighbouring planes and the lattice plane set: [50]

$$|\vec{G}| = \frac{2\pi}{d_{hkl}} \tag{5}$$

By means of the distance of $d_{hkl}$, which results from the reciprocal lattice, the lattice constants a, b, and c for a crystallographic system can be calculated. [50]
As shown in Subchapter 2.3, a plane (hkl) is uniquely characterised by three points not lying on a straight line. The crystal axes are then intersected at the points $\vec{P}_1 = \frac{1}{h}\vec{n}_1$, $\vec{P}_2 = \frac{1}{k}\vec{n}_2$, and $\vec{P}_3 = \frac{1}{l}\vec{n}_3$, where the prefactors $h^{-1}$, $k^{-1}$, and $l^{-1}$ indicate the reciprocals of the Miller indices. An arbitrary point on the plane can be described by the vector $\vec{r} = \vec{r}_0 + \vartheta \cdot \vec{y} + \varphi \cdot \vec{z}$. The vector is composed of a receptor point and two direction vectors that lie in the plane, but not on a straight line. Considering now two points in this plane, one can construct the direction vectors

$\vec{y} = \vec{P}_1 - \vec{P}_2$ and $\vec{z} = \vec{P}_2 - \vec{P}_3$. For the position vector $\vec{r}$ with the random receptor point $\vec{r}_0 = \vec{P}_1$ then follows: [50]

$$\vec{r} = \frac{\vec{n}_1}{h} + \vartheta \cdot \left(\frac{\vec{n}_1}{h} - \frac{\vec{n}_2}{k}\right) + \varphi \cdot \left(\frac{\vec{n}_2}{k} - \frac{\vec{n}_3}{l}\right) \tag{6}$$

If now the scalar product of the position vector and the reciprocal lattice vector is calculated, the result is: [50]

$$\vec{G} \cdot \vec{r} = \frac{\vec{n}_1}{h} \cdot \vec{G} + \vartheta \cdot \left(\frac{\vec{n}_1}{h} \cdot \vec{G} - \frac{\vec{n}_2}{k} \cdot \vec{G}\right) + \varphi \cdot \left(\frac{\vec{n}_2}{k} \cdot \vec{G} - \frac{\vec{n}_3}{l} \cdot \vec{G}\right) \tag{7}$$

Due to the orthogonality of the basis vectors $\vec{g}_i$ (i = 1,2,3) of the reciprocal lattice to the location vectors $\vec{n}_j$ (j = 1,2,3) of the spanned plane, the following relation is valid: [50]

$$\vec{g}_i \cdot \vec{n}_j = 2\pi \cdot \delta_{ij} \tag{8}$$

Here, $\delta_{ij}$ represents the Kronecker delta. Inserting equation (8) into equation (7), leads to the following result: [50]

$$\vec{G} \cdot \vec{r} = \frac{1}{h} \cdot 2\pi h + \vartheta \cdot \left(\frac{1}{h} \cdot 2\pi h - \frac{1}{k} \cdot 2\pi k\right) + \varphi \cdot \left(\frac{1}{k} \cdot 2\pi k - \frac{1}{l} \cdot 2\pi l\right) = 2\pi \tag{9}$$

From equation (9) it can be concluded that the scalar product of the normal vectors of a plane $\vec{n}$ with the direction vectors $\vec{y}$ and $\vec{z}$ are equal to zero. Hence, the vectors are orthogonal to each other. As a result, the reciprocal lattice vector $\vec{G}$ is perpendicular to the plane (hkl). Figure 8 is used in order to determine the distance between two adjacent planes (hkl). One plane (hkl) passes through the zero point of the coordinate system, which is characterised by the basis vectors $\vec{g}_1$, $\vec{g}_2$, and $\vec{g}_3$. The other adjacent plane (hkl) is parallel. This plane is characterised by the position vector $\vec{r}$, which has its origin in the zero point. $\vec{r}$ leads to an arbitrary point "P" on the plane. For the distance of the plane from the zero point passing through the neighbouring plane (hkl), the variable "d" is introduced. The equation of the plane is then a scalar product: [50]

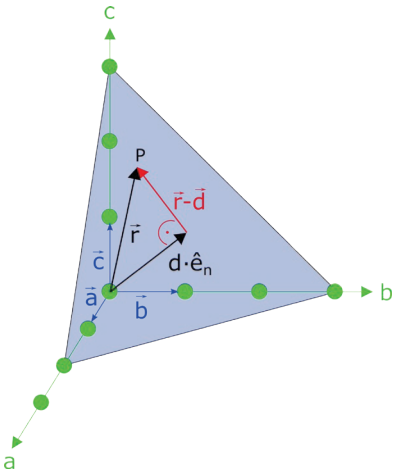


**Figure 8.** Lattice plane and position vector to determine the distance (d). Reproduced in a modified design from Ref. [50].

$$\vec{r} \cdot \hat{e}_n = d \tag{10}$$

Where $\hat{e}_n$ is a unit vector perpendicular to the plane. As shown before, the reciprocal lattice vector is also perpendicular to the plane. From this it can be concluded: [50]

$$\vec{G} = |\vec{G}| \cdot \hat{e}_n \;\rightarrow\; \hat{e}_n = \frac{\vec{G}}{|\vec{G}|} = \frac{d}{\vec{r}} \;\rightarrow\; d = \vec{r} \cdot \frac{\vec{G}}{|\vec{G}|} \tag{11}$$

If the results from equation (4) and equation (9) are now used for the distance between neighbouring planes, the following relationship is obtained: [50]

$$d_{hkl} = \frac{2\pi}{\left|\vec{G}\right|} = \frac{2\pi}{\left|h \cdot \vec{g}_1 + k \cdot \vec{g}_2 + l \cdot \vec{g}_3\right|} = \\ = \frac{2\pi}{\sqrt{h^2 \cdot \vec{g}_1^2 + k^2 \cdot \vec{g}_2^2 + l^2 \cdot \vec{g}_3^2 + 2 \cdot h \cdot k \cdot \vec{g}_1 \cdot \vec{g}_2 + 2 \cdot h \cdot l \cdot \vec{g}_1 \cdot \vec{g}_3 + 2 \cdot k \cdot l \cdot \vec{g}_2 \cdot \vec{g}_3}} \quad (12)$$

The lattice plane distance is to be determined first for a rhombic crystal lattice. As shown in Subchapter 2.3, in this crystal system the angles α, β, and γ are equal to 90° and the crystal axes a, b, and c have different lengths. The lattice vectors $\vec{n}_1 = a \cdot \hat{e}_x$, $\vec{n}_2 = b \cdot \hat{e}_y$, and $\vec{n}_3 = c \cdot \hat{e}_z$ can be expressed by the unit vectors $\hat{e}_x$, $\hat{e}_y$, and $\hat{e}_z$, as previously shown for the lattice plane spacing. Even the reciprocal lattice vectors can be expressed by means of unit vectors: $\vec{g}_1 = \frac{2\pi}{a} \cdot \hat{e}_x$; $\vec{g}_2 = \frac{2\pi}{b} \cdot \hat{e}_y$; $\vec{g}_3 = \frac{2\pi}{c} \cdot \hat{e}_z$. Additionally, the reciprocal lattice vectors $\vec{g}_1$, $\vec{g}_2$, and $\vec{g}_3$ are orthogonal, just as the reciprocal lattice is perpendicular to a plane (hkl). Since the scalar product $\vec{g}_i \cdot \vec{g}_j$ ($i \neq j$) is equal to zero, the term $(2 \cdot h \cdot k \cdot \vec{g}_1 \cdot \vec{g}_2 + 2 \cdot h \cdot l \cdot \vec{g}_1 \cdot \vec{g}_3 + 2 \cdot k \cdot l \cdot \vec{g}_2 \cdot \vec{g}_3)$ from equation (12) is also zero. If the lattice vectors as well as the reciprocal lattice vectors are inserted into equation (12), the lattice plane distance for a rhombic crystal system is finally obtained: [50]

$$d_{hkl} = \frac{2\pi}{\left|h \cdot \frac{2\pi}{a} \cdot \hat{e}_x + k \cdot \frac{2\pi}{b} \cdot \hat{e}_y + l \cdot \frac{2\pi}{c} \cdot \hat{e}_z\right|} = \frac{1}{\sqrt{\left(\frac{h}{a}\right)^2 + \left(\frac{k}{b}\right)^2 + \left(\frac{l}{c}\right)^2}} \quad (13)$$

For OLTPs the cubic and tetragonal crystal structures are relevant. For a tetragonal symmetry the lattice parameters are $a = b \neq c$ ($\alpha = \beta = \gamma = 90°$), therefore equation (13) simplifies to: [50]

$$d_{hkl} = \frac{1}{\sqrt{\left(\frac{h}{a}\right)^2 + \left(\frac{k}{a}\right)^2 + \left(\frac{l}{c}\right)^2}} = \frac{1}{\sqrt{\frac{1}{a^2} \cdot (h^2 + k^2) + \left(\frac{l}{c}\right)^2}} \quad (14)$$

The lattice parameters for a cubic symmetry are $a = b = c$ and $\alpha = \beta = \gamma = 90°$. For the lattice plane distance follows: [50]

$$d_{hkl} = \frac{1}{\sqrt{\left(\frac{h}{a}\right)^2 + \left(\frac{k}{a}\right)^2 + \left(\frac{l}{a}\right)^2}} = \frac{1}{\sqrt{\frac{1}{a^2} \cdot (h^2 + k^2 + l^2)}} = \frac{a}{\sqrt{(h^2 + k^2 + l^2)}} \quad (15)$$

## 2.6 Crystal Morphology

Crystals, especially OLTP crystals, can crystallise in regular geometric shapes and ideally have flat faces. Crystal faces and crystal edges characterise the outer boundary of a crystal and are summarised in the term morphology. The high symmetry of macroscopic crystals results from the internal crystal structure. Therefore, the crystal structure, which has been described in the previous chapters, is related to the crystal morphology. More specifically, each crystal face, which can be seen as a two-dimensional periodic arrangement of crystal building blocks, runs parallel to a set of lattice planes. Furthermore, parallel crystal faces belong to the same set of lattice planes. For this reason, the position of a crystal face can be determined by the Miller indices (hkl). A further reference to the crystal structure is made by the crystal edges, which are parallel to a set of lattice lines. Thus, an edge can be described by the coordinate triple [uvw]. Conversely, it is not possible to infer the lattice parameters of a crystal from its morphology because a crystal has an infinite number of lattice plane sets and lattice lines, but only a few crystal faces and crystal edges. [66]

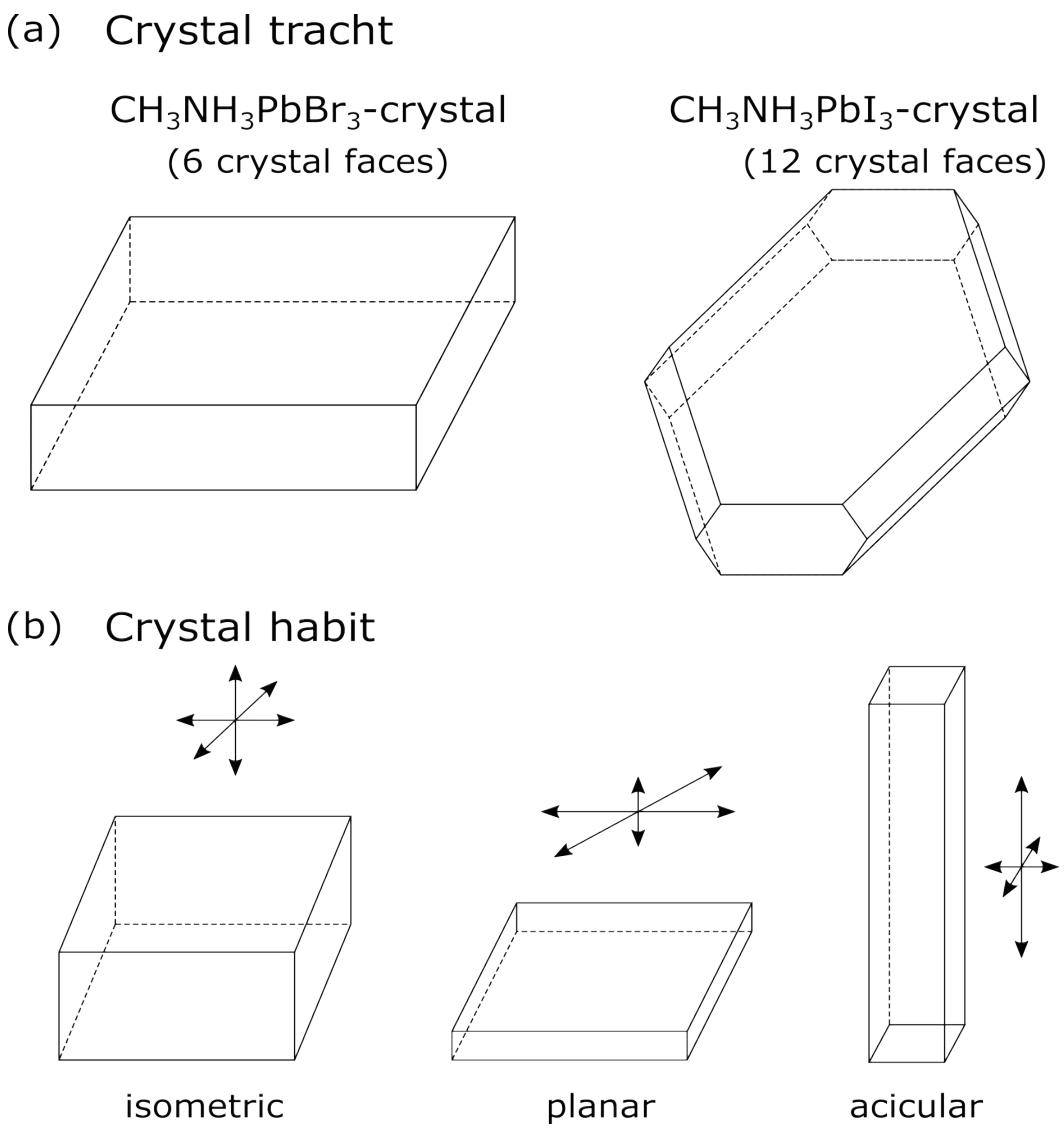


**Figure 9.** (a) Typical crystal shapes of the perovskite crystals $CH_3NH_3PbBr_3$ ($MAPbBr_3$) and $CH_3NH_3PbI_3$ ($MAPbI_3$). Due to the different number of crystal faces, the crystals have a different "tracht" to each other. (b) Possible basic types of a crystal habit for a $CH_3NH_3PbBr_3$ crystal. Depending on the growth direction, an isometric, planar or acicular habit is possible. Reproduced in a modified design from Ref. [66].

In the focus of the morphology are the "crystal tracht" and the "crystal habit" [4]. The amount of crystal faces that are present on a crystal is called crystal tracht. Figure 9a shows the typical crystal form of a perovskite with the stoichiometry $CH_3NH_3PbBr_3$. This perovskite crystallises preferentially as a cuboid and has six crystal faces. In contrast, the $CH_3NH_3PbI_3$ perovskite usually forms 12 crystal faces and has the shape of a hexagon. Due to the different number of faces, the two crystals differ in their crystal tracht. [66]

The relative size ratio of the crystal faces is described by the term crystal habit. A distinction is made between an isometric, planar, and prismatic/acicular habit. OLTP crystals usually have an isometric habit because the growth velocity is constant in all three directions in space. The growth velocity is illustrated by the arrows in Figure 9b. By changing the growth conditions, a crystal could exhibit a planar but also a needle-like shape, as it is illustrated for the $CH_3NH_3PbBr_3$ crystals in Figure 9b. In the case of a planar habit, the growth velocity is restricted in height, while crystal growth is unhindered in both, length and width. In the case of an acicular $CH_3NH_3PbBr_3$ crystal, growth in height is promoted, while growth in length and width is limited. [66]

## 2.7 Defects in Real Crystals

Ideal crystals with a strict periodicity of the crystal building blocks can only be approximated in nature and the laboratory. The regular arrangement of atoms in a real crystal is disturbed by lattice defects. As will be shown in Chapters 5 and 6, OLTP single crystals can be grown in suitable growth conditions, where lattice defects play only a minor role. In this case, it can be assumed that the number of atoms located at a wrong place in the crystal lattice is small compared to the number of atoms located on regular lattice sites. Nevertheless, even a few lattice defects can greatly affect the mechanical and electrical properties of crystalline solids. [50]

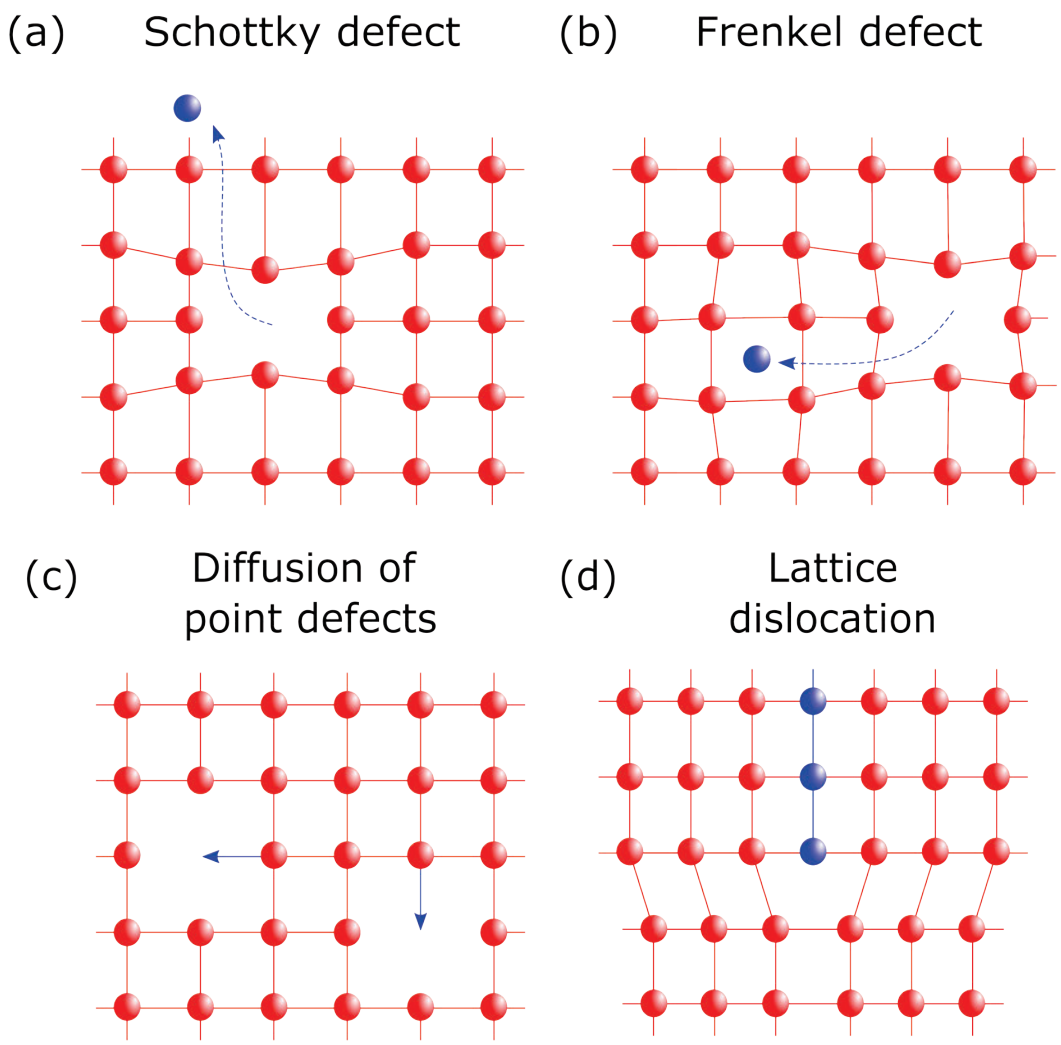


**Figure 10.** (a) "Schottky defect", (b) "Frenkel defect", (c) diffusion of point defects, and (d) lattice dislocation, which are possible defects in real crystals. Reproduced in a modified design from Ref. [50].

Lattice defects can be classified as "Schottky defect" or "Frenkel defect", as well as diffusion of point defects and lattice dislocations, which are illustrated in Figure 10. The Schottky defect is the simplest disorder in the crystal. Here, one atom is missing at a regular lattice site (Figure 10a). In the Frenkel defect, the atoms leave their lattice site and occupy an interstitial site (Figure 10b). However, they do not move to the surface of the crystal. Diffusion of point defects means the following: Unoccupied lattice sites can be occupied by neighbouring atoms (Figure 10c). Other atoms from the neighbourhood can then diffuse into the newly created vacancy. In

this way, the vacancy in the crystal can continuously diffuse. Lattice dislocations occur when atoms of one lattice plane push themselves between neighbouring lattice planes (Figure 10d). The inserted lattice plane thereby compresses and bends the planes in the immediate vicinity. [50]

## 2.8 Organolead Trihalide Perovskite Crystal Structure

OLTPs crystallise in the structure $ABX_3$ [69-74]. Here, the crystal structure is based on the inorganic perovskite calcium titanate with the molecular formula $CaTiO_3$ [70]. However, the base of the OLTP crystal structure consists of an organic cation, the divalent lead cation, and a halogen ion [74-76]. The "A" - cation is either the methylammonium cation

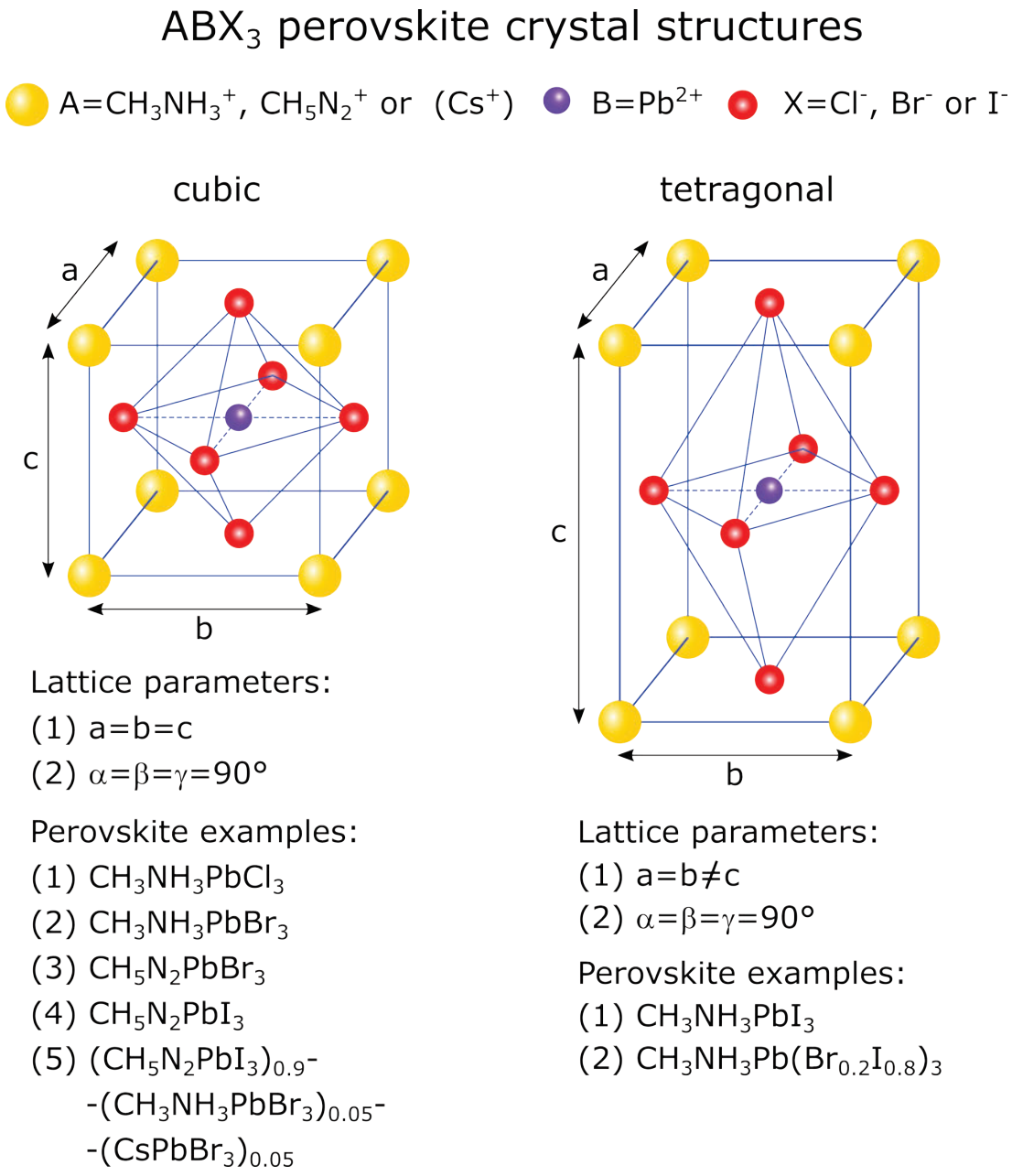


**Figure 11.** The $ABX_3$ perovskite crystal structure for (a) cubic and (b) a tetragonal symmetry, both with the corresponding lattice parameters. For each crystallographic symmetry, a few examples of OLTPs are given. The examples exclusively refer to the OLTP crystal structures at room temperature (RT). Reproduced in a modified design from Ref. [50].

($CH_3NH_3^+$; $MA^+$) or the formamidinium cation ($CH_5N_2^+$; $FA^+$) [58, 69]. The heavy metal cation lead ($Pb^{2+}$) acts as the "B" - cation [58, 69]. Usually the halogen ions chloride ($Cl^-$), bromide ($Br^-$) or iodide ($I^-$) provide the "X" - anion and bind the two cations together [58, 69-71]. Typical hybrid perovskites based on the molecule methylammonium, are $MAPbCl_3$, methylammonium lead tribromide ($MAPbBr_3$), and $MAPbI_3$ [77]. Well-known representatives with the cation formamidinium are formamidinium lead tribromide ($FAPbBr_3$) and $FAPbI_3$ [77]. In principle, perovskite crystals can also contain more than one anion, allowing a variety of different perovskite stoichiometry. For example, the perovskite $MAPb(Cl_{0.2}Br_{0.8})_3$ possesses the two anions chloride and bromide, while the perovskite $MAPb(Br_{0.4}I_{0.6})_3$ contains the two halide ions bromide and iodide [75, 78]. In addition to an increased number of anions, it is conceivable that the OLTP stoichiometry includes both organic cations [79]. A well-known perovskite with this property is formamidinium lead triiodide – methylammonium lead tribromide $(FAPbI_3)_{0.9}(MAPbBr_3)_{0.1}$, which has two cations as well as two anions [26, 80]. The molecular formula of the perovskites becomes even more complex when the number of "A" - cations is extended by including the alkali metal ion caesium ($Cs^+$) [79]. An important perovskite with this feature is formamidinium lead triiodide – methylammonium lead tribromide – caesium lead tribromide $(FAPbI_3)_{0.9}(MAPbBr_3)_{0.05}(CsPbBr_3)_{0.05}$ [81].

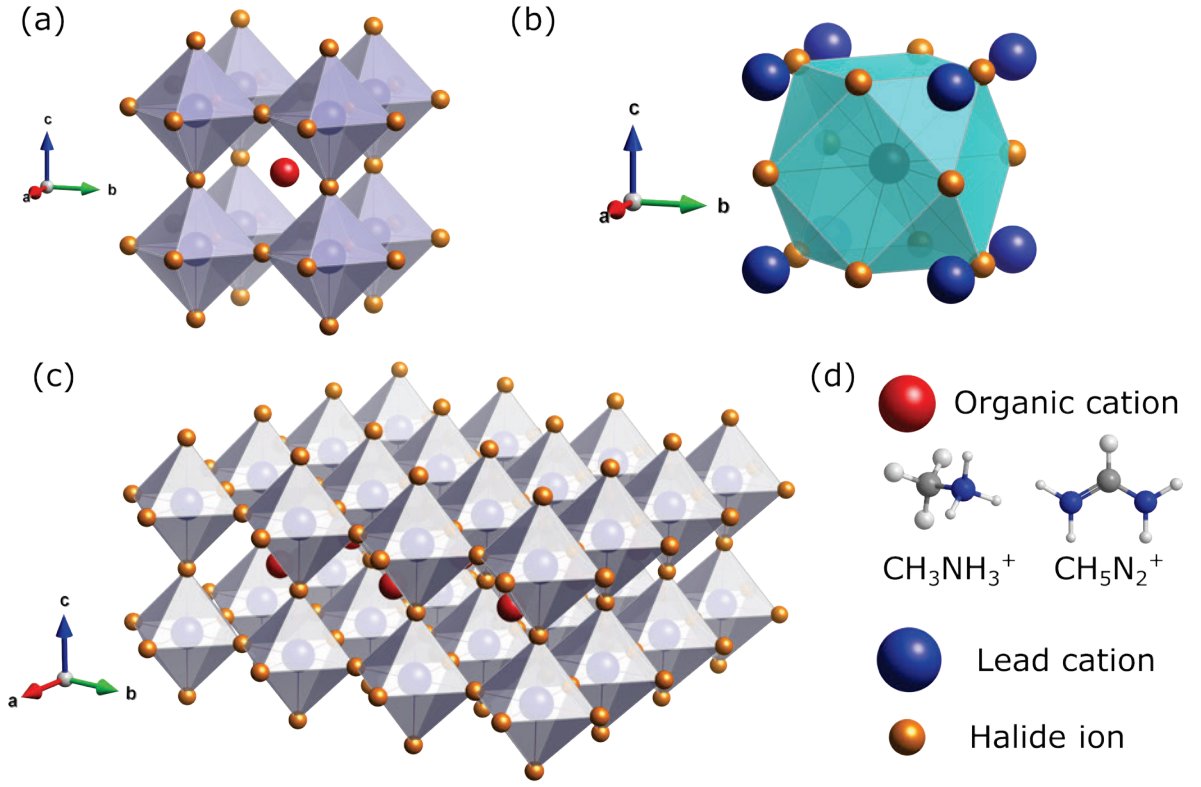


**Figure 12.** OLTP with (a) an octahedral coordination and (b) a cuboctahedral coordination. (c) The three-dimensional periodic arrangement of the organic cation, the lead cation, and the halide ion illustrate the basic structure of an ideal perovskite crystal. (d) Information about the ionic building blocks and the three-dimensional representation of the cations methylammonium and formamidinium. The crystal structures were drawn with the software VESTA. The organic molecules were prepared using the software ChemDraw. Reproduced in a modified design from Ref. [70].

Accordingly, the basis of a hybrid perovskite crystal lattice is much more complex than that of the atomic crystal lattice described in Subchapter 2.2. In general, OLTPs have a cubic crystal structure, but can also possess a tetragonal symmetry [70, 82]. The perovskites $MAPbCl_3$, $MAPbBr_3$, $FAPbBr_3$, $FAPbI_3$, $(FAPbI_3)_{0.9}(MAPbBr_3)_{0.1}$, and $(FAPbI_3)_{0.9}(MAPbBr_3)_{0.05}(CsPbBr_3)_{0.05}$ exhibit a cubic symmetry (Figure 11a) [62, 63, 80, 81, 83]. Perovskites containing the methylammonium cation and a large content of iodide ions

preferentially crystallise in a tetragonal structure. These include $MAPbI_3$ as well as $MAPb(I_{0.8}Br_{0.2})_3$ (Figure 11b) [82, 84, 85].
For a better understanding of the perovskite crystal structure, the crystal building blocks can also be shown in an octahedral or cuboctahedral coordination [86]. Figure 12a shows that six halogen ions (orange sphere) surround the lead ion (blue sphere), forming the $[PbX_6]^{4-}$-octahedron [69, 77, 87]. Another way to represent the perovskite crystal structure is shown in Figure 12b. Here, 12 halogen anions are coordinated around the central organic cation (red sphere), forming the shape of a cuboctahedron [70]. Furthermore, the octahedral perovskite structure was chosen to illustrate the three-dimensional periodicity of the individual ionic building blocks in Figure 12c, thereby giving an idea of an ideal OLTP crystal. It should be noted that the red spheres replace the cations methylammonium and formamidinium whose three-dimensional structures [88] are shown in Figure 12d.
The described cubic and tetragonal OLTP crystal symmetries can be estimated using the Goldschmidt tolerance factor (t) [89]. The tolerance factor refers to the ionic radii $r_A$, $r_B$, and $r_X$ of the "A", "B", and "X" - ions, respectively, and can be specified as follows [69, 71-74, 89]:

$$t = \frac{r_A + r_X}{\sqrt{2} \cdot (r_B + r_X)} \tag{16}$$

The tolerance factor is dimensionless, whereby its values for crystalline perovskite structures at RT can be classified as follows: Values in a range from 0.9 to 1 are equivalent to an ideal cubic perovskite structure [58, 70]. Smaller tolerance factors in a range of 0.7 – 0.9 suggest that either a tetragonal, rhombic or trigonal symmetry is present [58, 70]. This is an indication that either the "A" - cation is too small or the "B" - cation is too large [70]. In the case of a very large "A" - cation, the tolerance factor becomes larger than 1, and a variety of structures are conceivable [58, 70]. If the factor becomes less than 0.7, a precise assignment is no longer possible [58, 70]. An example of the effectiveness of the Goldschmidt factor can be seen in the examples $FAPbBr_3$ and $MAPbI_3$. Here, the radius of the formamidinium cation is 220 pm [69], while the ionic radius of the lead cation is 132 pm [90]. The radius of the bromide ion is 182 pm [91]. This results in a tolerance factor of 0.905 for $FAPbBr_3$, which is equivalent to an ideal cubic perovskite structure [69]. For $MAPbI_3$, the ionic radius of iodide (206 pm) [91] and the radius of the methylammonium cation (180 pm) [69] are required. Combined together with the lead ion radius, this gives a tolerance factor of 0.808 and suggests a non-cubic crystal symmetry [70]. Since the Goldschmidt factor does not provide any information about the lattice parameters, such as the lattice constant, a final determination of the OLTP crystal structure should always be based on X-ray experiments.

## 2.9 Crystal Growth from Solution

The preparation of crystals is diverse and can be performed from solution, the melt, the gas phase, by the formation of derivatives, and even in the solid state [92]. Crystallisation from solution aims to isolate a crystal from its dissolved precursor salts [92] to grow crystalline solids with different symmetries and morphology. In this way, OLTPs are also grown from solution in crystalline form [64, 93]. Terms such as solubility, saturated and supersaturated solutions, as well as nucleation and crystal growth are introduced in this subchapter, which are important to explain solution-based crystallisation methods [68].

### 2.9.1 Solubility and Supersaturated Solutions[1]

Saturated solutions are mostly the starting point for the crystal growth. In a saturated solution, the dissolved concentration of the salt is equal to the solubility of the salt [68]. In an unsaturated solution, the dissolved concentration is less than the solubility of the salt, and in a supersaturated solution, it is greater than the solubility of the salt. To obtain a crystalline precipitate in solution, a supersaturated solution is required because the solubility of finely divided substances is much higher in a saturated or in an unsaturated solution [68]. The solubility of salts and minerals is mostly temperature-dependent, as Figure 13 illustrates [68].

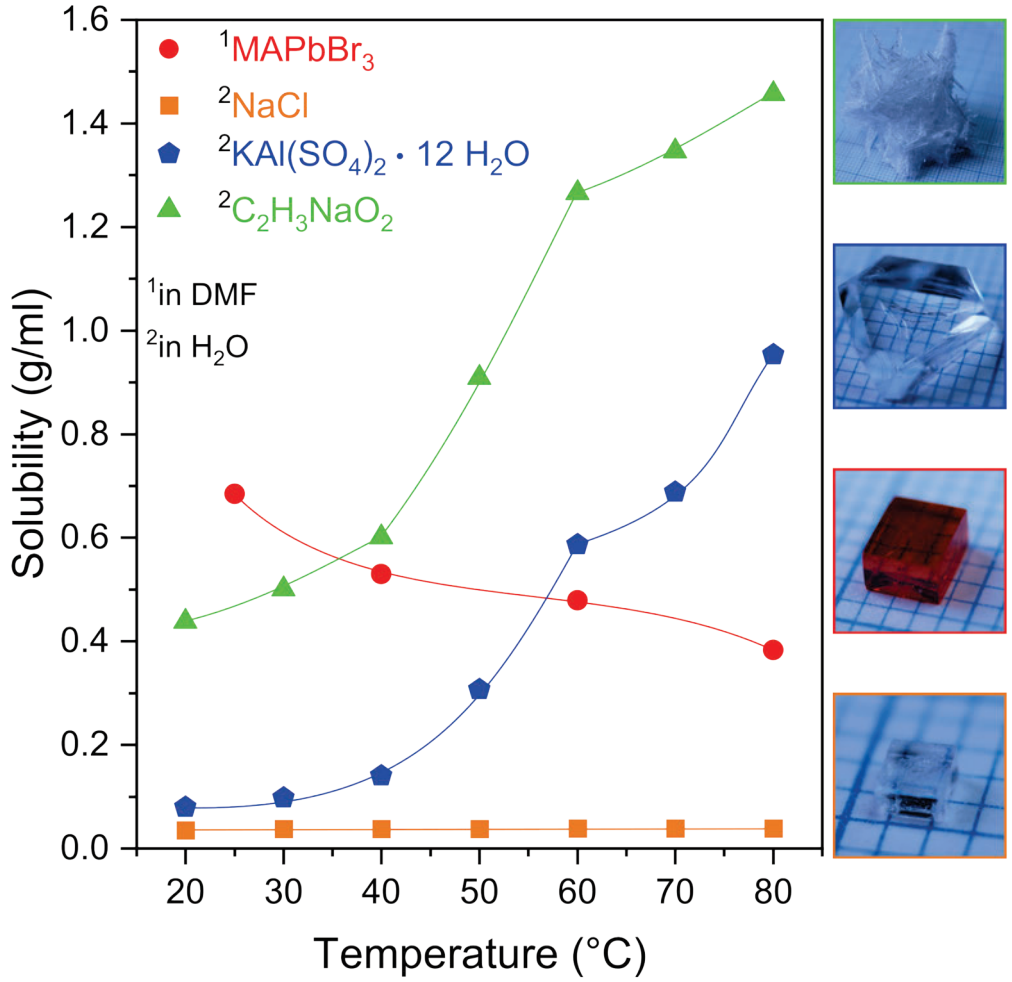


**Figure 13.** The solubility curve of methylammonium lead tribromide ($MAPbBr_3$) in DMF (red curve) shows a decreased solubility with rising temperature. Thus, $MAPbBr_3$ crystals were grown at high temperatures. Other materials such as potassium aluminium sulphate ($KAl(SO_4)_2 \cdot 12\ H_2O$) (blue curve) and sodium acetate ($C_2H_3NaO_2$) (green curve) show an increased solubility in deionized water with increasing temperature, which offers the possibility to grow the crystals at RT. In contrast, the solubility curve of sodium chloride (NaCl) in water (orange curve) does not significantly increase with increasing temperature. Accordingly, NaCl crystals are preferably grown by slowly evaporating the solvent. Reproduced from Ref. [35] with permission from the Royal Society of Chemistry.

Here, the solubility [$mg \cdot ml^{-1}$] describes the amount of a dissolved material per volume of the solution and is given as a function of temperature [68]. To show the dependence of solubility

[1] This subchapter is partially based on the paper *"Influence of crystallisation on structural and optical properties of lead-free $Cs_2AgBiBr_6$ perovskite crystals"* from Melina Armer, Julian Höcker (shared first author), Carsten Büchner, Sophie Häfele, Patrick Dörflinger, Maximilian Sirtl, Kristofer Tvingstedt, Thomas Bein, and Vladimir Dyakonov, published in the Journal CrystEngComm in 2021, volume 23, pages 6848-6854.

on temperature, the four different crystalline materials sodium acetate ($C_2H_3NaO_2$), potassium aluminium sulphate ($KAl(SO_4)_2 \cdot 12\ H_2O$/ alum), sodium chloride (NaCl), and $MAPbBr_3$ were selected. For each material system, the precursor solutions were prepared in a suitable solvent. The solvent for the salts $C_2H_3NaO_2$, alum, and NaCl was deionized water ($H_2O$). For the perovskite $MAPbBr_3$, the organic solvent *N*,*N*-dimethylformamide (DMF) was used. Starting at RT and ending at 80°C, the solubility was determined in 10°C steps. For each temperature step and for each material, a constant amount of the precursor was weighed into a vial. Afterwards, a small amount of the mentioned solvents was added in order to obtain a supersaturated solution. The prepared solutions were placed on a hot plate and stirred for 1 h. Subsequently, solvent amounts of 10 to 30 µl were added to convert a supersaturated solution into a saturated solution. For example, to prepare the alum solubility curve, 616 mg of the salt was weighed in a vial at 60°C. To finally obtain a saturated solution, a total of 1050 µl of distilled water was added. This resulted in a solubility value of 0.587 $mg \cdot ml^{-1}$. For the crystalline solids alum (blue curve) and sodium acetate (green curve) in water, the solubility increases with increasing temperature, whereas sodium acetate has a much higher solubility compared to alum. This is in contrast to the solubility curve of NaCl (orange curve). Although the solubility increases slightly with temperature, this is hardly noticeable in comparison with the solubility curves of alum and sodium acetate. The perovskite $MAPbBr_3$ shows a completely different solubility behaviour in DMF (red curve). Here, the solubility decreases with increasing temperature. [35]
The solubility curves are an important indication of the temperature needed to grow the different crystals, as shown in Figure 13. To grow sodium acetate and alum crystals, saturated solutions are prepared at high temperatures, such as 70°C. These are then cooled to RT to obtain supersaturated solutions and to finally grow crystals. To grow a $MAPbBr_3$ crystal, the effect is reversed. Here, a precursor solution is prepared at RT, which is then heated to generate supersaturation of the solution. In the hot solution, the perovskite crystals finally precipitate. The solubility curve of NaCl also provides an indication of the growth technique. However, since the solubility curve does not significantly increase, a supersaturated solution is achieved only by evaporating the solvent. [35]

### 2.9.2 Nucleation and Crystal Growth

The formation of a crystalline precipitate proceeds in the steps of nucleation and crystal growth. Crystal nuclei are spontaneously formed and are caused by collisions of a few crystal building blocks such as atoms, ions or molecules. If the concentration of building blocks is high in a solution, the probability of their collisions is also higher, resulting in multiple nuclei. Impurities in the solution or the walls of the growth vessels can also contribute to nucleation. If the nucleation rate (ω) is expressed in a formula, the following relationship is applicable: [68]

$$\omega = K' \cdot \frac{c_r - c_\infty}{c_\infty} \tag{17}$$

here $c_r$ is the solubility of a small crystal with the radius (r). The solubility of a macroscopic crystal is $c_\infty$. The term ($c_r$ - $c_\infty$) represents the absolute supersaturation and the term $\left(\frac{c_r - c_\infty}{c_\infty}\right)$ the relative supersaturation. K´ is an arbitrary constant. The formula provides the following information: A high solubility originates from a small supersaturation. For this reason, the nucleation work [94] is greater and thus the nucleation rate is smaller. As a result, a few nuclei grow into larger macroscopic crystals. However, if the supersaturation is high, the solubility of the material decreases. This reduces the nucleation work and increases the nucleation rate. Therefore, a large number of nuclei are formed in the solution, which can only grow into small crystals. [68]

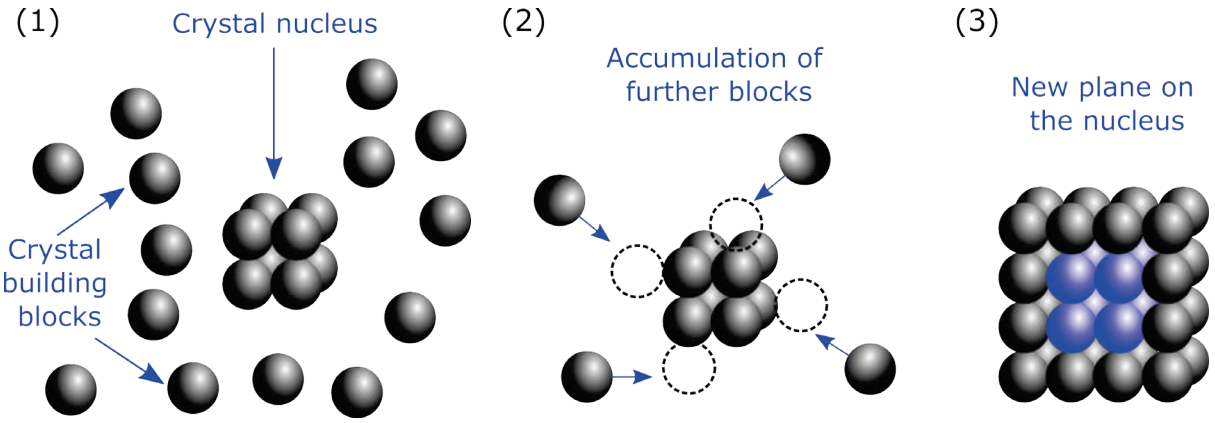


**Figure 14.** (1) Crystal nucleus and crystal building blocks in an OLTP precursor solution. (2) Accumulation of further building blocks on the nucleus. (3) New structural plane formed on the nucleus. Reproduced in a modified design from Ref. [70].

The enlargement of crystal nuclei is referred to as crystal growth and determines the crystal morphology. How fast a crystal grows, can be expressed by the function of the diffusion rate ($v_D$), the absolute supersaturation, and the diffusion constant (K´´): [68]

$$v_D = K'' \cdot (c_r - c_\infty) \tag{18}$$

The concentration $c_\infty$ of the saturated solution is present at the crystal surface, due to the deposited crystal building blocks. The concentration $c_r$ dominates inside the solution because of the supersaturation. This results in a concentration gradient whose diffusion shows in the direction of the crystal, and can be described by the absolute supersaturation. [68]
The nucleation and the growth to a macroscopic crystal are further illustrated by Figure 14. Here, a sphere is used to represent a crystal building block. A nucleus is formed by collisions of individual building blocks and has plane boundary surfaces whose edge lengths are only a few lattice translations in size. Further crystal building blocks attach themselves to the nucleus. Due to the attraction of additional building blocks, new structural planes are continuously formed on the surfaces of the crystal nucleus. This causes the formation of new lattice planes. When further atoms accumulate, a macroscopic crystal is finally formed in the solution [68]. The position at which an atom attaches during crystal growth is shown in Figure 15. The letter marked cubes represent attached atoms on a growing $MAPbBr_3$ crystal in a precursor solution. The probability that atom "X" attaches to an angular position with many neighbouring building

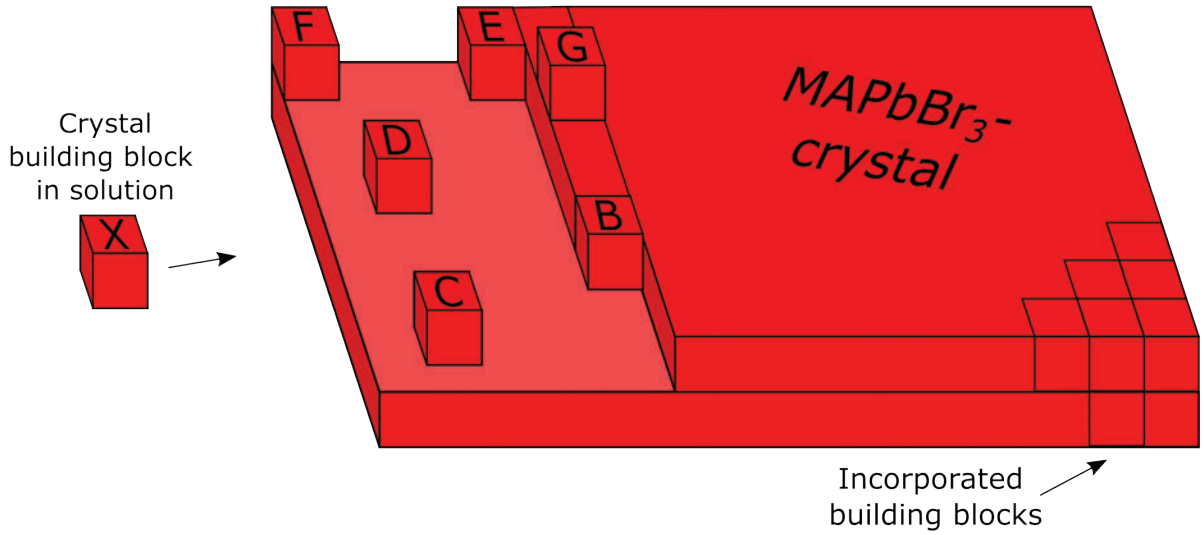


**Figure 15.** Illustration of the different possibilities for the deposition of a crystal building block exemplified by a $MAPbBr_3$ crystal. Reproduced in a modified design from Ref. [95].

blocks (“B”) is the highest. For isolated positions (“C” and “D”) the probability of attachment is the lowest. In general, corner positions (“E” and “F”) are preferred over edge positions (“G”). For this reason, crystal building blocks are more probable to form a new row from the edge rather than from the centre. It is further unlikely that the building blocks will directly be incorporated into the crystal. By adsorption, most of the building blocks initially occupy an energetically unfavourable place. By surface diffusion they occupy their final position. [95]

### 2.9.3 OLTP Crystal Growth Exemplified by Inverse Temperature Crystallisation

By means of the inverse temperature crystallisation (ITC) [62-64, 83], the crystal growth of OLTPs will be explained. The method is based on the fact that the solubility of a perovskite in a suitable organic solvent decreases with increasing temperature [23, 64]. This process is called inverse or retrograde solubility [62, 64]. In order to explain the phenomenon of inverse solubility in more detail, the solubility curve of the perovskite $MAPbBr_3$ was chosen, which is shown in Figure 16. The starting conditions of the solubility curve are the precursor salts lead bromide ($PbBr_2$) and methylammonium bromide (MABr), which react to the perovskite $MAPbBr_3$ in the solvent DMF [64]. The red points of the curve indicate the solubility values for the saturated $MAPbBr_3$ solution and divide the graph into individual sections. The area below the solubility curve marks unsaturated $MAPbBr_3$ solutions. Here, crystal growth is not possible from a diluted solution because the solubility of the dissociated perovskite is too high [68]. The area above the solubility curve represents supersaturated solutions. This means that in a supersaturated solution, there always is a certain amount of the undissolved perovskite $MAPbBr_3$ in a precursor solution. Even if these are supersaturated solutions, no macroscopic $MAPbBr_3$ crystal is usually present in the solution in a temperature range from RT up to a temperature of about 80°C. The precursor salts react to $MAPbBr_3$, but the perovskite is present as a crystalline powder in the solution. Several cm – sized $MAPbBr_3$ crystals grow in the supersaturated precursor solution within a few hours, only at a temperature of about 80°C [62] or higher. This area is called “crystal + solution” in Figure 16 and is separated from the area of the “supersaturated solution” with a dashed line. A dashed line was chosen because it is quite possible to grow macroscopic crystals at lower temperatures such as 75°C. However, this is associated with a longer growth time. With decreasing temperature, the growth of crystals becomes more and more improbable.

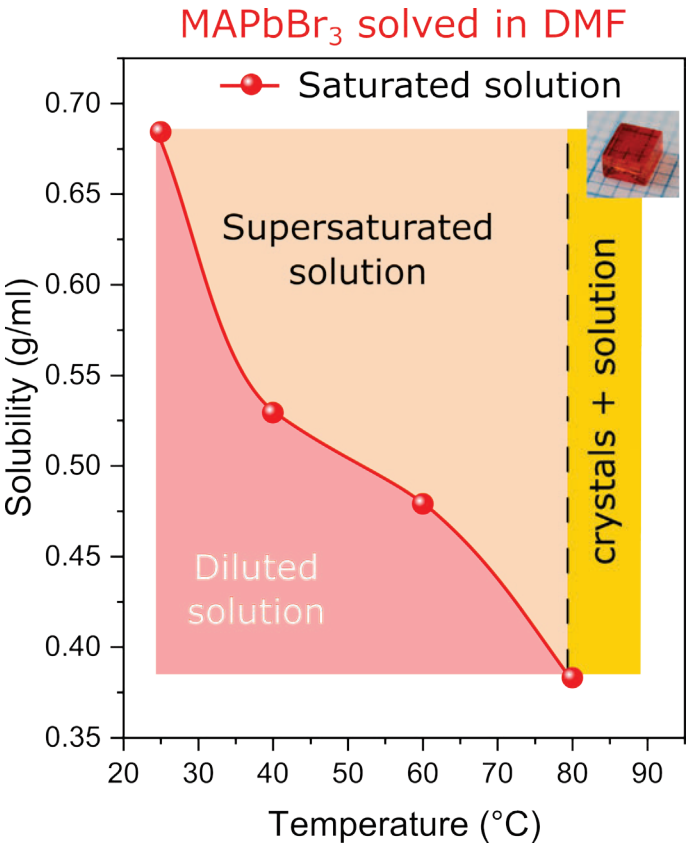


**Figure 16.** The phenomena inverse solubility is exemplified by the perovskite $MAPbBr_3$. The solubility curve splits the graph into the three parts: “diluted solution”, “supersaturated solution”, and “crystal + solution”.

From the observations, a general conclusion can be drawn for OLTPs: After a certain amount of perovskite is sufficiently dissolved at low temperatures, it forms a complex with the

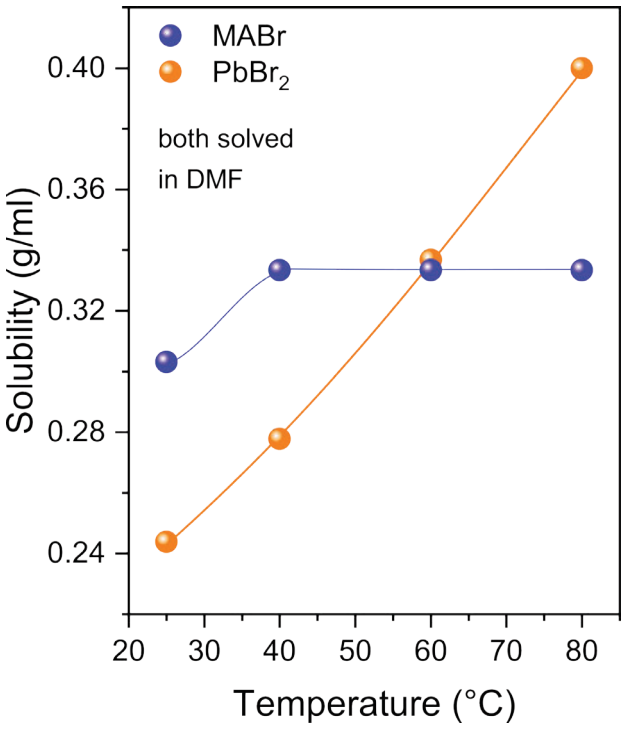


**Figure 17.** Solubility curves of the precursor salts methylammonium bromide (MABr) and lead bromide ($PbBr_2$), which do not show the effect of inverse solubility.

solvent [85, 96]. These coordinative bonds are very strong for OLTPs in a suitable solvent like DMF [85], and is one reason, why hybrid perovskites are well soluble at RT. The solubility of the perovskite is further dependent on the strength of the coordinative bond of the perovskite – solvent complex, which can be broken by heating the solution, resulting in crystal growth [85, 96]. Accordingly, an elevated temperature of the precursor solution and a suitable organic solvent are crucial for crystal growth with ITC [62, 63, 83]. For example, the bromine-containing perovskite $MAPbBr_3$ shows the effect of inverse solubility only in DMF, but not in other organic solvents such as γ-butyrolactone (GBL) [64]. In comparison, the iodine-containing perovskite $MAPbI_3$ shows inverse solubility only in GBL, but not in DMF [64]. The use of the different solvents for a variety of OLTPs is also discussed in Chapters 4 and 6. The inverse solubility behaviour of other OLTPs is furthermore described in Chapter 6.

Another interesting aspect is that only the solubility of OLTPs decreases with increasing temperature, but not their precursor salts [64]. This is clearly demonstrated in Figure 17. Just as for $MAPbBr_3$, the solubility of the precursor salts MABr and $PbBr_2$ were determined. The solubility first increases for the organic salt (blue curve) and then takes on a constant value of 0.33 $g \cdot l^{-1}$ from 40 to 80°C. The solubility of the lead salt (orange curve) even increases constantly with increasing temperature from 0.24 $g \cdot l^{-1}$ at 25°C to 0.40 $g \cdot l^{-1}$ at 80°C. The shape of the curve of $PbBr_2$ is therefore comparable to the ones of alum and sodium acetate in Subchapter 2.9.1, and shows exactly the opposite trend of $MAPbBr_3$. Therefore, the effect of the inverse solubility is solely attributable to the dissociated perovskite [64].

In addition to the description regarding the background of the ITC growth technique, its chronological sequence was considered. This is shown in Figure 18 by means of the perovskite $MAPbI_3$. For this purpose, the precursor salts methylammonium iodide (MAI) and lead iodide ($PbI_2$) were dissolved in the solvent GBL [62]. After this, the precursor solution was heated to 110°C to initiate the crystallisation process [62]. The photos of the $MAPbI_3$ precursor solution, which were taken at different times, are shown on the left in Figure 18. Furthermore, the colour scale in the middle highlights the different colours of the $MAPbI_3$ solutions. The provided time scale is used to describe the crystallisation process (right side).

At the beginning, a clear and yellow $MAPbI_3$ precursor solution was present. In the first half hour the saturated solution turned into a supersaturated solution, due to the high temperature of 110°C, and the first crystal nuclei formed. Over a period of up to 5 h, the nuclei grew into black macroscopic crystals with sharp corners and edges. During this time, the colour of the $MAPbI_3$ crystal solution changed from yellow to orange. After 5 h, the crystal growth stopped and after 25 h the solution turned wine red. The solution became turbid and its colour changed to deep brown after 35 h. During this period, it was observed that the sharp corners and edges of the crystals disappeared and adopted a rounded shape. After about 42 h, the crystals continued to dissolve. In addition, a phase separation of the solution occurred. The upper part of the solution

was deep black, while the lower part was yellowish turbid. The described process can be seen as an ageing of the solution caused by the high applied temperature [68]. Crystal growth with ITC is therefore limited to a few hours. Alternatives to the method are shown in Chapters 5 and 6.

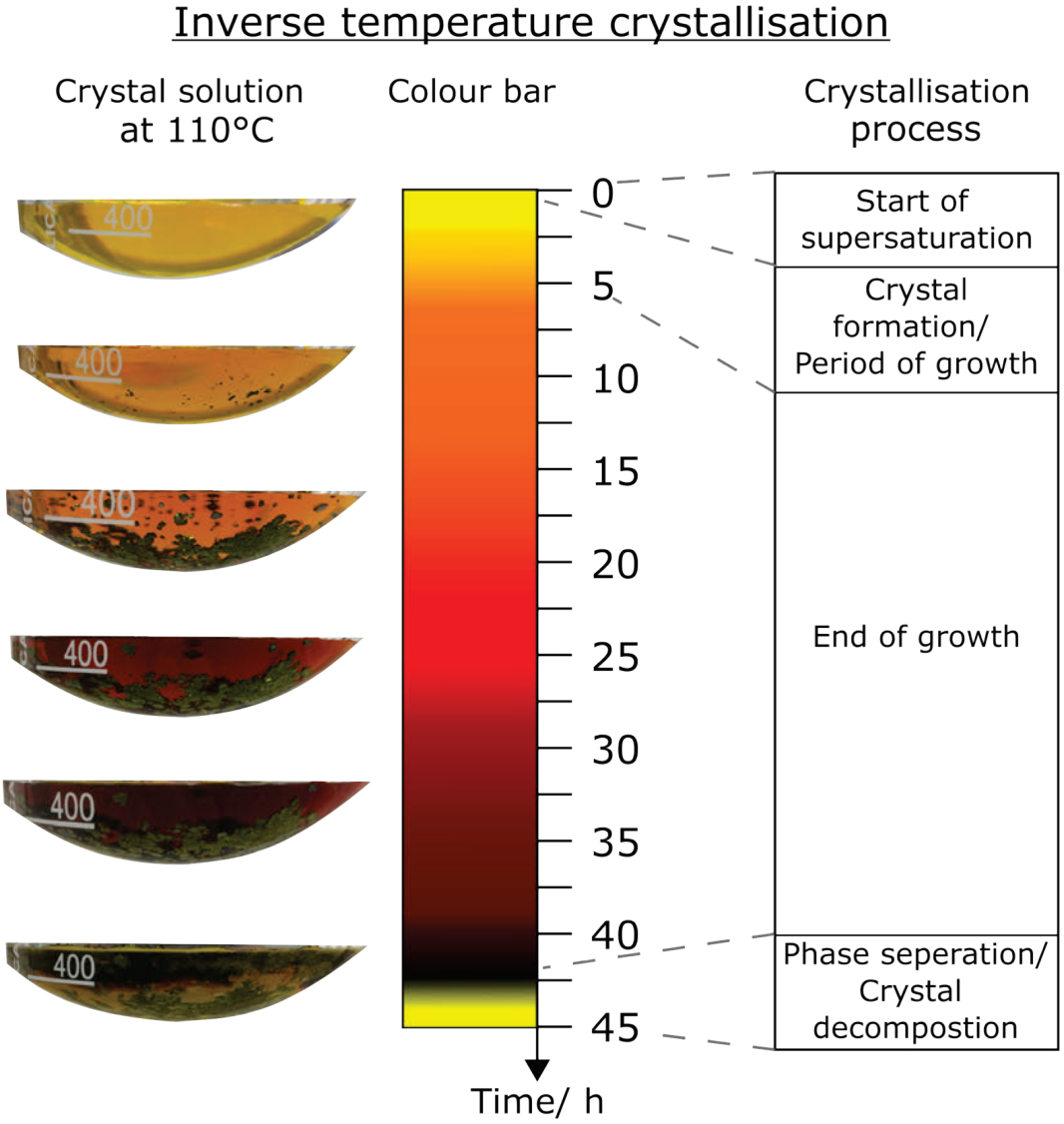


**Figure 18.** Chronological sequence of the inverse temperature crystallisation (ITC) method using the perovskite $MAPbI_3$ as an example. (left) Photos of the $MAPbI_3$ – γ-butyrolactone (GBL) precursor solution at 110°C taken at different times. (middle) Colour bar which highlights the colours of the precursor solution as a function of time. (right) Description of the crystallisation process in dependence of time.

## 2.10 Concluding Remarks

In this chapter, the theoretical background of crystallography concerning OLTPs was described. The focus was on the definition and structure of a single crystal as well as the classification of crystal lattices. In addition, the terms Miller indices and lattice plane distance were explained. The introduction of the reciprocal lattice was used to determine the lattice constant, which will be further elaborated in Chapter 3 using examples of X-ray measurements. In addition, crystal morphology, possible defects in real crystals, and OLTP crystal structures were presented. Furthermore the perovskite crystal growth from solution was described to gain an understanding of the crystallisation processes in Chapters 4 – 6.

# 3 Scientific Tools for the Investigation of Perovskite Crystals

This chapter is intended to give an overview of different measurement methods, which are necessary to characterise perovskite crystals. These scientific tools are illustrated by example measurements of OLTP crystals in order to provide a better understanding of the measurement results in Chapters 4, 5, and 6. One measurement method is X-ray diffraction, which was used for the structural investigation of the crystals. X-ray spectroscopy was applied to identify the elements that had been incorporated into the crystals. Another characterisation method was optical spectroscopy, which was performed to obtain absorption spectra and to determine the absorption edges of the crystals. The introduction of photovoltaic parameters, which were used to characterise photodetectors and solar cells based on perovskite crystals, conclude the chapter.

## 3.1 X-ray Diffraction

Important methods for material characterisation are XRD techniques. The spectroscopic technique of X-ray diffractometry is used to analyse the crystal structure of materials. X-rays are short-wave and high-energy electromagnetic radiations generated in an X-ray tube, such as the one shown in Figure 19. The X-ray tube is a vacuum tube, and contains the electron source and two electrodes. Here, the cathode is made of a heavy metal, such as copper (Cu). Since a lot of heat is released when X-rays are generated, the setup must be cooled. The generation of X-rays can be described as follows: Electrons escape from the heated cathode and are accelerated by a high-voltage field. The electrons, which have a high velocity, hit the anode and are decelerated there. When the electrons reach the Cu-anode, their kinetic energy of the electrons is converted into the energy of X-rays. Since the generated X-rays radiate in all directions, they are deflected in a specific direction by a built-in window. [50, 97]

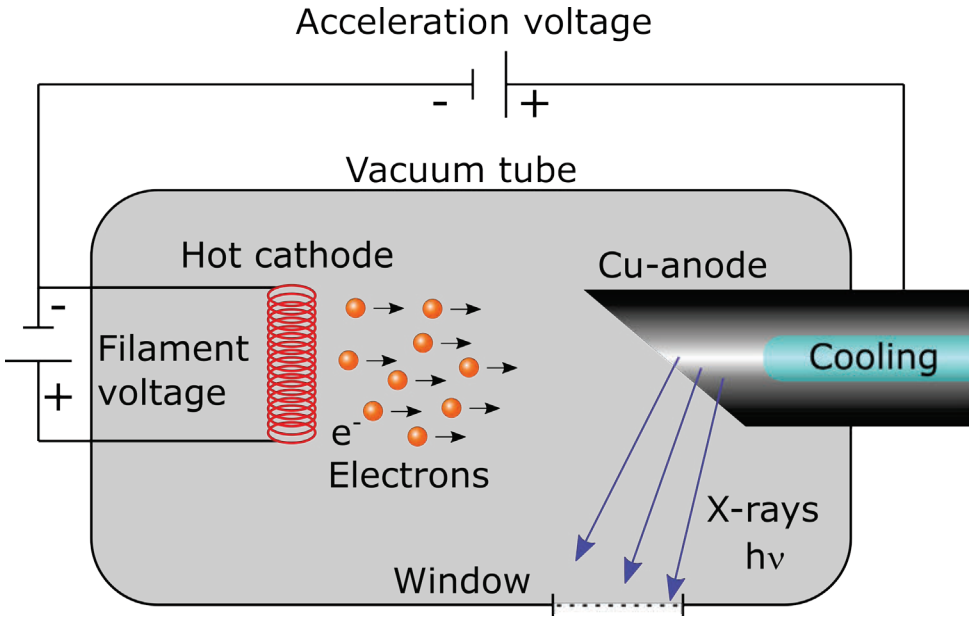


**Figure 19.** Illustration of an X-ray tube. Accelerated electrons hit the copper (Cu) anode, which generates X-rays, passing through a window for diffraction. Reproduced in a modified design from Ref. [97].

To induce characteristic X-rays, a generated electron needs enough energy to excite an electron in the inner shell of an atom to a higher-energy state. This causes a vacancy in the inner shell, which is occupied by an electron from an outer shell. The occupation of the inner shell releases energy through the emission of X-rays of a specific wavelength. Figure 20a illustrates the described process more clearly. Here, the atomic nucleus is surrounded by the shells "K", "L", and "M". A vacancy in the K-shell can be filled from either the L- or M-shell. This results in the emission of the characteristic $K_\alpha$ or $K_\beta$ X-rays. This is also applicable to the other shells, so that a vacancy in the L-shell can be filled by an electron from the M-shell. This results in the emission of the $L_\alpha$ radiation. However, the probability of a vacancy in the K-shell being filled by an L-shell electron is much higher than that of an electron from the M-shell. This leads to the conclusion that the intensity of $K_\alpha$ X-rays is much higher than the intensity of $K_\beta$ radiations. Due to the subshell structure of the L-shell, a further distinction is made between the characteristic lines $K_{\alpha1}$ and $K_{\alpha2}$. The formation of the two X-rays is illustrated in Figure 20b. If an electron from the $L_3$-shell falls into the vacancy of the K-shell, $K_{\alpha1}$ radiation is generated, and if an $L_2$-shell electron occupies the K-shell vacancy, $K_{\alpha2}$ radiation is emitted. In summary, $K_{\alpha1}$, $K_{\alpha2}$, and $K_\beta$ represent the X-rays with highest intensity. For the investigation of the OLTP crystals and their corresponding crystalline powders, the monochromatic $K_{\alpha1}$ X-rays with a wavelength of 0.15406 nm were employed *via* a filter system. [97]

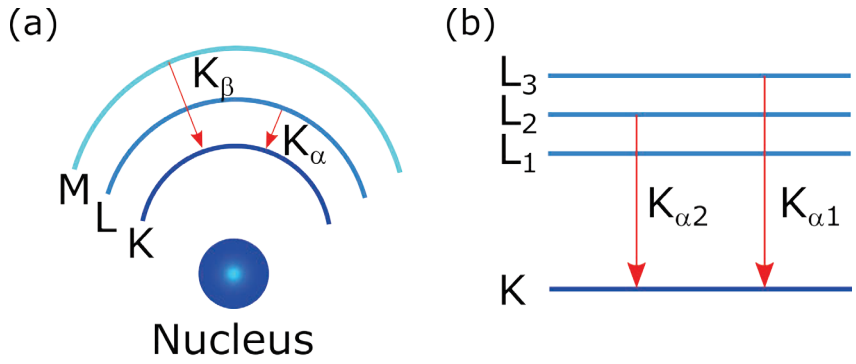


**Figure 20.** Illustration of the generation of the X-rays (a) $K_\alpha$, $K_\beta$, and (b) of $K_{\alpha1}$ as well as $K_{\alpha2}$. Reproduced in a modified design from Ref. [97].

### 3.1.1 Bragg's Law

One goal of X-ray examination is to determine the lattice constants of the OLTPs on the basis of crystal powders. Thereby, X-rays are directed onto the crystalline powder, whereas part of the radiation passes through the powder, while another part of the X-rays is deflected. This is called X-ray diffraction. The phenomenon is based on the reflection of the X-rays from the individual lattice planes of a crystal or a crystal powder and only occurs when the reflections are constructively superposed. This condition is described by Bragg's law, which is derived from Figure 21 in the following: Two incident waves 1 and 2 with the wavelength λ strike the lattice planes "X" and "Y". The lattice planes are parallel to each other at the distance $d_{hkl}$ (orange line). The grey spheres represent the atoms of the lattice planes and the distance $\overline{AC}$ of the atoms. "A" and "C" corresponds exactly to the distance of the lattice plane ($\overline{AC} = d_{hkl}$). The incident waves are diffracted at the crystal lattice that is shown by the deflecting waves 1' and 2'. The angle between the incident X-ray beam and the lattice planes is called Bragg angle (θ), which is shown exemplarily for wave 1 and the lattice plane "X". Due to the reflection law, the diffracted waves have the same angle as the incident waves. The incident waves can either constructively or destructively interfere. In the case of constructive interference, the two incoming waves have a phase difference of $(n \cdot \lambda)$, where "n" is an integer and represents the

diffraction order. When this condition is valid, the integer multiple of λ corresponds to the distance 2δ (two red lines) for the following reason: Since wave 2 must reach a lower lattice plane compared to wave 1, it has to cover a greater distance. Thus, both waves are phase-shifted with respect to each other. The path of wave 2 is then extended by the distance $\overline{BCD}$ between the points "B", "C", and "D". If the longer distance $\overline{BCD}$ of wave 2 is an integer multiple of the wavelength, the waves constructively interfere, according to equation (19): [97, 98]

$$\overline{BCD} = 2 \cdot \delta = n \cdot \lambda \tag{19}$$

To determine the distance δ, the simple geometric relationship of the sinus function can be used since the distances $\overline{AB}$ (green line), $\overline{AC}$, and $\overline{BC}$ span a triangle. Accordingly, the hypotenuse of the triangle is given by the lattice plane spacing $d_{hkl}$. The angle is the Bragg angle, and $\delta = \overline{BC} = \overline{CD}$ represents the opposite leg of the angle: [97, 98]

$$sin(\theta) = \frac{\delta}{d_{hkl}} \quad \rightarrow \quad \delta = sin(\theta) \cdot d_{hkl} \tag{20}$$

Inserting equation (20) into equation (19) yields the following: [97, 98]

$$n \cdot \lambda = 2 \cdot d_{hkl} \cdot sin(\theta) \tag{21}$$

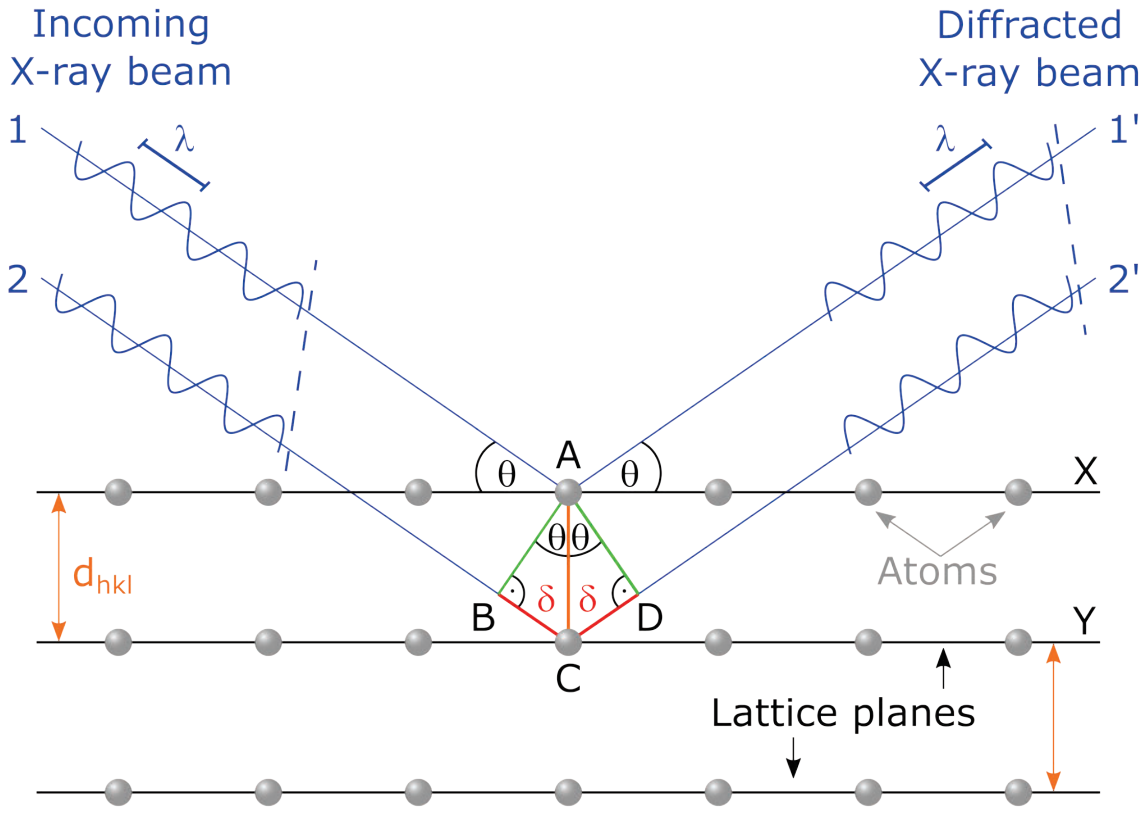


**Figure 21.** Illustration of the X-ray diffraction (XRD) at crystallographic planes. If the path distance $\overline{BCD}$ of wave 2 is an integer multiple of the wavelength λ, wave 1 and 2 constructively interfere and Bragg's law is applicable. Reproduced in a modified design from Ref. [97].

To sum up, it is possible to obtain information on the lattice spacing distance for any crystalline material by recording the corresponding Bragg reflex. Furthermore, by using the relationship between $d_{hkl}$, the Miller indices, and the lattice constant, which resulted from the derivation of

the reciprocal lattice in Subchapter 2.5, equation (15) can be inserted in equation (21). This leads to the following result for a cubic crystal: [97]

$$sin^2(\theta) = \frac{\lambda^2}{4 \cdot a^2} \cdot (h^2 + k^2 + l^2) \tag{22}$$

The Miller indices of the crystallographic planes are not directly given by equation (22), instead the expression $(h^2+k^2+l^2)$ must first be converted to the form (hkl). Since many perovskites have a cubic system, the expression is easy to determine for low-index planes. For example, if the index of the lattice plane is (110), the expression $(h^2+k^2+l^2)$ is then two. [97]

### 3.1.2 X-ray Measurements on Perovskites

To investigate the crystalline properties of perovskites, an X-ray diffractometer was used, which consisted of an X-ray source, a sample stage, and a detector. A monochromatic X-ray beam (copper $K_{\alpha 1}$) was focused on the investigated sample, where it was diffracted and finally detected. Either a perovskite powder or a crystal was used for the investigation. The X-ray source and detector are moved at a constant angle. The scattering angle formed by the incident X-ray beam with the sample under investigation is θ, and the diffraction angle is 2θ, which is illustrated in Figure 22. In the range of the diffraction angle 2θ, the diffraction intensity of the sample was measured. Thus, a diffraction pattern of the sample was obtained. [97]

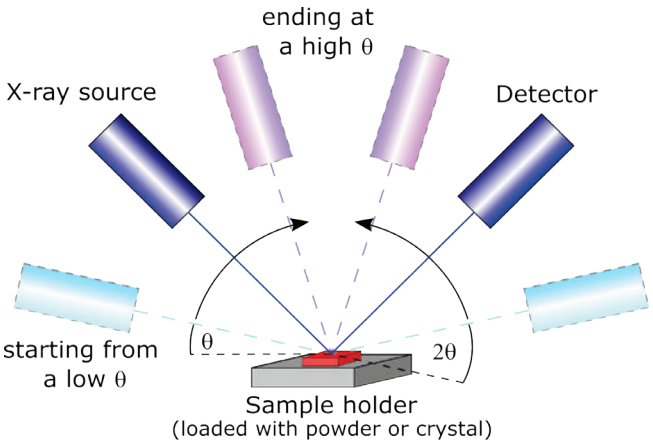


**Figure 22.** Illustration of the X-ray diffractometry and its geometric arrangement.

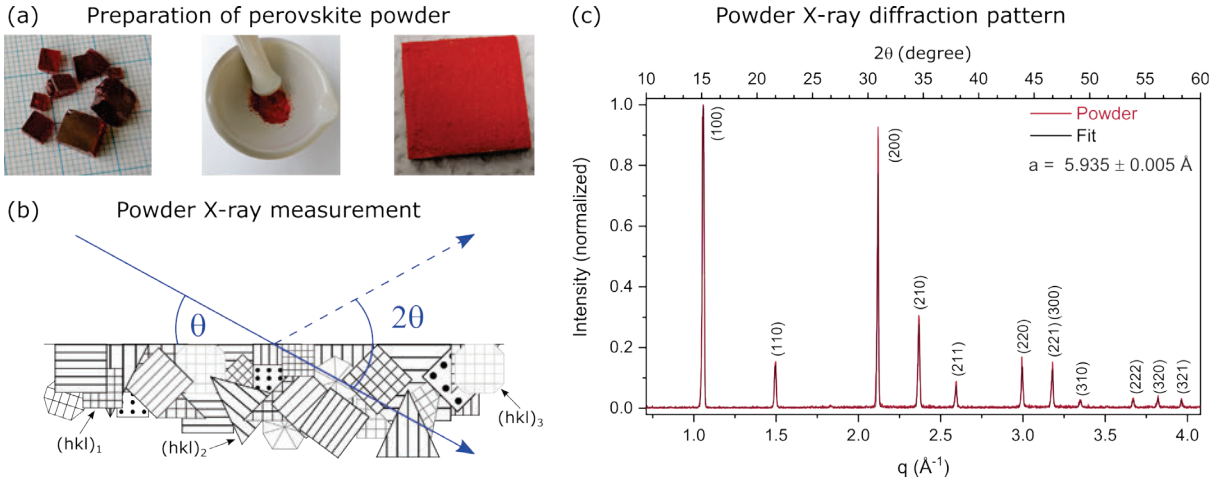


**Figure 23.** (a) Preparation of a perovskite powder exemplified by the Bi-doped perovskite $MAPbBr_3$. (b) The grinded powder is useful to investigate the lattice planes of the crystalline material with the X-ray reflectometry. (c) Powder X-ray diffraction (PXRD) pattern of the perovskite. The diffraction of the lattice planes is visualized by the obtained peaks. The diffraction intensities of the peaks are usually normalized to the highest peak in the diffraction pattern. Figure 21b is reproduced with permission from Ref. [99].

To obtain a powder X-ray diffraction (PXRD) pattern, the pre-grown perovskite crystals must be ground to a fine powder with a mortar and pestle. This is exemplified by the bismuth (Bi)-

doped $MAPbBr_3$ perovskite in Figure 23a. Through grinding, a large number of tiny crystals or grains are obtained, which are distributed randomly, so that the Miller indices for all crystallographic planes can be detected (Figure 23b) [99]. For the measurement, the diffractometer is moved from a low 2θ to a higher 2θ to record the change in diffraction intensity. To study the perovskite powders, diffraction angles were set from 10 to 60° and X-rayed at a step size of 0.02° and an integration time of 5 s. The intensity change is visible as a peak in the diffraction pattern, whereas each peak represents a diffraction at a specific lattice plane. A Miller index can then be assigned to each peak (lattice plane), respectively, as it was done for the PXRD pattern in Figure 23c. Furthermore, the peaks were fitted to determine their exact position in the pattern. Finally, the lattice constant of the material can be determined *via* the Bragg Law. The calculation of the lattice constant of the Bi-doped perovskite is shown in Table 2 as an example. [97]

**Table 2.** Evaluation of the X-ray diffraction (XRD) fitting data to determine the lattice plane ($d_{hkl}$) and the lattice constant (a) of the Bi-doped methylammonium lead tribromide ($MAPbBr_3$) crystal powder.

| Number | Fitting data 2θ (°) | Fitting data q ($Å^{-1}$) | Miller indices (hkl) | $d_{hkl}$ (Å) | a (Å) |
|---|---|---|---|---|---|
| 1 | 14.889 | 1.05687 | 100 | 5.945 | 5.94509 |
| 2 | 21.125 | 1.49521 | 110 | 4.202 | 5.94282 |
| 3 | 30.101 | 2.11812 | 200 | 2.966 | 5.93279 |
| 4 | 33.743 | 2.36737 | 210 | 2.654 | 5.93471 |
| 5 | 37.072 | 2.59314 | 211 | 2.423 | 5.93512 |
| 6 | 43.084 | 2.99509 | 220 | 2.098 | 5.93356 |
| 7 | 45.857 | 3.17783 | 221 | 1.977 | 5.93159 |
| 8 | 45.857 | 3.17783 | 300 | 1.977 | 5.93159 |
| 9 | 48.462 | 3.34778 | 310 | 1.877 | 5.93503 |
| 10 | 53.467 | 3.66935 | 222 | 1.712 | 5.93173 |
| 11 | 55.861 | 3.82072 | 320 | 1.645 | 5.92935 |
| 12 | 58.121 | 3.96214 | 321 | 1.586 | 5.93354 |

The perovskite has a cubic crystal structure with a lattice constant of 5.935 Å, which corresponds well with findings in the consulted literature [100]. The crystal system of the perovskite can further be considered as a simple cubic one because most of the diffraction possibilities are present in the PXRD pattern, which is in accordance with the structure extinction rules for lattice planes [97]. Since the measurement was carried out by using the X-ray wavelength of a copper anode, the PXRD pattern is not comparable to diffraction patterns obtained with diffractometers using iron, chromium or molybdenum anodes [97]. Therefore, the wavelength-independent scattering vector (q) is introduced to compare different XRD patterns [26, 101]:

$$q = \frac{4 \cdot \pi}{\lambda} \cdot sin\left(\frac{2\theta}{2}\right) \tag{23}$$

In addition to the determination of the lattice constants on the basis of crystalline perovskite powders, the X-ray reflectometry also provides meaningful insights about the crystal quality. For this purpose, the crystal surfaces are measured in the diffractometer. In the case of a high quality crystal, the diffraction pattern shows only the peaks of one crystal plane. Taking the perovskite crystal $MAPb(Br_{0.1}I_{0.9})_3$ as an example, such a measurement was performed (Figure 24). The XRD pattern was recorded in a diffraction angle range of 10 to 60° with a step width

of 0.01° and an integration time of 15 s. In the range of 19° – 21° and 40° – 42° a higher step width of 0.005° and a higher integration time of 15 s was applied, due to the expected peaks at these diffraction angles. The pattern reveals two sharp peaks, which can be assigned to the Miller indices (200) and (400) (Figure 24a). For an improved representation of the pattern, a logarithmic plot in dependence of the scattering vector is useful to identify possible other peaks (Figure 24b). If no other peaks are present in the logarithmic plot, no other lattice planes are present at the crystal's surface, which points towards a high quality.

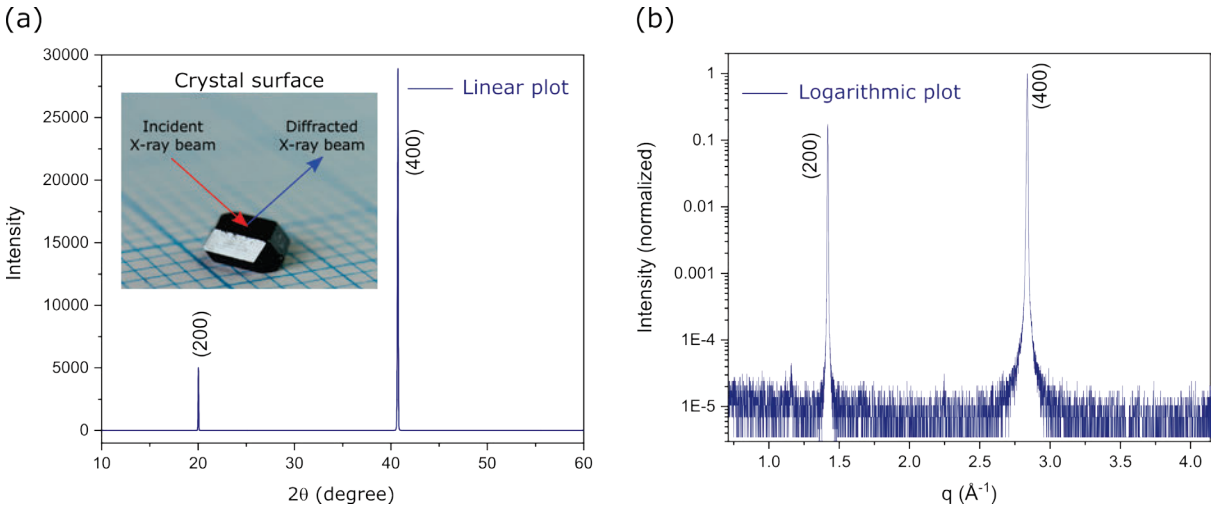


**Figure 24.** X-ray reflectometry to determine the quality of the $MAPb(Br_{0.1}I_{0.9})_3$ crystal surface. If there are only the peaks of one lattice plane visible in the (a) linear and (b) logarithmic plot, a high quality of the crystal surface can be assumed.

Another important method to investigate the quality of crystals is the rocking scan. A rocking scan is usually performed after a recorded XRD pattern since a reflection must be selected from the diffraction pattern for the measurement. Accordingly, the rocking scan is performed at a fixed diffraction angle 2θ, while the X-ray source and detector are moved by the Bragg angle θ to measure the intensity of the reflection (Figure 25a). A rocking curve is therefore also known as a reflection curve. When passing through the reflection range around the Bragg angle θ, disturbances in the crystal lattice structure can thus be visualized. Ideally, a rocking scan will contain only one sharp peak corresponding to the Bragg angle of the appropriately selected reflex. However, real crystals can consist of little tilted areas. This phenomenon is called "mosaicity". [102]

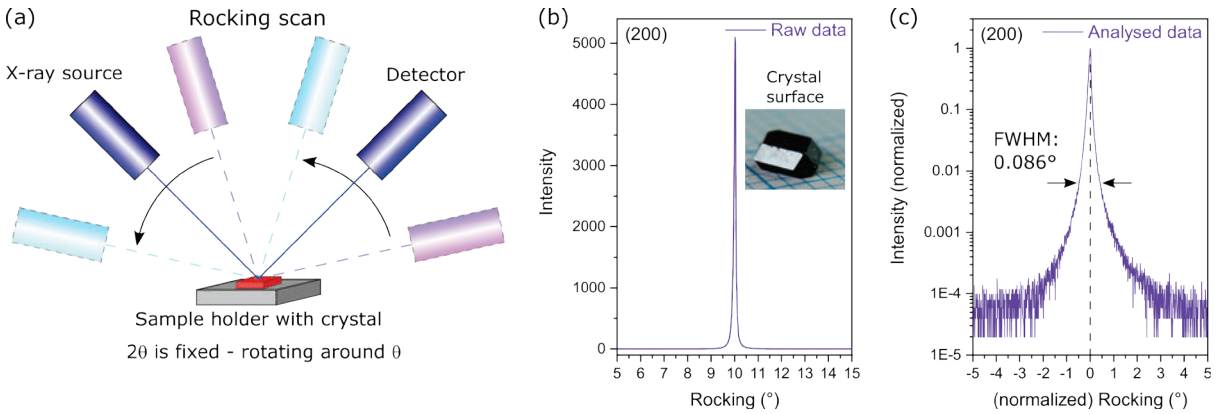


**Figure 25.** (a) Illustration of a rocking scan. (b) Linear and (c) logarithmic plot of a rocking scan, performed on crystal surface of the perovskite $MAPb(Br_{0.1}I_{0.9})_3$.

These mosaic blocks "shine up" as they pass through the reflection area by the Bragg angle. If these partial reflections are measured over a wide angular range, the result then is a rocking

curve. The wider a rocking curve is, the more tilted areas exist in the crystal. The narrower the rocking peak, the lower is its mosaicity. Accordingly, the full width at a half maximum (FWHM) of a rocking peak is also referred to as the mosaicity width and provides information about the crystal quality. Usually, dislocation-free crystals have a FWHM below 0.016°, while the FWHM of mosaic crystals are larger than 0.016°. [102]

For a better understanding of the rocking scan, such a scan was carried out by using the $MAPb(Br_{0.1}I_{0.9})_3$ crystal as an example. For this purpose, the reflection with the Miller indices (200) was selected. The diffraction angle of the reflection was 20.04°, which corresponds to a Bragg angle of 10.02°. To obtain a wide reflection range, Bragg angles were set from 5 to 15°, with a step size of 0.01° and an integration time of 15 s. The rocking scan revealed a sharp peak at $\theta = 10.02°$ with an intensity above 5000 counts (Figure 25b). Finally, to determine FWHM, a logarithmic plot was chosen (Figure 25c). In order to compare the rocking scan with those of other crystals, the intensity was normalised to one and the Bragg angle was set to zero. The FWHM for the $MAPb(Br_{0.1}I_{0.9})_3$ crystal was 0.086° and suggests a slightly increased mosaicity.

### 3.1.3 X-ray Spectroscopy to Identify the Composition of Perovskites

X-rays can also be used to study the chemical composition of perovskite crystals and their crystalline powders (Figure 26a). This technique is called X-ray spectroscopy and includes, among others, the X-ray fluorescence (XRF) spectroscopy, which is based on the photoelectric effect. In the XRF method, a primary X-ray beam strikes a sample. This excites the sample, which in turn emits X-rays. To distinguish this secondary emission from the primary X-ray radiation, the term X-ray fluorescence radiation is applied. If the energy of the primary X-ray

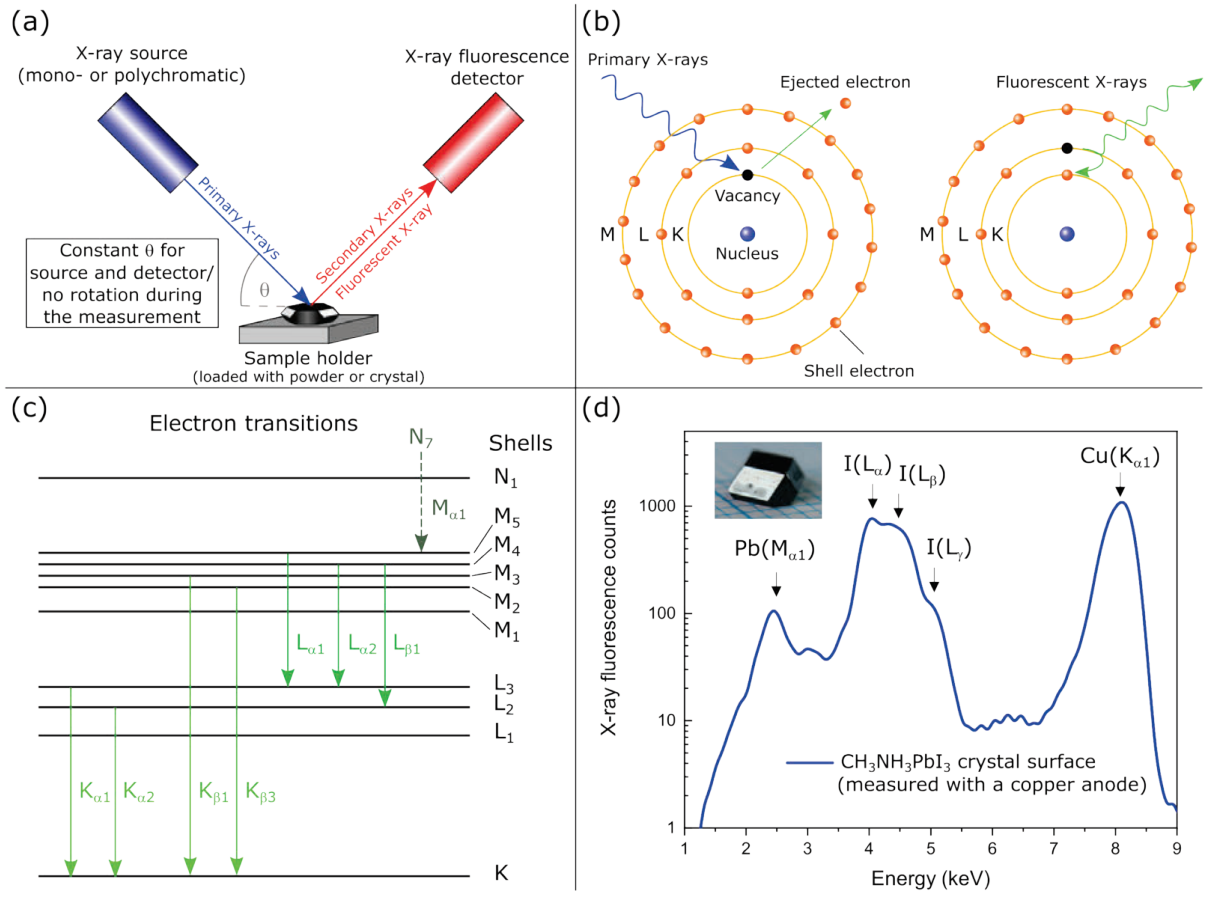


**Figure 26.** (a) Setup for X-ray fluorescence (XRF) measurements. (b) Physical principle of the generation of X-ray fluorescence radiation. Primary X-rays are used to knock-out an inner shell electron from the atom. An outer shell electron occupies the vacancy, which causes the generation of fluorescent X-rays. (c) Examples of possible electron transitions. (d) XRF spectrum of a $MAPbI_3$ crystal (inset), revealing some emission lines of the elements lead (Pb) and iodine (I). (b), and (c) reproduced in a modified design from Ref. [97].

beam is greater than the energy of the bond between the atomic nucleus and that of an electron close to the nucleus from an atom of the investigated sample, this inner shell electron can be ejected. The knocked-out electron then leaves the atom, which causes the atom to become ionised. The atom is now in an excited state and will only stabilise by an electron from a shell far from the nucleus, occupying the vacancy of the inner shell. Due to the energy difference between the outer shell electron and the inner shell electron, it is possible that an X-ray photon is generated (Figure 26b). The emitted radiation is detected and is element-specific. It therefore provides information about the elemental composition of the sample. [97]
As shown in Subchapter 3.1, a variety of characteristic X-rays can be emitted by an atom. The characteristic X-rays are assigned to the shells "K", "L", "M", and "N" depending on which electron vacancy is occupied. To classify the electron transitions, the Siegbahn notation is used, as demonstrated in Figure 26c. [97]
The occupation of a vacancy in an inner shell by an electron of an outer shell does not automatically result in the generation of an X-ray photon. In fact, there is also the possibility that another characteristic free electron is created, leaving the atom. This electron then is called "Auger electron". Hence, there is either the possibility of generating X-rays or the formation of Auger electrons. As the atomic number increases, photon emissions are more probable. This phenomenon is called "fluorescent yield". However, the formation of Auger electrons predominates at a low atomic number. Thus, in the case of OLTPs, only the halogens chlorine, bromine, and iodine as well as lead can be detected by means of the XRF spectroscopy, but not the elements carbon, nitrogen, and hydrogen. [97, 103]
To detect electron transitions of higher energy, anodes that have a high excitation energy are of primary interest. Therefore, in addition to a copper anode with monochromatic $K_{\alpha 1}$ radiation (8.05 keV), a molybdenum (Mo) source that emits polychromatic X-rays ($K_{\alpha 1}$, $K_{\alpha 2}$, and $K_{\beta 1}$) was used to study perovskites due its high energy range over 20 keV. A typical XRF spectrum of a perovskite is shown in Figure 26d. The XRF measurement, performed on the crystal surface of $MAPbI_3$, clearly identifies the emission line of Pb($M_{\alpha 1}$) at 2.5 keV [104]. Further, it is possible to assign the peaks at 4.1 keV, 4.3 keV, and 5.0 keV to the electron transitions $L_{\alpha}$, $L_{\beta}$, and $L_{\gamma}$ of the element iodine. [104]
Another important method to analyse the chemical composition of perovskites is the energy-dispersive X-ray spectroscopy (EDX). The technique is similar to the XRF method. Instead of X-rays, the atoms of a sample are excited with an electron beam. In addition to a qualitative analysis, EDX spectroscopy offers the advantage to quantify the elements of the examined sample. [105]

## 3.2 Optical Measurements for Perovskite Crystal Examination

The ultraviolet-visible (UV-VIS) spectroscopy is another important technique to investigate perovskite crystals. This technique uses visible light in a wavelength range from 350 to 850 nm. Compared to X-ray wavelengths, the electromagnetic waves of visible light are longer wavelengths by an order of magnitude of 0.1 nm [97]. A double-beam spectrophotometer with a photomultiplier tube detector [106] was used to examine the perovskite crystals. The crystals were irradiated with monochromatic light. By moving the wavelength stepwise and continuously, the intensities of transmission or reflection of the crystal were measured (Figure 27a) to record a spectrum in each case. To finally obtain an absorption spectrum, the law of energy conservation for transmittance (T), reflectance (R), and absorptance (A) was applied whose sum is one. By conversion, the wavelength-dependent absorptance values were determined, as follows [107]:

$$A = 1 - T - R \tag{24}$$

It should be noted here that the terms transmittance, reflectance, and absorptance are quantifiable and measurable terms. The terms transmission, reflection, and absorption describe the processes that occur when a crystal is illuminated, however, they are not measurable.
A typical absorption spectrum of a perovskite crystal, using $FAPbBr_3$ as an example, is shown in Figure 27b. The crystal shows a high absorption capacity in the wavelength range from 350 to 570 nm. The absorption edge at 570 nm marks the transition from a high to a low absorption capacity. For the near-infrared (NIR) region up to 850 nm, the $FAPbBr_3$ crystal then is almost transparent.
To precisely determine the absorption edge ($E_{AE}$) of perovskite crystals, the Tauc method was applied, which refers to the previously determined absorptance values [108]. Tauc et al. developed the method to determine the band gap ($E_g$) [109, 110]. While thin perovskite films with thicknesses in the nanometre range provide exact results for $E_g$ and thus represent the specific material property [78, 111], the method is only permissible for calculating the absorption edges for perovskite crystals with thicknesses in the millimetre range. Due to the better absorption capacity of the crystals compared to thin films, their absorption edges shift to longer wavelengths and accordingly to lower energies. This obscures the energy edges that allows to determine the band gaps of the materials *via* the Tauc method. Even though the Tauc method can only be used to determine the individual absorption edges of perovskite crystals, it is often used in the field of perovskite crystal research to obtain a rough estimation of the band gap [26, 62-64, 80, 81].

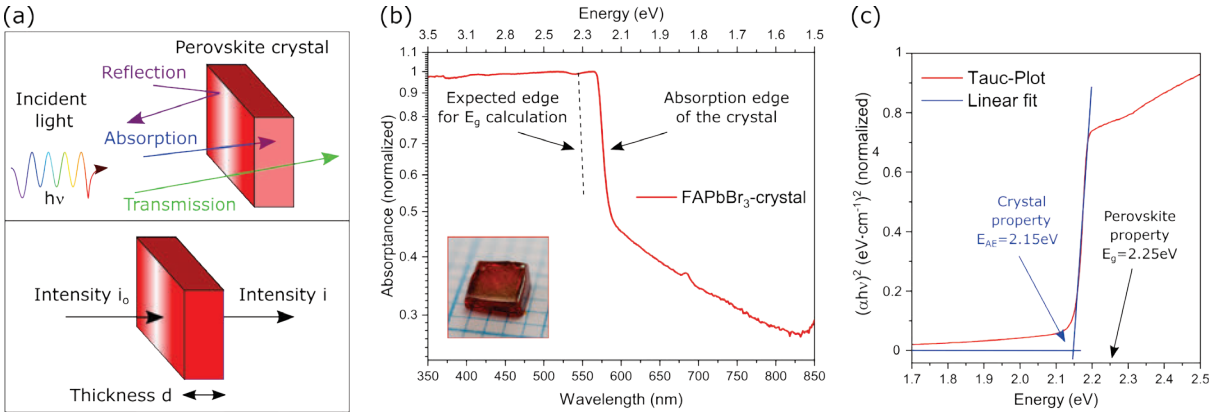


**Figure 27.** (a) (top) Illustration of the processes reflection, transmission, and absorption, which take place, when light shines on a perovskite crystal. (below) Illustration to understand the Bouguer-Lambert Law. Reproduced in a modified design from Ref. [95]. (b) Absorption spectrum of the perovskite crystal formamidinium lead tribromide ($FAPbBr_3$). (c) Calculated energy of the absorption edge *via* Tauc plot, representing the crystal property itself, but not the band gap of the perovskite.

For the calculation of the absorption edge, the model of Tauc, Davis and Mott was used, who established a connection between the strength of the absorption, and the difference between the photon energy and the band gap [108, 112, 113]:

$$(\alpha \cdot h\nu)^{\frac{1}{n}} = K \cdot (h\nu - E_g) \tag{25}$$

Thereby α is the absorption coefficient, “h” the Planck's constant, ν the photon frequency, and “K” a proportionality constant [108]. The exponent “n” describes in the case of OLTP crystals the directly allowed electron transition (n = 0.5) [26, 62-64, 80, 81]. With regard to perovskite crystals, equation (25) becomes [108]:

$$(\alpha \cdot h\nu)^2 = K \cdot (h\nu - E_{AE}) \tag{26}$$

The absorption coefficient indicates the dependence of equation (25) on the values of the absorption spectrum whose origin lies in the Bouguer-Lambert law. The law is illustrated for perovskite crystals in Figure 27a and is derived in the following: [95]

$$T = \frac{i}{i_0} = e^{-\alpha \cdot d} \tag{27}$$

Here, "$i_0$" is the intensity of the incident light on the crystal. The variable "i" is the intensity of the light emerging from the crystal. The thickness of the crystal is described by the variable "d". By transforming equation (27) the following is obtained: [95]

$$Abs = log\left(\frac{1}{T}\right) = log\left(\frac{i_0}{i}\right) = log(e) \cdot \alpha \cdot d \tag{28}$$

where "Abs" is the absorbance, sometimes called optical density [62], which is in contrast to the absorptance independent of the reflection. For the absorption coefficient, the final result is: [95]

$$\alpha = \frac{Abs}{log(e) \cdot d} \tag{29}$$

By means of the absorption coefficient, the term $(\alpha \cdot h\nu)^2$ is finally calculated for each wavelength and thus a Tauc plot can be plotted as a function of the photon energy ($h\nu$) [108]. A Tauc plot is shown in Figure 27c taking the $FAPbBr_3$ crystal as an example. The absorption edge can finally be determined by extrapolation of the linear range [108]. For the $FAPbBr_3$ crystal, an absorption edge of 2.15 eV was determined, which is very comparable with the literature [64], but as described above only roughly matches the band gap of the perovskite of 2.25 eV [38] (Figure 27c).

## 3.3 Photovoltaic Parameters for Perovskite Device Characterisation

Photodetectors and solar cells are important semiconducting devices [114] that can employ perovskite $MAPbI_3$ crystals and the corresponding polycrystalline thin films as light absorbers. [115]. Perovskite crystals are mostly used for the fabrication of photodetectors [87, 116, 117] while polycrystalline thin films are preferably used in solar cells [18, 118, 119].

### 3.3.1 Parameters for Perovskite Crystal Photodetectors

The task of a photodetector is to convert absorbing light into an electrical signal [114]. It consists of a semiconducting element and two electrodes [114]. When light is incident on the semiconductor, the photons are absorbed and if the photons have sufficient energy, electron-hole pairs are created in the semiconductor [114]. In the case of OLTP perovskites, this happens *via* the band-to-band transition [114] since they are intrinsic semiconductors [18, 120, 121]. Electrons and holes are transported to the respective electrodes when a voltage is applied, so that an electric current (I) can be measured. An important property of a photodetector is its photoresponsivity ($R_{ph}$) [122-125]. In order to determine the photoresponsivity of a perovskite crystal device, the current is first measured without illumination ($I_{dark}$) at an applied voltage. Then the current is measured under illumination ($I_{light}$). The photocurrent ($I_{Ph}$) is the difference of the current under illumination and the dark current as follows [122, 123, 125]:

$$I_{ph} = I_{light} - I_{dark} \tag{30}$$

By means of the photocurrent, the irradiance ($E_e$), and the illuminated area ($A_X$) of the photodetector, the photoresponsivity can finally be determined according to [122-126]:

$$R_{ph} = \frac{I_{ph}}{E_e \cdot A_X} \tag{31}$$

Accordingly, the photoresponsivity indicates the ratio of photocurrent to radiant flux [122, 123]. To obtain reliable data for the photoresponsivity, the irradiance of the light source is varied. For a functional photodetector, the photocurrent should increase with increasing irradiance as these parameters are directly proportional to each other according to equation (31) [116, 117]. In contrast, the photoresponsivity is indirectly proportional to the irradiance and should therefore decrease with increasing irradiance [117, 126]. As an orientation for a workable photodetector based on an OLTP crystal, a linear dependence of the photoresponsivity and the photocurrent with respect to the irradiance was found on the basis of the literature [87, 116, 117, 126].

### 3.3.2 Parameters for Perovskite Solar Cells

The task of a $MAPbI_3$ perovskite solar cell is to convert the energy of sunlight into electrical energy [18]. The solar cell consists of the perovskite absorber layer embedded between a hole transport layer (HTL) and an electron transport layer (ETL), which are in turn surrounded by two electrodes [127]. For incident light to be absorbed by the perovskite [128], one electrode and one transport layer must be transparent [127]. If the energy of the absorbed photons is higher than the band gap of the perovskite, both holes and electrons are generated in the intrinsic semiconductor [127, 129]. Due to the low exciton binding energy of $MAPbI_3$ of 2 meV, this perovskite is non-excitonic, so that direct generation of free charge carriers in the semiconductor can be assumed [130]. By applying an external electric field, the photogenerated charge carriers can drift to the respective transport layers so that an electric current is measurable [127]. The described photovoltaic cell is a p-i-n solar cell since the hole conductor layer is a p-type semiconductor and the electron layer is an n-type semiconductor [130-132]. The structure of the solar cell and the applied materials are described in detail in Subchapters 7.1 and 7.3.

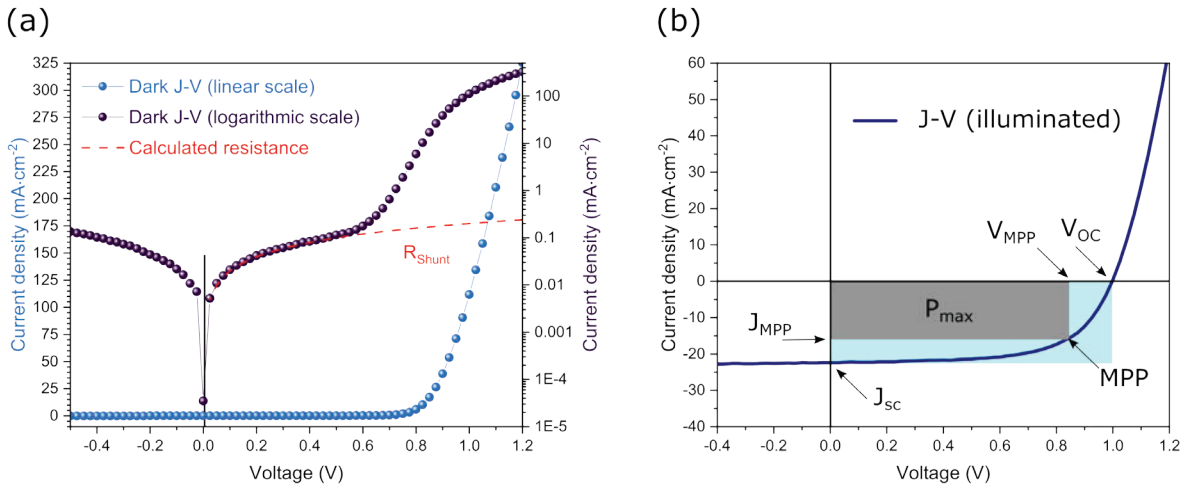


**Figure 28.** (a) Current density – voltage (J-V) curve without illumination in linear and logarithmic scale, obtained from a $MAPbI_3$ perovskite solar cell. The shunt resistance ($R_{Shunt}$) can be calculated from the logarithmic plot of the dark J-V characteristic. (b) Current density – voltage characteristic under illumination. Also shown are the photovoltaic parameters that can be determined from the J-V curve to calculate the fill factor (FF) and the power conversion efficiency (PCE) of the $MAPbI_3$ solar cell, respectively.

It should further be noted that the physical parameter of the charge carrier diffusion length ($L_D$) is decisive for a successful collection of the charge carriers [127]. This parameter indicates how

far the charge carriers can travel through the perovskite without recombining, which would reduce the performance of a photocell [127]. For example, a diffusion length of about 100 nm was determined for the perovskite $MAPbI_3$ based on a polycrystalline thin film [133]. Accordingly, the layer thickness of the perovskite absorber must be adjusted for loss-free charge transport [127], and thus to build an efficient perovskite solar cell.
For the characterisation of perovskite solar cells, the photovoltaic parameters open-circuit voltage ($V_{OC}$), short-circuit current ($I_{SC}$), fill factor (FF), and power conversion efficiency (PCE) are introduced [128, 134]. Typical current density – voltage (J-V) curves of a solar cell based on a $MAPbI_3$ thin film are shown in Figure 28. To calculate the current density (J), the ratio of the current and the active area of the solar cell is determined. Figure 28a shows the J-V characteristic of the $MAPbI_3$ solar cell without illumination, demonstrating a typical diode characteristic. The J-V curve shifts to the negative range of the current density under illumination due to generation of charger carriers (Figure 28b). From the J-V characteristic under illumination, the measurable parameters short-circuit current density ($J_{SC}$) and $V_{OC}$ can be found. While $V_{OC}$ indicates the voltage where no current flows ($I = 0$), $J_{SC}$ indicates the behaviour in the event of a short circuit ($V = 0$). Furthermore, the maximum power point (MPP) is directly readable from the J-V characteristics, indicating the operating point of the maximum electrical power ($P_{max}$) of the photovoltaic cell. The fill factor can then be expressed as the ratio of $P_{max}$ and the product of $J_{SC}$ and $V_{OC}$: [134]

$$FF = \frac{P_{max}}{J_{SC} \cdot V_{OC}} = \frac{J_{MPP} \cdot V_{MPP}}{J_{SC} \cdot V_{OC}} \tag{32}$$

The fill factor can also be illustrated with the J-V curve under illumination: $J_{SC}$ and $V_{OC}$ form a rectangle with the zero point of the axes. This can also be done for the maximum power point. Hence, FF represents the quality of the solar cell as it indicates the ratio of these two rectangles (Figure 28b) [50, 134]. FF is also dependent on the shunt resistance ($R_{Shunt}$) of a solar cell [134]. The shunt resistance is based on Ohm's law and can be determined by the logarithm of the dark J-V curve [135]. In general, high shunt resistances also result in high fill factors [136].
The key parameter for a photovoltaic element is the power conversion efficiency, which is the ratio of $P_{max}$ per light output ($P_L$) [134]:

$$PCE = \frac{P_{max}}{P_L} = \frac{J_{SC} \cdot V_{OC}}{E_e} \cdot FF \tag{33}$$

Consequently, for high-performance solar cells with high power conversion efficiencies, it is necessary to optimise the parameters $V_{OC}$, $J_{SC}$, and FF [134].

## 3.4 Concluding Remarks

In this chapter, the XRD measurement method (Subchapter 3.1) was introduced to be able to understand the measurements of OLTP crystal structure and crystal quality in chapters 4 – 7. Furthermore, qualitative statements about the composition of OLTP crystals can be made in the following through XRF analysis. To understand optical measurement results, UV-VIS spectroscopy, which includes the evaluation of optical parameters, was presented (Subchapter 3.2). The presentation of optoelectronic parameters in Subchapter 3.3 for the verification of perovskite based photodetectors and solar cells is essential for understanding Chapter 7.

# 4 Growth and Characterisation of a Wide Range of Single- and Double-halide Perovskite Crystals[2]

In this chapter, four different methods were applied to grow the single-halide perovskite crystals $MAPbCl_3$, $MAPbBr_3$, $MAPbI_3$, as well as the double-halide perovskite crystals $MAPb(Cl_{1-x}Br_x)_3$ (x = 0.2, 0.4, 0.6, 0.8) and $MAPb(Br_{1-y}I_y)_3$ (y = 0.2, 0.4, 0.6, 0.8, 0.9). Next to the established methods antisolvent vapour-assistant crystallisation (AVC) [137] and ITC [59, 62-64], the room temperature crystallisation (RTC) [138], and the alcohol-induced ITC (A-ITC) [139] were used to precisely control the stoichiometric ratio and the colour of the crystals. The large number of the methylammonium based crystals, in combination with the performed XRD measurements, provides a great overview of the structural properties of the perovskites. With an increase in the ionic radius of the halogens chlorine, bromine, and iodine, the lattice constants and therefore the unit cell of the perovskites became larger. Furthermore, optical measurements showed the potential of the crystals to absorb light in a range from 400 to 850 nm, covering nearly the entire range of the visible light and even a small part of the NIR region. The determination of the absorption edges *via* Tauc plots are an indication that the band gap can be modified by the incorporation of the different halogens into the crystal lattice and therefore makes the semiconducting crystals interesting for a wide variety of photovoltaic applications.

## 4.1 Introduction

The ability to change the optical properties of methylammonium lead trihalide perovskites (MLTPs) with the stoichiometry $ABX_3$ by varying and mixing the halogens chlorine, bromine, and iodine is a very important property of this semiconductor class [78, 111, 140-142]. This has already been done several times for the preparation of thin perovskite films in order to collect visible light of different wavelengths [75, 78, 141, 143]. By systematically changing the mixing ratio of the halogen precursors, thin films with different colours, such as yellow, orange, red, brown, and black were processed with increasing bromine and iodine concentration, respectively [78, 111, 140]. The colour change resulted in a different absorption behaviour and thus in a shift in the band gap [75, 78, 111, 141, 144]. Therefore, the perovskites were already used for a variety of technical applications such as photodetectors [145, 146], light emitting diodes [75, 141], and solar cells [78, 111]. The single-halide perovskites $MAPbCl_3$, $MAPbBr_3$, and $MAPbI_3$, both in polycrystalline [78, 111, 147, 148] and in single crystalline [63, 149, 150] form, are already applied for these kinds of optoelectronic applications. However, the technical use of double-halide perovskites to date relates mainly to perovskite thin films [75, 78, 111, 141, 147, 148]. Since perovskite crystals generally have higher stability as well as better structural properties compared to thin films, they might be better candidates for device fabrication [76, 87, 115, 144, 151-154]. Furthermore, the study of crystals also offers the unique

[2] This chapter is partially based on the section *"Hybrid perovskite crystals: Growth, characterization and application"* from Julian Höcker and Vladimir Dyakonov, which is part of the paper entitled *"Roadmap: Organic-inorganic hybrid perovskite semiconductors and devices"*, published in the Journal APL Materials in 2021, volume 9, pages 28 – 30 (109202).

advantage of investigating the fundamental properties of perovskites, due to the absence of grain boundaries which is a typical feature of polycrystalline films [115].
In order to systematically investigate double-halide perovskite crystals with the stoichiometry $MAPb(Cl_{1-x}Br_x)_3$ and $MAPb(Br_{1-y}I_y)_3$, the crystallisation techniques AVC, ITC, RTC, and A-ITC were selected. Here, the single-halide crystals $MAPbCl_3$, $MAPbBr_3$, and $MAPbI_3$ served as a reference. Following the synthesis, the qualitative XRF method was adopted to detect the halogens. For the determination of the stoichiometry, EDX spectra were recorded in addition to elemental analysis (EA). PXRD patterns were obtained from the crystalline perovskite powders to determine their lattice constants and crystal symmetry. Qualitative, quantitative, as well as the structural measurements were an evidence for the successful growth of the specific crystals with the different crystallisation techniques. Finally, optical transmittance measurements were used to gain the absorption spectra. The resulting Tauc plots showed the shift of the absorption edges with increasing bromine and iodine content in the crystal stoichiometry.

## 4.2 Solvents and Precursor Salts

**Organic solvents:** DMF (99.8 %), dimethylsulfoxide (DMSO) (>99.9 %), and 1-butanol (>99 %) were all bought from Sigma-Aldrich. GBL (>99 %) was acquired from Alfa Aesar. Dichloromethane (DCM, $CH_2Cl_2$) (99.8 %) and chloroform ($CHCl_3$) (99.8 %) were purchased from Fisher Chemical. The solvents were used as received without further purification.
**Perovskite precursor salts:** Lead chloride ($PbCl_2$) (99.99 %, trace metals basis), $PbBr_2$ (99.99 %, trace metals basis), methylammonium chloride (MACl) (>99.5 %, recrystallized 4 times), MABr (>99.5 %, recrystallized 4 times), and MAI (>99.5 %, recrystallized 4 times) were all purchased from Lumtec. $PbI_2$ (99.99 %, trace metals basis) was bought from TCI. The precursor salts were used as received without further purification.

## 4.3 MLTP Crystal Growth

All MLTP precursor solutions were prepared in a nitrogen-filled glovebox with a water and oxygen content lower than two part per million. The precursor solutions $MAPbCl_3$, $MAPbBr_3$, and the $MAPb(Cl_{1-x}Br_x)_3$ were stirred at least for 3 h at RT for complete dissociation of the precursor salts. The $MAPbI_3$ solution was stirred at 60°C for at least 4 h until it was completely dissolved. The prepared solutions were then transferred to a fume hood to start the crystal growth. Here, the MLTP precursor solutions were filtered *via* a 0.2 µm pore size polytetrafluoroethylene (PTFE) syringe filter. All crystals were grown in a 30 ml wide neck jar under ambient conditions at a temperature of 20±3°C and a humidity of 30±25 %. After the growth, the crystals were cleaned with a Kimtech cloth to remove the precursor solution.

### 4.3.1 $MAPbCl_3$ Crystal Growth with RTC

MACl (351.93 mg, 5.21 mmol) and $PbCl_2$ (2053.42 mg, 7.38 mmol) were dissolved in a 3.75 ml solvent mixture of DMF and DMSO (1:1). Then, the precursor solution was left at RT for a period of 2.5 months to obtain mm-sized $MAPbCl_3$ crystals.

### 4.3.2 $MAPbCl_3$, $MAPbBr_3$, and $MAPb(Cl_{1-x}Br_x)_3$ Crystal Growth with AVC

The $MAPbCl_3$ precursor solution (0.25 M) was prepared as follows: MACl (50.64 mg, 0.75 mmol) and $PbCl_2$ (208.58 mg, 0.75 mmol) were dissolved in a 3 ml solvent mixture of DMF and DMSO (1:1).
The $MAPbBr_3$ precursor solution (0.25 M) was prepared as follows: MABr (83.98 mg, 0.75 mmol) and $PbBr_2$ (275.26 mg, 0.75 mmol) were dissolved in 3 ml DMF. A higher

concentrated precursor solution with a molar concentration ($c_m$) of 0.5 mol·l$^{-1}$ is also suitable for the growth of $MAPbBr_3$ crystals.
The preparation of the $MAPb(Cl_{1-x}Br_x)_3$ precursor solution with a molar concentration of 0.25 mol·l$^{-1}$ are summarised in Table 3.

**Table 3.** Amount of materials for the preparation of the perovskite $MAPb(Cl_{1-x}Br_x)_3$ (x = 0.2, 0.4, 0.6, 0.8) precursor solutions.

| Stoichiometry | m(MACl) [mg] | m(MABr) [mg] | m($PbCl_2$) [mg] | m($PbBr_2$) [mg] | V(DMF) [µl] | V(DMSO) [µl] |
|---|---|---|---|---|---|---|
| $MAPb(Cl_{0.8}Br_{0.2})_3$ | 40.51 | 16.80 | 166.86 | 55.05 | 2000 | 1000 |
| $MAPb(Cl_{0.6}Br_{0.4})_3$ | 30.38 | 33.59 | 125.15 | 110.10 | 2250 | 750 |
| $MAPb(Cl_{0.4}Br_{0.6})_3$ | 20.26 | 50.39 | 83.43 | 165.15 | 3000 | - |
| $MAPb(Cl_{0.2}Br_{0.8})_3$ | 10.13 | 67.18 | 41.72 | 220.21 | 3000 | - |

Alternatively, the double-halide MLPT solutions can be prepared by using 12 ml $MAPbCl_3$ and $MAPbBr_3$ stock solutions with a molar concentration of 0.3 mol·l$^{-1}$. The exact stoichiometry for 3 ml $MAPb(Cl_{1-x}Br_x)_3$ precursor solutions were calculated as follows:

$$V_{Perovskite\ A} = x \cdot 3000\mu l \tag{34}$$

$$V_{Perovskite\ B} = (1 - x) \cdot 3000\mu l \tag{35}$$

where $V_{Perovskite\ A}$ and $V_{Perovskite\ B}$ are the volumes of the stock solutions $MAPbCl_3$ and $MAPbBr_3$, respectively. The value x is 0.2, 0.4, 0.6 or 0.8.
The filtered precursor solutions were each filled into a glass vial with a cannula in the cap. The use of the cannula prevents a rapid diffusion process of the volatile solvents dichloromethane and chloroform and contributes to a controlled crystal growth. Afterwards, each vial was placed in a low density polyethylene (LDPE) bottle, which was filled with 50 ml of DCM or chloroform. Finally, the bottles were placed on anti-vibration mats. For crystal growth under ambient conditions, one week should be maintained.

### 4.3.3 $MAPbCl_3$, $MAPbBr_3$, $MAPbI_3$, and $MAPb(Br_{1-y}I_y)_3$ Crystal Growth with ITC and A-ITC

The $MAPbCl_3$ precursor solution (1 M) was prepared by mixing MACl (202.55 mg, 3 mmol) and $PbCl_2$ (834.30 mg, 3 mmol) with a 3 ml solvent mixture of DMF and DMSO (1:1).
The $MAPbBr_3$ precursor solution (1 M) was prepared by mixing MABr (335.91 mg, 3 mmol) and $PbBr_2$ (1101.03 mg, 3 mmol) with 3 ml DMF.
The $MAPbI_3$ precursor solution (1 M) was prepared by mixing MAI (476.91 mg, 3 mmol) and $PbBr_2$ (1383.03 mg, 3 mmol) with 3 ml GBL.
The preparation of the $MAPb(Br_{1-y}I_y)_3$ precursor solution are summarised in Table 4.

**Table 4.** Amount of materials for the preparation of the perovskite $MAPb(Br_{1-y}I_y)_3$ (y = 0.2, 0.4, 0.6, 0.8, 0.9) precursor solutions.

| Stoichiometry | $c_m$ [mol·l$^{-1}$] | m(MAI) [mg] | m(MABr) [mg] | m($PbBr_2$) [mg] | m($PbI_2$) [mg] | V(GBL) [µl] | V(DMF) [µl] | V(Butanol) [µl] |
|---|---|---|---|---|---|---|---|---|
| $MAPb(Br_{0.8}I_{0.2})_3$ | 1 | 95.38 | 268.73 | 880.82 | 276.61 | 2400 | 600 | (100) |
| $MAPb(Br_{0.6}I_{0.4})_3$ | 1 | 190.76 | 201.55 | 660.62 | 553.21 | 1800 | 1200 | 100 |
| $MAPb(Br_{0.4}I_{0.6})_3$ | 1 | 286.15 | 134.36 | 440.41 | 829.82 | 1200 | 1800 | 100 |
| $MAPb(Br_{0.2}I_{0.8})_3$ | 0.8 | 305.22 | 53.75 | 176.16 | 885.14 | 3000 | - | - |
| $MAPb(Br_{0.1}I_{0.9})_3$ | 0.8 | 343.37 | 26.87 | 88.08 | 995.78 | 3000 | - | - |

The filtered solutions were then placed in an about 1 cm high oil bath, which was fixed on a hot plate. To start the crystal growth, the MLTP solutions were set to the growth temperatures ($T_{Crystal\ Growth}$), shown in Table 5. In order to avoid vibration during the crystal growth, the hot plate was located on a sand-filled box and an anti-vibration mat [23, 26].

**Table 5.** Optimal crystal growth temperatures ($T_{Crystal\ Growth}$) and the applied crystallisation techniques to grow the hybrid perovskites.

| Perovskites | Crystallisation technique | $T_{Crystal\ Growth}$ [°C] |
|---|---|---|
| $MAPbCl_3$ | ITC | 60 [23] |
| $MAPbBr_3$ | ITC | 80 [23, 62] |
| $MAPb(Br_{0.8}I_{0.2})_3$ | ITC or A-ITC | 100 (ITC)/ 90 (A-ITC) |
| $MAPb(Br_{0.6}I_{0.4})_3$ | A-ITC | 90 |
| $MAPb(Br_{0.4}I_{0.6})_3$ | A-ITC | 90 |
| $MAPb(Br_{0.2}I_{0.8})_3$ | ITC | 110 |
| $MAPb(Br_{0.1}I_{0.9})_3$ | ITC | 110 |
| $MAPbI_3$ | ITC | 110 [23, 62] |

To obtain mm-sized crystals, a period of 3 to 10 h is usually required.

### 4.3.4 Characterisation of the MLTP Crystals

For EA, XRF, and PXRD measurements, the MLTP crystals were crushed to a fine powder with mortar and pestle. For the X-ray measurements, the crystal powders were glued to a plastic substrate holder with a double-sided tape. The crystal powders were distributed as homogeneously and smoothly as possible on the substrates.
XRF measurements were carried out with an XR-100T detector from Amptek and an X-ray machine from PHYWE using an unfiltered Mo-$K_\alpha$ radiation source (V = 35 kV, I = 0.1 mA).
PXRD patterns were recorded by an X-ray diffraction system General Electric XRD 3003 TT using a Cu-$K_{\alpha 1}$ radiation source with a wavelength $\lambda$ of 1.5406 Å (V = 40 kV, I = 40 mA) in a range of 10 to 60° with a step width of 0.02° and an integration time of 5 s. The scattered X-ray intensities were plotted against the momentum transfer along the surface normal [26]. The measurements were carried out under ambient conditions.
A vario MICRO cube micro elemental analyser was used to determine the mass concentrations of the elements hydrogen (H), carbon (C), and nitrogen (N) from the MLTP crystal powders.
EDX measurements of the crystal surfaces were carried out with an INCAPentaFET-x3 Si(Li) detector. The measurements were performed in high vacuum.
The crystal transmittance measurements for the determination of the absorptance were performed with an UV-VIS Jasco V-650 spectrometer under ambient conditions.

## 4.4 Results and Discussion

### 4.4.1 The Synthesised MLTP Crystals

RTC is suitable for growing $MAPbCl_3$ crystals and is based on the slow evaporation method [77, 155], which is a common and simple crystal growth technique [31, 58, 156, 157]. Here, the organic solvent mixture DMF:DMSO evaporates over time, inducing supersaturation of the perovskite solution. The evaporation leads to the growth of $MAPbCl_3$ crystals, which is illustrated in Figure 29. In order to achieve supersaturation at all, a highly concentrated solution (> 1 M) must be prepared. Due to the high boiling points (Bp) of DMF (Bp = 153°C) [158] and DMSO (Bp = 189°C) [158], the solvents evaporate very slowly. For this reason, long growth cycles of several months are necessary.

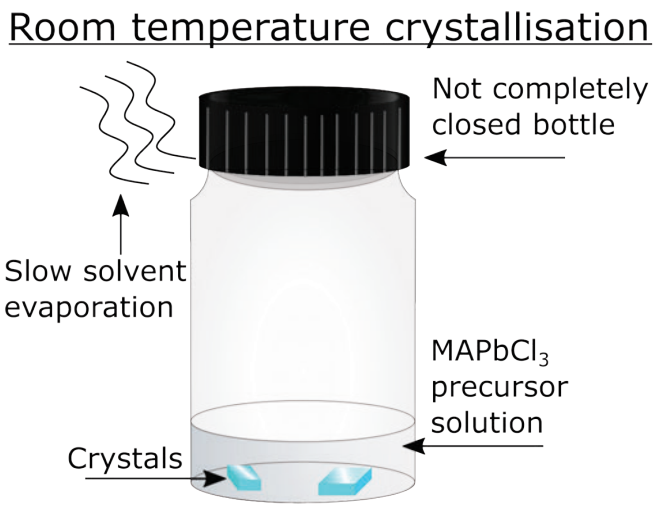


**Figure 29.** Illustration of the room temperature crystallisation (RTC) method for growing methylammonium lead trichloride ($MAPbCl_3$) crystals.

The AVC method (Figure 30) was also carried out at RT [137, 159], but the crystallisation principle is different compared to RTC: Here, the perovskite precursor salts MABr and $PbBr_2$ show a very good solubility in the solvent DMF, whereas the precursor salts MACl and $PbCl_2$ are easily soluble in the solvent mixture DMF:DMSO [23]. However, the precursor salts are poor soluble in DCM or chloroform, whereas DMF and DMSO are highly soluble in the chlorinated hydrocarbons [58, 74, 87, 160]. Due to the low boiling points of DCM (Bp = 40°C) [161] and chloroform (Bp = 61°C) [158], they evaporate already at RT and slowly mix with DMF or DMF:DMSO. If the solvents are mixed sufficiently, the perovskite precursor solution supersaturates and crystals will precipitate. In order to obtain a few, but mm-sized crystals, the diffusion process and the solvent mixing must be minimised and controlled, using the preparation technique described in Subchapter 4.3.2. In addition, the molar concentration of the precursor solutions should not

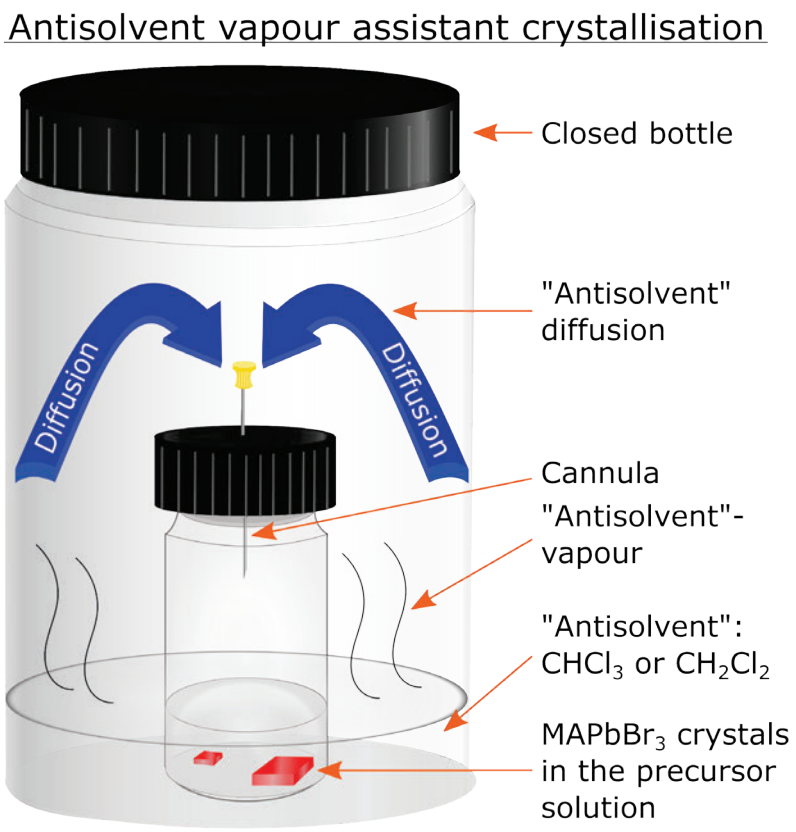


**Figure 30.** Illustration of the growth technique antisolvent vapour assistant crystallisation (AVC). The method is applicable for growing $MAPb(Cl_{1-x}Br_x)_3$.

be higher than 0.5 M, otherwise too many crystal nuclei are formed. This is a certain risk, as the crystals then grow into each other. Therefore, a controlled crystal growth process with AVC takes about 5 to 7 days. The method is very well suited for growing $MAPbCl_3$, $MAPbBr_3$, and $MAPb(Cl_{1-x}Br_x)_3$ crystals. For the growth of $MAPbI_3$ crystals, however, only to a limited extent, as the crystals are usually small and the side phase $PbI_2$ also crystallises.

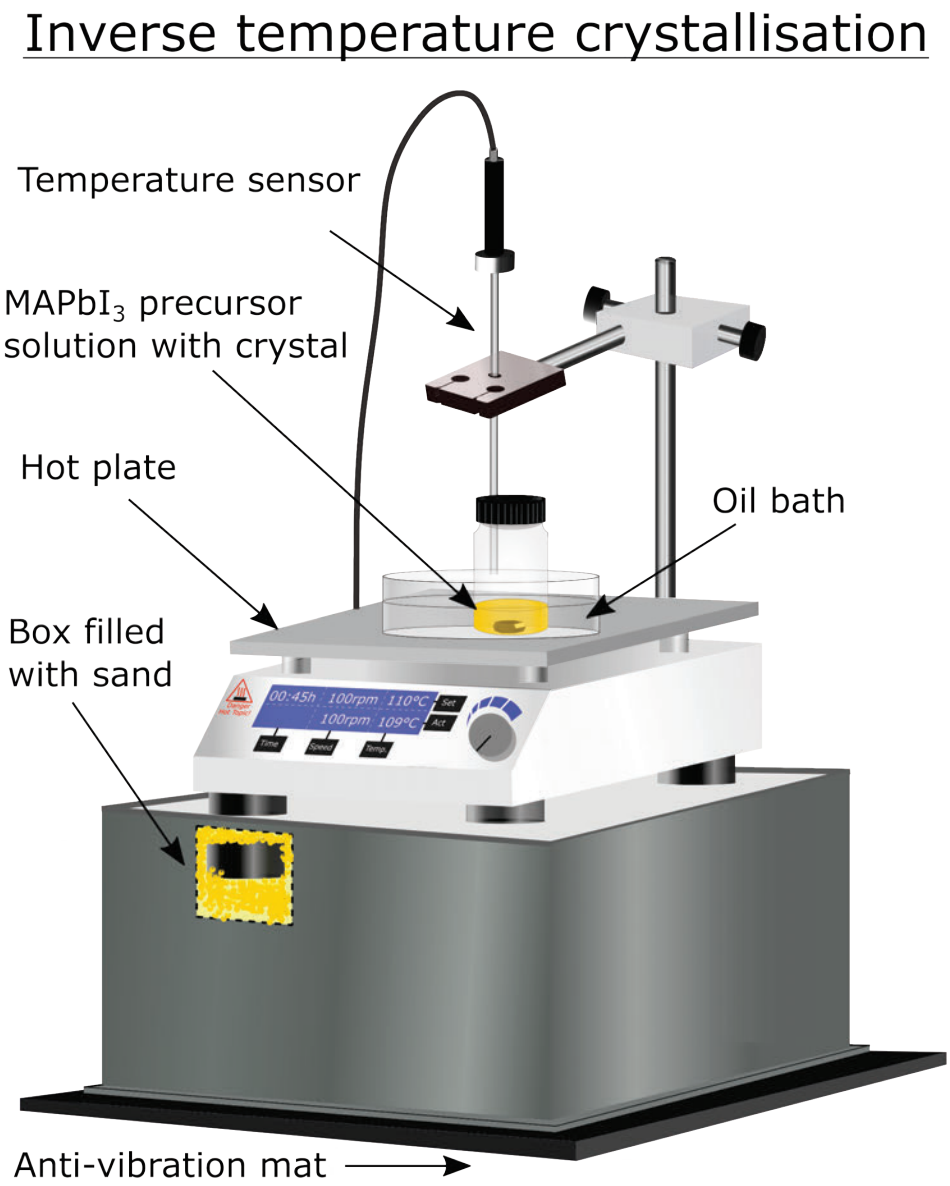


**Figure 31.** Setup for growing $MAPb(Br_{1-y}I_y)_3$ crystals with ITC and the alcohol-induced inverse temperature crystallisation (A-ITC). The anti-vibration mat and the sand-filled box are used to reduce vibration during the crystal growth.

In contrast to the methods RTC and AVC, the ITC method (Figure 31) enables the growth of perovskite crystals containing chlorine, bromine, and iodine as well [57, 62, 63, 93, 162-165]. Here, MLTP precursor solutions with molar concentrations of 1 M are usually required [23, 166]. The reason for the use of higher concentrated precursor solutions compared to them of AVC is that by heating the concentrated solution, mm-sized crystals can be grown within only a few hours, as the solubility of the perovskite decreases with increasing temperature (Subchapter 2.9.3) [23, 64, 153]. Another advantage of the method is that seed crystals can be used to grow cm-sized crystals in a new fresh and hot precursor solution [167]. The method is

also suitable for the growth of crystalline $MAPb(Br_{0.8}I_{0.2})_3$, $MAPb(Br_{0.2}I_{0.8})_3$ or $MAPb(Br_{0.1}I_{0.9})_3$. However, simply heating of the $MAPb(Br_{1-y}I_y)_3$ (y = 0.4 and 0.6) precursor solutions is not enough to grow crystals. In this case, the solubility of the perovskites is only reduced by the addition of a small amount of a primary alcohol to the hot precursor solution (Subchapter 4.3.3). The combination of alcohol additive and heating is the basis of the A-ITC method, which was first applied to grow inorganic caesium lead tribromide crystals [139, 168].

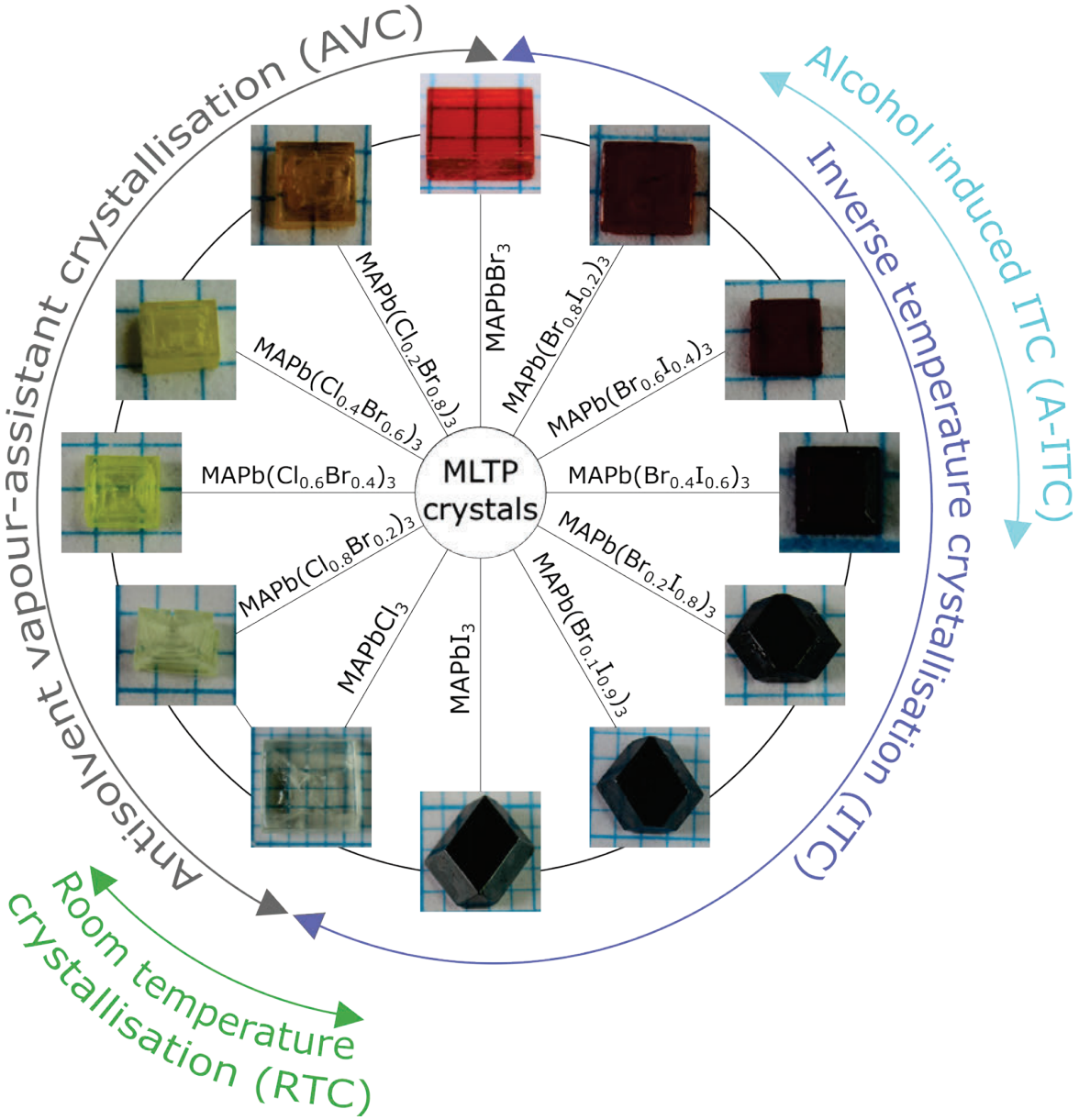


**Figure 32.** Methylammonium lead trihalide perovskite (MLTP) crystals grown either by the crystal growth methods RTC, AVC, ITC or A-ITC. Reproduced in a modified design from Ref. [310] with permission from APL Materials.

Figure 32 represents the successfully grown MLTP crystals with the growth methods RTC, AVC, ITC, and A-ITC. Apart from the transparent $MAPbCl_3$ and $MAPb(Cl_{0.8}Br_{0.2})_3$ crystals, the crystals show an intense colouring. Due to the substitution of bromine, the colour of the mixed chlorine-bromine crystals changes from yellow to orange. In contrast, a $MAPbBr_3$ crystal is coloured red. Similar to the chlorine-bromine crystals, the bromine-iodine crystals also show characteristic intermediate colour stages [21]. With increasing iodine content, a colour deepening from dark red to black is visible. However, the colours of the iodine-bromine crystals, starting from $MAPb(Br_{0.6}I_{0.4})_3$ to $MAPbI_3$, do not differ anymore.

With regard to the crystal morphology, it is noticeable that all crystals from $MAPbCl_3$ to $MAPb(Br_{0.6}I_{0.4})_3$ are cuboidal [162] and have six crystal faces, whereby the lower and upper faces are square and the side faces are rectangular. The $MAPb(Br_{0.4}I_{0.6})_3$ crystal also has six crystal faces, but its side faces are bevelled and therefore shows a different crystal habit compared to all other MLTP crystals. The crystals with the stoichiometry $MAPb(Br_{0.2}I_{0.8})_3$, $MAPb(Br_{0.1}I_{0.9})_3$, and $MAPbI_3$ show a completely different crystal morphology. These crystals are dodecahedral [162] and possess 12 crystal faces, which are either hexagonal or trapezoidal.

### 4.4.2 Qualitative, Quantitative, and Structural Analyses

For qualitative, quantitative, and structural measurements, the crystals were ground into powders (Subchapter 4.3.4), which are shown in Figure 33. Like the crystals, the crystalline powders with a high bromine content are very colour-intensive and are light yellow, yellow, orange, red, and dark red. In contrast, the $MAPbCl_3$ powder is white, while the crystal powders with a high iodine content are black.

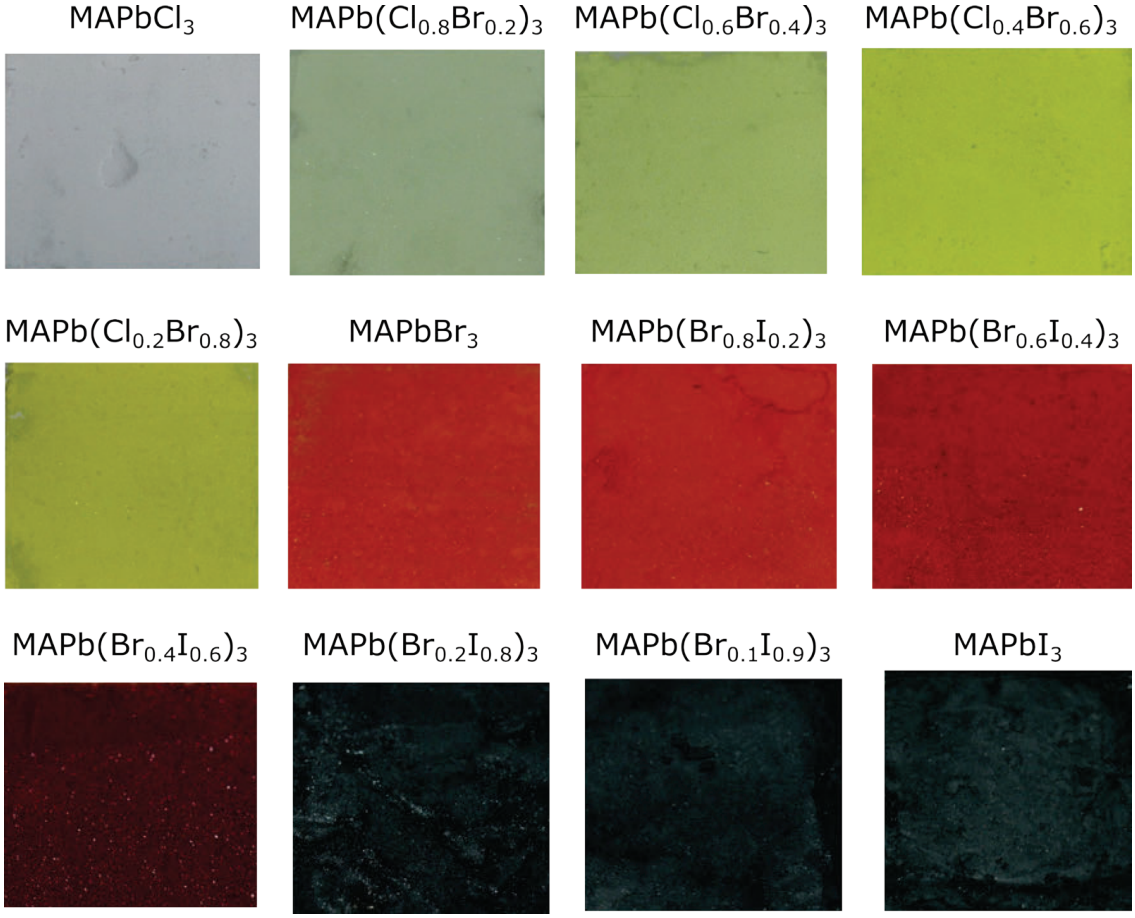


**Figure 33.** MLTP crystal powders for further analyse of the inherent properties of the perovskites. The higher the bromine content, the more colour-intensive is the powder.

Figure 34 shows the XRF and EDX spectra of the single-halide perovskites $MAPbCl_3$, $MAPbBr_3$, and $MAPbI_3$ to detect the heavy metal lead as well as the halogens chlorine, bromine, and iodine. Therefore, the XRF measurements were performed on the crystal powders and the EDX measurements on the crystal's surfaces. For all three perovskites, the energies of the X-ray emission lines $M_{\alpha 1}$, $L_\alpha$, $L_\beta$, and $L_\gamma$ of the element lead were detected at 2.4 keV, 10.5 keV, 12.6 keV, and 14.8 keV, respectively [104]. While in the XRF spectrum of $MAPbCl_3$ the $M_{\alpha 1}$ emission line of lead overlaps with the K-shell line of chlorine, the halogen can be accurately detected in the EDX spectrum by the sharp peaks at 2.6 keV ($K_\alpha$) and 2.8 keV ($K_{\beta 1}$) [104]. With

regard to the perovskite $MAPbBr_3$, both measurement techniques gave accurate results, as the element bromine was detected by the L, $K_\alpha$, and $K_{\beta1}$ emission lines [104] with X-ray energies of 1.5 keV, 11.9 keV, and 13.3 keV. The incorporation of iodine into the crystal structure of

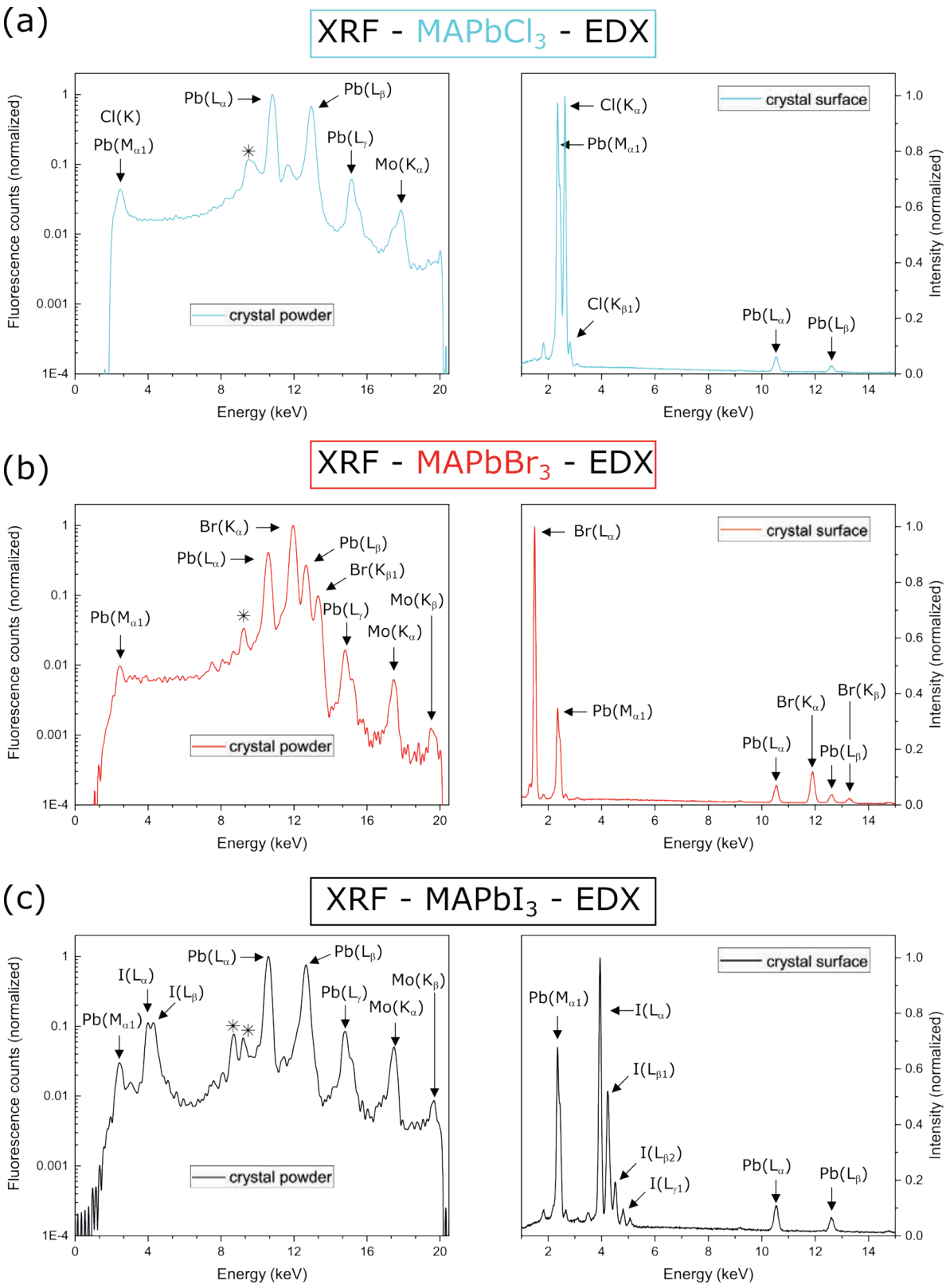


**Figure 34.** XRF and energy-dispersive X-ray spectroscopy (EDX) measurements from (a) $MAPbCl_3$, (b) $MAPbBr_3$, and (c) $MAPbI_3$, to verify the elements chlorine (Cl), bromine (Br), iodine (I), and lead (Pb). The recorded peaks matched the characteristic emission lines of the elements. The asterisks (*) in the XRF spectra can be assigned to the sample holder.

$MAPbI_3$ was confirmed by the emission lines $L_\alpha$, $L_{\beta1}$, $L_{\beta2}$, and $L_{\gamma1}$ at 3.9 keV, 4.2 keV, 4.5 keV, and 4.8 keV, respectively [104].
In addition to the measurements of the single-halide perovskites, the compositions of the double-halide perovskites were also investigated by XRF and EDX, which are shown in Figure A1 and A2 in the appendix. Also, in this case, the energy values of the detected X-ray fluorescence peaks were exactly assigned to the emission lines of lead and the halogens.
Besides a qualitative analysis, the EDX technique also served to quantify the elements on the crystal's surfaces. To fully identify the stoichiometry of the crystals, the organic cation methylammonium was analysed on crystal powders by means of the elemental analysis. Table 6 shows the experimentally determined mass fractions of the elements. The elements carbon, hydrogen, and nitrogen were clearly detected for all perovskites by the elemental analysis. This is a clear indication that starting from the precursor salts MACl, MABr, and MAI, methylammonium has been incorporated into the crystals. Furthermore, the experimentally determined mass fractions of methylammonium are consistent with the theoretical values in Table A1 in the appendix. Due to the low relative atomic mass of carbon ($A_r(C) = 12.01$ u), hydrogen ($A_r(H) = 1.01$ u), and nitrogen ($A_r(N) = 14.01$ u) compared to lead ($A_r(Pb) = 207.1$ u), their mass fractions in the crystals are also low [169]. Furthermore, it is evident that the mass fractions of C, H, N, and Pb decrease with increasing bromine and iodine substitution since iodine has the largest atomic weight ($A_r(I) = 126.9$ u) compared to bromine ($A_r(Br) = 79.9$ u) and chlorine ($A_r(Cl) = 35.5$ u) [169]. The results are comparable with the given stoichiometry (Table A1) because with increasing bromine content, the chlorine content of the double-halide $MAPb(Cl_{1-x}Br_x)_3$ perovskites decreases. The same is valid for the crystals with the stoichiometry $MAPb(Br_{1-y}I_y)_3$. Here, it becomes clear that the bromine content is reduced with increasing iodine substitution. The presented results allow the conclusion that MLTP crystals of different stoichiometric ratios can be grown with the crystallisation methods RTC, AVC, ITC, and A-ITC.

**Table 6.** Mass fraction of the perovskites obtained from EA and EDX for the elements carbon (C), hydrogen (H), nitrogen (N), lead (Pb), chlorine (Cl), bromine (Br), and iodine (I) to determine the MLTP stoichiometry.

| Stoichiometry | C [%] | H [%] | N [%] | Pb [%] | Cl [%] | Br [%] | I [%] |
|---|---|---|---|---|---|---|---|
| **$MAPbCl_3$** | 3.71 | 1.88 | 3.90 | 51.87 | 31.64 | - | - |
| **$MAPb(Cl_{0.8}Br_{0.2})_3$** | 3.60 | 1.71 | 3.74 | 48.45 | 25.76 | 9.26 | - |
| **$MAPb(Cl_{0.6}Br_{0.4})_3$** | 3.30 | 1.58 | 3.53 | 45.58 | 19.00 | 18.17 | - |
| **$MAPb(Cl_{0.4}Br_{0.6})_3$** | 2.97 | 1.41 | 3.19 | 43.60 | 14.56 | 27.30 | - |
| **$MAPb(Cl_{0.2}Br_{0.8})_3$** | 2.74 | 1.32 | 2.99 | 39.85 | 6.47 | 40.50 | - |
| **$MAPbBr_3$** | 2.44 | 1.22 | 2.79 | 38.06 | - | 51.85 | - |
| **$MAPb(Br_{0.8}I_{0.2})_3$** | 2.62 | 1.31 | 2.73 | 37.26 | - | 48.68 | 2.63 |
| **$MAPb(Br_{0.6}I_{0.4})_3$** | 2.47 | 1.23 | 2.77 | 36.72 | - | 43.48 | 8.76 |
| **$MAPb(Br_{0.4}I_{0.6})_3$** | 2.52 | 1.24 | 2.66 | 34.44 | - | 30.59 | 26.43 |
| **$MAPb(Br_{0.2}I_{0.8})_3$** | 2.12 | 1.06 | 2.28 | 32.31 | - | 10.63 | 50.62 |
| **$MAPb(Br_{0.1}I_{0.9})_3$** | 2.04 | 0.94 | 2.26 | 32.77 | - | 6.16 | 58.62 |
| **$MAPbI_3$** | 1.98 | 0.96 | 2.17 | 31.69 | - | - | 66.58 |

The MLTP crystal powders were further used for X-ray diffraction measurements. Figure 35a – c shows the powder XRD patterns of the single-halide perovskites $MAPbCl_3$, $MAPbBr_3$, and $MAPbI_3$. For the evaluation of the diffractograms, the detected peaks were fitted. In order to determine the lattice constant of the crystalline powders, the Miller indices were assigned (Table A2 – A4 in the appendix) by using the respective simulation. Regardless of the growth

technique, the $MAPCl_3$ and $MAPbBr_3$ crystals have a simple cubic symmetry [22, 167, 170, 171] and possess the lattice constants $a_{MAPbCl3}$ = 5.689 Å and $a_{MAPbBr3}$ = 5.937 Å, respectively, which is assigned to the space group Pm-3m [172]. In contrast, $MAPbI_3$ forms a body-centred tetragonal [22, 82, 137, 167] structure (space group I4/mcm) [59] based on the lattice constants $a_{MAPbI3}$ = 8.93 Å and $c_{MAPbI3}$ = 12.48 Å. All three powder patterns match the simulated data (Figure 35a – c). The determined lattice constants are further in very good accordance with the literature [21, 59, 63, 100, 155, 172-174]. In addition to the PXRD patterns of the single-halide perovskites, Figure 36a shows the PXRD measurements of the double-halide perovskites $MAPb(Cl_{1-x}Br_x)_3$ and $MAPb(Br_{1-y}I_y)_3$. For the mixed crystals from $MAPb(Cl_{0.8}Br_{0.2})_3$ to $MAPb(Br_{0.4}I_{0.6})_3$ a cubic lattice was assigned. The perovskite crystals with the stoichiometry $MAPb(Br_{0.2}I_{0.8})_3$ and $MAPb(Br_{0.1}I_{0.9})_3$ exhibit a tetragonal unit cell like $MAPbI_3$. The detailed evaluation of the double-halide crystal powders is shown in Figure A3 to A11 and in Table A5 to A13. Figure 36a further shows that the reflexes of the individual powder patterns shift to smaller scattering vectors with increasing bromine and iodine content. This becomes even more apparent in Figure 36b with the shift of the (100) and the (200) peak for the perovskites $MAPbCl_3$ to $MAPb(Br_{0.4}I_{0.6})_3$. While the (100) reflex of $MAPbCl_3$ was detected at a scattering vector of q = 1.10 $Å^{-1}$, the peak shifts to 1.06 $Å^{-1}$ for $MAPbBr_3$. The peak shift was also obvious

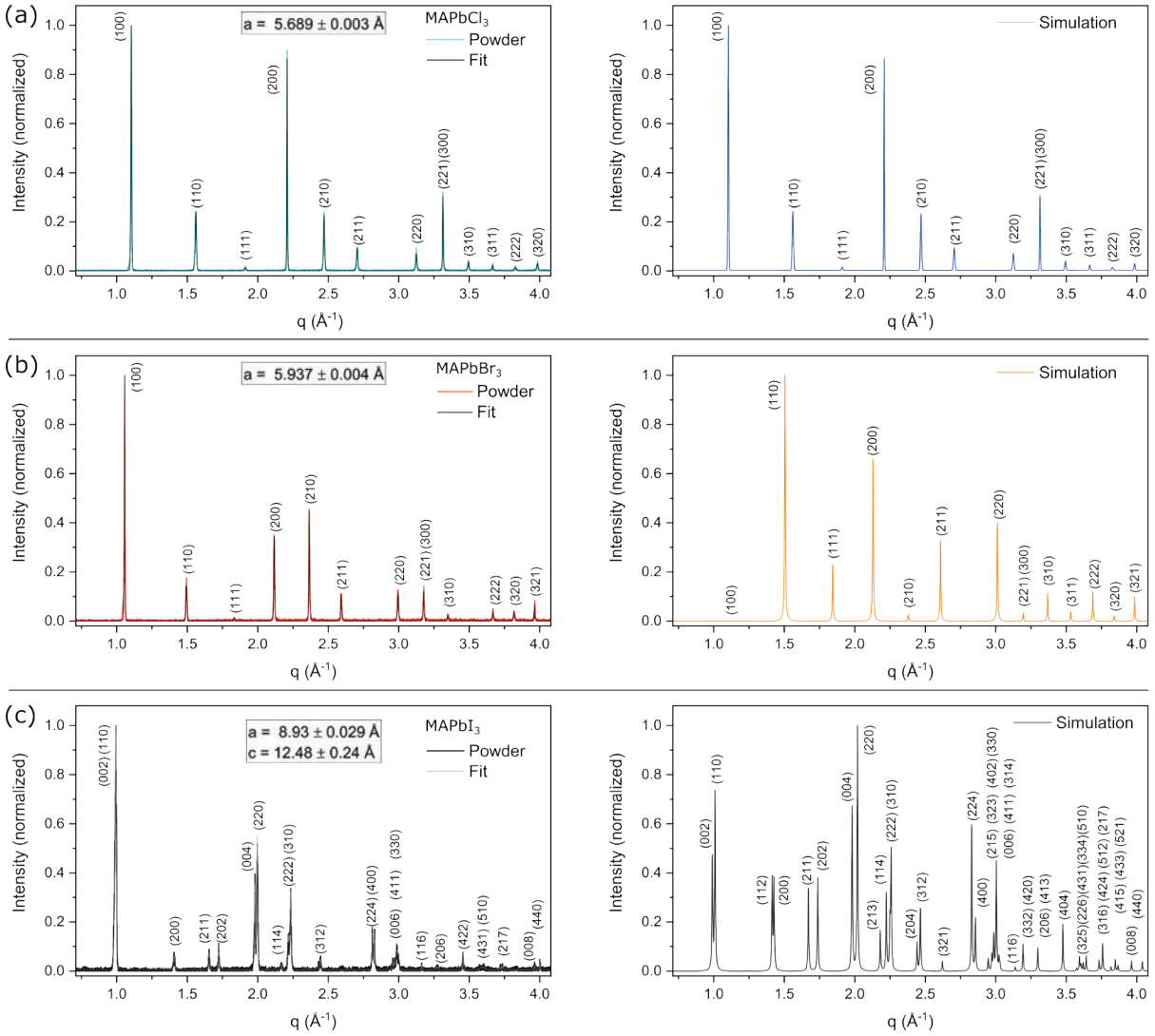


**Figure 35.** PXRD patterns, fits, and simulations of (a) $MAPbCl_3$, (b) $MAPbBr_3$, and (c) $MAPbI_3$. The PXRD simulation of $MAPbCl_3$, $MAPbBr_3$, and $MAPbI_3$ were made by using the crystallographic data from Ref. [155], [172], and [59], respectively. (b) reproduced partly from Ref. [26] with permission from the Royal Society of Chemistry.

in the double-halide perovskites. For example, the (100) and the (200) reflexes of $MAPb(Cl_{0.6}Br_{0.4})_3$ were measured at 1.09 $Å^{-1}$ and 2.19 $Å^{-1}$. At the same bromine concentration, the perovskite $MAPb(Br_{0.4}I_{0.6})_3$ exhibits smaller scattering vectors of 1.04 $Å^{-1}$ and 2.09 $Å^{-1}$ for the (100) and (200) peaks, respectively. Furthermore, with increasing iodine substitution, the

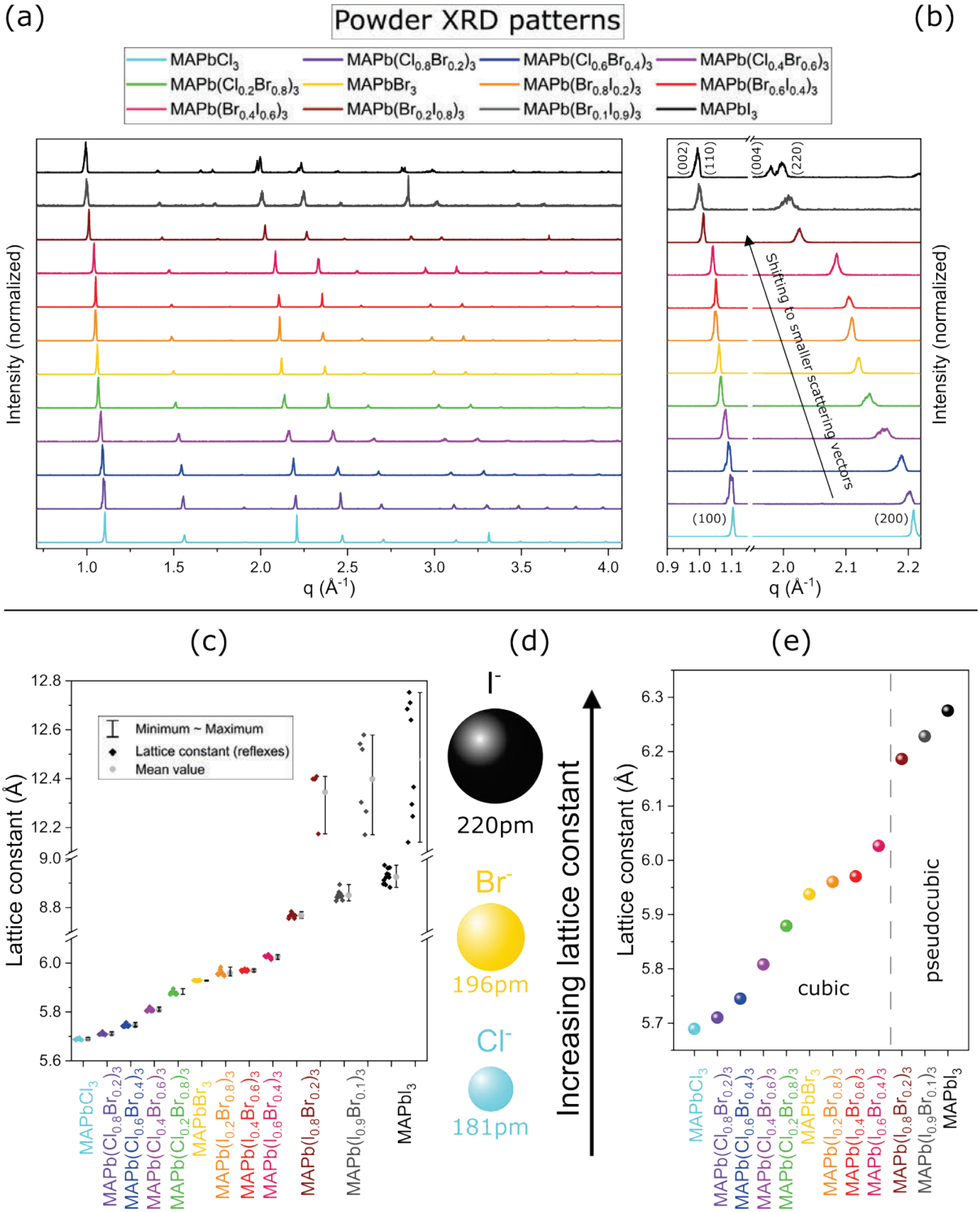


**Figure 36.** (a) Powder XRD patterns of the MLTP crystals. (b) Extract from the powder XRD patterns shows that the (100) reflex shifts towards smaller scattering vectors (q) with increasing bromine substitution, and further splits into the reflexes (002) and (110) with increasing iodine concentration. (c) Calculated lattice constants represent a simple cubic symmetry for $MAPbCl_3$ to $MAPb(Br_{0.4}I_{0.6})_3$ and a tetragonal crystal structure for $MAPb(Br_{0.2}I_{0.8})_3$, $MAPb(Br_{0.1}I_{0.9})_3$, and $MAPbI_3$. (d) Illustration of the ionic radii of $Cl^-$, $Br^-$, and $I^-$. (e) Mean values of the MLTP lattice constants. Pseudocubic lattice parameters were chosen for the perovskites $MAPb(Br_{0.2}I_{0.8})_3$, $MAPb(Br_{0.1}I_{0.9})_3$, and $MAPbI_3$. Reproduced partly from Ref. [310] with permission from APL Materials.

(100) reflex splits into the peaks (002) and (112). The same happens for the second higher order, whereas the peaks (004) and (224) were identified. The double peaks suggest that the high iodine content in the crystal distorts the crystal lattice, resulting in the formation of a tetragonal unit cell [151]. In the tetragonal crystals, the trend continues exactly as in the cubic crystals that the reflexes shift to smaller q-values [151]. Compared to $MAPb(Br_{0.2}I_{0.8})_3$ ($q_{(002)}$ = 1.01 Å$^{-1}$ and $q_{(004)}$ =2.03 Å$^{-1}$), $MAPbI_3$ reveals smaller q-values of 0.99 Å$^{-1}$ and 1.98 Å$^{-1}$ for the (002) and (004) peaks, respectively.
The shift to smaller scattering vectors with increasing bromine and iodine substitution also results in larger lattice constants as a result of the Bragg condition, and is shown in Figure 36c. Here, the determined lattice constant of each peak is plotted next to the mean-, maximum-, and minimum values. As the evaluations of the single halide perovskites have shown, the complete exchange of chlorine to bromine or bromine to iodine can increase the unit cell size and even change the crystal structure [85, 140, 151]. The unit cell of the mixed crystals from $MAPb(Cl_{0.8}Br_{0.2})_3$ to $MAPb(Br_{0.4}I_{0.6})_3$ also becomes larger with systematic increase in the bromine or iodine content. While $MAPb(Cl_{0.8}Br_{0.2})_3$ has a lattice constant of 5.71 Å, the lattice constant of $MAPb(Br_{0.4}I_{0.6})_3$ is 5.97 Å. Figure 36c also shows that with a sufficiently high iodine substitution in the crystal, the phase change from cubic to tetragonal occurs [151]. As with the cubic crystals, a shift towards larger lattice constants was observed, which is in very good agreement with the literature [75, 85, 144, 151]. The reason for the increasing lattice constant from $MAPbCl_3$ to $MAPbI_3$ is the increasing ionic radius ($r_{ion}$) of the iodine ion ($r_{I^-}$ = 220 pm) compared to the bromine ion ($r_{Br^-}$ = 196 pm) and the bromine ion compared to the chlorine ion ($r_{Cl^-}$ = 181 pm), which is illustrated in Figure 36d [85]. In order to facilitate the comparison of the lattice constants of the MLTP crystals, the crystal structure of the perovskites $MAPb(Br_{0.2}I_{0.8})_3$, $MAPb(Br_{0.1}I_{0.9})_3$, and $MAPbI_3$ can be considered as pseudocubic, although they have a tetragonal symmetry [85, 111, 151]. This assumption was made because the transition from the cubic to the tetragonal structure is only characterised by a slight rotation of the neighbouring $PbX_6$ octahedra [175]. This also means that in a pseudocubic system [176], the reflections (002) and (110), among others, are replaced by the reflection (100). Hence, the new pseudocubic lattice parameters can be calculated as follows [175, 177, 178]:

$$a_{pseudocubic} = \frac{\sqrt{2 \cdot a^2}}{2} \tag{36}$$

$$c_{pseudocubic} = \frac{c}{2} \tag{37}$$

For the calculation of "$a_{pseudocubic}$", the face diagonal ($d=\sqrt{2}\cdot a$) of a cube is applied. Both lattice constants (a and c) are divided by two, to obtain the new lattice constants $a_{pseudocubic}$ and "$c_{pseudocubic}$" [175]. Ideally, $a_{pseudocubic}$ should be equal to $c_{pseudocubic}$ [175]. For a better overview, only the mean values of the pseudocubic lattice parameters were plotted in Figure 36e. Here, it becomes clear, that with increasing bromine and/or iodine incorporation, and thus with increasing ionic radius, the lattice constants increase almost linearly, which is in accordance with Vegard's law [179] and other researches about double-halide perovskites [85, 144, 151].

### 4.4.3 Optical Properties

The research work was completed by analysing the optical properties of the MLTP crystals. For this purpose, transmittance measurements were performed to determine the absorptance. Figure 37a shows that with increasing bromine and iodine substitution, the absorption edge of the crystals shifts to higher wavelengths, which is consistent with the different colours of the crystals. Thus, the $MAPbCl_3$ crystal absorbs almost only ultraviolet light [180], while the

$MAPb(Cl_{1-x}Br_x)_3$ (x = 0.2, 0.4, 0.6, 0.8, 1) crystals can absorb blue, green, and/or orange light. If the halogen chlorine is replaced by iodine, red light is also absorbed.

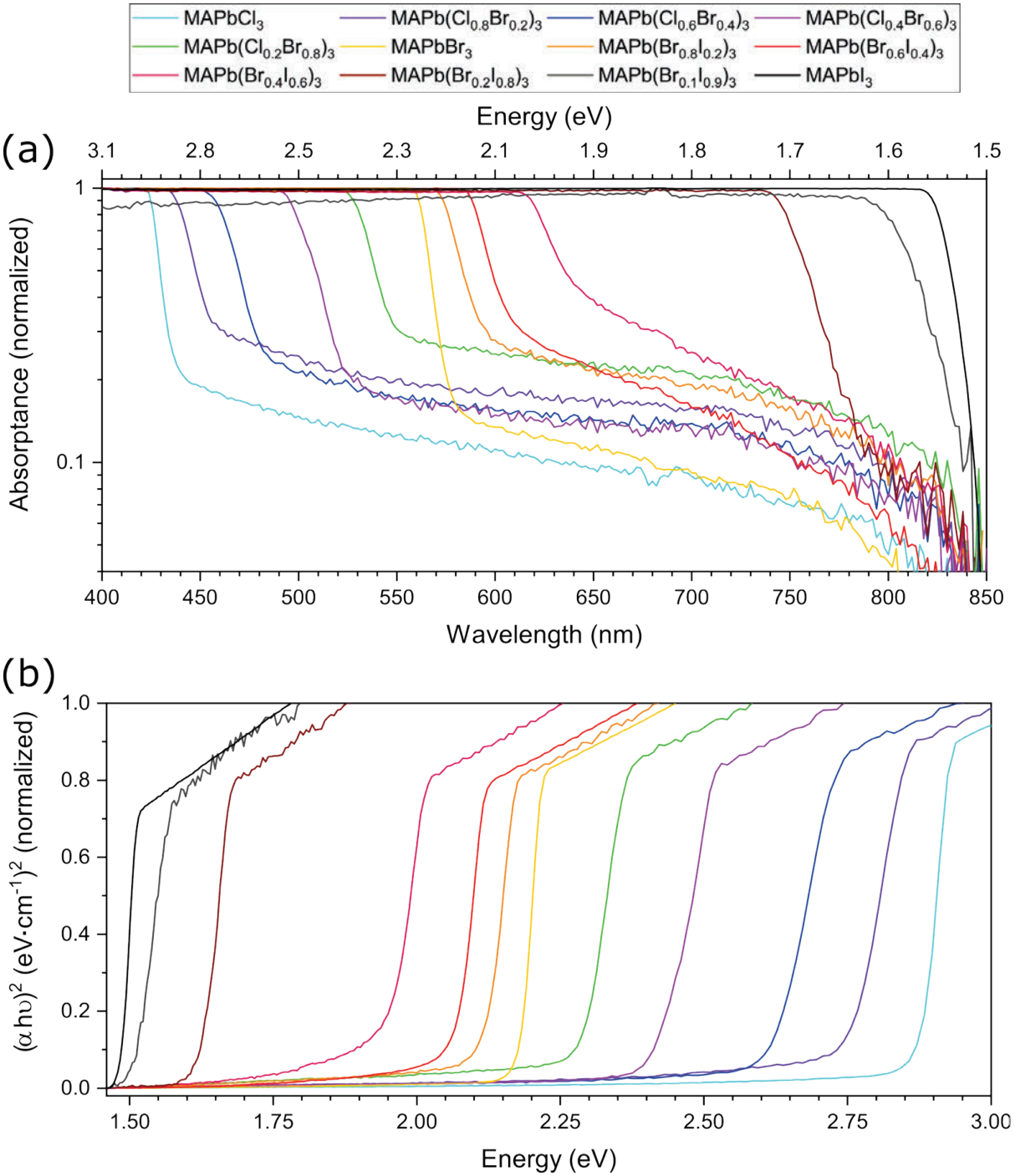


**Figure 37.** (a) Absorption spectra and (b) the Tauc plots of the single-halide perovskites $MAPbCl_3$, $MAPbBr_3$, $MAPbI_3$, as well as of the double-halide perovskites $MAPb(Cl_{1-x}Br_x)_3$ and the $MAPb(Br_{1-y}I_y)_3$ crystals. The Tauc plots were used to calculate the energies of the absorption edges of the crystals. (Since the transmittance significantly causes the absorption edge, and moreover an absolute value of the absorptance was not the aim of the optical study of the perovskite crystals, the reflectance was neglected for the calculation of the absorptance.)

The absorption capability of the $MAPb(Br_{0.1}I_{0.9})_3$ and $MAPbI_3$ crystals not only covers nearly the entire visible spectrum but even extends into the near-infrared region [151]. The absorption spectra were further used to prepare Tauc plots (Figure 37b) to finally determine the energies of the absorption edges of the crystals (Table 7). It is obvious that with increasing bromine and

iodine concentration, $E_{AE}$ is shifted to lower energies [144, 151, 181]. Thus, it can be concluded that the band gaps of the perovskites have also been systematically tuned by the varying halogen concentration [75, 85, 151, 152]. However, the Tauc plots do not allow an exact determination of the perovskite band gap due to the thickness of the crystals (Subchapter 3.2). For example, the absorption edge of the $MAPbCl_3$ crystal deviates from its band gap $E_g = 3.04$ eV [38] by 0.16 eV, while $E_{AE}$ of the $MAPbBr_3$ and $MAPbI_3$ crystals differs to their band gaps of $E_g(MAPbBr_3) = 2.30$ eV [38] and $E_g(MAPbI_3) = 1.59$ eV [38] by 0.13 eV and 0.11 eV, respectively, which is in very good accordance to previous reports about MLTP crystals [62, 63, 124]. Nevertheless, the determined absorption edges provide an approximation of the material properties of the perovskites.

**Table 7.** Calculated energies of the absorption edges ($E_{AE}$) of the single- and double-halide perovskite crystals. For the determination of the Tauc plots, a direct band gap of the perovskites was assumed [85, 151].

| **$MAPb(Cl_{1-x}Br_x)_3$** | **x = 0** | **x = 0.2** | **x = 0.4** | **x = 0.6** | **x = 0.8** | **x = 1** |
|---|---|---|---|---|---|---|
| **$E_{AE}$ (eV)** | 2.86 | 2.72 | 2.60 | 2.40 | 2.27 | 2.17 |
| | | | | | | |
| **$MAPb(Br_{1-y}I_y)_3$** | **y = 0.2** | **y = 0.4** | **y = 0.6** | **y = 0.8** | **y = 0.9** | **y = 1** |
| **$E_{AE}$ (eV)** | 2.1 | 2.05 | 1.93 | 1.61 | 1.51 | 1.48 |

## 4.5 Conclusions

Chapter 4 provided a broad overview of the MLTP crystals. By applying the crystallisation techniques RTC and AVC it was possible to grow the mm-sized single-halide crystals $MAPbCl_3$ and $MAPbBr_3$ as well as the double-halide $MAPb(Cl_{1-x}Br_x)_3$ crystals. The ITC and A-ITC enabled the growth of $MAPbI_3$ and the double-halide $MAPb(Br_{1-y}I_y)_3$ crystals. Moreover, PXRD patterns revealed a cubic symmetry for $MAPbCl_3$ to $MAPb(Br_{0.4}I_{0.6})_3$, while $MAPb(Br_{0.2}I_{0.8})_3$, $MAPb(Br_{0.1}I_{0.9})_3$, and $MAPbI_3$ exhibited a tetragonal structure. It was further shown that the Bragg reflections shifted to smaller scattering vectors with increasing bromine and iodine substitution, leading to a linear increase in the lattice constants. By changing the chlorine-bromine and bromine-iodine concentrations, the absorption properties were also modified. The different absorption edges of the MLTPs, which were clearly evaluated by the Tauc plots, are indications of the tuneability of their band gaps. The knowledge gained from the crystal growth techniques to structural measurements and optical properties formed the basis for Chapters 5, 6, and 7.

# 5 Single Crystal Growth of Complex Perovskites[3]

OLTPs form a highly interesting class of semiconductors, which might play an important role in future photovoltaics and optoelectronics. Particularly, the double cation – double halide perovskite $(FAPbI_3)_{0.9}(MAPbBr_3)_{0.1}$ or short FAMA, is one of the most important representatives of this material class [79, 182]. In order to estimate the full optoelectronic potential of this perovskite system and thus to foster its future technological use, it is essential to investigate high-quality single crystals with lowest structural as well as chemical defect density and with a stoichiometry relevant for their thin-film counterparts. However, the liquid growth of perovskite crystals without seed crystals is usually challenging and becomes even more demanding in the case of mixed cation – mixed halide single crystals, making it difficult to access their inherent properties. In this chapter, a new efficient seed crystal free re-fill crystallisation method (RFCM) based on ITC will be introduced to grow large-sized single crystals. Qualitative and quantitative analyses were performed to confirm the targeted elemental composition and the exact stoichiometry of the grown crystals. By means of crystal surface and bulk XRD measurements, the high crystal quality of the RFCM crystals will be demonstrated, which are superior to crystals obtained by the seed crystal method. Furthermore, steady-state photoluminescence (PL) and absorptance measurements were used to optically investigate the crystals. In addition, the crystals were successfully electrically contacted using self-made circuit boards to carry out current – voltage (I-V) as well as capacitance and conductance measurements. The hysteresis observed in the I-V curves, and the measurement of the conductivity clearly exhibits an ionic contribution, which is relevant for photovoltaic and optoelectronic implementation of this perovskite system. [26]

## 5.1 Introduction

OLTPs define a remarkable class of semiconductors exhibiting strong light absorption in the visible [183-186], tuneable band gaps [152, 187], long charge carrier lifetimes [170, 173], and high charge carrier mobilities [184, 188]. The optoelectronic properties enable a variety of technical applications ranging from light emitting diodes [189, 190], lasers [191, 192], photodetectors [193, 194] to solar cells [47, 149], which are usually made of solution [195] or vacuum-processed [196] polycrystalline perovskite layers with several hundreds of nanometres in thickness, but can now also be produced from thin single crystals [149, 194, 197]. For perovskite solar cells, power conversion efficiencies of almost 24 % [198] have been achieved in recent years by the incorporation of additives [198] as well as organic and inorganic cations and halides [47, 79, 199] into the lattice structure of $FAPbI_3$. Especially the double cation – double halide perovskite $(FAPbI_3)_{0.9}(MAPbBr_3)_{0.1}$ made a significant contribution to the field of solar cell research [47, 182] and became one of the most important compositions within the class of OLTPs. A decisive factor for further progress in this field and hence for commercialization is the comprehensive determination of the optoelectronic characteristics of

[3] This chapter is mainly based on the paper *"Seed Crystal Free Growth of High-quality Double Cation – Double Halide Perovskite Single Crystals for Optoelectronic Applications"* from Julian Höcker, Mehmet Ozcan, Sebastian Hammer, Mathias Fischer, Benedikt Bichler, Melina Armer, Philipp Rieder, Volker Drach, Jens Pflaum, Bert Nickel, and Vladimir Dyakonov, published in the Journal of Chemistry C in 2020, volume 8, pages 8275-8283.

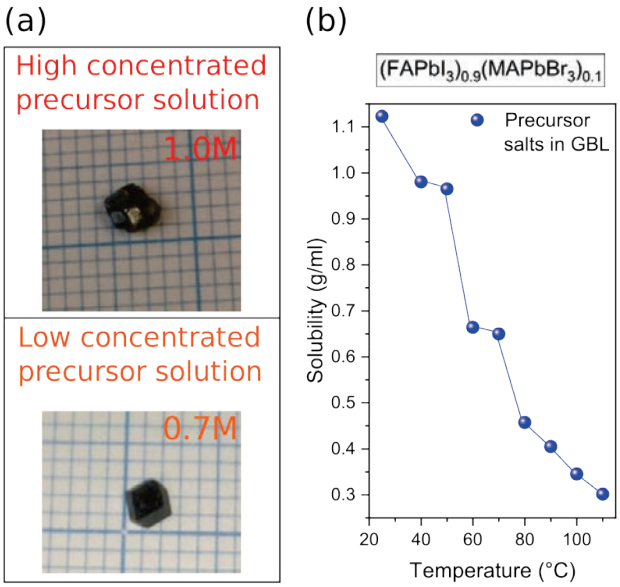


**Figure 38.** (a) $(FAPbI_3)_{0.9}(MAPbBr_3)_{0.1}$ crystal growth with a high concentrated and low concentrated precursor solution. (b) Inverse solubility behaviour of the $(FAPbI_3)_{0.9}(MAPbBr_3)_{0.1}$ precursor solution in GBL.

$(FAPbI_3)_{0.9}(MAPbBr_3)_{0.1}$ single crystals with the same stoichiometry as their polycrystalline thin film analogues. Methods commonly used to grow OLTP single crystals are liquid growth methods [56], such as the ITC [62] method. Fast crystal growth [62], easy handling, and low solvent-consumption are the key advantages of this method and is therefore most suitable for the growth of $(FAPbI_3)_{0.9}(MAPbBr_3)_{0.1}$ crystals. However, growing large-sized perovskite crystals to study their optoelectronic properties without seed crystals is difficult and becomes even more difficult for mixed cation – mixed halide perovskite crystals like $(FAPbI_3)_{0.9}(MAPbBr_3)_{0.1}$ [80]. In case of the latter, highly concentrated perovskite precursor solutions lead to the formation of polycrystals due to the strong nucleation of bromine [80] in the presence of iodine (Figure 38a). Diluted perovskite precursor solutions on the other hand allow the growth of mixed perovskite crystals, but reduce the time span of crystal growth and thus the crystal size, forcing the use of seed crystals (Figure 38a). Even though it is possible to obtain large-sized crystals by seed crystal methods, these crystals show a poor crystallinity, which is confirmed here by XRD patterns. On these accounts, studying the single crystal properties of large-sized perovskite crystals of high-quality is very demanding. To overcome these challenges, a new efficient seed crystal free re-fill crystallisation method was developed for control of an ITC-based process to grow $(FAPbI_3)_{0.9}(MAPbBr_3)_{0.1}$ perovskite single crystals. The key role of the utilized synthesis apparatus is a simple and fast exchange of perovskite precursor solution during the *in-situ* crystal growth, which facilitates the control of crystal size and avoids the use of seed crystals. By this approach, large-sized $(FAPbI_3)_{0.9}(MAPbBr_3)_{0.1}$ perovskite single crystals were synthesised and their high-quality was confirmed by surface and bulk XRD measurements. Particularly, in the case of mixed cation – mixed halide crystals like the $(FAPbI_3)_{0.9}(MAPbBr_3)_{0.1}$, it is essential to prove the incorporation of $MAPbBr_3$ into the $FAPbI_3$ crystal lattice by qualitative analyses. Consequently, the Fourier-transform infrared spectroscopy (FT-IR) was applied for the cation methylammonium and the cation formamidinium, as well as XRF measurements for Br, I, and Pb. Furthermore, it is important to verify the stoichiometry of the crystals. That is why the elemental analysis was used to quantify the mass fraction of hydrogen, carbon, and nitrogen. Furthermore, the EDX analysis as well as the inductively coupled plasma optical emission spectrometry (ICP-OES) were applied to determine the relevant amount of Br, I, and Pb. In total, the correct chemical composition and the proof of the expected ionic species provide evidence of the growth of $(FAPbI_3)_{0.9}(MAPbBr_3)_{0.1}$ perovskite single crystals enabling in the following a correct assignment of the measured absorptance and PL as well as the temperature- and frequency dependent electrical conductivity ($\sigma$) and dielectric constant ($\varepsilon_r$) of the crystals. [26]

## 5.2 Experimental Section

### 5.2.1 Chemicals

$PbI_2$ (99.99 %, trace metals basis) was obtained from TCI. $PbBr_2$ (99.999 %, trace metals basis), MABr (>99.5 %, recrystallized 4 times), and formamidinium iodide (FAI) (>99.5 %, recrystallized 4 times) were all purchased from Lumtec. GBL was acquired from Alfa Aesar with a purity of >99 %. Caesium bromide (CsBr) (99.999 %, trace metals basis) was bought from Sigma-Aldrich. All chemicals and solvents were used as received without further purification. [26]

### 5.2.2 Growth of $(FAPbI_3)_{0.9}(MAPbBr_3)_{0.1}$ Crystals and Reference Crystals

The perovskite precursor solutions were prepared in a nitrogen-filled glovebox with water and oxygen content lower than one part per million. The crystal growth took place under ambient conditions at a temperature of 21.5±1°C and a humidity of 35±10 %.
The $(FAPbI_3)_{0.9}(MAPbBr_3)_{0.1}$ precursor solution (0.7 M) was prepared as follows: MABr (94.05 mg, 0.84 mmol), $PbBr_2$ (308.29 mg, 0.84 mmol), FAI (1300.09 mg, 7.56 mmol), and $PbI_2$ (3485.23 mg, 7.56 mmol) were dissolved in 12 ml GBL.
The $(FAPbI_3)_{0.9}(MAPbBr_3)_{0.05}(CsPbBr_3)_{0.05}$ precursor solution (0.8 M) was prepared as follows: CsBr (102.15 mg, 0.48 mmol), MABr (53.75 mg, 0.48 mmol), $PbBr_2$ (352.33 mg, 0.96 mmol), FAI (1485.82 mg, 8.64 mmol), and $PbI_2$ (3983.12 mg, 8.64 mmol) were dissolved in 12 ml GBL.
The $FAPbI_3$ precursor solution (0.8 M) was prepared as follows: FAI (1650.91 mg, 9.6 mmol) and $PbI_2$ (4425.69 mg, 9.6 mmol) were equally dissolved in 12 ml GBL.
All precursor solutions were heated up to 80°C and stirred for 2 h for full solubility. 3 ml of a specified precursor solution was filtered *via* a 0.2 µm pore size PTFE syringe filter and heated up to 110°C to start the crystallisation. To obtain crystals with sizes of 0.5 to 0.8 cm, the precursor solution was changed 3 to 4 times. [26]

### 5.2.3 Crystal Characterisation

**Structural analyses techniques:** FT-IR measurements were carried out with a Bruker IFS 66v/S FTIR-spectrometer. For this purpose, 0.091 g of potassium bromide (KBr) and 0.014 g of $(FAPbI_3)_{0.9}(MAPbBr_3)_{0.1}$ crystal powder were mixed together to form a pellet.
XRF measurements were carried out with an XR-100T detector from Amptek and an X-ray machine from PHYWE as it was already described in Subchapter 4.3.4. Further XRF measurements, as well as powder and single crystal XRD patterns were recorded by an X-ray diffraction system General Electric XRD 3003 TT using a Cu-$K_{\alpha 1}$ radiation source with a wavelength λ of 1.5406 Å (V = 40 kV, I = 40 mA). The measurements were performed under ambient conditions.
The elemental analysis to determine the elements hydrogen, carbon, and nitrogen was performed on a vario MICRO cube micro elemental analyser. Measurements to determine the mass fraction of lead were performed with a Vista-MPX CCD Simultaneous ICP-OES spectrometer. For this, 15.1 mg of $(FAPbI_3)_{0.9}(MAPbBr_3)_{0.1}$ crystal powder was solved in 16 ml diluted acqua regia (12 $H_2O$ : 12 HCl : 1 $HNO_3$). To determine the mass fraction of iodine with ICP-OES, 13.83 mg of the crystal powder was solved in 7.5 ml of a 1 molar solution of sodium hydroxide (NaOH) and placed in an ultrasonic bath for full solubility. After this, 0.5 ml of a sodium borohydride ($NaBH_4$) solution was added.
Scanning electron microscope (SEM) images were taken with a SEM Carl Zeiss Ultra 55+ using a secondary electron detector. EDX measurements were carried out with the same detector as described in Subchapter 4.3.4. The measurements were performed in high vacuum. [26]

**Optical and electrical characterisation:** Reflectance and transmittance measurements were carried out in air using a Perkin Elmer Lambda 950 UV/VIS spectrometer to determine the absorptance. Steady-state PL measurements were performed by means of an Acton SpectraPro SP-2300 monochromator coupled to a nitrogen cooling CCD system from Princeton Instruments using a blue laser for excitation ($\lambda$ = 405 nm).
For electrical measurements, the crystal surface was coated with gold (Au) (d = 80 nm) using a Polaron Emitech SC7640 sputter coater. Photocurrent transients and I-V characteristics of the crystal device were measured in a nitrogen-filled glovebox under conditions of AM 1.5 G global spectral irradiance of 100 $mW \cdot cm^{-2}$ with a xenon lamp-based solar simulator. The Keithley MODEL 2612 B was used for recording the electrical measurements. Further I-V as well as impedance measurements were performed in a closed-cycle cryostat filled with helium. Capacitance and conductance measurements were carried out by using an Agilent E4980A Precision LCR Meter in four terminal configuration. An alternating current amplitude of 1 V was used to probe the crystal. The capacitance ($C_p$), the electrical conductance ($G_p$), and the inverse of the electrical resistance ($R_p$) were derived from the impedance (Z) using the following relationship:

$$\frac{1}{Z} = \frac{1}{R_p} + i\omega C_p \tag{38}$$

These values can be used to determine the relative frequency dependent permittivity according to

$$\varepsilon_r = \frac{d \cdot C_p}{\varepsilon_0 \cdot A_X} \tag{39}$$

as well as to calculate the conductivity

$$\sigma = G_p \cdot \frac{d}{A_X} \tag{40}$$

with the vacuum permittivity ($\varepsilon_0$), the thickness (d) and the area ($A_X$) of the plate capacitor. [26]

## 5.3 Results and Discussion

### 5.3.1 Crystal Growth with RFCM

RFCM is designed for growing OLTP single crystals by ITC without seed crystals and is based on the supersaturation of the precursor materials in an appropriate solvent [56] to form a precipitation in two steps: the spontaneous crystal nucleation and the crystal growth [68]. To grow $(FAPbI_3)_{0.9}(MAPbBr_3)_{0.1}$ perovskite crystals, inorganic lead halides $PbX_2$ ($X = Br^-, I^-$) and organic salts ZX ($Z = CH_3NH_3^+, CH_5N_2^+$) are mixed together in the polar solvent GBL. Subsequently, the dissolved precursor solution ($T_{Dissolving}$ = 80°C, $V_{Precursor\ solution}$ = 4 ml) is heated up to a defined temperature ($T_{Growing}$ = 110°C). The solubility of the target mineral $ZPbX_3$ decreases in the solvent with rising temperature [56, 64] (Figure 38b), resulting in a supersaturated solution and formation of crystal seeds [68]. In order to prevent the formation of polycrystals (Figure 38a), a diluted precursor solution of 0.7 M was used to grow $(FAPbI_3)_{0.9}(MAPbBr_3)_{0.1}$ crystals. The interval of crystal nucleation in diluted conditions ($T_{Growing}$ = 1.5 – 2 h) and the crystals, which form on the bottom of the vessel, are rather small. However, the construction of RFCM (Figure 39) allows to extract some volume fraction ($V_{Extracted\ solution}$ = 3 ml) of the supernatant and to simultaneously add fresh concentrated precursor solution of 110°C. The construction principle of the RFCM setup is explained in the

following: An anti-vibration mat (1) and a sand-filled box (2) reduce vibrations, which would induce structural defects during the extended growth phase and thus would hinder the preparation of high-quality crystals. The temperature sensor (3) of the hot plate (4) guarantees a constant oil temperature of 110°C in the petri dish (5). The perovskite crystal growth takes place in a custom-made vessel (6) with two glass tubes. After the initial crystal-growing interval, 110°C hot precursor solution (7) was slowly add to the vessel and the used solution (8) was simultaneously removed by a syringe. During this procedure, the crystal remains in the same position. The attached Dimroth condenser (9 – 11) minimises the effect of condensed and cooled GBL droplets, which would disturb the crystal growth by the temperature gradient induced in the vessel. [26]

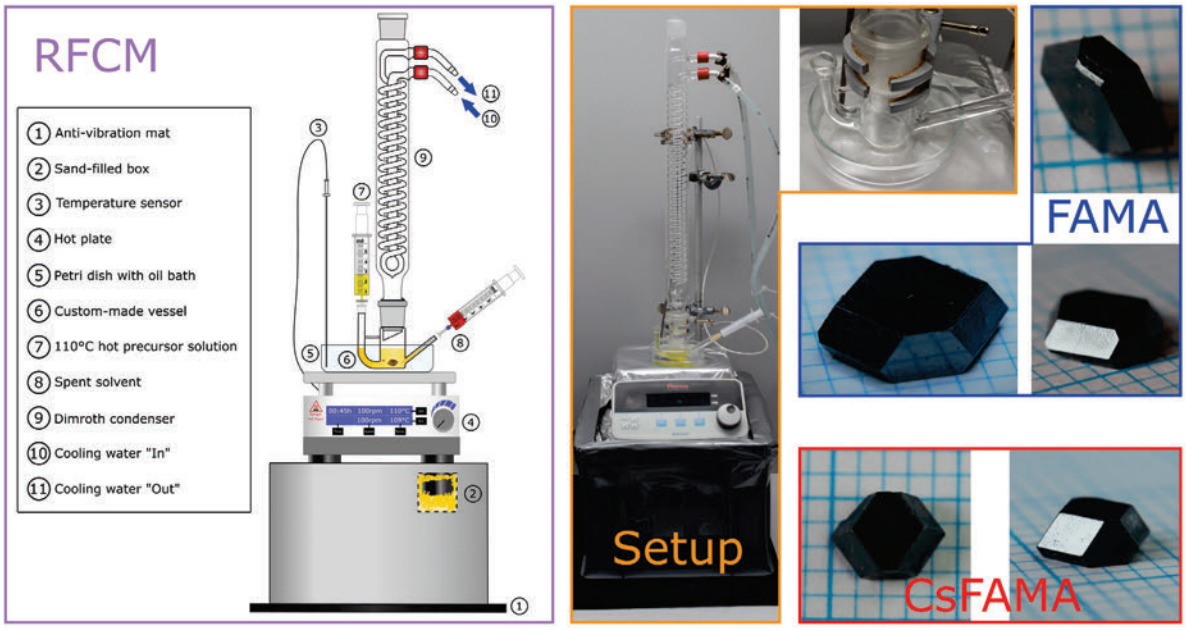


**Figure 39.** (left) Schematic illustration of the *in-situ* re-fill crystallisation method (RFCM) to control the OLTP crystal size, together with a description of the main parts. (middle) RFCM setup with custom-made vessel with two glass tubes to re-fill the precursor solution. (right) Images of $(FAPbI_3)_{0.9}(MAPbBr_3)_{0.1}$ and $(FAPbI_3)_{0.9}(MAPbBr_3)_{0.05}(CsPbBr_3)_{0.05}$ perovskite single crystals, grown by RFCM. Reproduced mainly from Ref. [26] with permission from the Royal Society of Chemistry.

In summary, this sophisticated but mechanically simple construction provides extra control on the growth conditions of $(FAPbI_3)_{0.9}(MAPbBr_3)_{0.1}$, which favour large single crystals [26]. A typical crystal with pronounced facets obtained from a successful growth is shown in Figure 39 [26]. The method is not limited to grow $(FAPbI_3)_{0.9}(MAPbBr_3)_{0.1}$ crystals, but can also be applied to all other known OLTPs to grow large-sized crystals. Moreover, RFCM is also applicable to synthesise crystals with the even more complex stoichiometry $(FAPbI_3)_{0.9}(MAPbBr_3)_{0.05}(CsPbBr_3)_{0.05}$ or short CsFAMA [81]. Further information about this crystal can be found in the appendix (Figure B1 and Table B1).

### 5.3.2 Qualitative and Quantitative Analyses

In a first step, the convenient and accurate XRF technique was used to qualitatively verify the presence of Br, I, and Pb in the crystal. The corresponding experimental data of the crystal powder and the crystal surface reveal the $K_\alpha$ (11.9 keV) and $K_\beta$ (13.3 keV) lines of the K-shell emission of Br [104]. Besides the detection of Br, Figure 40a and b shows the $L_\alpha$, $L_\beta$, and $L_\gamma$ emission lines of I [104] as well as the lines $L_\alpha$, $L_\beta$, $L_\gamma$, and $M_\alpha$ of Pb [104]. The data of the XRF-measurements can be found in Table B2 in the appendix.
The incorporation of the organic cations $CH_3NH_3^+$ and $CH_5N_2^+$ into the crystal structure was qualitatively proved by FT-IR. Figure 40c shows the peaks of the $CH_3NH_3^+$ rock [200] at the

wavenumbers 912 $cm^{-1}$ and 1286 $cm^{-1}$, as well as the symmetrical $NH_3^+$ bending and stretching [200] at 1471 $cm^{-1}$ and 3161 $cm^{-1}$. The transmittance spectrum also shows the (=C–H) bending [201] at 1049 $cm^{-1}$ and the (C=N) stretching [201] at 1711 $cm^{-1}$, which are unambiguous indicators for the integration of the $CH_5N_2^+$ cation.
EDX measurements of the crystal surface were carried out to quantitatively prove the incorporation of the elements Br, I, and Pb. The clear evidence of the three elements is confirmed by Figure 40d. The exact assignment of the emission lines of Br, I, and Pb was used to determine the mass fraction of the three elements by the respective peak areas (Table 8) and confirms the homogeneous distribution of the elements within the crystalline lattice by mapping images (Figure 40e).

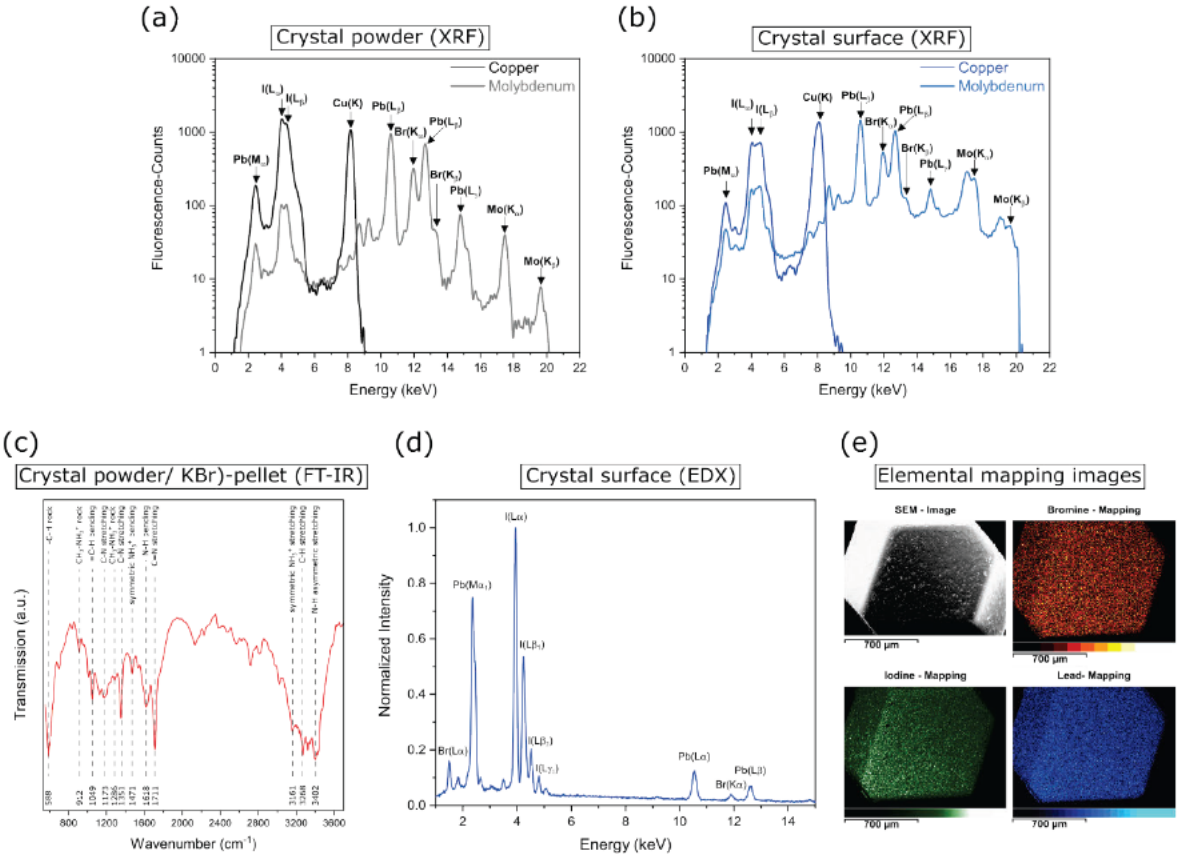


**Figure 40.** XRF results of (a) the $(FAPbI_3)_{0.9}(MAPbBr_3)_{0.1}$ crystal powder and (b) of the crystal surface to qualitatively determine the incorporation of the elements Br, I, and Pb using an unfiltered Mo-$K_\alpha$ and a Cu-$K_{\alpha 1}$ radiation source, respectively. (c) FT-IR spectrum of the $(FAPbI_3)_{0.9}(MAPbBr_3)_{0.1}$ crystal powder to qualitatively determine the organic cations $CH_3NH_3^+$ and $CH_5N_2^+$ with peak assignment of the vibrational modes. (d) EDX spectrum measured on the $(FAPbI_3)_{0.9}(MAPbBr_3)_{0.1}$ crystal surface to quantify the elements Br, I, and Pb. (e) Elemental mapping images determine the distribution elements. The brighter the colour, the higher the density of the respective element on the crystal surface. Reproduced from Ref. [26] with permission from the Royal Society of Chemistry.

To verify the stoichiometry of the $(FAPbI_3)_{0.9}(MAPbBr_3)_{0.1}$ crystal more quantitatively, the crystal powder was analysed by elemental analysis and by ICP-OES. The experimental values of the elements in Table 8 are in good agreement with the theoretical predictions. It thus can be concluded, that the stoichiometric compositions of $(FAPbI_3)_{0.9}(MAPbBr_3)_{0.1}$ precursor solution and resulting crystal fully coincide. [26]

**Table 8.** Theoretical mass fraction (M) values of the $(FAPbI_3)_{0.9}(MAPbBr_3)_{0.1}$ crystal and the experimental determined values measured with EDX, EA, and ICP-OES. Reproduced from Ref. [26] with permission from the Royal Society of Chemistry.

| M [%] | Theory | EA | EDX | ICP-OES |
|---|---|---|---|---|
| **H** | 0.832 | 0.81±0.02 | | |
| **C** | 1.945 | 1.98±0.02 | | |
| **N** | 4.309 | 4.20±0.05 | | |
| **Br** | 3.882 | | 5.17±0.23 | |
| **I** | 33.550 | | 31.74±0.48 | 33.76±0.63 |
| **Pb** | 55.482 | | 59.87±0.38 | 55.46±0.77 |

### 5.3.3 Structural Properties

The XRD results of the crystal powder obtained from ground crystals in Figure 41a and Table B3 matches the simulated data for the simple cubic lattice of $(FAPbI_3)_{0.9}(MAPbBr_3)_{0.1}$

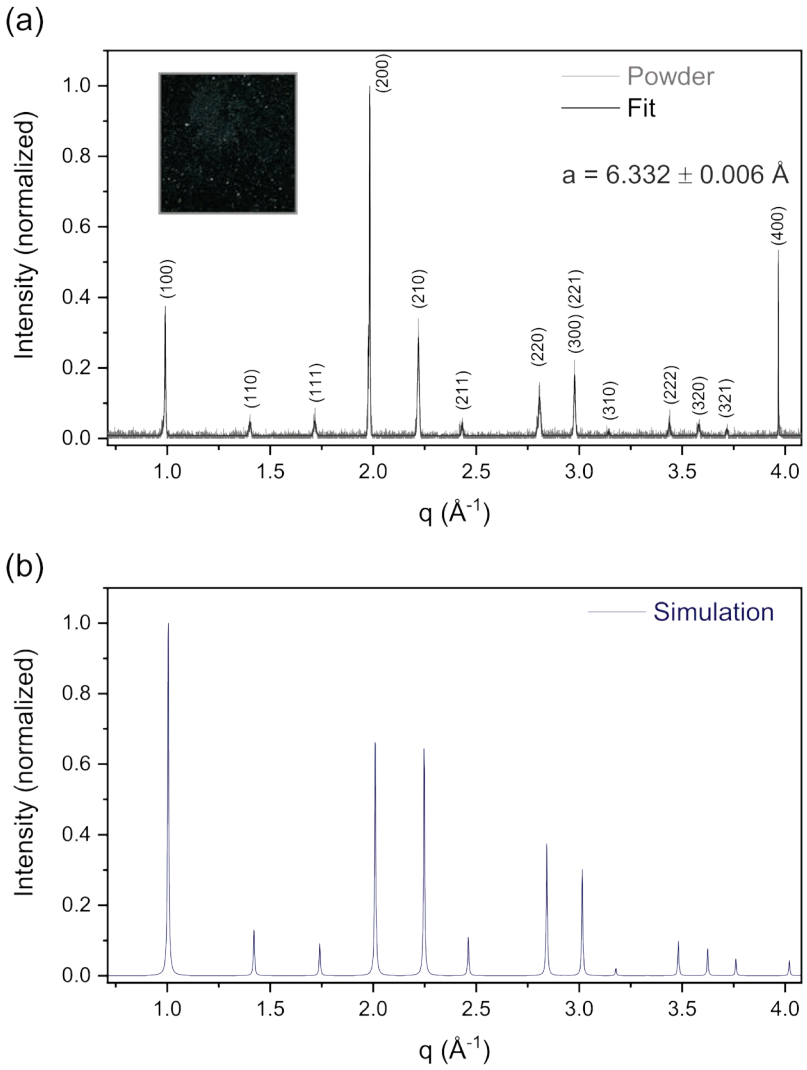


**Figure 41.** (a) Measured XRD pattern of the $(FAPbI_3)_{0.9}(MAPbBr_3)_{0.1}$ crystal powder with associated fit and image of the crystal powder. (b) Simulated XRD pattern indicates a simple cubic system. The PXRD simulation of the perovskite were made by using the crystallographic data from Ref. [81]. Reproduced from Ref. [26] with permission from the Royal Society of Chemistry.

very well [202] (Figure 41b). A detailed analysis of the Bragg peak positions of the $(FAPbI_3)_{0.9}(MAPbBr_3)_{0.1}$ crystal powder yield a cubic lattice constant of a = 6.332±0.006 Å. In contrast, the determined value of the cubic phase of pure α-$FAPbI_3$ (Figure B2 and Table B4 in the appendix) is a = 6.382±0.015 Å, while the evaluation of the cubic phase of $MAPbBr_3$ shows a = 5.929±0.001 Å (Figure 35b and Table A3), both in good agreement with the literature [22, 32, 80]. The smaller unit cell of the $(FAPbI_3)_{0.9}(MAPbBr_3)_{0.1}$ system indicates that the incorporation of the cation $CH_3NH_3^+$ and of the halide ion $Br^-$ condenses the α-$FAPbI_3$ lattice by 0.78 % due to smaller effective radiuses compared to the anion $I^-$ and the cation $CH_5N_2^+$, respectively [203, 204]. Compositional engineering may enhance the stabilisation of the crystal lattice by tuning lattice parameters and bond environment [72, 205].

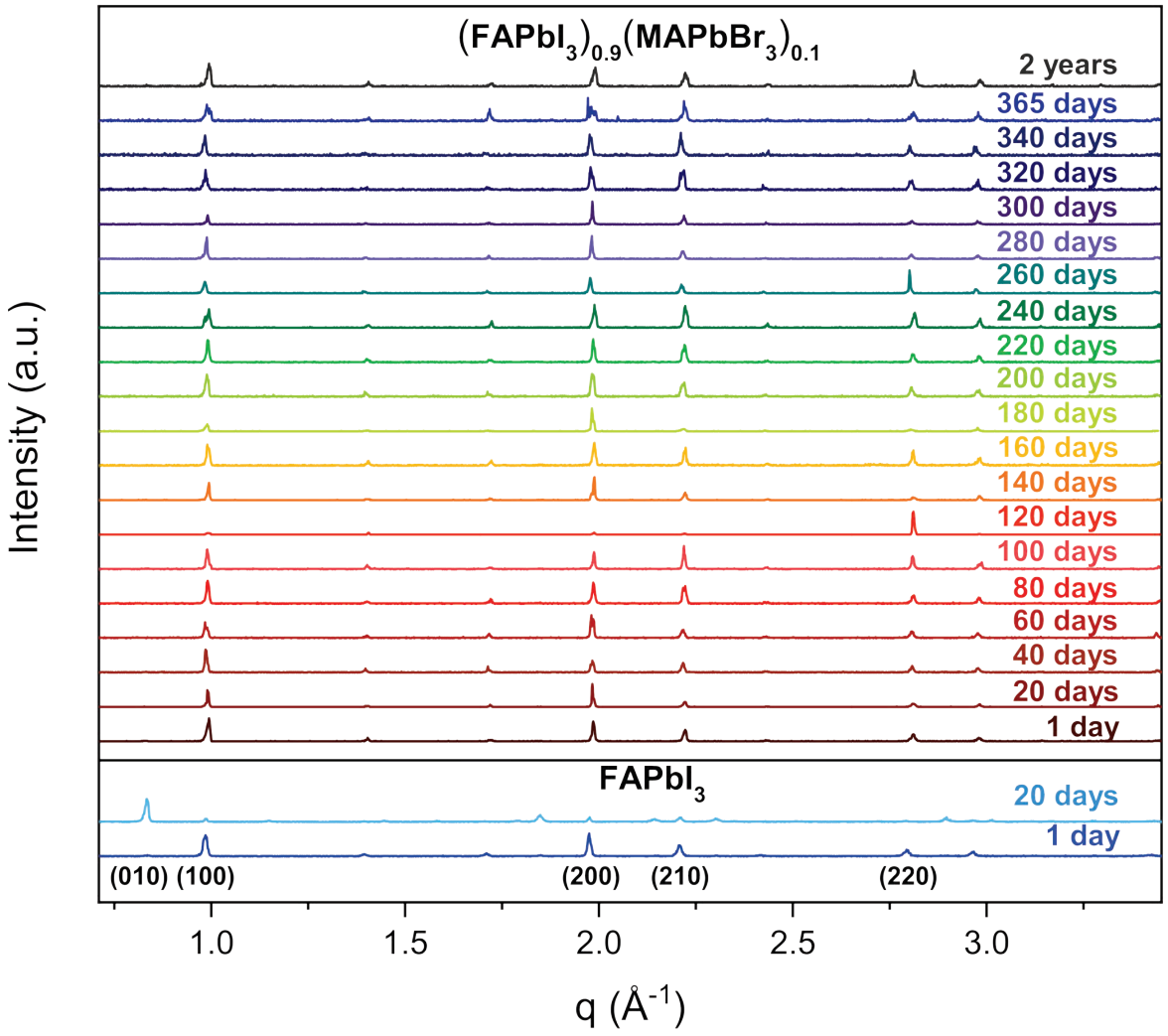


**Figure 42.** Long-term stability XRD – test over two years of the $(FAPbI_3)_{0.9}(MAPbBr_3)_{0.1}$ crystal powder. Compared to the $FAPbI_3$ crystal powder, the double cation – double halide perovskite powder is stable under ambient conditions. The δ-peak (010), an indication of decomposed crystal powder, is only observed by the pattern of the $FAPbI_3$ crystal powder. Reproduced from Ref. [26] with permission from the Royal Society of Chemistry.

Moreover, from the absence of the $PbI_2$ peak at 0.83 $Å^{-1}$, which is usually a clear indicator of decomposition, it can be concluded that the crystal powder was stable under ambient conditions over two years (Figure 42). Therefore, the incorporation of $MAPbBr_3$ stabilizes the crystal [80], and makes it superior to the unstable $FAPbI_3$ crystal [64, 83], which decomposes immediately after completion of the growth process, as shown in Figure B2.

In order to demonstrate the benefit of the *in-situ* growth process inherent to RFCM in comparison to the seed crystal method, out-of-plane XRD measurements of crystals grown by

RFCM and by the seed crystal technique were compared, respectively (Figure 43). RFCM crystals were grown as described by simultaneous exchange of precursor and used solution.

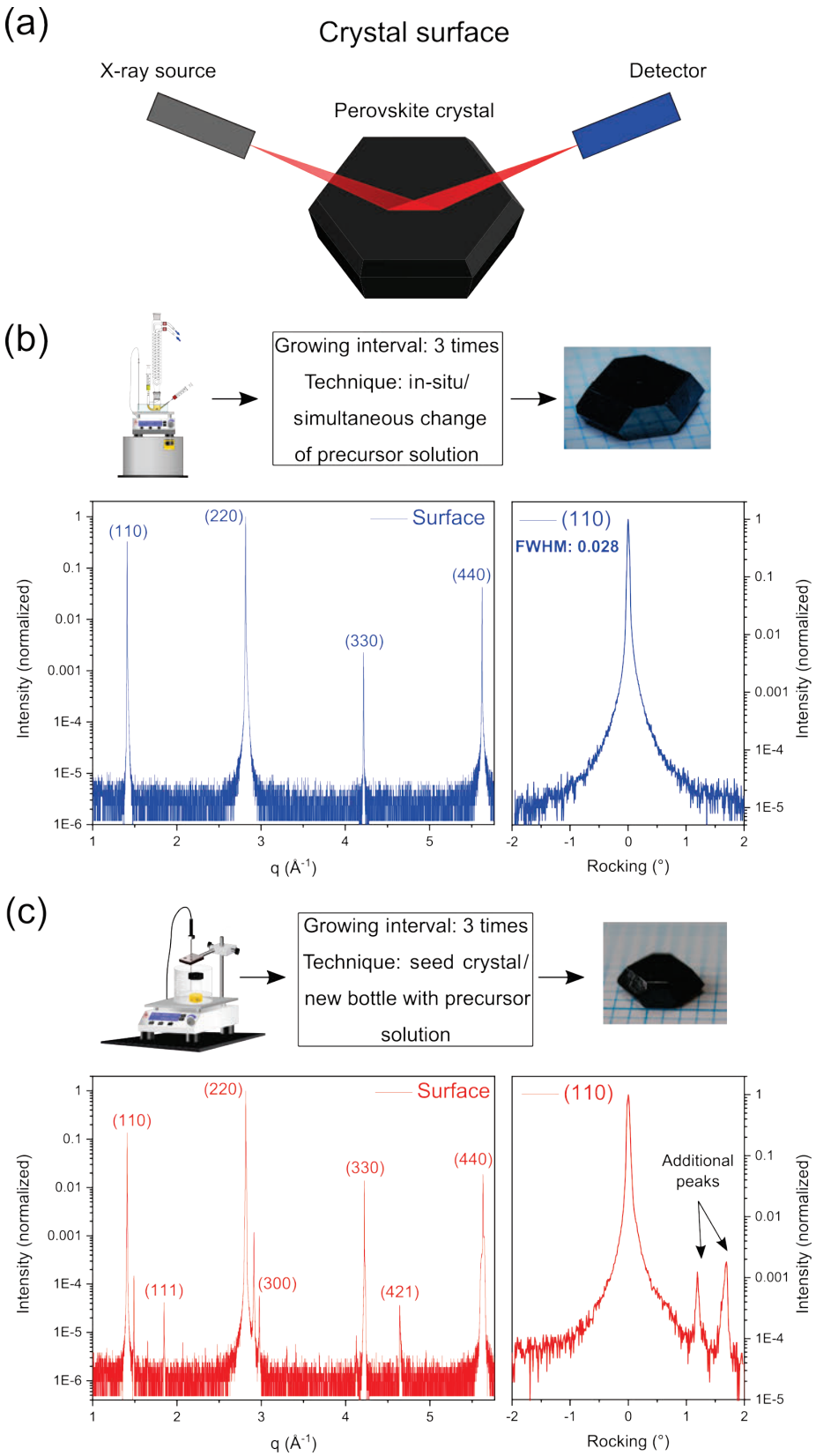


**Figure 43.** (a) Schematic illustration of the out-of-plane surface XRD measurements. Comparison of large-sized crystals grown by RFCM and by the seed crystal technique: XRD results and corresponding (110) rocking scans (b) of a single crystal grown *in-situ* and (c) of a crystal grown with a seed crystal. Reproduced from Ref. [26] with permission from the Royal Society of Chemistry.

For the seed crystal technique, a small crystal was taken from the used solution and placed in a new bottle with fresh precursor solution. Both methods result in samples of polyhedral shape and sharp edges (see images in the insets of Figure 43) and visually imply single crystals in both cases. X-ray Bragg scattering in reflection geometry was obtained for both crystals (Figure 43a). The RFCM crystal reveals a {110} peak series for the dominant surface, cf. Figure 43b.

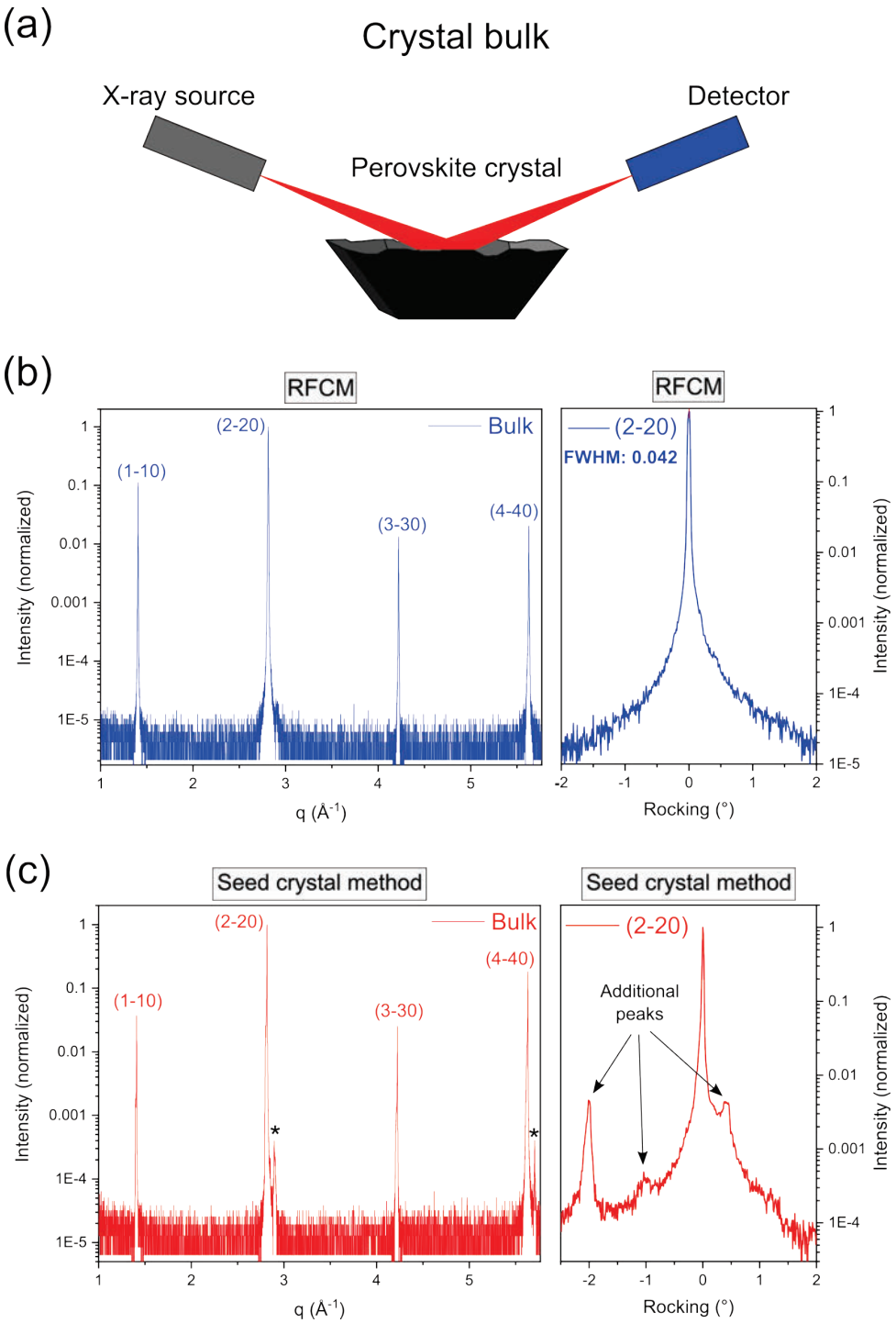


**Figure 44.** (a) Schematic illustration of the out-of-plane bulk XRD measurements. Comparison of out-of-plane XRD bulk measurements and corresponding (2-20) rocking scans (b) of a single crystal and (c) of a crystal grown with a seed crystal. The crystals were cut along the [110] direction with a scalpel to measure the centre of the crystal. Additional *-signed peaks can be associated to further Bragg reflexes. Reproduced from Ref. [26] with permission from the Royal Society of Chemistry.

Instead, a closer inspection of the X-ray data of crystals grown conventionally by a seed crystal are of overall lower quality. For example, while also the main {110} peak series in both samples can be found for the seed crystal grown sample, additional diffraction peaks occur, which can be identified as (111), (300), and (421) Bragg reflexes (Figure 43c). Moreover, the so-called rocking scan of the (110) reflex, which probes for mosaicity (Subchapter 3.1.2), reveals two additional peaks in comparison to the rocking scan on the RFCM crystal, indicating the presence of twinned structural domains at the sample surface. Further out-of-plane XRD measurements were obtained from the crystal bulk by dividing the crystal into two equal parts with a scalpel along the [110] direction (see Figure 44a). The XRD results confirmed the single crystal growth by RFCM (Figure 44b) due to the dominant {110} peak series and the sharp rocking peak of the (2-20) plane. The X-ray data of the conventional grown crystal (Figure 44c) are comparable to those of Figure 43c with additional Brag reflexes and further peaks in the rocking scan, which underlines the above mentioned statements. [26]

### 5.3.4 Optical Properties

The absorption spectrum of the $(FAPbI_3)_{0.9}(MAPbBr_3)_{0.1}$ single crystal in Figure 45a covers the full visible range of the electromagnetic spectrum from 400 to 850 nm elucidating its importance as light absorber in photovoltaics. The energy of the absorption edge of 1.447 eV estimated by the Tauc plot (Figure 45b) is in good accordance with the direct $E_g$ of $(FAPbI_3)_{0.9}(MAPbBr_3)_{0.1}$ found in the literature [80] and comparable with $E_g$ of α-$FAPbI_3$ single crystals [64, 83]. Accordingly, the stabilisation of the crystal through the incorporation of $MAPbBr_3$ into the crystal lattice causes only a slight blue shift, but generally maintains the optical properties of α-$FAPbI_3$. The blue shift is also observed in PL for $(FAPbI_3)_{0.9}(MAPbBr_3)_{0.1}$ single crystals (Figure 45a), as compared to the literature value for α-$FAPbI_3$ single crystal with its PL maximum at 820 nm [206]. The PL spectral shape with two peaks at 794 nm and 844 nm may be due to self-absorption and multiple reflection [207], though such a line shape has not yet been observed in double cation – double halide perovskite single crystals. [26]

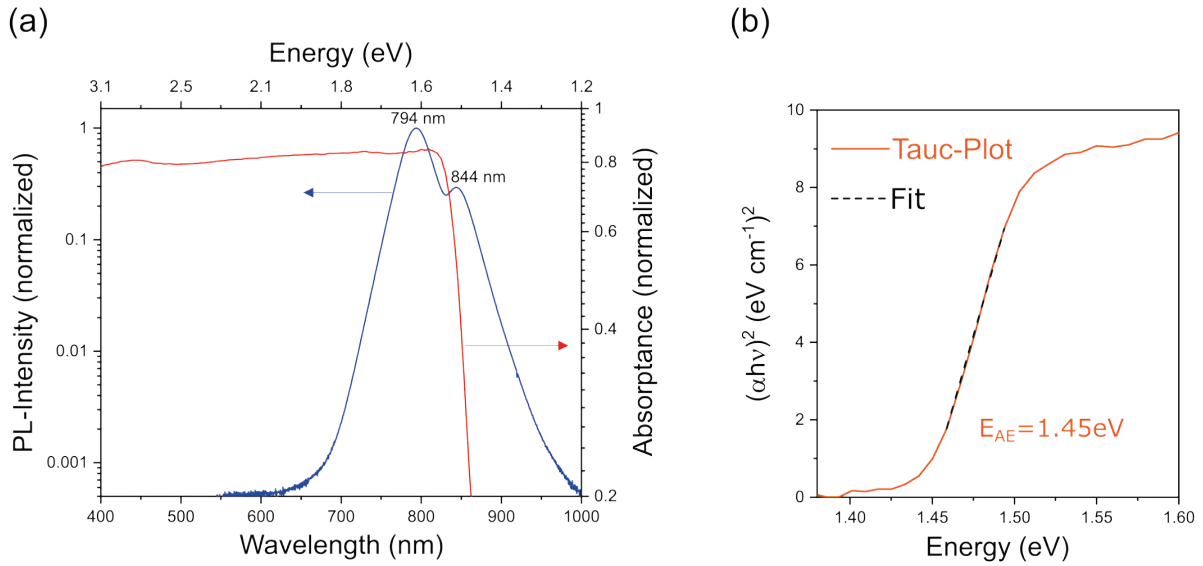


**Figure 45.** (a) Absorption spectrum (red) and photoluminescence (PL) spectrum (blue) of the crystal. (b) Tauc plot of a 2.3 mm thick $(FAPbI_3)_{0.9}(MAPbBr_3)_{0.1}$ crystal to determine the absorption edge of the crystal. Reproduced from Ref. [26] with permission from the Royal Society of Chemistry.

### 5.3.5 Electronic Properties

To study the electrical properties of $(FAPbI_3)_{0.9}(MAPbBr_3)_{0.1}$ single crystals, gold electrodes were vacuum deposited on two opposing surfaces of a single crystal, as shown as an illustration in Figure 46a. The prepared crystal was then placed on a copper plate sputtered with

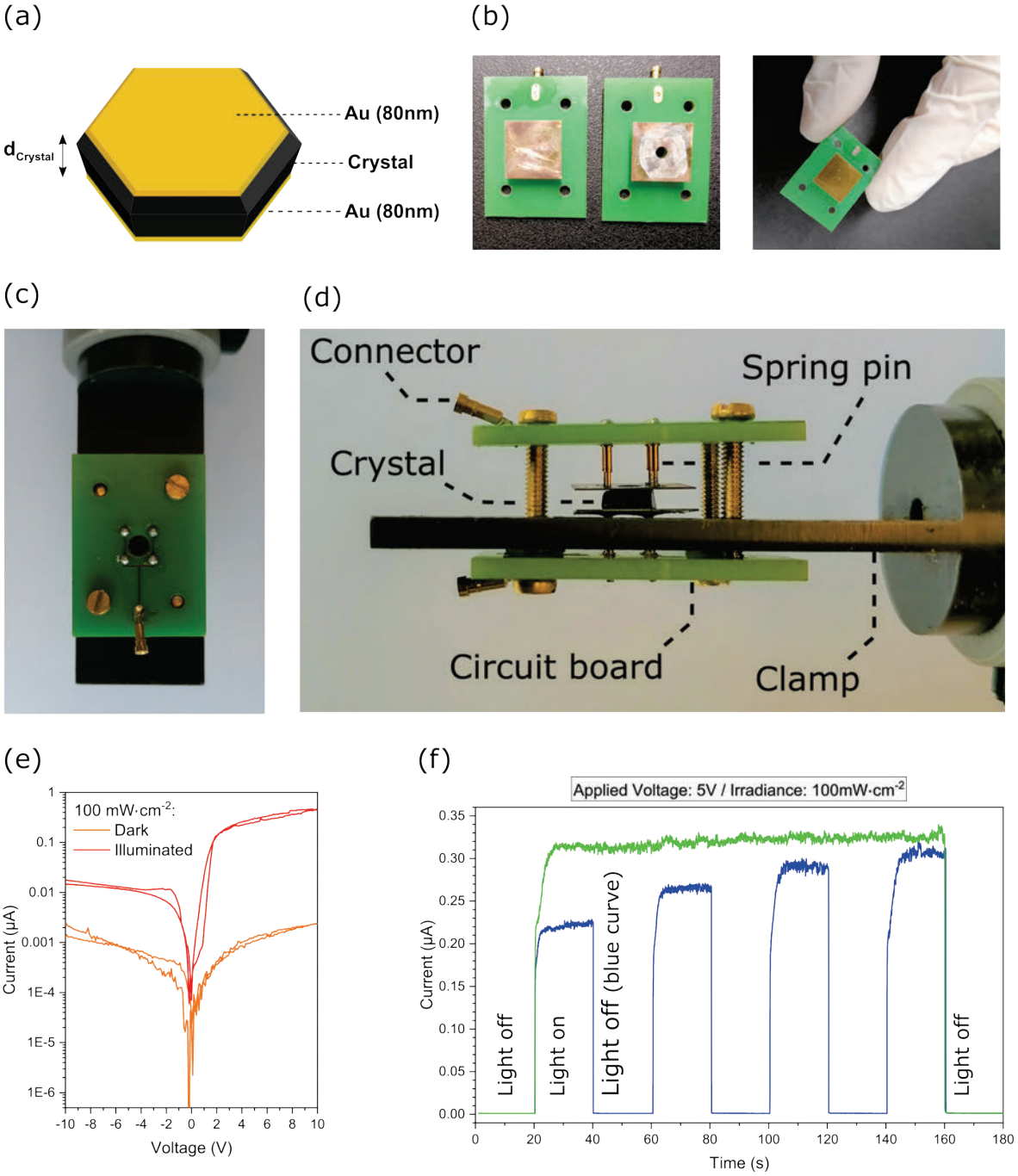


**Figure 46.** (a) Schematic illustration of a gold (Au) sputtered $(FAPbI_3)_{0.9}(MAPbBr_3)_{0.1}$ crystal. Reproduced from Ref. [26] with permission from the Royal Society of Chemistry. (b) – (d) Self-made circuit boards for electrical contacting the OLTP crystals. (e) Dark and illuminated current – voltage (I-V) curves of a double cation – double halide perovskite crystal. (f) Photocurrent transients of a $(FAPbI_3)_{0.9}(MAPbBr_3)_{0.1}$ crystal with different illumination times.

gold, to which four spring pins were soldered. The spring pins in turn were soldered to a board. With the help of the plug connector on the circuit board, an electrical contact to the crystal can easily be established. The top of the crystal was also contacted in this way. One gold sputtered

copper plate has a hole with a 2 mm radius to irradiate the crystal with light. The circuit boards including the crystal is fixed to a holder with screws so that the crystal cannot slide around on the copper plates. This self-made setup, which is shown in Figure 46b – d, ensures a gentle contacting of the brittle $(FAPbI_3)_{0.9}(MAPbBr_3)_{0.1}$ crystals and is also suitable for contacting any other OLTP crystal. To verify the functionality of the circuit boards, I-V curves were recorded from the crystal, both in the dark and under an irradiance of 100 $mW \cdot cm^{-2}$ (Figure 46e). In the dark, the current, which flows through the crystal, was only 0.002 µA at an applied voltage of 10 V. At the same voltage, the photocurrent was 0.446 µA when the crystal was illuminated. Since the current measured under illumination is over 200 times higher than in the dark, it can be assumed that the crystal is correctly contacted. Furthermore, this is a first indication that a sputtered $(FAPbI_3)_{0.9}(MAPbBr_3)_{0.1}$ crystal may also serve as photodetector [122]. Both, the successful crystal contacting and the possible use

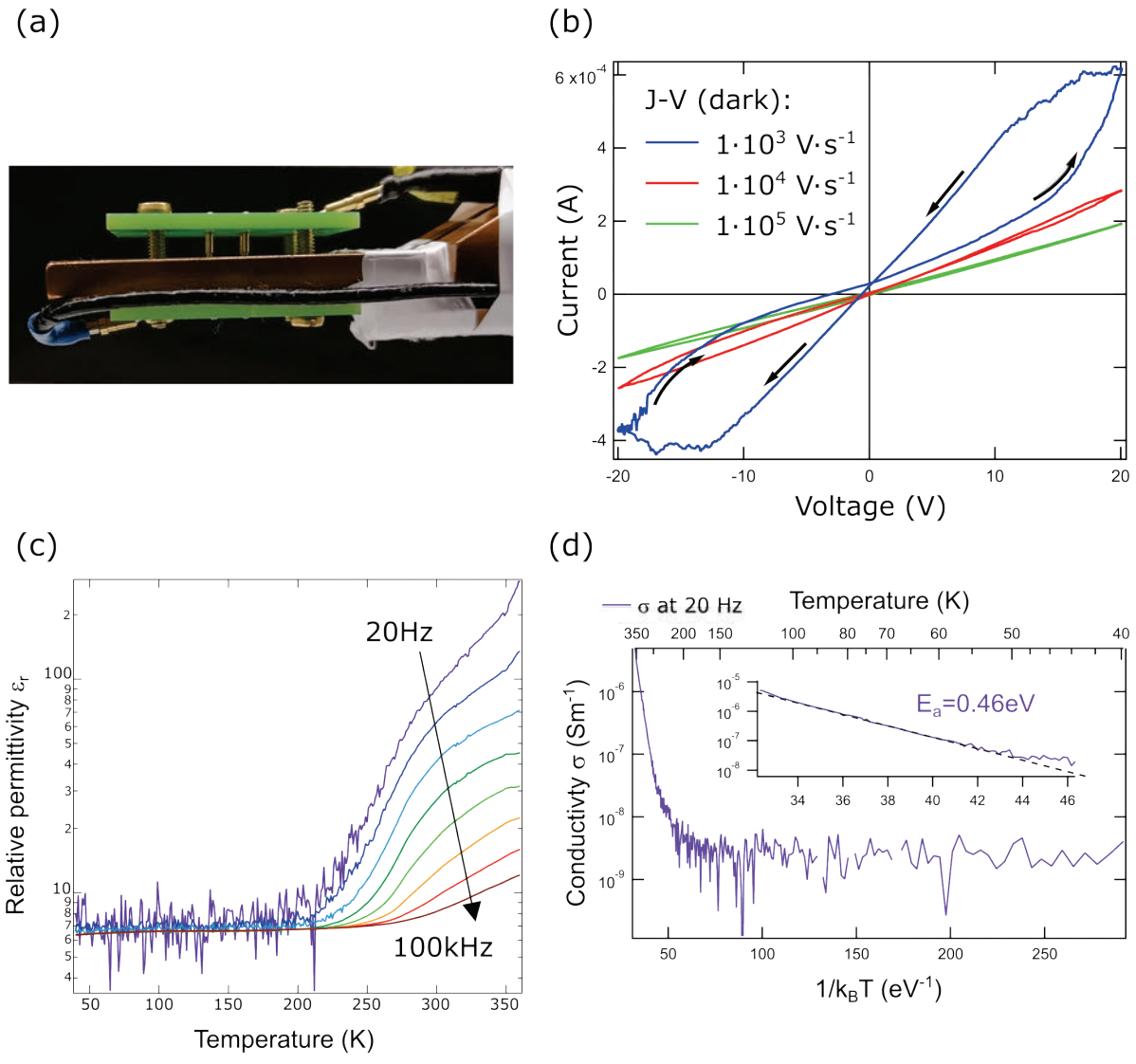


**Figure 47.** (a) Circuit boards for a $(FAPbI_3)_{0.9}(MAPbBr_3)_{0.1}$ single crystal device fixed on a copper block for measurements in the cryostat. (b) I-V curves with hysteresis loops of the $(FAPbI_3)_{0.9}(MAPbBr_3)_{0.1}$ single crystal device with the geometry of a plate capacitor. The same single crystal device was used for the determination of the relative permittivity and the alternating current electrical conductivity. (c) Temperature-dependent relative permittivity ($\varepsilon_r$), measured in the frequency range of 20 Hz – 100 kHz. d) Temperature-dependent electrical conductivity ($\sigma$) measured at 20 Hz. The inset shows an Arrhenius law for temperatures above 200 K. (b), (c), and (d) reproduced from Ref. [26] with permission from the Royal Society of Chemistry.

as a photodetector are supported by the measurement of the photocurrent as a function of time at an applied voltage of 5 V, which can be seen in Figure 46f. When the xenon lamp is switched on, a jump in the photocurrent is immediately detected. The instantaneous increase in the photocurrent could be detected for certain illumination intervals (blue and green curves), suggesting successful crystal contacting.
A more detailed study of the electronic properties of the $(FAPbI_3)_{0.9}(MAPbBr_3)_{0.1}$ crystal was performed in the cryostat. Therefore, the crystal device was placed on a copper block, which is necessary for temperature-dependent measurements (Figure 47a). Since the geometry of the device corresponds to that of a plate capacitor, it was possible to measure the temperature-dependent relative permittivity (Figure 47c) and the electrical conductivity (Figure 47d) with a temperature ramp of $0.7\ K \cdot min^{-1}$. At temperatures below 200 K, the observed $\sigma\ (20\ Hz) = 2 \cdot 10^{-9}\ S \cdot m^{-1}$ is about two orders of magnitude below the conductivity of undoped Gallium arsenide [114]. As the crystal behaves like an intrinsic semiconductor in this temperature range, it is possible to conclude on an extremely low density of impurities. Above 200 K, an exponential increase of $\sigma$ is observed. The increase in $\sigma$ is accompanied by an increase in $\varepsilon_r$ from 7 to more than 100 at low frequencies. Such a frequency behaviour can be associated with ion migration effectively contributing to electrical transport. The activation energy of $E_a = 0.46$ eV obtained from temperature-dependent measurements of $\sigma$ is related to the increase of the ionic diffusion coefficient with temperature, comparable with ion migration studies of other perovskite compositions [208-211]. The effect of ion migration is also observed by measuring I-V characteristics (Figure 47b) of the same single crystal device in the dark. By changing the operating conditions, sweep rate or polarity of the voltage, different shapes for the I-V curves are obtained due to the occurrence of hysteresis. This phenomena is widely observed in the field of perovskite solar cells [212-214] and has recently also been discovered for a $MAPbBr_3$ single crystal device [215], highlighting in all of them the major contribution of ion migration to the formation of current – voltage hysteresis, which was also visible in Figure 46e. The characteristic frequency dependence observed in $\varepsilon_r$ further supports this assignment [216] and the increase in low frequencies matches well with the behaviour found in other metal-halide perovskites [217, 218]. Due to the single crystallinity of the perovskite, a major contribution by grain boundaries can be excluded as transport channels for ion migration and rather assign the observed activation energy to a bulk transport mechanism in the $(FAPbI_3)_{0.9}(MAPbBr_3)_{0.1}$ crystal. Phase transitions, as observed for the perovskite $\alpha$-$FAPbI_3$ from a simple cubic symmetry to a ditetragonal dipyramidal system in the range of 285 to 290 K [219, 220] and to a ditetragonal phase at around 140 K [219-221] are not obvious from the dielectric measurements of the $(FAPbI_3)_{0.9}(MAPbBr_3)_{0.1}$ crystal. [26]

## 5.4 Conclusions

In conclusion, the new method RFCM was established to grow stable, stoichiometric, and large-sized $(FAPbI_3)_{0.9}(MAPbBr_3)_{0.1}$ single crystals of superior structural quality without need for seed crystals. The high degree of crystallinity of the crystal bulk and surface was confirmed by means of X-ray reflectometry. In contrast, crystals of the same composition but grown by the conventional seed crystal method showed higher textural imperfections when examined by out-of-plane reflectometry and rocking scans, although they are visually as perfect and have the same optical properties of $E_{AE} = 1.447$ eV as the RFCM grown samples. For the electrical contacting of the crystals, circuit boards were developed and successfully tested by recording I-V curves and photocurrent transients. These circuit boards allow easy and soft handling of the crystals and additionally eliminate the use of conductive adhesives. Temperature and frequency dependent capacitance measurements on single crystal devices show a more than tenfold increase of the relative permittivity from 7 to above 100, which can be attributed to an ionic

contribution to electrical transport. Grain boundaries as main transport channels were ruled out regarding the exceptional crystallinity of the samples and assign the electrical transport properties to the crystal bulk. The control and confirmation of the exact stoichiometry by complementary qualitative and quantitative measurements in combination with the determination of lowest structural as well as chemical defect density therefore impose fundamental requirements to unravel the optoelectronic properties of complex lead-halide perovskite systems. [26]

# 6 Temperature-reduced and Rapid Growth of OLTP Single Crystals[4]

In Chapter 5, a mechanical approach was adopted to increase the crystal growth time interval and to finally grow large-sized OLTP single crystals. In this chapter, a chemical approach is described to synthesise large-sized perovskite single crystals. For this purpose, the OLTP precursor solutions with the stoichiometry $ABX_3$ ($A = MA^+$ or $FA^+$; $B = Pb^{2+}$; $X = Cl^-$, $Br^-$ or $I^-$) were mixed with primary alcohols. As a result, the blends lead to a significant reduction in their retrograde solubility's and enables a temperature-reduced crystallisation pathway to grow high-quality single crystals. [23]

## 6.1 Introduction

OLTP single crystals are gaining more and more interest in the field of semiconductor research since they can be used for a variety of technical applications. In addition to being applied in optoelectronic sensors such as photodetectors [61, 63] or electronic semiconductor components like transistors [222, 223] and solar cells [197, 224, 225], OLTP crystals can also serve as X-ray detectors [226, 227] in medical diagnostics. The extensive application potential of the crystals is predicated on their extraordinary optoelectronic properties like high carrier mobilities [173, 206], long carrier lifetimes [83, 173, 206], long carrier diffusion lengths [83, 173], and high photoconductivity [63, 206]. With hardly any grain boundaries or other structural defects, OLTP crystals also meet high structural quality requirements [228] and therefore are superior to polycrystalline OLTP thin films. To allow flexible use of the semiconducting crystals with the chemical formula $ABX_3$ in optoelectronic applications, the absorption behaviour can be modified by varying the halide ions [56] chloride ($X = Cl^-$), bromide ($X = Br^-$) or iodide ($X = I^-$) to obtain the band gaps of the perovskite crystals $MAPbCl_3$ ($E_g = 2.9$ eV) [63], $MAPbBr_3$ ($E_g = 2.2$ eV) [62], and $MAPbI_3$ ($E_g = 1.5$ eV) [62]. A detailed optical analysis of the mentioned crystals has already been conducted in Subchapter 4.4.3. Moreover, the organic cation methylammonium ($A = MA^+/ CH_3NH_3^+$) can be exchanged with the larger formamidinium ion [64] ($A = FA^+/ CH_5N_2^+$) and enables the growth of the crystals $FAPbBr_3$ and $FAPbI_3$ with $E_g$ of 2.1 eV and 1.4 eV, respectively. All these hybrid perovskite crystals are based on the heavy metal ion lead ($B = Pb^{2+}$) [63, 64], which forms a three-dimensional Bravais lattice [229, 230] together with the other mentioned ionic components, which was already described in detail in Subchapter 2.8.
To date, exclusively solution-processed OLTP crystals [22, 64, 227, 231, 232] have been used for the fabrication of device prototypes. A supersaturated perovskite solution is caused either by a temperature change [22, 62, 93, 144, 162], solvent evaporation [137, 162, 233], chemical reaction [61] or a combination of the methods [60, 233]. The aim of the various processes is to achieve a rapid growth of crystals with controlled structure, size, shape, and yield [64, 234]. In addition, the crystalline components must exhibit high physical and chemical qualities [235] in order to be applied as semiconducting components or to improve existing optoelectronic devices [64, 197, 233]. However, these high requirements and numerous criteria cannot always

[4] This chapter is based on the paper *"A temperature-reduced method for the rapid growth of hybrid perovskite single crystals with primary alcohols"* from Julian Höcker, Felix Brust, Melina Armer, and Vladimir Dyakonov, published in the Journal CrystEngComm in 2021, volume 23, pages 2202-2207.

be fully met: For example, the cooling crystallisation [22] enables a controlled growth [186], but is also a very time-consuming process [59]. The antisolvent crystallisation has the benefit that crystalline solids grow at RT [137], but the difficulty in controlling the nucleation rate as well as the long growth cycles [56] are disadvantages of the technique. Whereas the great advantage of the ITC is that crystals are rapidly and simply pulled from solutions [62-64, 83]. However, to make full use of ITC, very hot precursor solutions are required (Subchapter 2.9) [62, 64]. The high temperatures increase the probability that dislocation defects are generated due to thermal stress during the crystal growth [168, 236]. Furthermore, the hot growth conditions limit the crystal pulling to a few hours [26]. Seed crystals can be used for further growth, however, in Chapter 5 it was already proven that the structural quality of these crystals suffers greatly [26].
In order to grow large-sized OLTP single crystals in a controlled and simple manner from solution in the shortest possible time with low energy consumption, a crystallisation process based on primary alcohols was developed. For the understanding of the crystallisation pathway and to compare it with the related ITC method, solubility diagrams were first prepared to serve as a link between unsaturated, saturated, and supersaturated OLTP solutions. [23]

## 6.2 Experimental Section

### 6.2.1 Chemicals

1-propanol (>99 %), 1-butanol (>99 %), 1-pentanol (>99 %), 1-hexanol (>99 %), DMF (99.8 %), DMSO (>99.9 %), and FAI (>99 %) were all acquired from Sigma-Aldrich. GBL (>99 %) and $PbBr_2$ (>98 %, trace metals basis) were purchased from Alfa Aesar. $PbI_2$ (99.99 %, trace metals basis) was bought from TCI. $PbCl_2$ (99.99 %, trace metals basis), $PbBr_2$ (99.99 %, trace metals basis), MACl (>99.5 %, recrystallized 4 times), MABr (>99.5 %, recrystallized 4 times), formamidinium bromide (FABr) (>99.5 %, recrystallized 4 times), and MAI (>99.5 %, recrystallized 4 times) were all purchased from Lumtec. All chemicals and solvents were used as received without further purification. [23]

### 6.2.2 Preparation of Solubility Curves

Saturated OLTP solutions were prepared in a nitrogen-filled glovebox with water and oxygen content lower than one part per million. First, the precursor salts were weighed into a small bottle with an amount of substance of 0.1 mmol in a ratio of 1:1. The corresponding solvents or solvent mixtures were added stepwise to the precursor salts. The mass concentrations from the literature [63, 64] were used as basis for preparing the solubility curves without the admixture of alcohols. In order to indicate the mass concentrations of saturated OLTP solutions as accurately as possible and to avoid diluted solutions, 200 µl less solvent was added to each of the precursor salts than described in the literature [63, 64]. Afterwards, the solutions were stirred for 3 h at the temperatures listed in Figure 48 and Figure 49. To finally obtain a saturated OLTP solution, 10 – 15 µl additional solvent was added per hour.
To prepare the solubility curves of the OLTP solutions with the addition of the primary alcohols, 40 µl of propanol, butanol, pentanol or hexanol were first added to each of the weighed precursor salts. At first, the same amounts of solvents or solvent mixtures as for the saturated solutions without alcohol were added, due to the expected poorer solubility of OLTPs with alcohol. The solutions were stirred for 3 h at the temperatures listed in Figure 48 and Figure 49. Further solvent was finally added in steps of 10 – 15 µl per hour, until the OLTP solutions were completely dissolved.
For the addition of solvents and solvent mixtures to achieve a saturated OLTP solution, an error of ±5 µl is given. [23]

### 6.2.3 OLTP Crystal Growth with RITC

The precursor solutions $MAPbCl_3$, $MAPbBr_3$, $FAPbBr_3$, and $FAPbI_3$ were stirred for 3 h at RT until they were completely dissolved. The $MAPbI_3$ solution was stirred at 60°C for 4 h for complete dissociation of the precursor salts. The OLTP solutions were then filtered *via* a 0.2 µm pore size PTFE syringe filter as described in Chapters 4 and 5. To start RITC, above 100 µl of a primary alcohol was added before heating the solution to the required growth temperature. The crystal growth took place under ambient conditions at a temperature of 22.5±1°C and a humidity of 40±20 %.
To ensure successful crystal growth with the RITC method, the following aspects must also be considered: The amount of alcohol added to the precursor solution must be in the range of 90 to 120 µl to grow crystals at the temperatures indicated in Figure 51. However, if much less alcohol is added to the precursor solution, the crystallisation temperature must be increased because the polarity effect of the alcohol is strongly reduced. If large amounts of alcohol (ca. 250 µl) are added to the precursor solution, the polarity effect of the alcohol is much stronger and crystals are formed in a few minutes, which is comparable to Figure 50. However, it is no longer possible to grow single crystals from these solutions because the nucleation rate is too high. [23]

### 6.2.4 Characterisation of the RITC Crystals

The mass fractions of the elements hydrogen, carbon, and nitrogen were determined by using the elemental analysis. EDX measurements were performed to determine the mass fractions of chlorine, bromine, iodine, and lead on the crystal surfaces. Powder, single crystal XRD patterns, and rocking scans were carried out by XRD measurements. The detailed description of the individual measuring instruments can be found in Chapters 4 and 5. [23]

## 6.3 Results and Discussion

### 6.3.1 Explanation of the Reduced Inverse Solubility

As already described in detail in Subchapter 2.9, the precondition for crystal growth with ITC is the retrograde or inverse solubility [56, 62, 64] of an OLTP in a saturated solution. For this purpose, an organic halide AX and the corresponding lead halide $PbX_2$ are dissolved in a suitable solvent or solvent mixture.

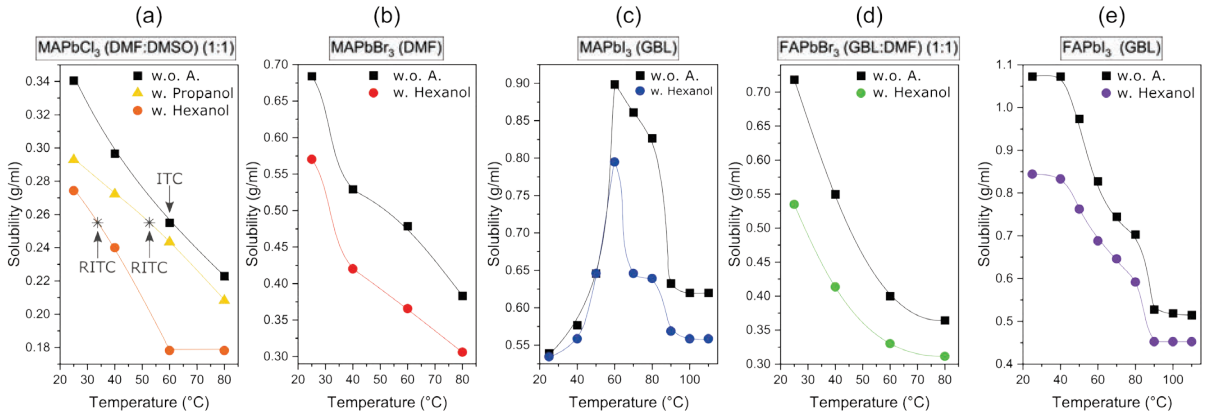


**Figure 48.** (a) $MAPbCl_3$ solubility curves with (w.) propanol, hexanol, and without alcohol (w.o. A.). The solubility curves and the growth temperature of ITC serve as estimates for the growth conditions of the method reactive inverse temperature crystallisation (RITC). Solubility diagrams of (b) $MAPbBr_3$, (c) $MAPbI_3$, (d) $FAPbBr_3$, and (e) $FAPbI_3$ with and without hexanol. Reproduced from Ref. [23] with permission from the Royal Society of Chemistry.

Here, the chlorine-containing precursor salts MACl and $PbCl_2$ preferably dissociate in a mixture of DMF and DMSO (1:1) to react to dissociated $MAPbCl_3$ [63]. A $MAPbBr_3$ ion solution is prepared by dissolving the precursors MABr and $PbBr_2$ in DMF (Subchapter 2.9.3) [62, 64, 83]. However, FABr and $PbBr_2$ show a good solubility in the mixture of DMF and GBL (1:1) [64, 83]. The dissociation of the iodine-containing salts MAI and FAI, each with $PbI_2$, occurs in pure GBL to form dissolved $MAPbI_3$ and $FAPbI_3$ [62, 64, 83]. While $MAPbCl_3$, $MAPbBr_3$, $FAPbBr_3$, and $FAPbI_3$ are highly soluble at RT, the solubility of $MAPbI_3$ reaches its maximum at 60°C [64]. As the saturated solutions are further heated, the solubility of the OLTPs decreases significantly [63, 64]. At sufficiently high temperatures the solutions supersaturate and spontaneous nucleation occurs, followed by crystal growth [26, 56, 62-64]. The underlying phenomenon here, the inverse solubility, is clarified by the black-labelled curves in Figure 48a – e. The quantitative solubility of the OLTPs is given in values of mass concentration. Further details about the preparation of the solubility curves can be found in Subchapter 6.2.2. The curves are comparable to those in the literature [63, 64] as they drop with increasing temperature. [23]

Under the same experimental conditions, the solubility curves for the OLTP solutions containing a small amount of the alcohols 1-propanol, 1-butanol, 1-pentanol or 1-hexanol were prepared. Figure 48a shows the solubility curves of $MAPbCl_3$ with and without the admixture of propanol and hexanol. When comparing the coloured and black-labelled curves, it becomes clear that $MAPbCl_3$ is less soluble in the solvent mixture (DMF/DMSO) with alcohol additives. Furthermore, the solubility of the perovskite decreased much more with hexanol than with propanol. The effect of the strongly reduced retrograde solubility, when hexanol was added to the OLTP precursor solution, is also confirmed by the solubility curves for $MAPbBr_3$, $MAPbI_3$ ($T_{Initial}$ = 60°C), $FAPbBr_3$, and $FAPbI_3$ in Figure 48b – e. OLTP precursor solutions containing butanol and pentanol were found to have similar solubility behaviour to solutions containing hexanol, which is shown in Figure 49a – e. [23]

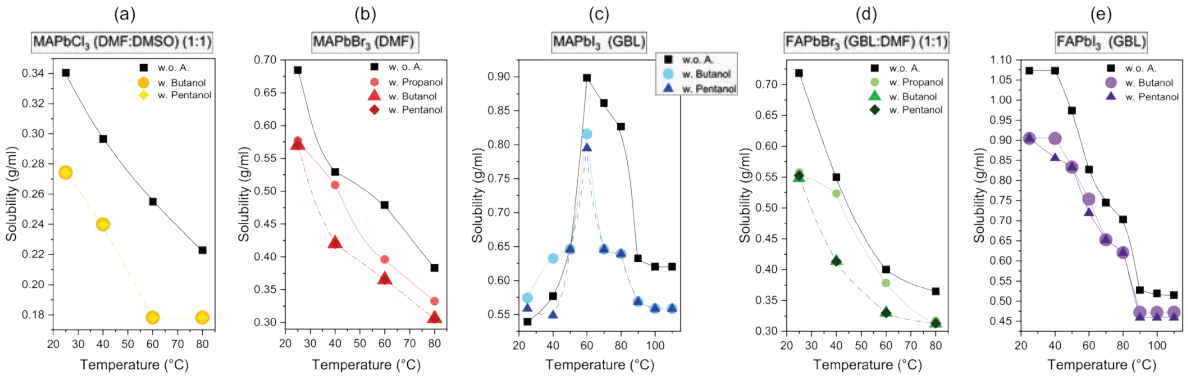


**Figure 49.** (a) – (e) Solubility curves of the OLTP solutions with propanol, butanol, and pentanol. The black-labelled curves represent the retrograde solubility of the OLTP solutions without additives. Reproduced from Ref. [23] with permission from the Royal Society of Chemistry.

From the results, it can be concluded that very small amounts of alcohol have a decisive influence on the solubility behaviour of the OLTPs. With additive, the same saturated solutions at lower temperatures are obtained than without alcohol. In addition, the solubility curves of the solutions with propanol and hexanol also differ from each other at the same saturation. Correspondingly, a possible influence of polarity on the inverse solubility of the perovskites needs to be clarified since the alcohols become less polar with increasing alkyl chain. According to Reichardt, the polarity of aliphatic alcohols can be determined by UV-VIS/NIR spectroscopic measurements with the negatively solvatochromic pyridinium N-phenolate betaine dye (Betaine 30) in solution [237]. Herein, the molar electronic transition energy ($E_T$) in kilocalories

per mole (kcal·mol$^{-1}$) is calculated with the measured wavelength $\lambda_{max}$ of the maximum absorption band of the dissolved dye according to

$$E_T(kcal \cdot mol^{-1}) = \frac{h \cdot c}{\lambda_{max}} \cdot N_A \quad (41)$$

with the Planck's constant, the speed of light (c), and the Avogadro constant ($N_A$) [237]. By including the $E_T$ values of the extremely polar and nonpolar reference solvents $H_2O$ and tetramethylsilane (TMS), respectively, the normalized $E_N^T$ value can be introduced:

$$E_N^T = \frac{E_T(solvent) - E_T(TMS)}{E_T(H_2O) - E_T(TMS)} \quad (42)$$

This dimensionless value indicates the polarity of the solvents and is one for $H_2O$ and zero for TMS [237]. The polarity parameters of the primary alcohols are the following: $E_N^T$(Propanol) = 0.617; $E_N^T$(Butanol) = $E_N^T$(Pentanol) = 0.586; $E_N^T$(Hexanol) = 0.559 [237]. Additionally, a reference must be established to the polarity values of the solvents and solvent mixtures used for dissolving the OLTPs: $E_N^T$(DMSO/DMF) = 0.415; $E_N^T$(DMF) = 0.386; $E_N^T$(DMF/GBL) = 0.403; $E_N^T$(GBL) = 0.420 [237]. It is noticeable that the values of butanol, pentanol, and hexanol are closest to the values of solvents and solvent mixtures compared to propanol. The solubility diagrams and polarity values suggest that additions of small amounts of less polar primary alcohols to the solutions will cause a greater decrease in the inverse solubility of OLTPs than additions of small amounts of polar alcohols. Finally, the polarity values were used to explain the differences and similarities of the solubility curves with reagents. Here, the polarity value of propanol is the highest and draws conclusions about the differing solubility in Figure 48a and Figure 49a – e. Since the polarity values of butanol, pentanol, and hexanol differ only slightly, the corresponding curves of the OLTPs are almost identical. [23]

### 6.3.2 The Reactive Inverse Temperature Crystallisation

The solubility diagrams are further used to estimate the growth temperature with the new crystallisation method, which is exemplified in Figure 48a. With ITC, the crystallisation of $MAPbCl_3$ starts at about 60°C. Moreover, a solubility value of 0.255 g·ml$^{-1}$ at the same temperature was specified. The equally saturated $MAPbCl_3$ solution was obtained with the additives propanol at 52.5°C and with hexanol at 33.5°C, respectively, as marked by the arrows in Figure 48a. However, since the coloured dots indicate the mass concentrations of saturated solutions, the temperature must be increased slightly to exceed the equilibrium of the solution [234]. Thereby, a temperature increase of 2.5°C is sufficient to induce spontaneous nucleation.

As an interim conclusion, reducing the solubility of OLTPs by mixing the solution with very small amounts of alcohols has a significant effect on the growth temperature of the crystals. In addition, the less polar hexanol allows the growth at lower temperatures than the polar propanol. This is an indication of a reactive crystallisation (RC) process [234, 235]. Nevertheless, a small amount of heat is required to generate supersaturation of a crystallising OLTP compound. The combination of the two crystallisation processes RC and ITC is referred to as RITC in the following.

In order to compare the growth temperatures ($T_{Perovskite}$) of RITC with ITC, mm-sized OLTP single crystals were grown in 3 – 5 h from a 3 ml solution. The crystallisation temperatures in dependence of the molar concentrations of the precursor solutions were the following: $T_{MAPbCl3}$ = 60°C ($c_m$ = 1 mol·l$^{-1}$), $T_{MAPbBr3}$ = 80°C ($c_m$ = 1 mol·l$^{-1}$), $T_{MAPbI3}$ = 110°C

($c_m$ =1 mol·l$^{-1}$), $T_{FAPbBr3}$ = 60°C ($c_m$ = 1 mol·l$^{-1}$), and $T_{FAPbI3}$ = 115°C ($c_m$ = 0.8 mol·l$^{-1}$) which are comparable to those in the literature [62-64, 180].

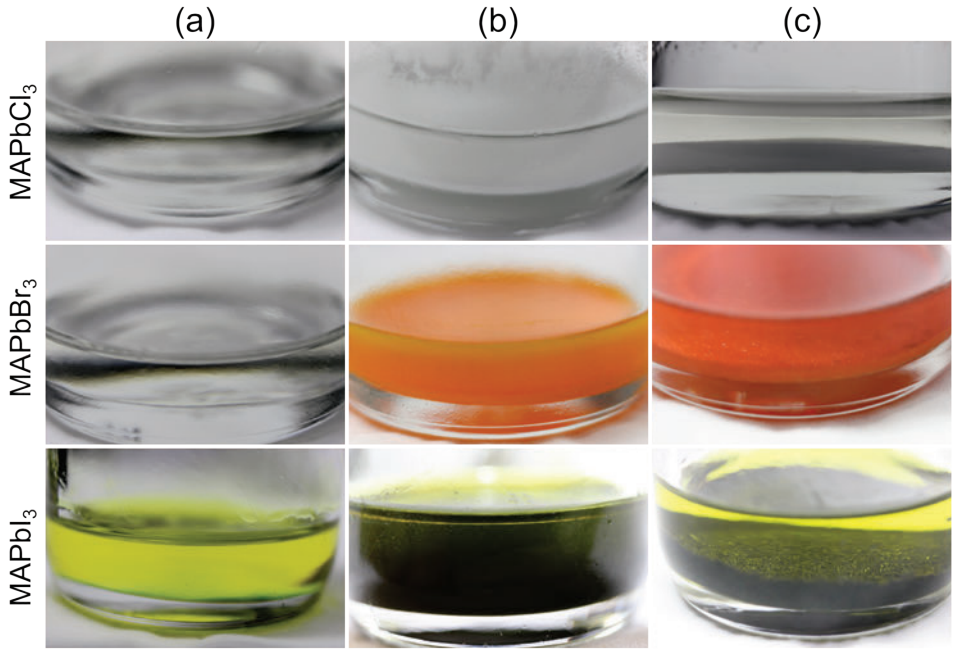


**Figure 50.** (a) Preliminary precipitation tests with saturated $MAPbCl_3$, $MAPbBr_3$, and $MAPbI_3$ solutions based on the insights from the solubility curves to grow OLTP crystals with RITC. The expected growth temperatures for $MAPbCl_3$, $MAPbBr_3$, and $MAPbI_3$ were set at 45°C, 50°C, and 95°C, respectively. (b) Perovskite precursor solutions after adding an excess of butanol (250 µl). (c) Supersaturated perovskite solutions with polycrystalline carpets on the vessel bottom. Reproduced from Ref. [23] with permission from the Royal Society of Chemistry.

However, to grow mm-sized OLTP single crystals with RITC, preliminary precipitation tests were necessary to choose the right blend of perovskite precursor solution and alcohol. These prior precipitation experiments are shown in Figure 50 and were carried out for saturated $MAPbCl_3$, $MAPbBr_3$, and $MAPbI_3$ solutions. For this, the $MAPbCl_3$, $MAPbBr_3$, and $MAPbI_3$ precursor solutions were heated up to temperatures of 45°C, 50°C, and 95°C, respectively (Figure 50a). The perovskite particles precipitated directly in solution by adding a 250 µl excess of butanol (Figure 50b). The transparent $MAPbCl_3$ and $MAPbBr_3$ solutions and the clear yellow solution of $MAPbI_3$ suddenly became white, red, and black. As a result, the admixture of the alcohol directly disturbed the chemical equilibrium of the perovskites. In the supersaturated solutions, the finely dispersed perovskite sediments were deposited on the vessel bottoms and grew into polycrystalline carpets within 15 min (Figure 50c).

Finally, to grow high-quality crystals with RITC, about 100 µl of one of the primary alcohols was added to each precursor solution at RT. The profit of blending small quantities of alcohols with the perovskite solutions before heating ensures a controlled growth [235] and lowers the nucleation rate [234], making it possible to grow large-sized crystals in the given time interval. Further details can be found in Subchapter 6.2.3.

Figure 51 shows the successfully grown RITC single crystals with the reagent hexanol. In contrast to ITC, the admixture of the additives enables crystal pulling at lower temperatures as presented in Figure 51a – e. The coloured dots represent the coldest growth temperatures that were possible with the addition of the respective alcohols. The predictions of the growth temperatures from the solubility curves with the reagents propanol and hexanol find a good agreement. However, for pulling mm-sized crystals from solutions with pentanol and butanol, the temperatures had to be increased by 5°C and 10°C, respectively. While crystals started to grow in the vessel from butanol and pentanol containing solutions at the same operating

conditions as for hexanol containing solutions, they did not reach the desired size within the given time span. Even though the solubility curves of the OLTP-alcohol mixtures provide a good estimate for the crystallisation temperatures, it can only be fully clarified *via* crystal growth experiments, how fast a crystal grows. To sum up, in a given time interval, the crystal growth velocity increases with increasing alkyl chain of the here presented alcohols, although the polarity values of butanol, pentanol, and hexanol differ only slightly from each other.

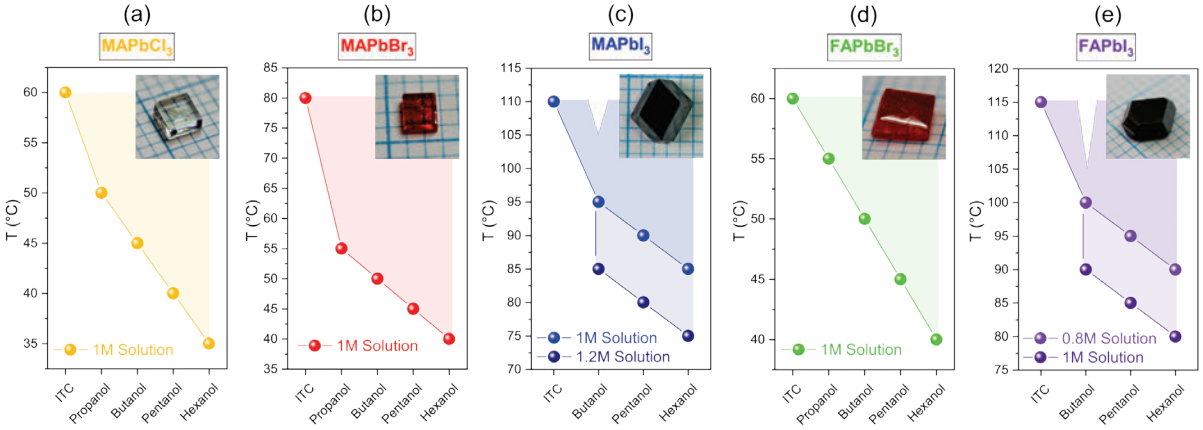


**Figure 51.** (a) – (e) OLTP crystallisation temperatures in dependence of the applied alcohols and the molar concentration of the solutions to grow crystals in 3 – 5 h. The coloured dots indicate the lowest and the edges of the coloured areas the highest growth temperatures. Note the incisions in the blue and purple areas of $MAPbI_3$ and $FAPbI_3$ to prevent evaporation of butanol during crystal growth. The presented OLTP crystals were grown from a hexanol based precursor solution at the lowest specified growth temperatures. Reproduced from Ref. [23] with permission from the Royal Society of Chemistry.

With RITC, the growth temperatures were reduced by up to 40°C using the reagent hexanol for the above mentioned molar concentrations: $T_{MAPbCl3} = 35°C$, $T_{MAPbBr3} = 40°C$, $T_{MAPbI3} = 85°C$, $T_{FAPbBr3} = 40°C$, and $T_{FAPbI3} = 90°C$. While the $MAPbCl_3$, $MAPbBr_3$, and $FAPbBr_3$ precursor solutions are already saturated, the molar concentration can be further increased for the iodine-containing solutions. Here, $MAPbI_3$ ($c_m = 1.2\ mol \cdot l^{-1}$) and $FAPbI_3$ ($c_m = 1\ mol \cdot l^{-1}$) crystals

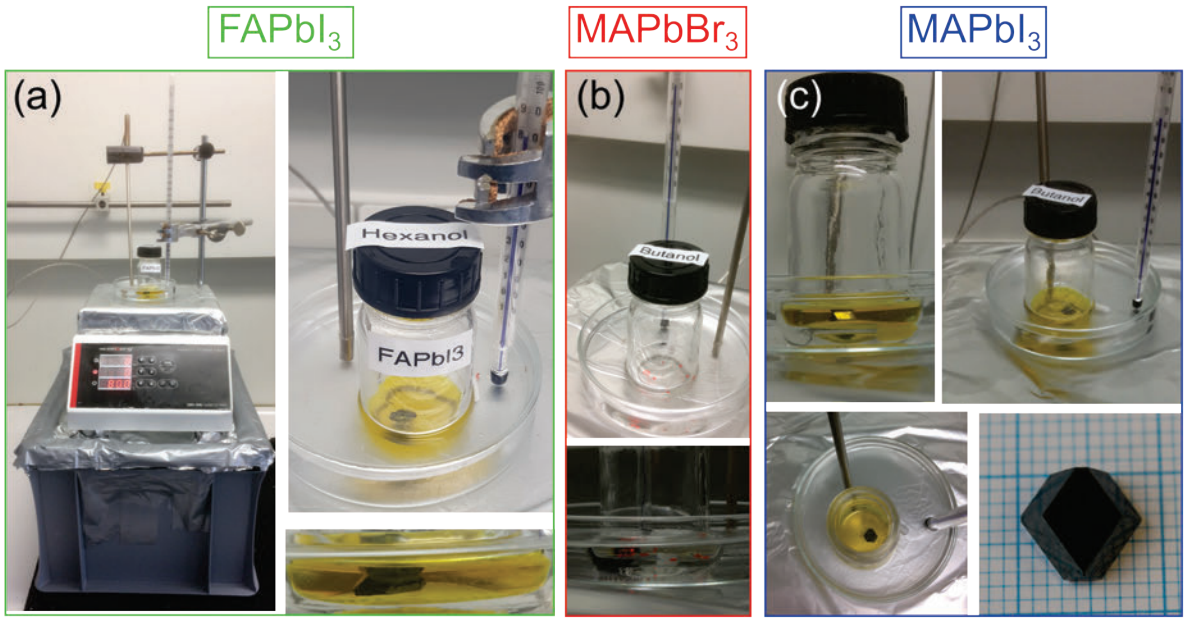


**Figure 52.** (a) Setup to grow OLTP crystals with RITC. Evidence for growing a $FAPbI_3$ crystal at 80°C with the reagent hexanol. $FAPbI_3$ crystal in a hexanol containing solution (3 ml) at 80°C, with a size of above 0.81 $cm^2$, obtained after 7 h. (b) $MAPbBr_3$ crystals in a butanol containing solution (3 ml) at 50°C. (c) $MAPbI_3$ crystals in butanol containing solutions (4 ml) at 95°C. The $MAPbI_3$ crystal reached a maximum size of above 0.69 $cm^2$ after a growth period of 8 h. Reproduced from Ref. [23] with permission from the Royal Society of Chemistry.

started to grow at even 75°C and 80°C (Figure 51c and e), respectively, which represents a temperature difference of 35°C to ITC. Due to the colder growth conditions, the precursor solutions were also used for growth periods longer than 5 h (Subchapter 2.9.3) to grow large-sized OLTP crystals (Figure 52a – c).
Another benefit of RITC is that OLTP crystal growth is no longer limited to one temperature value. The coloured areas in Figure 51a – e illustrate the crystal growth range from the lowest temperatures of RITC up to the temperatures of ITC. For $MAPbBr_3$, the largest growth range was obtained from 40 to 80°C (Figure 51b). However, only pentanol and hexanol are suitable for the growth of $MAPbI_3$ and $FAPbI_3$ crystals above 105°C due to their higher boiling points of 138°C [158, 238] and 157 °C [158, 238] compared to propanol (Bp = 97°C) [158, 238] and butanol (Bp = 118°C) [158, 238]. This is indicated by the incisions in the blue and violet areas of $MAPbI_3$ and $FAPbI_3$ in Figure 51c and e for the reagent butanol. [23]

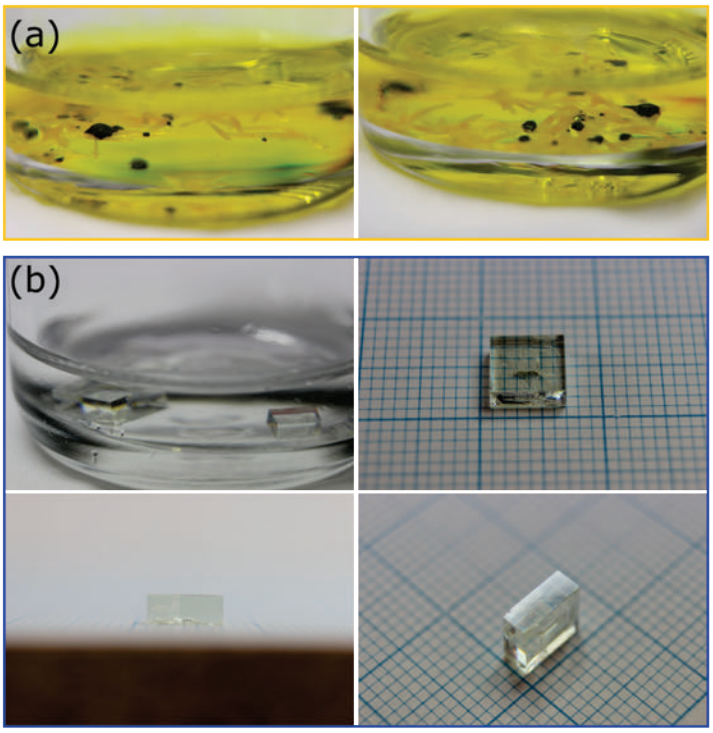


**Figure 53.** (a) Black $FAPbI_3$ perovskite crystals and yellow $PbI_2$ needles, appearing both in a 1.2 M $FAPbI_3$-hexanol blend at 70°C. (b) $MAPbCl_3$ crystal which was grown with the RC method at RT. Reproduced from Ref. [23] with permission from the Royal Society of Chemistry.

As previously shown, in addition to the use of primary alcohols, an increase in the molar concentration also resulted in a further reduction of the growth temperature [197]. This was also the case for a high concentrated $FAPbI_3$ ($c_m$ = 1.2 mol·l$^{-1}$) hexanol mixture where crystals are already grown at 70°C. However, in addition to small $FAPbI_3$ crystals, the yellow side phase $PbI_2$ was also grown in the form of small crystal needles, as shown in Figure 53a. A further increase in the molar concentration of a $FAPbI_3$ precursor solution to grow large-sized single crystals is therefore unsuitable as growth condition.
Besides the growth of OLTP crystals by RITC, it is also possible to grow $MAPbCl_3$ crystal at RT *via* a simple RC process induced by the addition of alcohol, which is shown in Figure 53b. Here, $MAPbCl_3$ crystals were successfully pulled at RT by adding 100 µl of propanol to the precursor solution. However, since an elevated growth temperature has a significant effect on the growth velocity of the crystals, the crystal growth in the RC process required more than one

month. The crystals reached a maximum size of 0.36 $cm^2$ and exhibited a clear cubic shape. [23]

### 6.3.3 Structural Characterisation of the RITC Crystals

After the successful crystal growth with RITC, the mass fractions of $CH_3NH_3$ and $CH_5N_2$ were experimentally determined by elemental analysis for each OLTP crystals, which are listed in Table 9. To fully work out the stoichiometry of the crystals, EDX was applied for the elements Cl, Br, I, and Pb by measuring the crystal surfaces. Further details about the EDX spectra can be found in the appendix (Figure C1). The experimental data of EDX together with the crystal powder results of the elemental analysis are in good agreement with the theoretical predictions, which are written in cursive letters. [23]

**Table 9.** Mass fractions of the elements carbon, hydrogen, nitrogen, chlorine, bromine, iodine, and lead determined by EDX and elemental analysis to verify the stoichiometry of the perovskite crystals. The theoretical predictions are written in cursive letters. Reproduced from Ref. [23] with permission from the Royal Society of Chemistry.

| M [%] | $CH_3NH_3PbCl_3$ | | $CH_3NH_3PbBr_3$ | | $CH_3NH_3PbI_3$ | | $CH_5N_2PbBr_3$ | | $CH_5N_2PbI_3$ | |
|---|---|---|---|---|---|---|---|---|---|---|
| **C** | *3.48* | 3.62 | *2.51* | 2.51 | *1.94* | 1.94 | *2.44* | 2.53 | *1.90* | 2.04 |
| **H** | *1.75* | 1.77 | *1.26* | 1.22 | *0.98* | 0.98 | *1.02* | 1.03 | *0.80* | 0.84 |
| **N** | *4.05* | 4.32 | *2.92* | 2.79 | *2.26* | 2.26 | *5.69* | 5.54 | *4.43* | 4.31 |
| **Pb** | *59.95* | 58.09 | *43.26* | 41.12 | *33.42* | 29.67 | *42.12* | 40.03 | *32.73* | 31.85 |
| **Cl, Br or I** | *30.77* | 35.70 | *50.05* | 55.48 | *61.41* | 61.89 | *48.72* | 52.78 | *60.15* | 61.79 |

In addition to quantitative measurements, the structure of the OLTP crystals was investigated. The crystals were crushed to a fine powder to record XRD patterns.

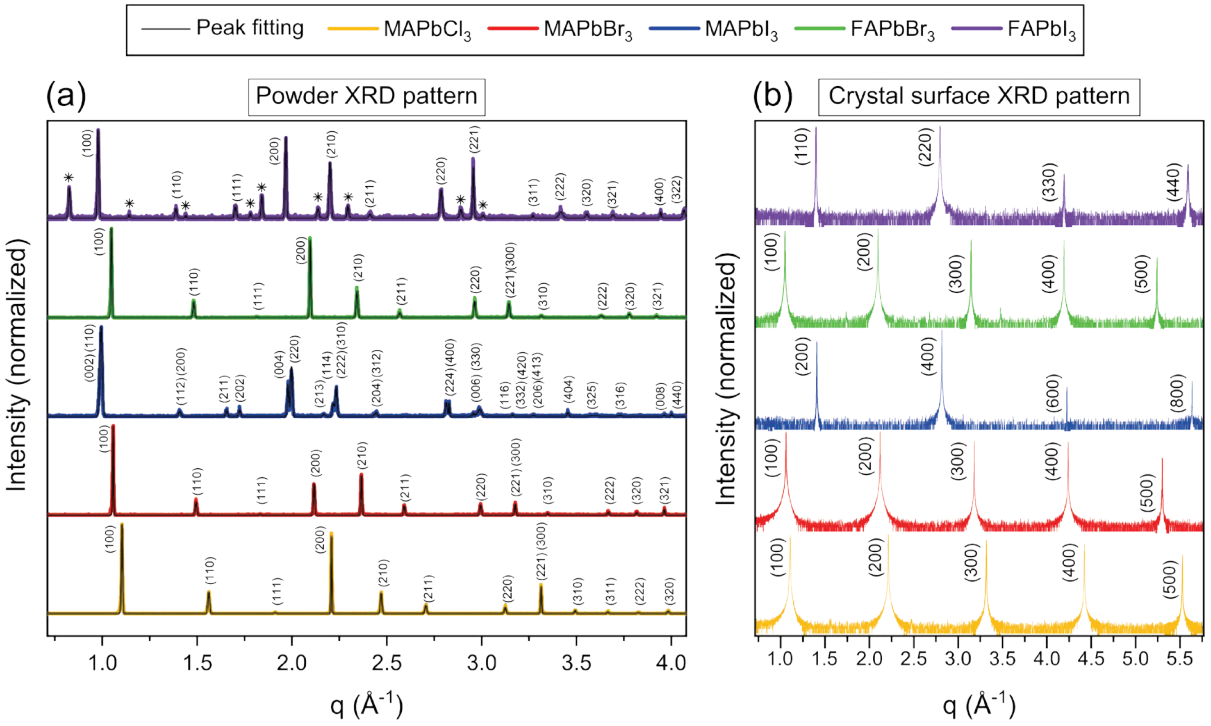


**Figure 54.** (a) XRD patterns of the OLTP crystal powders in dependence of the scattering vector. The fits (black-labelled) were used to determine the lattice constants of each OLTP crystal. Note *-labelled peaks are assigned to the δ-phase of $FAPbI_3$. (b) Out-of-plane XRD crystal surface measurements, proving the high quality of the RITC single crystals. Reproduced from Ref. [23] with permission from the Royal Society of Chemistry.

Figure 54a demonstrates the XRD patterns of the crystal powders in dependence of the scattering vector. The peaks were analysed by fits to assign their corresponding Miller indices in order to determine the lattice constants: $a_{MAPbCl3} = 5.689 \pm 0.003$ Å, $a_{MAPbBr3} = 5.937 \pm 0.004$ Å, $a_{MAPbI3} = 8.93 \pm 0.03$ Å and $c_{MAPbI3} = 12.5 \pm 0.2$ Å, $a_{FAPbBr3} = 5.996 \pm 0.002$ Å, as well as $a_{\alpha\text{-}FAPbI3} = 6.307 \pm 0.008$ Å. Thus, the crystals $MAPbCl_3$, $MAPbBr_3$, $FAPbBr_3$, and α-$FAPbI_3$ show a simple cubic system [62, 63, 83], whereas the $MAPbI_3$ crystal consists of a body-centred tetragonal Bravais lattice [62]. Next to the α-phase,

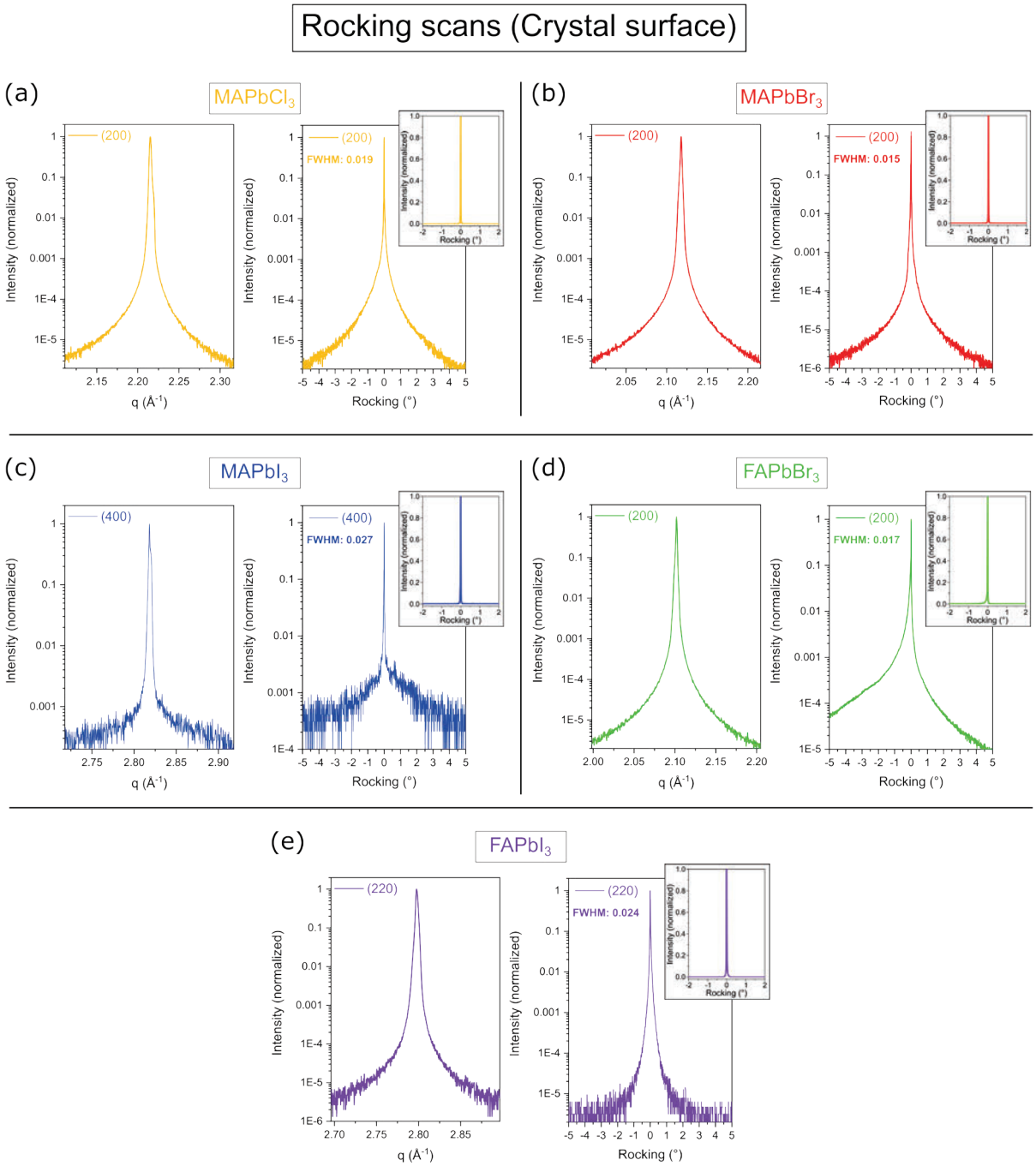


**Figure 55.** (a) – (e) X-ray reflexes with the corresponding rocking curves, obtained for each OLTP single crystals. The measurements were performed on the surfaces of the crystals. The rocking curves are plotted in a logarithmic and a linear plot (inset). The sharp rocking curves verified a high quality for each crystalline perovskite lattice. Reproduced from Ref. [23] with permission from the Royal Society of Chemistry.

the XRD pattern of the $FAPbI_3$ powder also contains the δ-phase (*-assigned). Since the $FA^+$-cations can rapidly decompose under ambient conditions, the thin polycrystalline $FAPbI_3$ layer is already unstable during the measurement, which is consistent with the results presented in Chapter 5 [26, 32, 239].
To confirm single crystal growth with RITC, X-ray Bragg scattering in reflection geometry was measured, as shown in Figure 54b. The $MAPbCl_3$, $MAPbBr_3$, and $FAPbBr_3$ crystals show a {100} peak series for their dominant surfaces up to the fifth order. Instead, the $MAPbI_3$ crystal reveals a {200} peak series and the $FAPbI_3$ crystal demonstrates a {110} peak series up to the fourth order. Besides the very sharp peaks, the XRD patterns do not show any additional Bragg reflexes, which suggests a single crystalline surface for each OLTP solid. The presented radiographic investigations in Figure 55a – e were used to determine the real structure [102] of the RITC crystals. First, the reflexes of the different OLTP crystal surfaces were determined to record rocking curves in the following, which can reveal possible disturbances in the lattice structure [102]. The rocking curves (diffraction curves) show in each case a sharp peak. The full width at half maxima are in the range of 0.015 to 0.027°. The narrow rocking peaks and the fact that no further peaks are present in the linear as well as in the logarithmic plots suggest a very high crystal quality. [23]

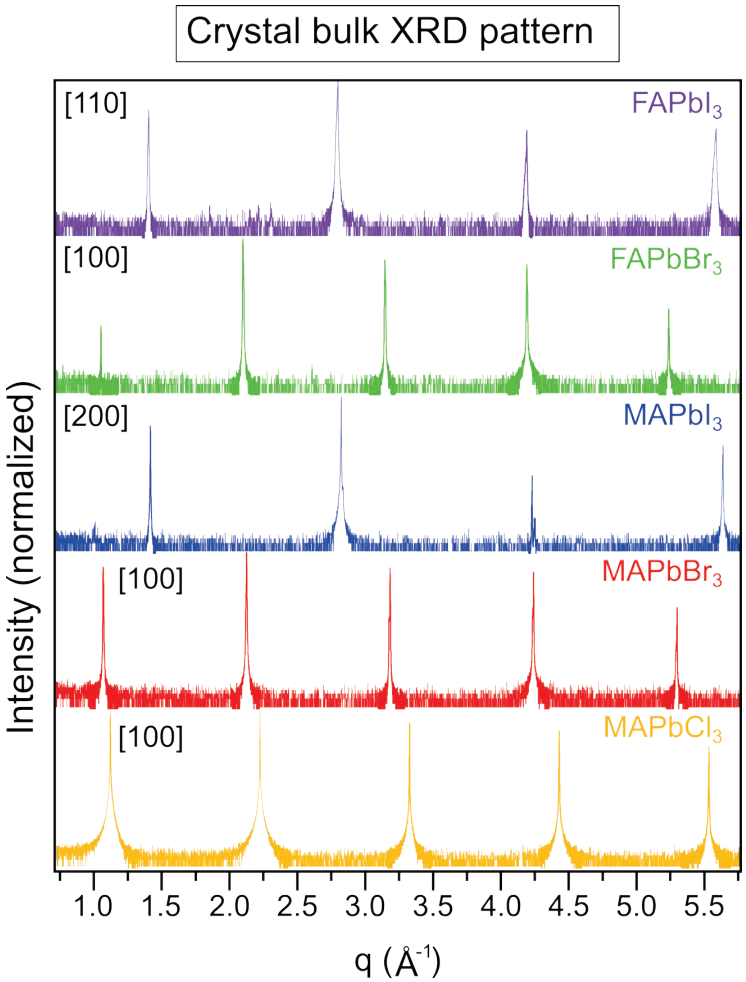


**Figure 56.** Out-of-plane XRD bulk measurements to confirm OLTP single crystal growth with RITC. To perform the bulk measurements, the crystals were halved with a scalpel along their crystallographic directions: [100] direction for $MAPbCl_3$, $MAPbBr_3$, and $FAPbBr_3$; [200] direction for $MAPbI_3$ and [110] direction for $FAPbI_3$. Reproduced from Ref. [23] with permission from the Royal Society of Chemistry.

To prove the high quality of the crystals in their entirety, they were halved with a scalpel along their corresponding directions to record out-of-plane XRD measurements of the crystal bulk (Figure 56). The XRD data obtained from the bulk show only one dominant peak series for the respective crystals and again confirm the high quality of the single crystals. [23]

## 6.4 Conclusions

To summarise, the simple and reproducible temperature-reduced crystal growth method RITC was presented in this chapter. The mixtures of primary alcohols and OLTP solutions offer the opportunity to grow the crystals $MAPbCl_3$, $MAPbBr_3$, $MAPbI_3$, $FAPbBr_3$, and $FAPbI_3$ at low temperatures within 3 to 5 h. With the long-chained less polar hexanol, the inverse solubility of the OLTPs was decreased most, lowering the crystallisation temperatures by up to 40°C compared to ITC. Furthermore, the single crystal growth was confirmed by surface and bulk XRD measurements in reflection geometry and by means of rocking curves. The knowledge gained in this work constitutes an important contribution to the further understanding of retrograde solubility of OLTPs and paves the way to high-quality and rapid perovskite single crystal growth at low temperatures with minimised energy consumption. [23]

# 7 Towards Photovoltaic Applications Based on Perovskite Crystals

In this chapter, photoelectronic devices based on high-quality $MAPbI_3$ crystals are presented. This includes the fabrication of a photodetector as well as a solar cell prototype. To introduce the topic of perovskite photovoltaics in general, photovoltaic cells based on polycrystalline $MAPbI_3$ thin films are presented first because they have significantly contributed to the success of high-efficient perovskite solar modules [119, 131, 240-252] and still arouse intense research interest today [18, 135, 253-261]. Here, in addition to the processing of photovoltaic cells, their architecture is described. Furthermore, current density – voltage characteristics were used to determine their physical properties. The knowledge gained from this preliminary study was essential to manufacture photodetector as well as solar cell prototypes based on crystal wafers and crystal "films" in the following.

## 7.1 $MAPbI_3$ Thin-film Solar Cells[5,6]

During the last decade perovskite solar cells based on thin polycrystalline films have attracted a lot of attention and experienced a rapid development in the PCE from 3.8 % [240] in 2009 to above 25.5 % [262] in 2021. The remarkable development in this relatively short time span was enabled by different beneficial material properties such as ambipolar transport with high charge carrier mobilities [188], high absorption coefficients [256], as well as respectable radiative efficiencies [257], which all paved the way to very efficient thin-film photovoltaic devices. Recent studies demonstrate that the p-i-n structure can compete with the frequently used n-i-p structure in terms of PCE. Different groups already demonstrated that (mesoporous) titanium dioxide, which requires an additional high temperature annealing step during processing, is not necessary to achieve high efficiencies [47, 195, 196, 199, 251, 263], due to the introduction of new hole transport layers for p-i-n devices which reduce energy losses at the perovskite/HTL interface and increase the charge collection efficiency of holes. The match between the highest occupied molecular orbital (HOMO) energy level of the HTL and the valence band (VB) of the $MAPbI_3$ perovskite is pivotal in this regard to guarantee an effective hole transport to the anode. Furthermore, the HTL should exhibit a high hole conductivity and a high optical transmittance in the photoactive wavelength range of the perovskite absorber material [246]. So far, poly(3,4-ethylenedioxythiophene) polystyrene sulfonate (PEDOT:PSS) has been widely used as HTL for the fabrication of p-i-n perovskite solar cells due to its tuneable conductivity, low-temperature solution processability, and its high optical transmittance in the visible light wavelength range [264-266]. However, PEDOT:PSS is not an ideal HTL. The semi-metallic nature [267] of the hybrid polymer system leads to an insufficient electron blocking ability, promoting leakage and surface recombination losses at the perovskite/ anode interface [135, 268]. In order to minimise these parasitic processes and thus increase the open-circuit voltage

[5] This subchapter is based on the paper *"Efficient solution processed $CH_3NH_3PbI_3$ perovskite solar cells with polyTPD hole transport layer"* from Julian Höcker, David Kiermasch, Philipp Rieder, Kristofer Tvingstedt, Andreas Baumann, and Vladimir Dyakonov, published in the Journal Zeitschrift für Naturforschung A in 2019, volume 74, pages 665-672.

[6] This subchapter is also based on the E-Poster *"The polymer polyTPD as hole transport layer for efficient solution processed $MAPbI_3$ perovskite solar cells"* from Julian Höcker, David Kiermasch, Philipp Rieder, Kristofer Tvingstedt, Andreas Baumann, and Vladimir Dyakonov, presented at the OrgMatPerPV conference in 2021.

of the solar cells, different research groups have tried to modify its work function [245] or to use additional electron-blocking interface layers [269]. Conductive polymers such as poly[bis(4-phenyl)(2,4,6-trimethylphenyl)amine] (PTAA) [195, 199, 248, 251, 263] and poly[*N*,*N*'-bis(4-butilphenyl)-*N*,*N*'-bis(phenyl)-benzidine] (polyTPD) [244, 259, 270] are promising alternatives to replace PEDOT:PSS as HTL. In this work, polyTPD was used as HTL to fabricate perovskite solar cells *via* a solution-processing route. This material embodies a particularly suited HTL due to its beneficial energy levels, whereby its HOMO level of -5.4 eV perfectly matches the VB level of $MAPbI_3$ perovskite with -5.4 eV [259]. The energy level matching therefore provides an essentially ohmic hole transport to the indium doped tin oxide (ITO) anode. Moreover, the poly(triaryl)amine acts very well as an electron blocking layer because of its extremely high-lying lowest unoccupied molecular orbital (LUMO) of -2.4 eV. As a consequence, interfacial electron-hole recombination processes are heavily suppressed [135, 271, 272]. However, the hydrophobic character of polyTPD has posed a substantial challenge in order to fabricate solution-processed perovskite solar cells. The chemical characteristics of the hydrophobic butylene group of polyTPD and the hydrophilic perovskite precursor solution induce a serious dewetting problem during solution processing. To overcome the wettability-issue, different groups have tried to improve the surface coverage of the perovskite by using ultraviolet-ozone treatment [273] or poly[(9,9-bis(3-(*N,N*-dimethylamino)propyl)-2,7-fluorene)-*alt*-2,7-(9,9-dioctylfluorene)] (PFN) as an amphiphilic interfacial compatibilizer [244]. In this study, the dewetting problem was solved by varying the concentration of the polyTPD precursor solution and by applying an optimized two-step $MAPbI_3$ deposition technique to increase both, the surface coverage of the perovskite layer as well as the PCE of the corresponding solar cell device. [131]

### 7.1.1 Tools for the Fabrication and Characterisation of the Solar Cells

**Device fabrication:** The spin-coating process was implemented in a nitrogen-filled glovebox with oxygen and water levels below one part per million. Pre-patterned ITO was cleaned in detergent and subsequently sonicated in deionized water, acetone, and isopropanol for 10 min each. After this, the substrates were exposed to an $O_2$-plasma for 30 s. PolyTPD (1-Material, $M_W$ = 45800, $M_n$ = 18320, PDI = 2.5) was dissolved in the solvent 1,2-dichlorobenzene (DCB) (Sigma-Aldrich, anhydrous) overnight at 70°C under constant stirring. The polyTPD-precursor solution was spin-coated onto the cleaned substrates at 5000 rpm for 30 s. The samples were annealed at 110°C for 10 min. The $MAPbI_3$ films were fabricated based on the interdiffusion method. Thereby, $PbI_2$ (TCI, 99.999 %, trace metals basis) and MAI (Lumtec, 99 %) were consecutively spun onto the substrate, followed by a solvent annealing process to recrystallize the small-size crystals into large perovskite grains with reduced pinhole formation [274]. The concentration of $PbI_2$ was fixed at 600 $mg \cdot ml^{-1}$ with a molar fraction of 0.2 mol MAI. The precursor layers were spin-coated with 125°C pre-heated $PbI_2$/MAI solution in DMF (Sigma-Aldrich, anhydrous) at a spin speed of 5000 rpm to obtain a better wettability [24]. Thereafter, the $PbI_2$/MAI films were thermally annealed at 70°C for 10 min. The concentration of MAI was fixed at 40 $mg \cdot ml^{-1}$, dissolved in isopropanol (Sigma-Aldrich, anhydrous). The deposition of the MAI film was taken at 3400 rpm. To ensure a controlled crystallisation, the stacked perovskite films were annealed at 100°C for 60 min in boxes, which contained a solvent atmosphere of DMSO and chloroform (1:5) (both solvents, Sigma-Aldrich, anhydrous). Next, $PC_{61}BM$ (Solennebv, 99 %) was dissolved in DCB with a mass concentration of 20 $mg \cdot ml^{-1}$ and spin-coated on top of the $MAPbI_3$ layer with a spin speed of 6000 rpm. The films were annealed at 100°C for 60 min. After this, $C_{60}$ (Solennebv, 99.5 %) was thermally evaporated onto the substrate with a final thickness of 20 nm. The solar cell devices were completed by the evaporation of 8 nm BCP (Sigma-Aldrich, 99.5 %) and a 60 nm thick gold electrode. The thermal evaporation process was realised under high vacuum with a pressure of $10^{-7}$ mbar.

**Solar cell characterisation:** HTL/$MAPbI_3$ films were imaged with the SEM setup described in Subchapter 5.2.3. The measurements were performed in high vacuum. The J-V characteristics of the devices were measured in a nitrogen-filled glovebox under conditions of AM 1.5 G global spectral irradiance of 100 $mW \cdot cm^{-2}$ with a xenon lamp-based solar simulator (ORIEL 68811). Keithley MODEL 2612 B was applied for recording the J-V measurements. The exact illumination intensity was calibrated with a reference silicon solar cell (VLSI Standards Incorporated). The solar cells were directly measured (forward and backward scan) without any pre-treatments after the evaporation process. The values of $V_{OC}$, $J_{SC}$, and FF were obtained by the backward-scan of the J-V measurements. [131]

### 7.1.2 Characterisation of the Fabricated $MAPbI_3$ Thin Films

To overcome the wettability issue, which is illustrated in Figure 57, a 600 $mg \cdot ml^{-1}$ $PbI_2$/

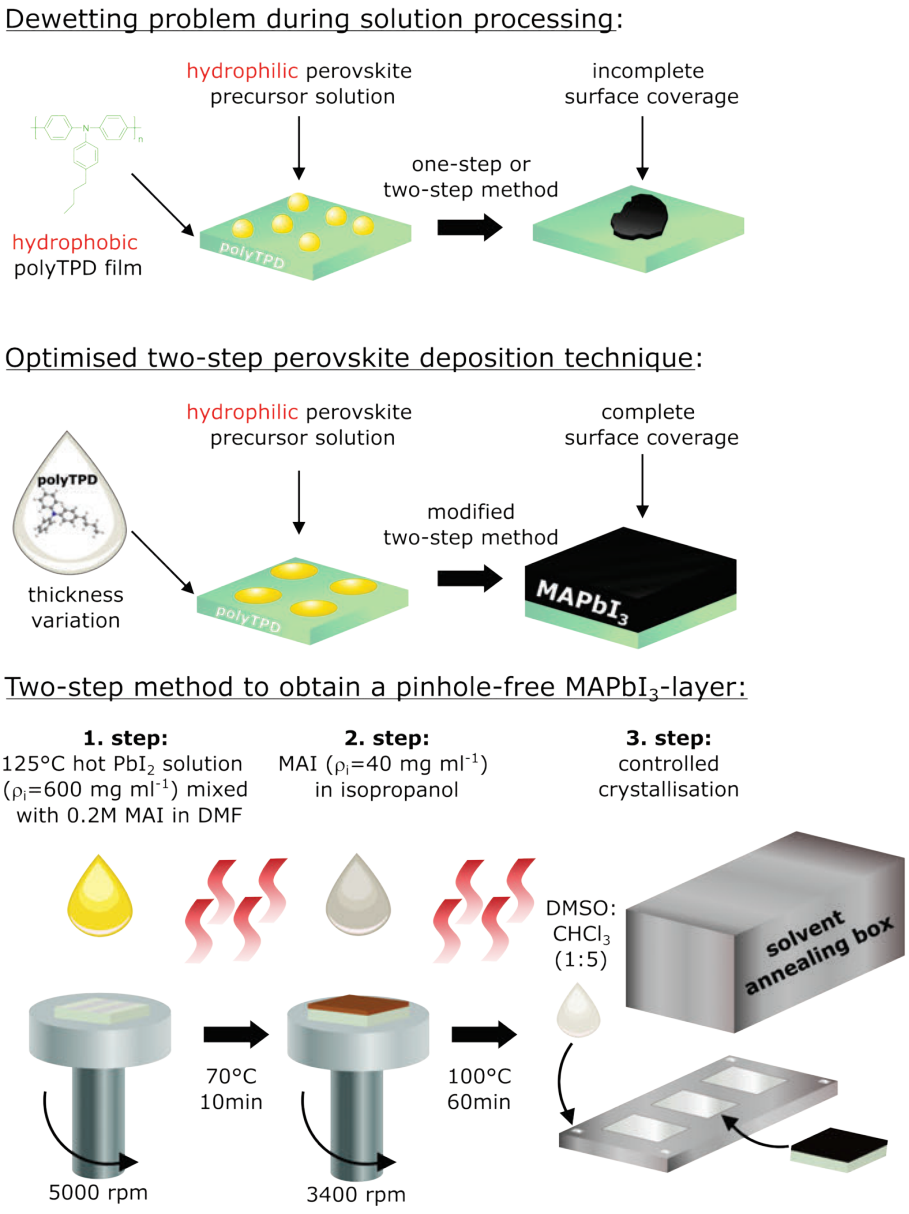


**Figure 57.** Schematic illustration of the fabrication of a pinhole-free $MAPbI_3$ film based on the modified two-step thermal annealing-assisted interdiffusion method. Reproduced from Ref. [131] with permission from Zeitschrift für Naturforschung A (De Gruyter).

MAI precursor solution with a molar ratio of 1/0.2 was applied and further heated to 125°C, to obtain a complete surface coverage of the solution-processed $MAPbI_3$ layer [195]. Furthermore, it should be noted, that also an optimization of the polyTPD film thickness, *via* a variation of the mass concentration ($\rho_i$) from 3, 5, 6, 7, 8 to 10 mg·ml$^{-1}$ is essential to produce pinhole-free $MAPbI_3$ films. In fact, differences in the $MAPbI_3$ film formation were observed by varying the polyTPD concentration: The wettability of the perovskite precursor solution on polyTPD increases with diminishing concentration, which leads to a complete surface coverage of the $MAPbI_3$ perovskite without the formation of pinholes at low polyTPD-concentrations of $\rho_i$ = 3, 5, and 6 mg·ml$^{-1}$. [131]

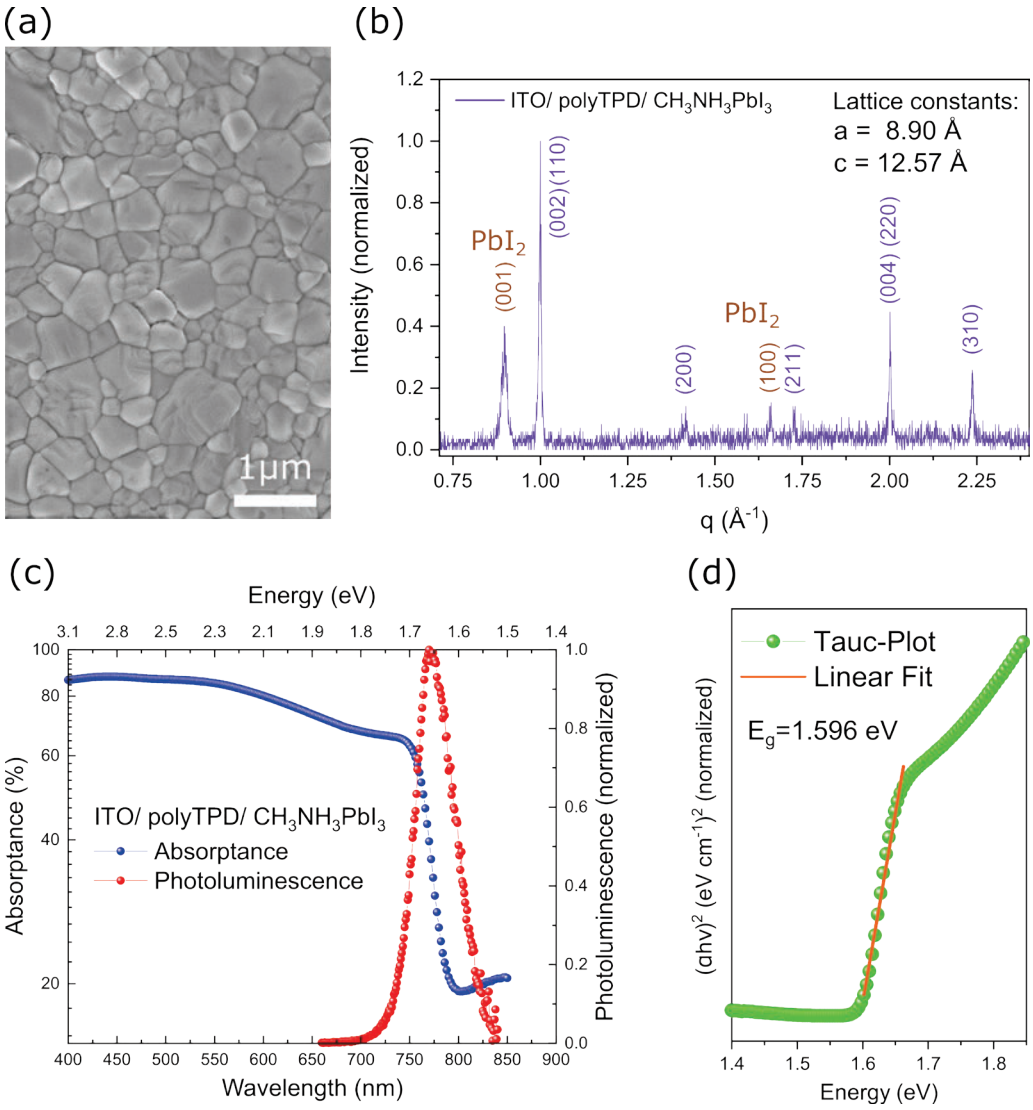


**Figure 58.** (a) Scanning electron microscope (SEM) image of a $MAPbI_3$ film fabricated on polyTPD. (b) XRD pattern of a $MAPbI_3$ perovskite film grown on polyTPD. (c) Absorption spectrum and normalized steady-state PL spectrum of the polyTPD/$MAPbI_3$ layers spin-coated onto ITO. (d) Tauc plot to evaluate the band gap of the processed $MAPbI_3$ film. Reproduced from Ref. [131] with permission from Zeitschrift für Naturforschung A (De Gruyter).

The resulting $MAPbI_3$ films exhibited a high film quality, as confirmed by the SEM image in Figure 58a. In addition, the thin films were characterised by XRD (Figure 58b) and revealed a typical polycrystalline behaviour. By further evaluating the Bragg reflexes of the obtained pattern, the lattice constants a = 8.9 Å and c = 12.57 Å were specified. This is consistent with the typical tetragonal crystal structure of $MAPbI_3$ [82, 242, 260]. The recorded XRD pattern is further comparable to the X-ray measurement of a $MAPbI_3$ crystal powder, shown in

Chapter 4. In addition to the Bragg reflexes of $MAPbI_3$, the XRD pattern also shows those of $PbI_2$ [242]. However, this is not an indication that the film is degraded. The reason for this is the film processing itself. Since a high concentration of $PbI_2$ is required to fabricate pinhole-free perovskite films on polyTPD compared to MAI, the precursors do not fully react to the perovskite. Figure 58c shows the absorption spectrum as well as the steady-state PL spectrum of a $MAPbI_3$ film grown on polyTPD. The characteristic of the perovskite structure is given by the sharp absorption edge at around 780 nm, which is equivalent to the band gap of 1.596 eV, evaluated by the Tauc plot in Figure 58d. PolyTPD itself shows no impact on the absorption behaviour of the perovskite due to its transparency and colourlessness. The maximum peak of the PL spectrum was detected at a wavelength of 776 nm and is a further indicator for the successful growth of polycrystalline $MAPbI_3$ thin films on hydrophobic polyTPD layers. [131]

### 7.1.3 Characterisation of the Manufactured Solar Cells

In a next step, solar cells in the p-i-n layout were fabricated to validate the presented approach. The solar cell configuration is based on the p-i-n device architecture using polyTPD as HTL and $MAPbI_3$ as active layer. The electron transport layer [6,6]-phenyl-C61-butyric acid methyl ester ($PC_{61}BM$) [275, 276] is deposited on top of the perovskite (Figure 59a – c) followed by vacuum deposited $C_{60}$ layer [275, 276]. Finally, 2,9-dimethyl-4,7-diphenyl-1,10-phenatroline (BCP) [277] is directly vacuum deposited on the $C_{60}$ layer. The metal electrode gold on top of the organic multi-layer system completes the structure of the solar cell device. Figure 59b illustrates the cross-section SEM image of the $MAPbI_3$ perovskite film on the polyTPD substrate with grain sizes up to 350 nm, which is comparable to its film thickness. [131]

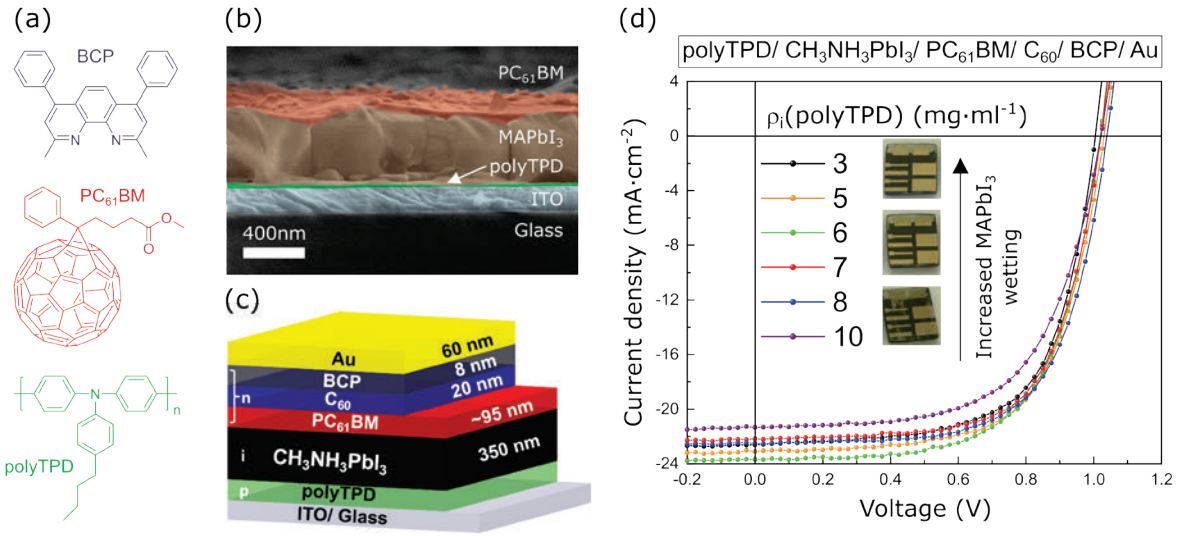


**Figure 59.** (a) Chemical structures of the used molecules. (b) Cross-section SEM image of the spin-coated layers with $PC_{61}BM$ on top of the $MAPbI_3$ layer. (c) Device structure of the $MAPbI_3$ perovskite solar cell using the p-i-n architecture. (d) J-V characteristics under illumination of $MAPbI_3$ perovskite solar cells with varying concentration of polyTPD and with inset of the prepared solar cells. Reproduced from Ref. [131] with permission from Zeitschrift für Naturforschung A (De Gruyter).

After the fabrication of the solar cells was completed, J-V curves were recorded in the dark and light to determine the power conversion efficiency depending on the respective polyTPD concentration and thus the thickness of the HTL. Figure 59d demonstrate the J-V curves under illumination of the best fabricated perovskite solar cells for each polyTPD concentration. Table 10 gives an overview of their device parameters $J_{sc}$, $V_{OC}$, FF, PCE, and the series resistance ($R_{Series}$).

**Table 10.** Average of short-circuit current density ($J_{SC}$), open-circuit voltage ($V_{OC}$), fill factor (FF), power conversion efficiency (PCE), and series resistance ($R_{Series}$) of the $MAPbI_3$ solar cells in dependence of the polyTPD mass concentration ($\rho_i$).

| $\rho_i$ (polyTPD) ($mg \cdot ml^{-1}$) | Analysed devices | $J_{SC}$ ($mA \cdot cm^{-2}$) | $V_{OC}$ (mV) | FF (%) | PCE (%) | $R_{Series}$ ($\Omega \cdot cm^{-2}$) |
|---|---|---|---|---|---|---|
| **3** | 10 | 20.77±2.10 | 999±23 | 66±5 | 13.63±0.96 | 474±11 |
| **5** | 10 | 22.12±1.08 | 1054±14 | 67±4 | 15.65±0.31 | 424±18 |
| **6** | 10 | 21.15±1.97 | 1026±19 | 67±3 | 14.46±1.24 | 477±27 |
| **7** | 7 | 20.40±1.57 | 1027±11 | 68±4 | 14.27±1.67 | 498±11 |
| **8** | 12 | 20.97±2.18 | 1024±22 | 62±3 | 13.46±1.16 | 526±26 |
| **10** | 7 | 20.18±2.17 | 996±25 | 59±4 | 11.79±1.63 | 547±112 |

In $J_{SC}$ no clear dependence on the choice of the polyTPD mass concentration was observed, with average values ranging from 20.18 to 22.1 $mA \cdot cm^{-2}$. Looking at the $V_{OC}$, it is evident that this parameter reaches its maximum value of 1054 mV at a mass concentration of 5 $mg \cdot ml^{-1}$, which is comparable to vacuum sublimated $MAPbI_3$ perovskite solar cells [259]. In addition, the average of FF (66 – 68 %) is highest for the concentrations 3 to 7 $mg \cdot ml^{-1}$ but decreases to 62 – 59 % for the polyTPD concentration 8 and 10 $mg \cdot ml^{-1}$. This increase in polyTPD precursor concentration and therefore the increase in polyTPD layer thickness leads to an increase in $R_{Series}$ of the devices from a minimum value of 424 $\Omega \cdot cm^2$ up to a maximum value of 547 $\Omega \cdot cm^2$. In summary, the devices with a polyTPD concentration of 5 $mg \cdot ml^{-1}$ show the highest average PCE with reproducible values in the range of 15.6 to 16.4 %. [131]

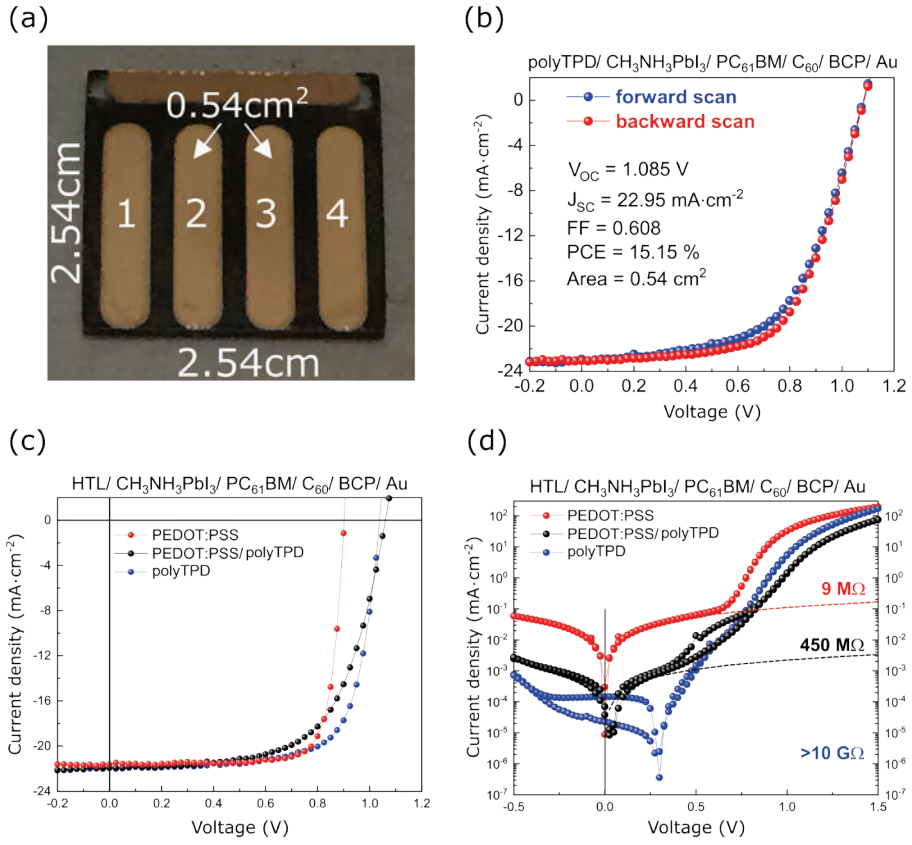


**Figure 60.** (a) Photograph of an $MAPbI_3$ perovskite solar cell fabricated on a large substrate (1·1 $inch^2$). (b) J-V curve of the best $MAPI_3$ perovskite solar cell. Comparison of J-V curves of the best (c) illuminated and (d) dark $MAPbI_3$ solar cells with different HTLs. The extracted values of $R_{Shunt}$ are further shown for each cell. Reproduced from Ref. [131] with permission from Zeitschrift für Naturforschung A (De Gruyter).

To verify the applicability of the approach to upscaling, solar cells on 1-inch substrates were manufactured. Figure 60a shows the photograph of an 1·1 inch$^2$ substrate containing four perovskite solar cells with a total active area of 0.54 cm² for each cell. All devices exhibit high PCE values with only small deviations. The best performing solar cell displays a PCE of 15.15 % with a $V_{OC}$ as high as 1.085 V (Figure 60b), only slightly lower than for small-area devices with active areas of below 0.09 cm². The possibility to fabricate solution-processed perovskite solar cells with untreated polyTPD as HTL allows for a direct comparison to otherwise identical solar cells based on the commonly used HTL PEDOT:PSS, as well as a bi-layer stack of both HTLs, with regard to their photovoltaic performance: The J-V characteristics of the devices are shown in Figure 60c. Compared to the previously discussed polyTPD-only record device, the PEDOT:PSS solar cell demonstrates a higher FF of 80.3 %, but a substantially lower $V_{OC}$ of only 0.903 V, resulting in a PCE of 15.51 %. If both HTLs are combined in a bilayer device, where polyTPD is processed on PEDOT:PSS, a high $V_{OC}$ of 1.07 V will be achieved. Nonetheless, the poor FF of 63.6 % limits the device performance to 15.5 %. This 130 to 160 mV increase in $V_{OC}$ can be explained by the superior ability of polyTPD to block electrons compared to PEDOT:PSS, underlining its great potential for further use in solution-processed perovskite solar cells. This property results in another advantage of polyTPD as HTL, as can be seen in the comparison of the respective dark J-V curves in Figure 60d: PEDOT:PSS as HTL displays the lowest parallel resistance $R_{Shunt}$ of 9 MΩ of the three devices compared to the $MAPbI_3$ solar cell based on PEDOT:PSS/polyTPD with $R_{Shunt}$ of 450 MΩ and the neat polyTPD device with a remarkably high $R_{Shunt}$ of above 10 GΩ. As a consequence, leakage currents are significantly suppressed, which enables the solar cell to operate under low light conditions as well and comparable to evaporated perovskite solar cells [135]. Furthermore, the retaining $V_{OC}$ visible for the polyTPD-only device is caused by very weak stray light, which was present during all dark J-V measurements. Nonetheless, it can only be seen in the polyTPD device for the reasons discussed above. [131]

### 7.1.4 Concluding Remarks on the Thin-film Solar Cells

A route to process planar p-i-n $MAPbI_3$ perovskite solar cells with polyTPD as HTL was presented in this subchapter. Without the use of an interfacial layer such as PFN, it was possible to process efficient perovskite devices by varying the polyTPD concentration and by applying a modified two-step-technique. First, the wettability of the perovskite precursor solution was optimized on the polyTPD layer, which was prepared by varying the mass concentrations, to achieve full surface coverage on the substrate. The best performing $MAPbI_3$ perovskite device with a high FF of 74 % was realized, using a polyTPD layer with a concentration of 5 mg·ml$^{-1}$. Moreover, this approach allowed to prepare pinhole free $MAPbI_3$ perovskite devices on 1·1 inch$^2$ substrates with PCE values above 15 %. In addition, it was shown that polyTPD HTL prepared in this way has exceptional hole-selective properties under low-light conditions due to high $R_{Shunt}$. The presented results offer an alternative approach to the processing planar p-i-n $MAPbI_3$ solar cells from the solution without the need of vacuum depositing $MAPbI_3$ or the use of additional interface layers to prevent layer dewetting. The knowledge gained here about the properties of the poly(triaryl)amine with respect to the wettability of $MAPbI_3$ is also of great importance to manufacture a crystal wafer and a crystal solar cell with the same perovskite and will be shown in the following Subchapters 7.2 as well as 7.3. [131]

## 7.2 High-quality $MAPbI_3$ Crystal Wafers for the Fabrication of Light-sensitive Photodetectors[7,8]

Subchapter 7.1 showed that the perovskite $MAPbI_3$ is an excellent light absorber, has a suitable band gap to the respective charge transport layers, and accordingly is used as active semiconducting component for the fabrication of efficient solar cells [131]. However, to commercialize hybrid perovskite solar cells, the problem of degradation must be solved [250, 278-283]. Typically, the solar cells are processed and measured under inert gas to ensure the device stability [131, 278, 280, 284]. Under ambient conditions, the thin polycrystalline $MAPbI_3$ films of a few 100 nm degrade rapidly [281, 285-287], greatly reducing the efficiency of the solar cells [250, 286, 287]. To avoid expensive solar cell encapsulation [287-289], perovskite single crystals are increasingly coming into focus for photovoltaic applications [122] due to their much better stability under atmospheric conditions. Based on the structural analyses in Chapters 5 and 6, the high structural quality of the crystals compared to the polycrystalline films in Subchapter 7.1 was obvious. However, to ensure efficient charge transport of electrons and holes through the crystal bulk, the optoelectronic parameter, the charge-carrier diffusion length, must be introduced, which assumes a value of about 175 µm for $MAPbI_3$ crystals [83, 122, 170, 173]. In comparison, for polycrystalline $MAPbI_3$ thin films, a thickness of about 100 nm is sufficient to successfully harvest light and to largely prevent recombination of the charge carriers at the electrodes [122, 133, 274]. In order to achieve the appropriate layer thickness, a wide variety of processing techniques can be applied, such as spin- [47, 79, 131], dip- [290] or blade-coating [291]. However, to guarantee balanced electron-hole transport in $MAPbI_3$ crystals [122], other techniques must be employed to control their thickness. The key factor here is the reduction of the crystal thickness. Typically, $MAPbI_3$ crystals reach a thickness in the range of 1 to 3 mm [23] by applying the established inversion temperature crystallisation [62, 64, 83]. Therefore, the crystal thickness must drastically be reduced to meet the condition of the charge carrier diffusion length [122]. Based on the existing techniques for limiting crystal thickness [55, 122], a new setup for fabricating high-quality $MAPbI_3$ crystal wafers [55, 56, 122] is presented in the following. After the successful fabrication of the crystal wafers, they were examined with regard to their quality by means of X-ray experiments. Moreover, optical properties were investigated by measuring the transmittance in order to build a crystal photodetector in the next step. Thereby, current – voltage curves were first recorded in the dark and light to test the electrical contact from crystal to the circuit boards. In a final step, and to verify the fabrication of a photodetector, the effect on the photocurrent was verified by varying the irradiance of the applied sun simulator to eventual determine the photoresponsivity.

### 7.2.1 Fabrication of $MAPbI_3$ Crystal Wafers

**Chemicals:** Information about the precursor materials $PbI_2$, MAI, and GBL can be found in Chapters 4 and 6. PTAA ($M_W$ = 5500, $M_n$ = 3595, PDI = 1.53) was bought from Electronic Materials Index Co. Toluene (anhydrous, 99.8 %) was purchased from Sigma-Aldrich. All chemicals and solvents were used as received.
**Fabrication:** Two different techniques can be used for the growth of $MAPbI_3$ crystal wafers:

[7] This chapter is partially based on the section *"Hybrid perovskite crystals: Growth, characterization and application"* from Julian Höcker and Vladimir Dyakonov, which is part of the paper entitled *"Roadmap: Organic-inorganic hybrid perovskite semiconductors and devices"*, published in the Journal APL Materials in 2021, volume 9, pages 28 – 30 (109202).
[8] This subchapter is partially based on the E-Poster *"High-quality $MAPbI_3$ crystal wafers and crystal "films" for optoelectronic applications"* from Julian Höcker, Philipp Rieder, and Vladimir Dyakonov presented at the HOPV conference in 2021.

(1) Two silicon wafers (front surface polished with 200 nm thermal oxide) were cut to a size of 2·2 $cm^2$. On one of the Si-wafers, silicone was additionally glued with a glass rod to fix two narrow spacers, made either of plastic (d = 300 µm), silicon (d = 500 µm) or glass (d = 1 mm). The silicone was cured for one week to ensure maximum hold of the spacers. Then, the prepared Si-wafers were cleaned with deionized water, acetone, and isopropanol in an ultrasonic bath for 10 min each. Afterwards, the Si-wafers were exposed to an $O_2$-plasma for 30 s. Besides this, PTAA was dissolved in toluene with a concentration of 10 $mg \cdot ml^{-1}$ and spin-coated on top of the pre-cleaned Si-wafers with a spin speed of 3000 rpm for 60 s. The PTAA films were then annealed at 110°C for 10 min. In a next step, the PTAA-coated Si-wafer with the fixed spacers was placed in a growth vessel located on a hot plate. Subsequently, a PTFE-filtered $MAPbI_3$ precursor solution was added and the solution was heated to 100°C. A small seed crystal was placed on the centre of the Si-wafer to ensure that a large $MAPbI_3$ wafer could be grown. Following this, the other coated Si-wafer was placed on top of the spacers to limit the thickness of the $MAPbI_3$ wafer during the growth. Finally, the solution was slowly heated to the growth temperature of $MAPbI_3$ crystals at 110°C [23, 62]. The precursor solution was exchanged two to six times to grow $MAPbI_3$ wafers with sizes of about 0.6 to 0.7 $cm^2$. After the growth, the synthesised $MAPbI_3$ wafers were directly cleaned with a lint-free cloth to remove the solution and to obtain a shiny crystal surface.

(2) To grow $MAPbI_3$ crystal wafers in a different way, a custom-made setup is used that avoids sticking the spacers. Here, a round Si-wafer with a radius of 2 cm is used, otherwise the preparation of the Si-substrate is the same as described above. The PTAA-coated Si-wafer is placed on a screw thread onto which a spacer is screwed. The further procedure for $MAPbI_3$ wafer growth is the same as described above. After successful growth, the spacer can be unscrewed with an opener and the $MAPbI_3$ wafer can be easily removed from the Si-substrate.
**Characterisation:** SEM images of the crystal wafers, transmittance and X-ray measurements were recorded with the equipment as described in Chapters 4, 5, and 6.
For the electrical measurements, the wafers were sputtered with gold electrodes (d = 80 nm), and then fixed onto circuit boards. I-V and photocurrent measurements of the crystal devices were measured in a nitrogen-filled glovebox under conditions of AM 1.5 G global spectral irradiance of 100 $mW \cdot cm^{-2}$ with a xenon lamp-based solar simulator (ORIEL 68811). To perform the I-V and photocurrent measurements, the Keithley MODEL 2612 B was used. The illuminated area of the wafer was $A_X = \pi \cdot r^2$ with a radius of r = 2 mm. As described in Subchapter 7.1 a reference silicon solar cell was applied to calibrate the exact irradiance.

### 7.2.2 Characterisation of the $MAPbI_3$ Crystal Wafers

For the successful growth of crystal wafers *via* ITC, a few aspects must be considered, which are listed in the following: (1) Polished silicon substrates enable the growth of flat and smooth crystal wafers, as hybrid perovskites have the property to adopt the shape of the respective growth vessel [62]. (2) Due to the spontaneous nucleation [68], crystals can grow at any place in the vessel. Therefore, it is possible that crystal nuclei do not nucleate on the mentioned Si-substrate. This can be avoided by using a seed crystal, placed in the centre of the Si-substrate. (3) In addition, controlled and slow heating of the precursor solution to the define growth temperature of $MAPbI_3$ is conducive to minimise crystal nuclei and thus to facilitate the growth of large-sized perovskite wafers. (4) Due to the limited growth time by using the ITC method [26], the $MAPbI_3$ solution has to be exchanged 3 – 4 times to grow large-sized wafers. This can be done by simultaneous exchange of old and new precursor solution using the previously presented re-fill crystallisation method (Chapter 5) [26]. (5) Another decisive criterion is the detachment of the crystal wafers from the Si-substrate after successful synthesis. Due to the strong adhesion of the Si-substrate, precursor solution, and $MAPbI_3$ wafer, the crystals can break into small pieces during detachment. To overcome this problem, both Si-

substrates are first coated with PTAA. As explained in Subchapter 7.1.1, poly(triaryl)amines like polyTPD as well as PTAA are hydrophobic [131]. Moreover, it was evident that with a high polyTPD concentration of 10 mg·ml$^{-1}$, the adhesion of the polycrystalline $MAPbI_3$ thin films decreased most during processing [131]. However, these hydrophobic properties are beneficial for wafer fabrication. If the Si-substrates are coated with PTAA ($\rho_i$ = 10 mg·ml$^{-1}$), the adhesion of the $MAPbI_3$ wafer to the coated Si-substrate is suppressed, thus enabling easier detachment of the grown crystal. (6) In order to control the thickness of the crystal wafers, materials such as thin plastic (d = 300 µm), silicon (d = 500 µm) or glass pieces (d = 1mm) were successfully used as spacers in initial experiments (Figure 61a) [122]. The spacers are cut to a length of approx. 2 cm and a width of approx. 5 mm and glued on the Si-substrates using liquid silicone. The use of silicone guarantees a very good adhesion to the Si-substrate. In addition, the adhesive ensures that the spacers do not unstuck due to the high temperature of 110°C [23, 62] for growing $MAPbI_3$ wafers. (7) The many foreign substances, which are present in the growth vessel, can often contribute to nucleation [68]. Especially at the breaking edges of the silicon and glass spacers, undesired crystal growth often occurred, hindering the growth of large-sized crystal wafers. Furthermore, to allow exact wafer layer thicknesses, and thus to avoid gluing the spacers, a new setup was constructed, which is also shown in Figure 61a. Here, a PTAA-coated Si-substrate is deposited on a screw thread and then fixed with a spacer made of PTFE or stainless steel. Again, a seed crystal is placed on the coated Si-substrate and another Si-substrate limits the thickness of the $MAPbI_3$ wafer from above. After successful wafer growth, the components of the setup (Figure 61b) could be easily disassembled by using an opener to remove the grown wafer from the Si-substrate. To sum up, the new self-made setup for growing $MAPbI_3$ wafers guarantees not only precise crystal thickness, but also an easier handling.

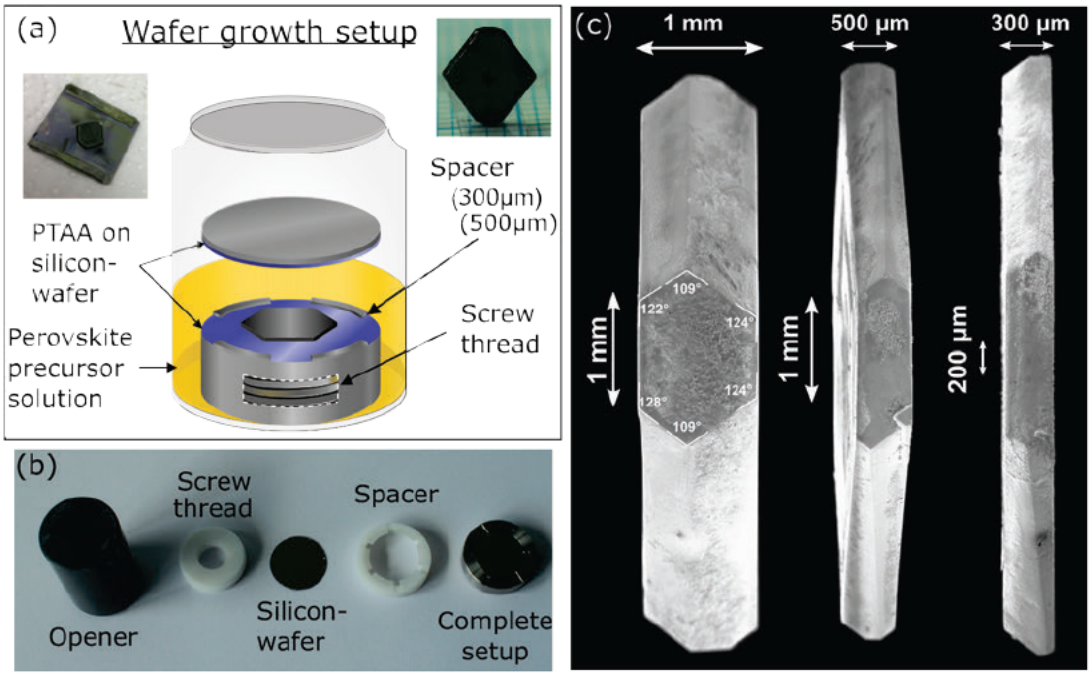


**Figure 61.** (a) Two different techniques to grow $MAPbI_3$ crystal wafers with different thicknesses. The images of the grown wafers are further shown. (b) Tools for growing perovskite wafers with the self-made setup. (c) SEM images of the successfully grown $MAPbI_3$ wafers with thicknesses of 1 mm, 500 µm, and 300 µm. Reproduced partly from Ref. [310] with permission from APL Materials.

Figure 61c shows the SEM images of the successfully grown $MAPbI_3$ crystal wafers with thicknesses of 1 mm, 500 µm, and 300 µm. The limitation of the wafer thickness leads to a change in their crystal habit [4, 292] because the size ratio of the individual planes changes

compared to thick $MAPbI_3$ crystals [293], shown in Chapters 4 and 6. The $MAPbI_3$ wafers shown in Figure 61c exhibit a planar habit [294, 295] because the diameters of the wafers are much larger than their thicknesses [4]. In contrast, a thick $MAPbI_3$ crystal has an isometric habit [296] since the ratio of the diameter to the thickness of the crystal is approximately the same (Subchapter 2.6). Interestingly, a decrease of the crystal thickness does not automatically cause a change of the crystal tracht [292, 293]. This means that the number of crystal planes, which formed the crystal wafers, remains unchanged [4, 293]. This is evident for all $MAPbI_3$ wafers, but is best seen on the wafer with a thickness of 1 mm. A total of 12 planes could be counted here, which is the same for thick $MAPbI_3$ crystals, as shown in Chapters 4 and 6. Moreover, just like thick $MAPbI_3$ crystals, the bottom and upper faces of $MAPbI_3$ wafers show the geometry of a hexagon. This is also evident from the upper crystal face of the wafer with a thickness of 1 mm. Its angular sum is 716°, which is in accordance with the condition for hexagons, where the sum of the internal angles must be 720° [4].

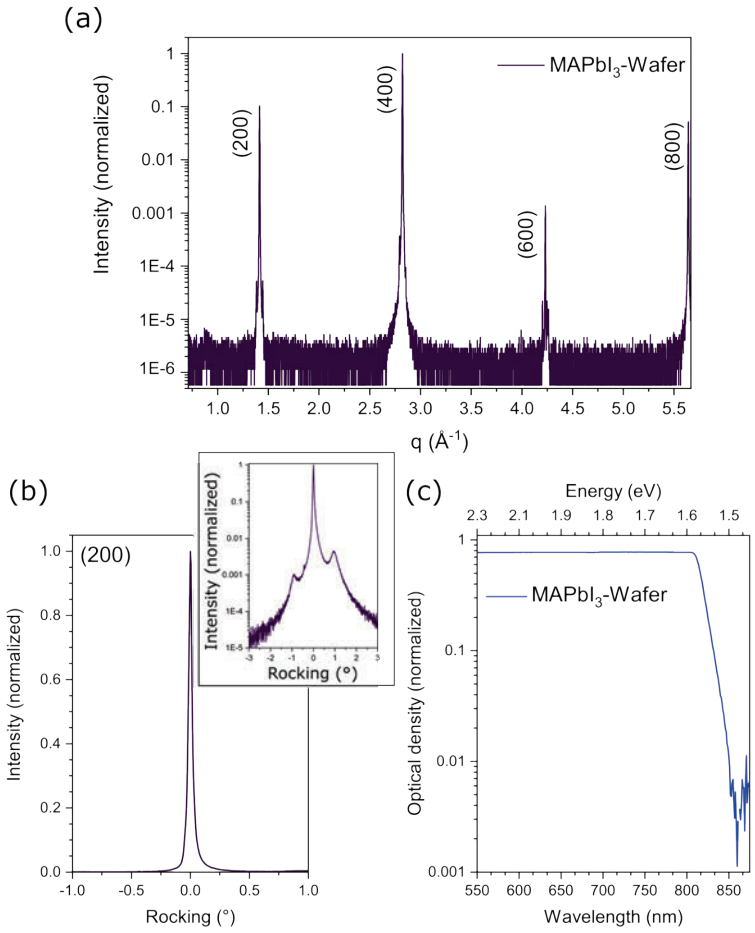


**Figure 62.** (a) Out-of-plane XRD measurement to prove the crystal surface quality of a $MAPbI_3$ wafer. (b) Rocking scan in the linear and logarithmic plot, performed on the (200) Bragg reflex. (c) The normalized optical density spectrum of a $MAPbI_3$ wafer.

In addition to the investigation of the crystal morphology, the $MAPbI_3$ wafers were examined with respect to their structural quality. X-ray scattering in reflection geometry was recorded from the wafer surface and is shown in Figure 62a. Based on the detected Bragg reflexes of the out-of-plane measurement, the Miller indices were accurately assigned and indicate the growth direction of the wafer. It is interesting to note here that the diffractogram of the wafer indicates the {200} peak series for the dominant surface, which is exactly the same for a thick $MAPbI_3$

crystal, as shown in Chapter 6. From this, it can be concluded that limiting growth in one direction does not affect the wafer´s crystallographic properties. Another characterisation possibility to determine the surface quality of the wafer is the rocking scan, shown in Figure 62b. Although only one peak is noticeable in the linear plot, two further peaks become visible in a logarithmic representation. A possible explanation for the low symmetry of the rocking scan are grain boundaries resulting from the use of seed crystals, which was already shown in Chapter 5 [26]. However, the results indicate an overall high wafer quality because impurities from the precursors $PbI_2$ and MAI can be excluded as discontinuities since their peaks are absent from the XRD pattern [122].
Another important step in the realisation of a photodetector based on a $MAPbI_3$ wafer are optical measurements. For this reason, a transmittance measurement was performed to determine the optical density, which is shown in Figure 62c. Here, the absorption capability of the wafer becomes clear because the wafer absorbs visible light in the range from 550 nm to its absorption edge of 810 nm.

### 7.2.3 Characterisation of a $MAPbI_3$ Wafer Photodetector

Figure 63a shows the schematic illustration of the $MAPbI_3$ wafer contacting. The same circuit boards, as described in detail in Chapter 5, were used to perform electrical measurements of the

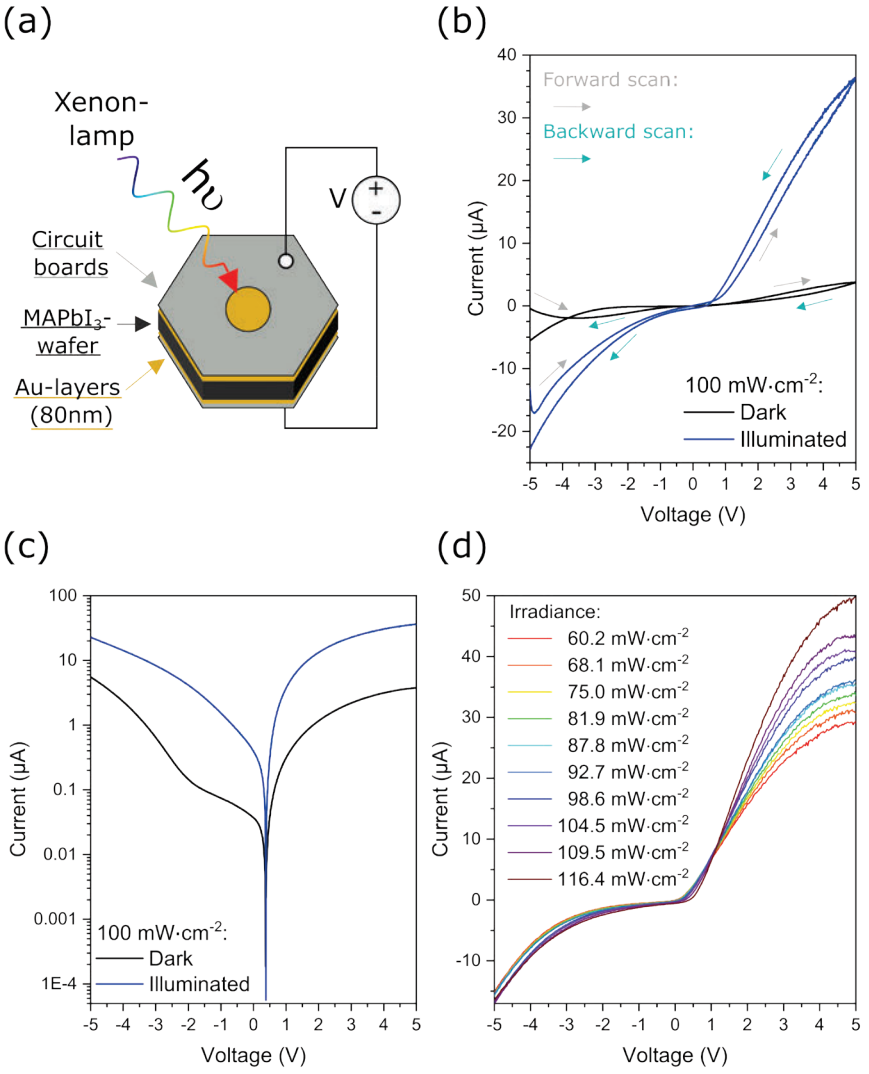


**Figure 63.** (a) Schematic illustration of the $MAPbI_3$ wafer contacting. (b) Linear and (c) logarithmic plotted I-V curves, measured in the dark and light, with an irradiance of 100 mW·cm$^{-2}$. (d) Linear plotted I-V curves in dependence of the irradiance.

Au-sputtered $MAPbI_3$ wafer. First of all, I-V curves were recorded in the dark and under illumination (100 $mW \cdot cm^{-2}$), each in forward and reverse sweep, to test the electrical contact from the circuit boards to the wafer (Figure 63b). Both I-V curves show the phenomenon of hysteresis [212, 297, 298], which is mainly caused by ion migration [297] and has already been discussed in Chapter 5. In addition, it can be seen that a higher current was measured than in the dark. To provide a more accurate reading of the current, the reverse scans were plotted in logarithmic scale, which is shown in Figure 63c. Here, it is obvious that e.g. with an applied voltage of 5 V only a very small current of 4 µA was measured in the dark. In contrast, a current of 36 µA was detected under illumination. In a next step, different irradiances from 60.2 to 116.4 $mW \cdot cm^{-2}$ were set to measure the current (Figure 63d). Here, the current increases constantly from 29.6 µA (lowest irradiance) to 49.7 µA (highest irradiance) with an applied voltage of 5 V.

Furthermore, the photocurrent of the $MAPbI_3$ wafer was recorded as a function of time at different applied voltages from 1 to 10 V in steps of 1 V. The irradiance was kept constant at 100 $mW \cdot cm^{-2}$. In addition, the light was switched off and on at regular intervals of 20 s. Figure 64a shows clearly that directly after switching on the light, an increased current was measured. After switching off the light again, only a small dark current was recorded. Here, the current under illumination reached values from 3 µA for 1 V to 78 µA for 10 V.

In addition, the photocurrent was measured as a function of time with 10 different irradiances. Here, the voltage was kept constant at 4 V and the light was switched on and off after 20 s. Figure 64a shows a similar behaviour as before Figure 64b. When the light was switched on, a higher current was detected than in the dark. Moreover, the current response was constantly increasing with rising irradiance. From this, it can be concluded that at a higher irradiance the $MAPbI_3$ wafer absorbs more photons, which in turn results in an increased current. These

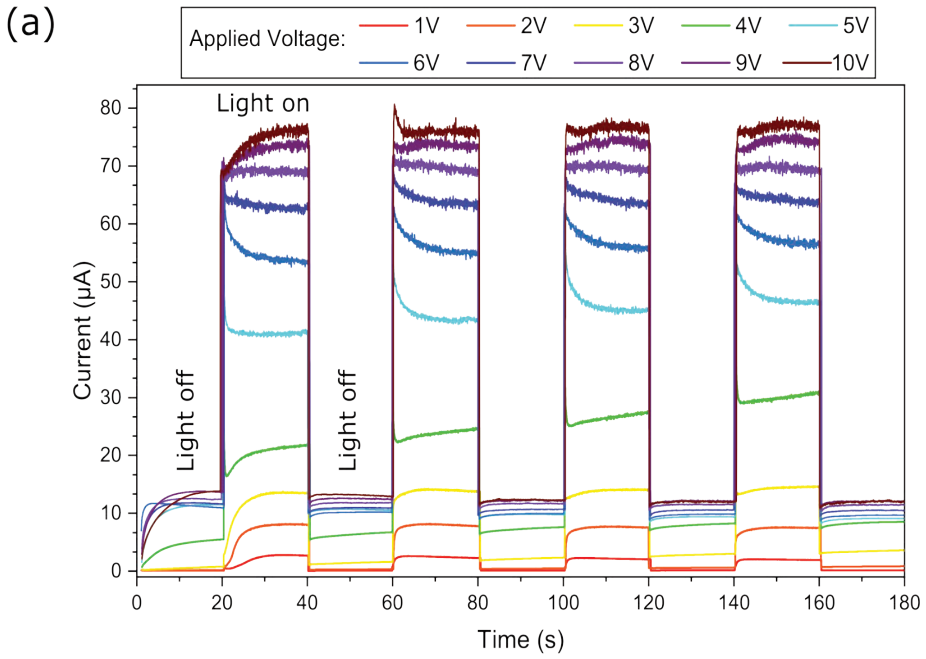


**Figure 64.** (a) Current response as a function of time and different applied voltages. The irradiance was kept constant at 100 $mW \cdot cm^{-2}$. (b) Current as a function of time and different applied irradiances. The voltage was kept constant at 4 V. (c) Plot of the photoresponsivity and the photocurrent as a function of the irradiance to test the use of a $MAPbI_3$ wafer as a photodetector.

measurements are additionally used to determine the photoresponsivity, which is an important parameter to verify the construction of a photodetector (Subchapter 3.3.1) [122-125].

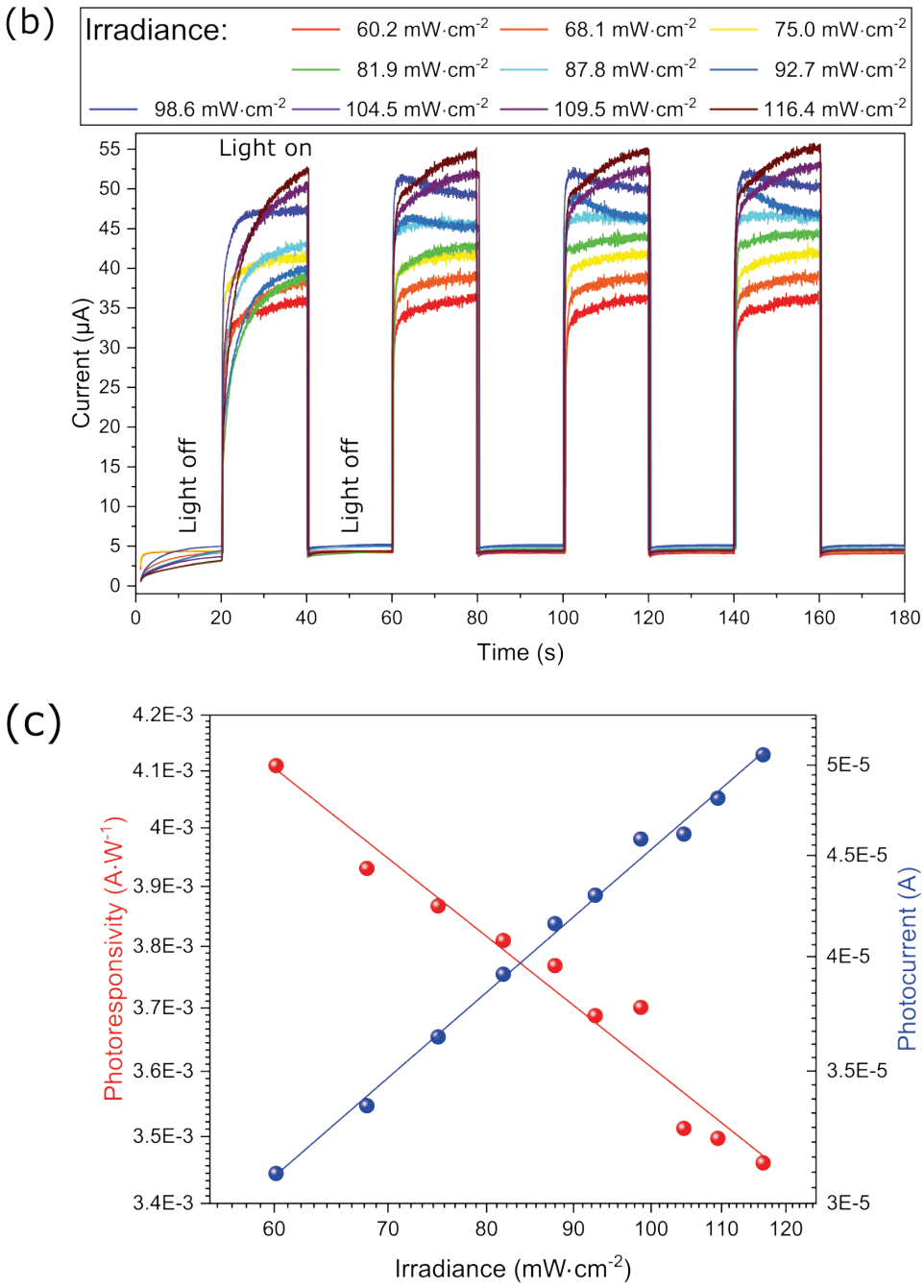


**Figure 64.** (continued).

Accordingly, the photoresponsivity and the photocurrent in dependence of the irradiance is shown in Figure 64c. Both, the direct proportionality of the photocurrent to the irradiance and the indirect proportionality of the photoresponsivity to the irradiance become apparent since the photocurrent increases with rising irradiance while simultaneously the photocurrent decreases. The measurements shown here, as well as the determination of the photoresponsivity are in good agreement with the literature [122] and accordingly confirm the successful construction of a photodetector prototype based on a $MAPbI_3$ wafer.

### 7.2.4 Concluding Remarks on the $MAPbI_3$ Wafer Photodetector

In this subchapter, the successful growth of $MAPbI_3$ wafers with thicknesses of 1 mm, 500 µm, and even with 300 µm has been described in detail by using two different setups. The use of seed crystals, PTAA-coated Si-substrates, and the choice of the suitable spacers guaranteed the growth of large-sized, smooth, and thin $MAPbI_3$ crystals. When looking at the crystal morphology, a difference of the crystal habit compared to common $MAPbI_3$ crystals was observed, but not in their crystal tracht. X-ray measurements revealed a high structural quality with the {200} series as growth direction of the wafer. In addition, $MAPbI_3$ wafers are excellent light absorbers in a wavelength range from 500 to 800 nm and accordingly appropriate for the fabrication of photodetectors. This was investigated by measuring the electric current as a function of time at different voltages and irradiances. The evaluations revealed a direct proportionality of the photocurrent to the irradiance and an indirect proportionality of the photoresponsivity to the irradiance. These results represent another important contribution to consider perovskite crystals/wafers commercially for optoelectronic applications in the near future.

## 7.3 High-quality Perovskite Crystal "Films" for the Fabrication of Solar Cells[9]

The key motivation for the research on OLTPs are their applications of polycrystalline perovskite thin films for the fabrication of high-efficient solar cells [131, 225]. Nevertheless, for some years now, efforts have also been made to produce solar cells based on thin perovskite crystals [149, 150, 186, 197, 224, 225, 233, 299-308]. The reasons for the scientific interest are the excellent structural qualities, low trap densities, as well as the high charge carrier diffusion lengths of the perovskite crystals compared to their thin films with the same stoichiometry [26, 149, 173, 197, 225]. However, the fabrication of crystal "film" [174, 197, 225, 299] solar cells is much more difficult than the processing of thin polycrystalline film solar cells [225]. Just as with perovskite wafers, the thickness of the crystal "films" must be reduced to a few µm to be suitable as semiconducting component for a photovoltaic application [308]. In this last subchapter, the growth of $MAPbBr_3$ and $MAPbI_3$ crystal "films" is described in detail using the RITC method [23]. In addition, the thicknesses of the thin crystals were measured and structural X-ray analyses were performed. In a final experiment, a thin $MAPbI_3$ crystal was selected for the construction of a p-i-n solar cell, which was characterised by J-V curves and MPP tracking (MPPT).

### 7.3.1 Fabrication and Characterisation of Perovskite Crystal "Films" and a $MAPbI_3$ Solar Cell

**Crystal "film" growth":** For the growth of the $MAPbBr_3$ and $MAPbI_3$ crystal films, ITO substrates with a size of $1 \cdot 2$ inch$^2$ were first cleaned using the purification process described in Subchapter 7.1.1. The HTL PTAA was spun onto the ITO substrates in a nitrogen-filled glovebox at a spin speed of 5000 rpm for 30 s and then annealed at 100°C for 10 min. Here, PTAA with a mass concentration of 2 mg·ml$^{-1}$ was dissolved in toluene at RT overnight. The dried substrates were finally transferred to a fume hood and deposited on a metal plate, which was placed on a heating plate. Then, 15 – 30 µl of a mixture of $MAPbBr_3$ (1 M) or $MAPbI_3$ (1.2 M) precursor solution, each with a small amount of hexanol, was dropped onto the substrate. The other coated ITO-substrate was placed on top afterwards [308]. Detailed information on the perovskite-alcohol mixtures [23] can be found in Chapter 6. To grow $MAPbBr_3$ crystals, the substrates were heated from RT to 40°C in 5°C steps. After the first crystals began to grow, the temperature was increased to 50°C to accelerate the growth process. For the growth of $MAPbI_3$ crystals, the temperature was increased from 60 to 85°C in 5°C steps each. After the first crystals started to grow, the temperature was increased to 90°C. For the growth of perovskite crystals with an area of a few millimetres, approximately one week is required. After the growth process, the ITO-substrates were separated with a scalpel.
**Solar cell fabrication:** For the construction of a solar cell, the substrate with the $MAPbI_3$ crystal was cut to a size of approximately $1 \cdot 1$ inch$^2$, to ensure better handling for the evaporation process. In order to provide a direct contact to the ITO substrate, the PTAA layer next to the crystal was removed first by dissolving it with DCM, and finally by scraping the HTL layer with a scalpel. For a better contact to the ITO, a thin layer of conductive silver lacquer was spread on the cleaned surface. Furthermore, part of the substrate was covered with Kapton tape up to the crystal, which acted as an insulating layer. The entire substrate was masked except for the crystal and part of the Kapton tape. The substrate was then mounted in the evaporation chamber. The structure of the vapour-deposited electron transport layers and

[9] This subchapter is partially based on the E-Poster *"High-quality $MAPbI_3$ crystal wafers and crystal "films" for optoelectronic applications"* from Julian Höcker, Philipp Rieder, and Vladimir Dyakonov, presented at the HOPV conference in 2021.

the electrode was the same as for high-efficient polycrystalline thin-film solar cells [309]. In a first step, lithium fluoride (LiF) with a layer thickness of 1 nm and $C_{60}$ with a layer thickness of 20 nm were thermally deposited. The fabrication of the p-i-n solar cell was completed by evaporating the BCP layer (d = 8 nm) and the Au electrode (d = 70 nm). Both evaporation steps were performed under high vacuum at a pressure of $10^{-7}$ mbar.

**Characterisation:** SEM images and X-ray measurements of the crystal "films" were recorded with the equipment as described in Chapters 4, 5, and 6. Thickness measurements of the crystals were carried out with the device "Veeco Dektak 150" on a vibration-damped table (Model: VH3036-OPT) from Newport. The J-V curves (forward and backward scan), the MPPT, and the measurement of $V_{OC}$ and $J_{SC}$ in dependence of time were directly measured after the fabrication of the solar cell in a nitrogen-filled glove box. The setup for all measurements, the calibration of the illumination intensity, and the valuation of the significant physical parameters data were the same as described in Subchapter 7.1.3. To accurately determine the power conversion efficiency, the active area of the solar cell was determined using an optical microscope (Carl Zeiss Axiotech vario 2HD), which was 3.375 mm² in total.

### 7.3.2 Crystal "Film" Growth with RITC

The space-limited growth method was used to synthesise the crystal "films" [149, 197, 225, 308]. For this, the perovskite solution was embedded between two PTAA-coated ITO substrates [308]. Due to the capillary effect, the perovskite solution homogeneously disperses on the hydrophobic polymer [299]. The growth method was the RITC method, which is based on a reduced inverse solubility, in order to pull crystals at lower growth temperatures compared to ITC [23]. Furthermore the growth method enables the synthesis of crystals with an excellent structural quality [23], as shown in Chapter 6. To verify the space-limited RITC method both, $MAPbI_3$ and $MAPbBr_3$ crystal films were grown.

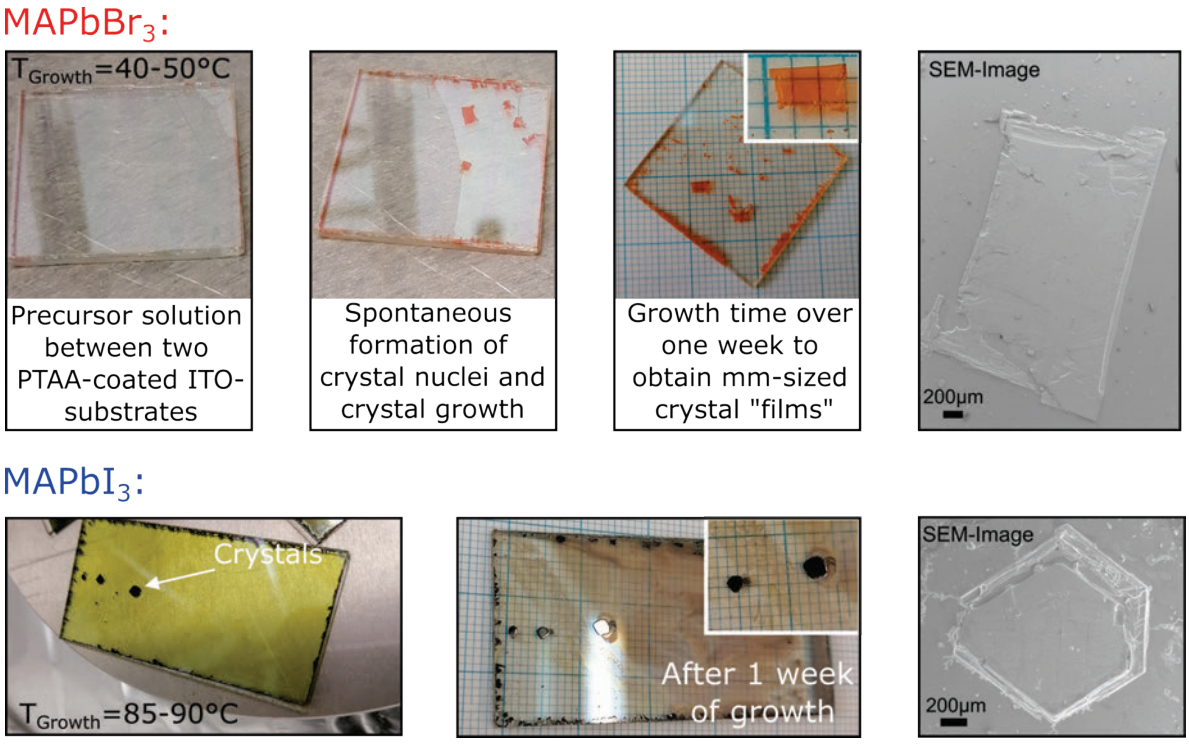


**Figure 65.** (left) Description of the growth of $MAPbBr_3$ and $MAPbI_3$ crystal films with the space-limited RITC method. (right) SEM images of the thin crystals, showing a rectangular surface for $MAPbBr_3$ and a hexagonal surface for $MAPbI_3$

Figure 65 shows the preparation of the two crystal films. Here, the transparent blend of $MAPbBr_3$ precursor solution and the primary alcohol hexanol is located between two PTAA-

coated ITO substrates (left photo). The substrates were then heated up to 40°C in 5°C steps to avoid immediate crystallisation and to generate only a few crystal nuclei. As can be seen in the centre photo, the red crystals began to grow while at the same time the amount of precursor solution started to vanish. To accelerate the growth process, the substrates were finally heated up to 50°C. After one week, the thin $MAPbBr_3$ crystals reached a maximum size of 2·2 mm (inset in the right photo). A perovskite solution with hexanol was also used to grow crystalline $MAPbI_3$ "films". Here, the substrates were first heated slowly from 60 to 85°C to initiate the crystallisation process. After small black crystals had formed in the yellow precursor solution (left photo), the substrates were further heated to 90°C to accelerate the crystal growth. Again, a week was needed for controlled crystal pulling (right photo). The shape of the thin $MAPbI_3$ crystal is that of a hexagon, and is comparable to the surface of thick $MAPbI_3$ crystals (Chapter 4 and 6), as well as the previously shown wafers in Subchapter 7.2.
It is interesting that the thickness limitation has no effect on the shape of the thin crystals, which is evident when looking at the SEM images: Here, the thin $MAPbBr_3$ crystal shows a rectangular shape and the thin $MAPbI_3$ crystal exhibits the shape of a hexagon. This is comparable to the surfaces of regular $MAPbBr_3$ and $MAPbI_3$ crystals. Furthermore, in contrast to the SEM image of the polycrystalline $MAPbI_3$ thin film in Subchapter 7.1, both crystal "films" show no grain boundaries or cracks, which is in good agreement with the literature [308].

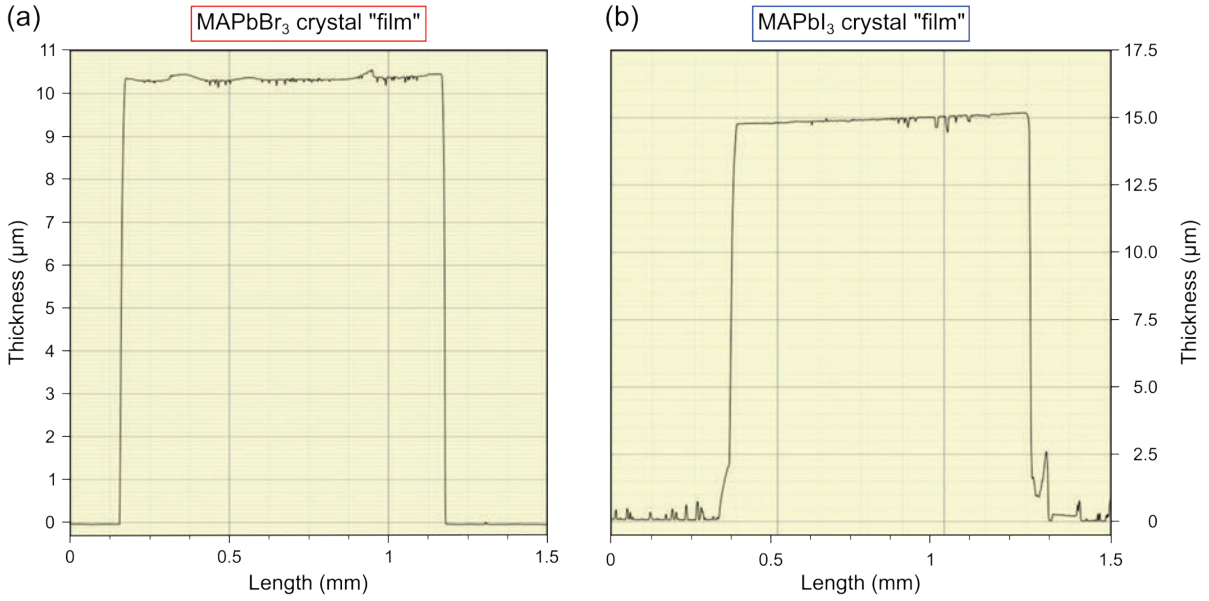


**Figure 66.** Thickness measurement of (a) a $MAPbBr_3$, and (b) a $MAPbI_3$ crystal "film", confirming both a controllable growth by the space-limited RITC method.

After the growth process, the crystal thicknesses were measured. Figure 66a – b shows that the thickness of the thin $MAPbBr_3$ crystal was about 10.5 µm and that of the $MAPbI_3$ crystal about 15 µm. The difference in the crystal thicknesses can be explained by the different molar concentrations of the two precursor solutions. Since a slightly higher concentrated solution was used for $MAPbI_3$ ($c_m = 1.2\ mol \cdot l^{-1}$) compared to $MAPbBr_3$ ($c_m = 1\ mol \cdot l^{-1}$), the amount of liquid between the two PTAA-coated ITO substrates was a little higher. This allowed the growth of thicker $MAPbI_3$ crystal "films". The layer thickness measurements also showed that very smooth and flat crystal "films" could be grown with the space-limited RITC method and suggests a controlled crystal pulling with this technique.

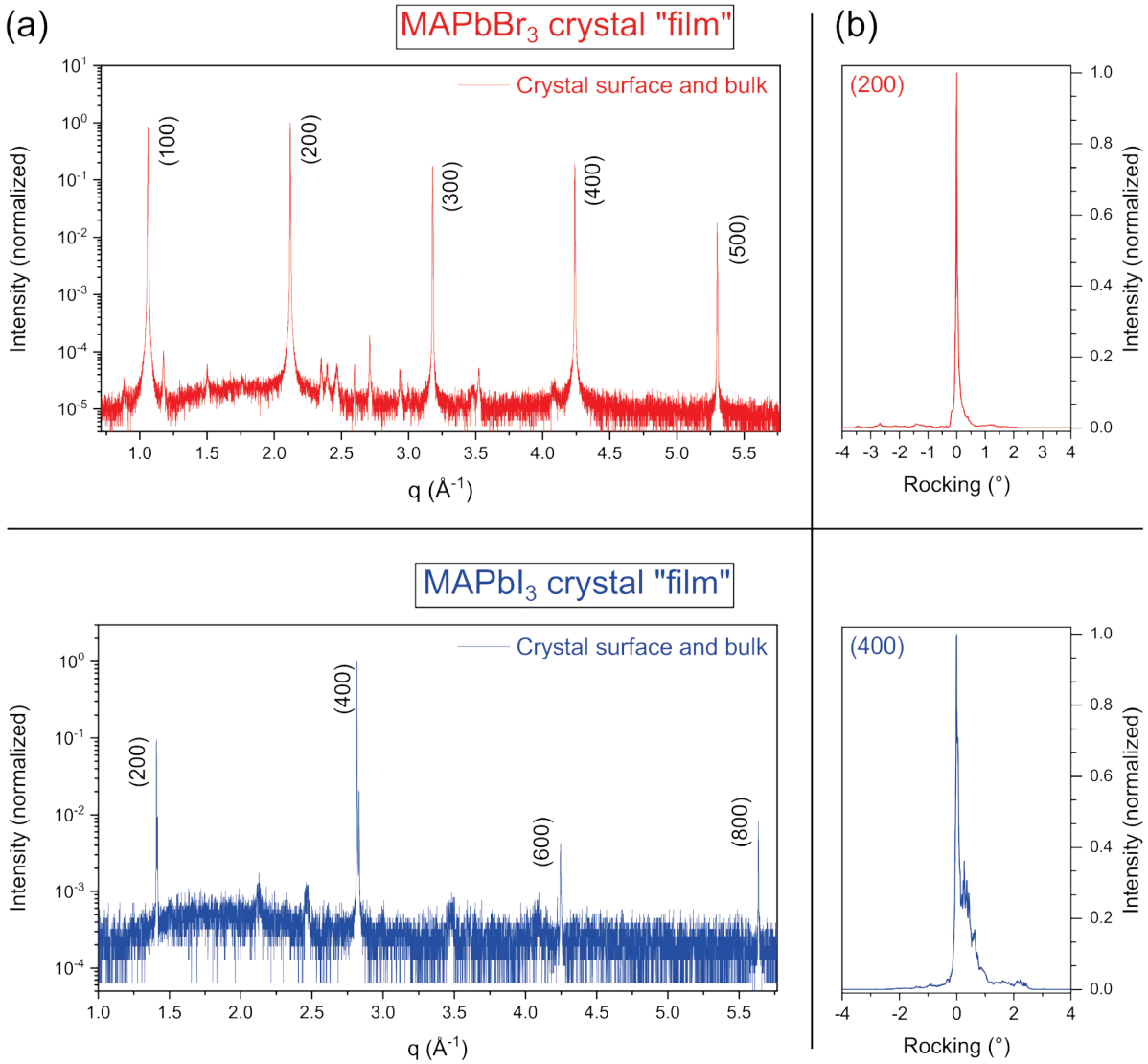


**Figure 67.** (a) Out-of-plane XRD measurement of a $MAPbBr_3$ and of a $MAPbI_3$ crystal "film". Due to thickness of a few µm, it was possible to simultaneously measure the crystal surface and the crystal bulk. (b) The rocking curves were performed on the (200) reflex of the $MAPbBr_3$ crystal and on the (400) reflex of the $MAPbI_3$ crystal.

To verify the crystal quality, XRD measurements were performed. Since the typical penetration depth of the 8 keV X-rays was around 10 µm, which is comparable to the thickness of the crystals, the surface and the bulk of the crystals were simultaneously measured. Figure 67a shows the XRD patterns of the thin $MAPbBr_3$ and $MAPbI_3$ crystals in logarithmic order. The diffraction peaks with high intensity can clearly be assigned to the [100] direction for $MAPbBr_3$ up to the 5th order and the [200] direction for $MAPbI_3$ up to the 4th order. With far less intensity, other Bragg reflexes are visible in the diffractograms. As grain boundaries and cracks have been excluded from the SEM images, and the purity of $MAPbBr_3$ as well as $MAPbI_3$ crystals has been already proven in Chapters 4 and 6, these irregularities are rather due to defects and dislocations in the crystal lattices. This is also shown by the rocking scans of $MAPbBr_3$ and $MAPbI_3$ in Figure 67b. Here, the misorientation of the crystallites becomes clear from the strongly broadened peak of the rocking measurement of $MAPbI_3$. The cause of the crystal structure defects can be found in the applied growth technique: The length of the growth period, the limitation of the crystal thickness, and the associated restriction in their preferential growth can represent stress for the growing crystal "films". Since the quality of the crystal lattice is

determined by its regularity and the growth directions of the two crystal "films" were clearly assigned, a good crystal quality can still be assumed despite the mentioned imperfections.

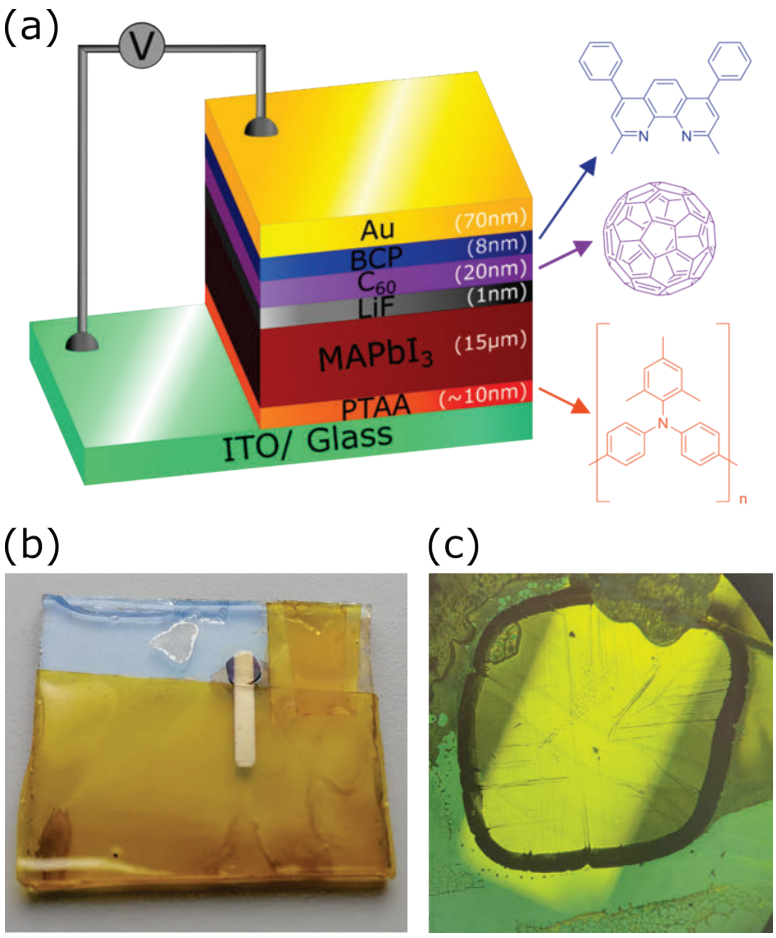


**Figure 68.** (a) The p-i-n architecture of the $MAPbI_3$ crystal "film" solar cell with the used HTL, ETL, and electrode layers. Further shown are the molecules of PTAA, $C_{60}$, and BCP. (b) Photograph and (c) optical microscope image of the solar cell.

In a final step, a solar cell based on a thin $MAPbI_3$ crystal was fabricated. The architecture of the solar cell was that of a p-i-n device and is shown in Figure 68a. The PTAA layer served as the p-type semiconductor and the $MAPbI_3$ crystal "film" as the intrinsic semiconductor. On top of the crystal, the interfacial layer LiF [309], the n-type semiconductor $C_{60}$ [251], and the buffer layer BCP [277] were evaporated. Finally, a gold electrode was deposited to complete the solar cell structure. The fabricated solar cell is shown as a photograph in Figure 68b and as an optical microscope image in Figure 68c.

After the fabrication process, current density – voltage curves were recorded in the dark and light to test the functionality of the $MAPbI_3$ crystal "film" solar cell. Figure 69a shows the J-V curve without illumination in a linear and a logarithmic plot. The measurement in the dark is comparable to those of the solar cells based on polycrystalline perovskite films in Subchapter 7.1 and shows a characteristic diode curve. In addition, the curves clearly show the previously mentioned phenomenon of hysteresis in the forward and backward scan.

To further provide accurate information about the electrical properties of the solar cell, the active area of the cell was precisely determined using a light microscope image. Thus, the short-circuit current (V = 0V), which was measured as a function of time, was converted into the short-circuit current density, and is shown in Figure 69b. Here, the light was switched on and

off at intervals of 20 s. When the solar cell is illuminated, a $J_{SC}$ of over 0.55 mA·cm$^{-2}$ was detected, which dropped back to zero as soon as the lamp was turned off. The measurement successfully shows the potential of the solar cell to convert the absorbed photons into electric current. However, compared to the polycrystalline solar cells in Subchapter 7.1, $J_{sc}$ was an order of magnitude lower. Remarkably, this first attempt of making a crystal "film" solar cell resulted in an open-circuit voltage of over 1 V, which is comparable to the $MAPbI_3$ devices from Subchapter 7.1. This is clearly demonstrated by Figure 69c. Like $J_{sc}$, $V_{OC}$ (J = 0) was measured as a function of time in an interval of 20 s with and without illumination. Finally, to determine the power conversion efficiency of the solar cell, a J-V curve was recorded under illumination (Figure 69d). The evaluation of the backward scan provided a fill factor of 24 %. Thus, considering the parameter $J_{SC}$ and $V_{OC}$, a PCE of 0.13 % could be determined, which was confirmed by the MPPT (inset in Figure 69d).

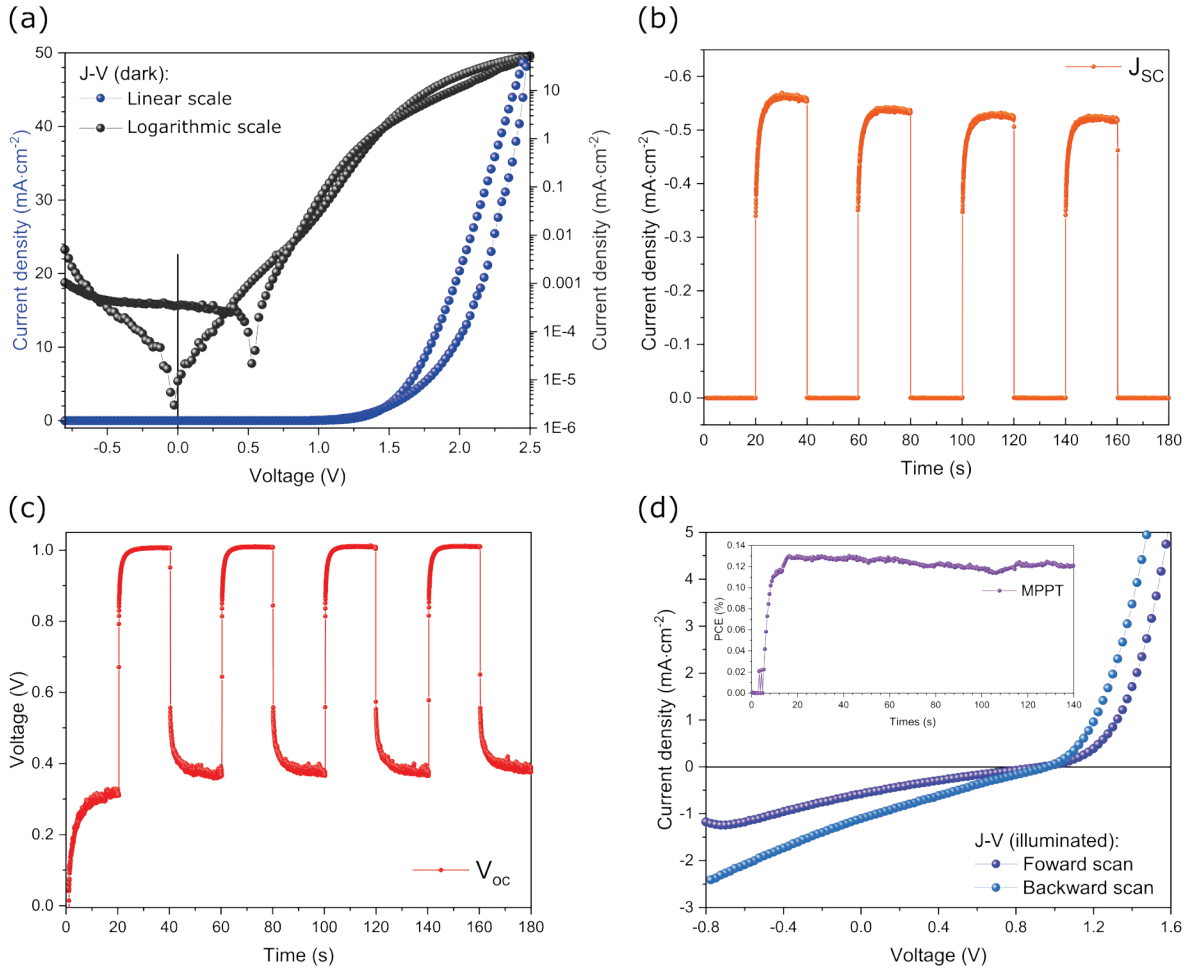


**Figure 69.** Electronic measurements of a $MAPbI_3$ based crystal "film" solar cell. (a) Dark J-V measurement. (b) $J_{sc}$ and (c) $V_{OC}$ as a function of time, recorded in the dark and under illumination. (d) J-V measurement under illumination. Further shown is the maximum power point tracking (MPPT) as a function of time.

### 7.3.3 Concluding Remarks on the $MAPbI_3$ Crystal "Film" Solar Cell

In summary, it can be noted that flat and smooth $MAPbBr_3$ and $MAPbI_3$ crystal "films" were successfully grown by the space-limited RITC method without any grain boundaries and cracks. Thereby, the crystal thicknesses could be limited to a range of 10 to 15µm, which makes them interesting for optoelectronic applications in contrast to thick crystals. Compared to polycrystalline films, the thin crystals had a very high structural quality, which was evident from the X-ray measurements of the crystal surface and of the bulk. In addition, a prototype of

a solar cell was designed and fabricated on the basis of a $MAPbI_3$ crystal “film”. The outstanding parameter of the solar cell was the open-circuit voltage of 1 V, which can compete with those of thin-film solar cells. The results shown here are promising, but should only give an outlook that OLTP crystals can also be applied for optoelectronic especially, for photovoltaic applications, just like their corresponding thin films.

# 8 Summary[10]

**Overview of the Organolead Trihalide Perovskite Crystal Area**

Studies of perovskite single crystals with high crystallographic quality is an important technological area of the perovskite research, which enables to estimate their full optoelectronic potential, and thus to boost their future applications [26]. It was therefore essential to grow high-quality single crystals with lowest structural as well as chemical defect densities and with a stoichiometry relevant for their thin-film counterparts [26]. Optoelectronic devices, e.g. solar cells, are highly complex systems in which the properties of the active layer (absorber) are strongly influenced by the adjacent layers, so it is not always easy to define the targeted properties and elaborate the design rules for the active layer. Currently, organolead trihalide perovskite (OLTP) single crystals with the structure $ABX_3$ are one of the most studied crystalline systems. These hybrid crystals are solids composed of an organic cation such as methylammonium ($A = MA^+$) or formamidinium ($A = FA^+$) to form a three-dimensional periodic lattice together with the lead cation ($B = Pb^{2+}$) and a halogen anion such as chloride, bromide or iodide ($X = Cl^-$, $Br^-$ or $I^-$) [23]. Among them are methylammonium lead tribromide ($MAPbBr_3$), methylammonium lead triiodide ($MAPbI_3$), as well as methylammonium lead trichloride ($MAPbCl_3$) [62, 63]. Important representatives with the larger cation $FA^+$ are formamidinium lead tribromide ($FAPbBr_3$) and formamidinium lead triiodide ($FAPbI_3$) [23, 64]. Besides the exchange of cations as well as anions, it was possible to grow crystals containing two halogens to obtain mixed crystals with different proportions of chlorine to bromine and bromine to iodine, as it is shown in Figure 70. By varying the mixing ratio of the halogens, it was therefore possible to vary the colour and thus the absorption properties of the crystals [85], as it can be done with thin polycrystalline perovskite films. In addition, since a few years it is also doable to grow complex crystals that contain several cations as well as anions [26, 80, 81]. These include the perovskites double cation – double halide formamidinium lead triiodide – methylammonium lead tribromide $(FAPbI_3)_{0.9}(MAPbBr_3)_{0.1}$ (FAMA) [26, 80] and formamidinium lead triiodide – methylammonium lead tribromide – caesium lead tribromide $(FAPbI_3)_{0.9}(MAPbBr_3)_{0.05}(CsPbBr_3)_{0.05}$ (CsFAMA) [81], which have made a significant contribution to increase the power conversion efficiency (PCE) in thin-film photovoltaics [47, 79, 182]. The growth of crystals to this day is performed exclusively from solution [23, 26, 56, 62]. Important preparation methods are the cooling acid-based precursor solution crystallisation [22], the inverse temperature crystallisation (ITC) [62], and the antisolvent vapour-assistant crystallisation (AVC) [137]. In the cooling crystallisation, the precursor salts AX and $PbX_2$ are dissolved in an aqueous halogen-containing acid at high temperatures [56]. Controlled and slow cooling finally results in a supersaturated precursor solution, which leads to spontaneous nucleation of crystal nuclei, followed by subsequent crystal growth. The ITC method is based on the inverse or retrograde solubility of a dissociated perovskite in an organic solvent [23, 64]. With increasing temperature, the solubility of the perovskite decreases and mm-sized crystals can be grown within a few hours [23]. In the AVC method, the precursors are also dissolved in an organic solvent as well [137]. By slow evaporation of a so-called antisolvent [137], the solubility of the perovskite in the now present

[10] This chapter is partially based on the section *"Hybrid perovskite crystals: Growth, characterization and application"* from Julian Höcker and Vladimir Dyakonov, which is part of the paper entitled *"Roadmap: Organic-inorganic hybrid perovskite semiconductors and devices"*, published in the Journal APL Materials in 2021, volume 9, pages 28 – 30 (109202).

solvent mixture decreases and it finally precipitates. In addition, there are many other methods with the goal of growing high quality and large crystals in a short period of time [60, 61, 233, 310].

**Current and Future Challenges in the OLTP Crystal Area**

The investigation of high-quality crystals not only offers the advantage of studying the pure perovskite material system, but also that the crystals have fewer lattice defects in contrast to their thin-film counterparts. Their excellent optoelectronic properties range from high carrier mobilities [311], long charge carrier lifetimes [173] and diffusion lengths [83, 173], to high photoconductivity [206], high sensitivity, and high energy radiation [61]. For these reasons, they are already used as semiconducting components in solar cells [149], X-ray- [61], gamma-ray- [312], and photo-detectors [122]. However, there are some challenges on the way from crystal growth to the device prototypes: Many crystallisation methods, such as cooling crystallisation, but also AVC method need much longer period of time for single crystal growth [23]. Moreover, it is difficult to adjust the nucleation rate to grow few, but large-sized crystals [74]. The ITC method can overcome these challenges [23, 64]. However, the inverse solubility effect can be a problem in growing defect-free crystals because the probability of lattice defects is rising with increasing growth temperature [23]. The use of seed crystals to obtain large crystalline solids can also be a problem, as this leads to irregularities in the crystal lattice [26]. Although the ITC method is used in many publications for growing perovskite crystals, its origin, the inverse solubility, has hardly been researched [64, 313]. Therefore, in addition to the requirements of time, temperature, controllable nucleation rate, and the associated crystal size, the background to the respective crystallisation processes must also play an important role for the development of future crystal growth techniques. Moreover, there are many new crystallisation processes that are only valid for growing a specific perovskite, such as for $MAPbCl_3$ [314] or $MAPbI_3$ [60]. Beyond this, another overriding goal must be to pull large-sized hybrid single crystals from the melt rather than from solution, as is already possible with the "Bridgeman method" for the growth of inorganic $CsPbBr_3$ [315], in order to find large-scale applications such as with gallium arsenide and silicon (Si). In addition to the preparative challenges, it is also worth mentioning that the term "single crystal" is often used in publications without confirming this by a detailed X-ray analyses. However, this should be an important part of any research work to exclude discontinuities such as defects, dislocations, and impurities. Furthermore, this aspect is also important with regard to device-relevant optoelectronic parameters. In the literature, there are often strongly deviating values, for example, the charge carrier mobility, which can be determined by time-of-flight, space charge limited current, or Hall effect methods [56, 77]. Similarly, the experimentally determined values of carrier lifetime and diffusion length can vary by up to two orders of magnitude according to the literature [56]. Moreover, many optoelectronic parameters, especially for more complex crystals such as FAMA or CsFAMA are not yet known. Finally, in order to carry out electronic measurements at all, the problem of electrical contact must be solved, as the hybrid crystals are very brittle and can break very quickly. [310]

**Scientific Contribution of this Work to Meet the Challenges**

With the AVC and ITC methods, all methylammonium-based perovskites known from thin-film applications were grown as mm-sized crystals (Chapter 4). Detailed qualitative and quantitative analyses revealed the same stoichiometry of the crystals as their corresponding precursor solution. As already mentioned, it was possible to obtain crystals with a variety of colours and optical band gaps that can serve as photodetectors in the UV-VIS/NIR range by selectively changing the halogen ratio. However, the variation of the halogens does not only

result in a change of the optical properties, but also in an increase of the lattice constant with increasing bromine to chlorine and iodine to bromine ratios, respectively (Figure 70). In addition, the lattice structure changes from a simple cubic lattice [22, 62, 63] for $MAPbCl_3$ and $MAPbBr_3$ to a body-centred tetragonal lattice for $MAPbI_3$ [22, 62].
The number of techniques for growing OLTP single crystals is constantly increasing [58, 60, 77, 180, 316]. The above-mentioned crystallisation techniques can be combined to grow high quality perovskite crystals. A mechanical approach to grow complex and large-sized crystals without the use of seed crystals was realized by the re-fill crystallisation method (RFCM) [26], which is based on the inverse solubility of ITC [64]. By introducing new precursor solution and simultaneously removing depleted solution, it was possible to grow *in-situ* large-sized crystals with excellent structural quality, as confirmed by the out-of-plane X-ray diffraction (XRD) measurement and the rocking curve of a FAMA single crystal in Figure 70. The method not only enables the growth of complex large-sized FAMA and CsFAMA crystals, but it is also superior to the established seed crystal technique, as demonstrated by radiographic measurements of the crystal surface and bulk in Chapter 5 [26]. In order to meet the challenge of electrical contacting, circuit boards were developed that gently contact the crystals to enable electronic measurements (Figure 70).

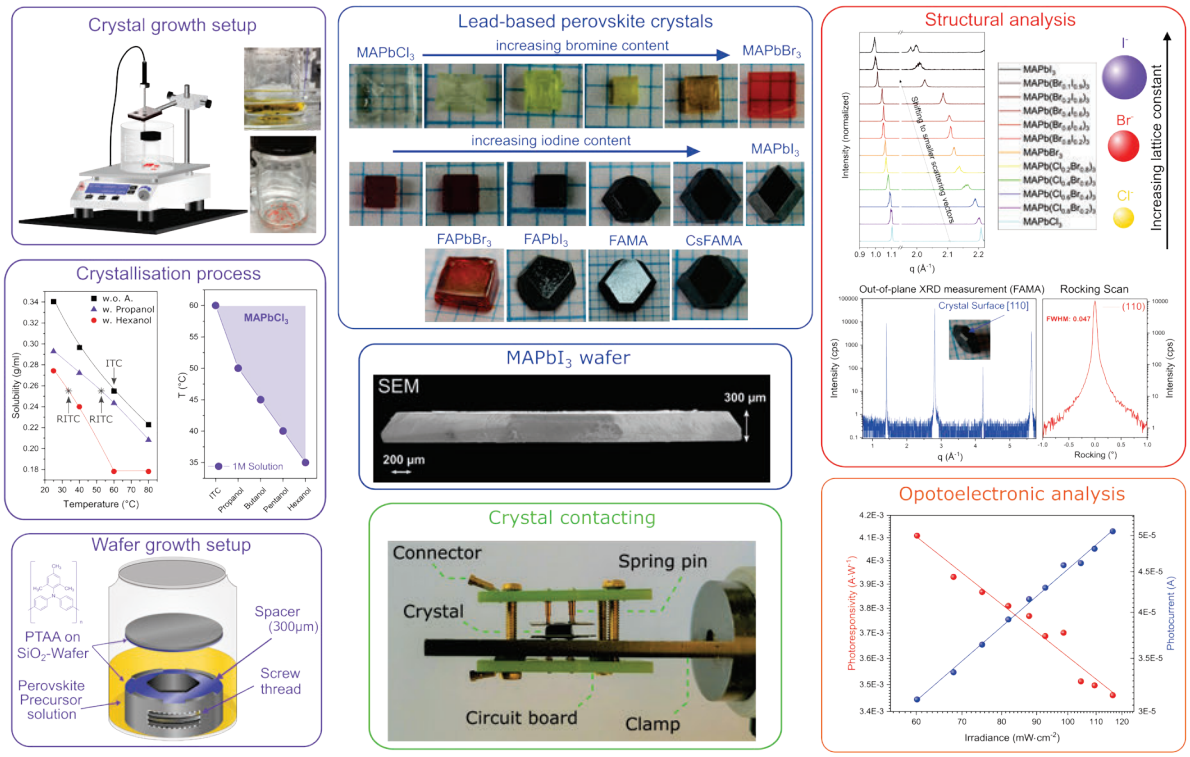


**Figure 70.** (left) Crystal and wafer growth setup to grow mm-sized perovskite single crystals from solution with explanation of the crystallisation processes ITC and RITC. (middle) $MAPbX_3$ crystals with different chlorine/bromine ratio and bromine/iodine content. Due to change in the stoichiometry, it is possible to change the band gap of the crystals. $FAPbX_3$ crystals and the complex crystals FAMA and CsFAMA. SEM image of a $MAPbI_3$ crystal wafer with a maximum thickness of 300 µm. Circuit boards for contacting the perovskite crystals. (right) Powder XRD patterns of $MAPbX_3$ crystals to examine the lattice constants. Out-of-plane XRD measurements of a FAMA single crystal surface with corresponding rocking curve, revealing the high quality of the single crystal. Photocurrent and photoresponsivity in dependence of the irradiance to demonstrate the capability of the $MAPbI_3$ wafer as a photodetector. Reproduced partly from Ref. [310] with permission from APL Materials.

An important contribution to the understanding of the inverse solubility was made by the development of a new crystallisation process, which is called reactive inverse temperature crystallisation (RITC) (Chapter 6). This represents a combination of reactive and inverse temperature crystallisation. By adding a small amount of a primary alcohol to the perovskite

precursor solution, it was possible to drastically reduce the inverse solubility of the perovskite (Figure 70). This was determined by the polarity values of the alcohols, whereby the solubility of the solution dropped with decreasing polarity. The reduction in solubility allowed crystals to grow at much lower temperatures than with the ITC method. In addition, the method is suitable for growing all known OLTPs and allowed the growth of high-quality single crystals, which was confirmed by XRD measurements [23].
In order to use perovskite crystals for photovoltaic applications, just like their corresponding polycrystalline thin films, their thicknesses must be reduced because mm-thick crystals are less suitable for this purpose (Chapter 7). However, before growing µm-thick crystals, polycrystalline $MAPbI_3$ thin films with a few 100 nm were processed on the hole conductor poly[*N*,*N*'-bis(4-butilphenyl) - *N*,*N*'-bis(phenyl)-benzidine] **(**polyTPD) in order to produce efficient solar cells in the following [131]. The achieved results not only offered another important contribution to perovskite thin-film photovoltaics, but the gained knowledge also provided a better understanding for the fabrication of crystal wafers and crystal "films" in the following. Especially the hydrophobic property of poly(triaryl)amines facilitated the handling of $MAPbI_3$ wafers. A self-made setup was used to control the wafer thickness and to grow crystals with a high structural quality. As shown in Figure 70, a crystal wafer can easily be grown on a poly[bis(4-phenyl) (2,4,6-trimethylphenyl) amine] (PTAA)-coated silicon wafer, while the growth height of the crystal is limited by spacers. The grown $MAPbI_3$ wafers with a thickness of a few hundred µm were very promising for the fabrication of photodetectors, which was confirmed by evaluating the photocurrent and photoresponsivity as a function of time (Figure 70). Finally, the thickness of the perovskite crystals $MAPbBr_3$ and $MAPbI_3$ was successfully reduced to only 10 to 15 µm using space-limited RITC. Like the wafers, the crystal "films" also exhibited high structural quality and were used for the construction of a $MAPbI_3$ based solar cell. The evaluation of the characteristic solar cell parameters of the $MAPbI_3$ crystal "film" solar cell provided first promising results and showed the potential to use OLTP crystals for photovoltaic devices, even though the production of the thin perovskite crystal solar cells is still very difficult today. [310]

**Final Remarks**

The field of OLTP single crystals is both inspired and driven by the fact that the most efficient silicon solar cells are made with the highest quality large-area crystalline absorbers. Encouragingly, a power conversion efficiency over 22.8 % for solar cells based on the mixed cation perovskite $FA_{0.6}MA_{0.4}PbI_3$ was reported recently [299]. Interestingly, other major activities in the field are focused on single-crystal-based X-ray- [317], gamma-ray- [312], and photo-detectors [122], which show promising performance in terms of sensitivity, response speed, and lowest detectable dose rate. In the future, large-area single crystalline wafers with controlled thickness are logically expected to come into focus. One of the possible barriers for studying optoelectronic properties even in high-quality crystals remains ion migration with the resulting complex electric field distribution, which is a similar problem as known for perovskite thin films and devices [215]. It should further be noted that a general goal of growing large-sized crystals with a complex composition must be done together with a critical evaluation of the term "single crystal" in relation to these crystals. On the other hand, the crystallographic and stoichiometric qualities alone do not allow any conclusions about the "electronic quality", which should also be verified. Nevertheless, the development of large-area, highly crystalline, and low-defect density perovskites remains an important platform to design the easy-to-grow and highly functional materials on the one hand, and further to understand their optoelectronic properties on the other hand, enabling new applications beyond what scientists are mainly dealing with to date. [310]

# Zusammenfassung

### Übersicht über das Feld der Organobleitrihalogenid Perowskite

Die Untersuchung von Perowskit-Einkristallen mit hoher kristallographischer Qualität ist ein wichtiger technologischer Bereich der Perowskit-Forschung, der es ermöglicht ihr volles optoelektronisches Potenzial abzuschätzen und damit ihre künftigen Anwendungen zu fördern [26]. Es war daher von entscheidender Bedeutung, qualitativ hochwertige Einkristalle mit niedrigsten strukturellen und chemischen Defektdichten und mit einer für ihre Dünnschicht-Pendants relevanten Stöchiometrie zu züchten [26]. Optoelektronische Bauelemente, z. B. Solarzellen, sind hochkomplexe Systeme bei denen die Eigenschaften der aktiven Schicht (Absorber) stark von den angrenzenden Schichten beeinflusst werden, sodass es nicht immer einfach ist, die angestrebten Eigenschaften zu definieren und die Gestaltung der aktiven Schicht festzulegen. Gegenwärtig sind die Einkristalle bestehend aus Organobleitrihalogenid-Perowskiten mit der Struktur $ABX_3$ eines der am besten untersuchten kristallinen Systeme. Bei diesen Hybridkristallen handelt es sich um Festkörper, die aus einem organischen Kation wie Methylammonium ($A = MA^+$) oder Formamidinium ($A = FA^+$) bestehen und zusammen mit dem Blei Kation ($B = Pb_2^+$) und einem Halogenid-Ion wie Chlor, Brom oder Iod ($X = Cl^-$, $Br^-$ oder $I^-$) ein dreidimensionales periodisches Gitter bilden [23]. Dazu gehören Methylammoniumbleitribromid ($MAPbBr_3$) und Methylammoniumbleitriiodid ($MAPbI_3$) sowie Methylammoniumbleitrichlorid ($MAPbCl_3$) [62, 63]. Wichtige Vertreter mit dem größeren Kation $FA^+$ sind Formamidiniumbleitribromid ($FAPbBr_3$) und Formamidiniumbleitriiodid ($FAPbI_3$) [23, 64]. Neben dem Austausch von Kationen und Anionen war es möglich Kristalle zu züchten, die zwei Halogene enthielten, um Mischkristalle mit unterschiedlichen Verhältnissen von Chlor zu Brom und Brom zu Iod zu erhalten, wie in Abbildung 70 zu sehen ist. Durch Variation des Mischungsverhältnisses der Halogene ist es also möglich die Farbe und damit die Absorptionseigenschaften der Kristalle zu variieren [85], wie es auch bei dünnen polykristallinen Perowskitfilmen möglich ist. Darüber hinaus ist es seit einigen Jahren möglich, komplexe Kristalle zu züchten, die sowohl mehrere Kationen als auch Anionen enthalten [26, 80, 81]. Dazu gehören die Perowskite Formamidiniumbleitriiodid – Methylammoniumbleitribromid $(FAPbI_3)_{0.9}(MAPbBr_3)_{0.1}$ (FAMA) [26, 80] und Formamidiniumbleitriiodid – Methylammoniumbleitribromid – Cäsiumbleitribromid $(FAPbI_3)_{0.9}(MAPbBr_3)_{0.05}(CsPbBr_3)_{0.05}$ (CsFAMA) [81], die wesentlich zur Erhöhung der Wirkungsgrade in der Dünnschichtphotovoltaik beigetragen haben [47, 79, 182]. Die Züchtung dieser Kristalle erfolgt bis heute ausschließlich aus Lösungen [23, 26, 56, 62]. Wichtige Präparationsmethoden sind die säurebasierende Kühlungskristallisation aus einer Vorläuferlösung [22], die inverse Temperaturkristallisation (ITC) [62] und die Antisolvent-Kristallisation (AVC) [137]. Bei der Kühlungskristallisation werden die Vorläufersalze AX und $PbX_2$ bei hohen Temperaturen in einer wässrigen halogenhaltigen Säure gelöst [56]. Durch kontrolliertes und langsames Abkühlen entsteht schließlich eine übersättigte Vorläuferlösung, die zur spontanen Keimbildung von Kristallkeimen und anschließendem Kristallwachstum führt. Die ITC-Methode basiert auf der inversen oder retrograden Löslichkeit eines dissoziierten Perowskits in einem organischen Lösungsmittel [23, 64]. Mit steigender Temperatur nimmt die Löslichkeit des Perowskits ab und innerhalb weniger Stunden können mm-große Kristalle gezüchtet werden [23]. Bei der AVC-Methode werden die Vorläufersalze ebenfalls in einem organischen Lösungsmittel gelöst [137]. Durch langsames Verdampfen eines sogenannten Antisolvents [137] nimmt die Löslichkeit des Perowskits in dem nun vorhandenen Lösungsmittelgemisch ab und es fällt schließlich aus. Darüber hinaus gibt es viele weitere

Methoden mit dem Ziel qualitativ hochwertige und große Kristalle in kurzer Zeit zu züchten [60, 61, 233, 310].

**Aktuelle und Zukünftige Herausforderungen im Bereich der Organobleitrihalogenid-Perowskite Kristalle**

Die Untersuchung hochwertiger Kristalle bietet nicht nur den Vorteil, dass das reine Perowskit-Materialsystem untersucht werden kann, sondern auch, dass die Kristalle im Gegensatz zu ihren Dünnschicht-Gegenstücken weniger Gitterfehler aufweisen. Ihre hervorragenden optoelektronischen Eigenschaften reichen von hohen Ladungsträgerbeweglichkeiten [311], langen Ladungsträgerlebensdauern [173] und Diffusionslängen [83, 173], bis hin zu hoher Photoleitfähigkeit [206], hoher Empfindlichkeit und hochenergetischer Strahlung [61]. Aus diesen Gründen werden sie bereits als Halbleiterkomponenten in Solarzellen [149], Röntgen- [61], Gammastrahlen- [312] und Photo-Detektoren [122] eingesetzt. Auf dem Weg von der Kristallzüchtung zu den Prototypen der Bauteile gibt es jedoch einige Herausforderungen: Viele Kristallisationsmethoden, wie die Kühlungskristallisation, aber auch die AVC-Methode, benötigen einen sehr langen Zeitraum für das Einkristallwachstum [23]. Außerdem ist es schwierig die Keimbildungsrate so einzustellen, dass nur wenige aber große Kristalle gezüchtet werden können [74]. Mit der ITC-Methode können diese Herausforderungen überwunden werden [23, 64]. Allerdings kann der inverse Löslichkeitseffekt ein Problem bei der Züchtung defektfreier Kristalle darstellen, da die Wahrscheinlichkeit von Gitterdefekten mit steigender Wachstumstemperatur zunimmt [23]. Die Verwendung von Impfkristallen zur Gewinnung großer kristalliner Festkörper kann ebenfalls ein Problem darstellen, da dies zu Unregelmäßigkeiten im Kristallgitter führt [26]. Obwohl die ITC-Methode in vielen Veröffentlichungen zur Züchtung von Perowskit-Kristallen verwendet wird, ist ihr Ursprung, die inverse Löslichkeit, kaum erforscht [64, 313]. Daher müssen neben den Anforderungen an Zeit, Temperatur, kontrollierbare Keimbildungsrate und die damit verbundene Kristallgröße auch die Hintergründe der jeweiligen Kristallisationsprozesse eine wichtige Rolle für die Entwicklung zukünftiger Kristallzuchttechniken spielen. Darüber hinaus gibt es viele neue Kristallisationsverfahren, die nur für die Züchtung eines bestimmten Perowskits gültig sind, wie z. B. für $MAPbCl_3$ [314] oder $MAPbI_3$ [60]. Deshalb muss ein weiteres übergeordnetes Ziel darin bestehen, großformatige hybride Einkristalle aus der Schmelze und nicht aus der Lösung zu ziehen, wie dies bereits mit der „Bridgeman Methode“ für die Züchtung von anorganischem $CsPbBr_3$ [315] möglich ist, um großtechnische Anwendungen wie mit Galliumarsenid und Silizium (Si) zu finden. Neben den präparativen Herausforderungen ist auch erwähnenswert, dass in Veröffentlichungen häufig der Begriff „Einkristall“ verwendet wird, ohne dies durch eine detaillierte Röntgenanalyse zu bestätigen. Dies sollte jedoch ein wichtiger Teil jeder Forschungsarbeit sein, um Diskontinuitäten wie Defekte, Versetzungen und Verunreinigungen auszuschließen. Zusätzlich ist dieser Aspekt auch im Hinblick auf baurelevante optoelektronische Parameter wichtig. In der Literatur finden sich oft stark abweichende Werte, z. B. für die Ladungsträgerbeweglichkeit, die mit Flugzeit-, Raumladungsbegrenzungsstrom- oder Hall-Effekt-Methoden bestimmt werden kann [56, 77]. Auch die experimentell ermittelten Werte für Ladungsträgerlebensdauer und Diffusionslänge können laut Literatur um bis zu zwei Größenordnungen variieren [56]. Darüber hinaus sind viele optoelektronische Parameter, insbesondere für komplexere Kristalle, wie FAMA oder CsFAMA noch nicht bekannt. Schließlich muss, um überhaupt elektronische Messungen durchführen zu können, das Problem der elektrischen Kontaktierung gelöst werden, da die Hybridkristalle sehr spröde sind und sehr schnell brechen können. [310]

## Wissenschaftlicher Beitrag dieser Arbeit zur Bewältigung der Herausforderungen

Mit den AVC- und ITC-Methoden konnten alle aus der Dünnschichtanwendungen bekannten Perowskite auf Basis von Methylammonium als mm-große Kristalle gezüchtet werden (Kapitel 4). Detaillierte qualitative und quantitative Analysen ergaben die gleichen Stöchiometrie der Kristalle wie die ihrer entsprechenden Vorläuferlösung. Wie bereits erwähnt, war es möglich Kristalle mit einer Vielzahl unterschiedlicher Farben und dementsprechend variierenden Bandlücken zu erhalten, die durch selektive Änderung des Halogenverhältnisses als Photodetektoren im UV-VIS/NIR Bereich dienen könnten. Die Variation der Halogene führt jedoch nicht nur zu einer Veränderung der optischen Eigenschaften, sondern auch zu einer Erhöhung der Gitterkonstante mit zunehmendem Brom/Chlor- bzw. Iod/Brom-Verhältnis (Abbildung 70). Darüber hinaus ändert sich die Gitterstruktur von einem einfachen kubischen Gitter [22, 62, 63] für $MAPbCl_3$ und $MAPbBr_3$ zu einem tetragonal-raumzentrierten Gitter für $MAPbI_3$ [22, 62].
Die Zahl der Verfahren zur Züchtung von OLTP-Einkristallen nimmt ständig zu [58, 60, 77, 180, 316]. Die oben genannten Kristallisationsverfahren können kombiniert werden, um qualitativ hochwertige Perowskitkristalle zu züchten. Ein mechanischer Ansatz zur Züchtung komplexer und großformatiger Kristalle ohne Verwendung von Impfkristallen wurde mit der Wiederauffüllbaren-Kristallisationsmethode (RFCM) [26] realisiert, die auf der inversen Löslichkeit von ITC beruht [64]. Durch das Einleiten einer frischen Vorläuferlösung und die gleichzeitige Entfernung der verbrauchten Lösung war es möglich *in-situ* große Kristalle mit hervorragender struktureller Qualität zu züchten, wie die Röntgenbeugungsmessung (XRD) und die Rocking-Kurve eines FAMA-Einkristalls in Abbildung 70 bestätigen. Die Methode ermöglicht nicht nur die Züchtung komplexer großer FAMA- und CsFAMA-Kristalle, sondern ist auch der etablierten Impfkristalltechnik überlegen, wie die radiographischen Messungen der Kristalloberfläche und des Kristallinneren in Kapitel 5 zeigten [26]. Um die Herausforderung der elektrischen Kontaktierung zu meistern, wurden Leiterplatten entwickelt, die die Kristalle sanft kontaktieren, um so elektronische Messungen zu ermöglichen (Abbildung 70).
Ein wichtiger Beitrag zum Verständnis der inversen Löslichkeit wurde durch die Entwicklung eines neuen Kristallisationsverfahrens geleistet, das als reaktive inverse Temperaturkristallisation (RITC) bezeichnet wird (Kapitel 6). Dabei handelt es sich um eine Kombination aus reaktiver und inverser Temperaturkristallisation. Durch Zugabe einer geringen Menge eines primären Alkohols zur Perowskit-Vorläuferlösung konnte die inverse Löslichkeit des Perowskits drastisch reduziert werden (Abbildung 70). Dies konnte durch die Polaritätswerte der Alkohole bestimmt werden, wobei die Löslichkeit der Lösung mit abnehmender Polarität sank. Durch die geringere Löslichkeit konnten die Kristalle bei viel niedrigeren Temperaturen als mit der ITC-Methode gewachsen werden. Darüber hinaus eignet sich die Methode für die Züchtung aller bekannten bleiorganischen Trihalogenid-Perowskite und ermöglichte die Züchtung von qualitativ hochwertigen Einkristallen, was durch Röntgenmessungen bestätigt wurde [23].
Um Perowskit-Kristalle für photovoltaische Anwendungen zu nutzen, müssen sie wie die entsprechenden polykristallinen Dünnschichten in ihrer Dicke reduziert werden, da mm-dicke Kristalle für diesen Zweck weniger geeignet sind (Kapitel 7). Bevor jedoch µm-dicke Kristalle gezüchtet wurden, wurden polykristalline $MAPbI_3$-Dünnschichten mit einigen 100 nm auf dem Lochleiter Poly[*N*,*N*'-bis(4-butilphenyl) - *N*,*N*'-bis(phenyl)-benzidine] (polyTPD) prozessiert, um im Folgenden effiziente Solarzellen herzustellen [131]. Die erzielten Ergebnisse lieferten nicht nur einen weiteren wichtigen Beitrag zur Perowskit-Dünnschichtphotovoltaik, sondern die gewonnenen Erkenntnisse ermöglichten im Folgenden auch ein besseres Verständnis für die Herstellung von halbleitenden Bauteilen auf Basis von Kristallwafern und Kristall-„Filmen“. Insbesondere die hydrophobe Eigenschaft von Poly(triaryl)aminen erleichterte die

Handhabung von $MAPbI_3$-Wafern. Um die Waferdicke zu kontrollieren und Kristalle mit einer hohen Strukturqualität zu züchten, wurde ein selbst gebauter Aufbau verwendet. Wie in Abbildung 70 zu sehen ist, kann ein Kristallwafer leicht auf einem mit Poly[bis(4-phenyl) (2,4,6-trimethylphenyl) amine] (PTAA)-beschichteten Siliziumwafer gezüchtet werden, wobei die Wachstumshöhe des Kristalls durch Abstandshalter begrenzt ist. Die gewachsenen $MAPbI_3$-Wafer mit einer Dicke von wenigen hundert µm erwiesen sich als sehr vielversprechend für die Herstellung eines Photodetektor-Prototyps, was durch die Auswertung des Photostroms und der Photoresponsivität in Abhängigkeit von der Zeit bestätigt wurde (Abbildung 70). Schließlich gelang es die Dicke der Perowskitkristalle $MAPbBr_3$ und $MAPbI_3$ mit Hilfe der raumbegrenzten RITC-Methode auf nur 10 bis 15 µm zu reduzieren. Wie die Wafer, wiesen auch die Kristall-„Filme“ eine hohe Strukturqualität auf und wurden für die Fabrikation einer $MAPbI_3$-basierten Solarzelle verwendet. Die Auswertung der charakteristischen Solarzellenparameter der $MAPbI_3$-Kristall-„Film“-Solarzelle lieferte erste vielversprechende Ergebnisse und zeigt das Potenzial der Verwendung von Kristallen für photovoltaische Zellen, auch wenn die Herstellung von dünnen Perowskit-Kristall-Solarzellen heute noch sehr schwierig ist. [310]

**Abschließende Bemerkungen**

Der Bereich der OLTP-Einkristalle wird durch die Tatsache inspiriert und vorangetrieben, dass die effizientesten Silizium-Solarzellen mit den hochwertigsten großflächigen kristallinen Absorbern hergestellt werden. Erfreulicherweise wurde kürzlich ein Wirkungsgrad von über 22,8 % für Solarzellen auf der Basis des Mischkation-Perowskits $FA_{0.6}MA_{0.4}PbI_3$ berichtet [299]. Interessanterweise konzentrieren sich andere wichtige Aktivitäten auf diesem Gebiet auf einkristalline Röntgen- [317], Gammastrahlen- [312] und Photo-Detektoren [122], die vielversprechende Leistungen in Bezug auf Empfindlichkeit, Ansprechgeschwindigkeit und niedrigste nachweisbare Dosisleistung zeigen. In Zukunft dürften großflächige einkristalline Wafer mit kontrollierter Dicke in den Fokus rücken. Eines der möglichen Hindernisse für die Untersuchung optoelektronischer Eigenschaften selbst in qualitativ hochwertigen Kristallen bleibt die Ionenmigration mit der daraus resultierenden komplexen Verteilung des elektrischen Feldes, ein ähnliches Problem, wie es für Perowskit-Dünnschichten und -Bauteilen bekannt ist [215]. Ferner ist zu beachten, dass das allgemeine Ziel der Züchtung großflächiger Kristalle mit komplexer Zusammensetzung mit einer kritischen Bewertung des Begriffs „Einkristall“ im Zusammenhang mit diesen Kristallen einhergehen muss. Andererseits lassen die kristallographischen und stöchiometrischen Eigenschaften allein noch keine Rückschlüsse auf die „elektronische Qualität“ zu, die ebenfalls überprüft werden sollte. Nichtsdestotrotz bleibt die Entwicklung großflächiger, hochkristalliner und defektarmer Perowskite eine wichtige Voraussetzung, um einerseits leicht-züchtende und hochfunktionalen Materialien zu entwickeln und andererseits ihre optoelektronischen Eigenschaften zu verstehen, um schließlich neue Anwendungen zu ermöglichen, die über das hinausgehen, womit sich die Wissenschaftler derzeit beschäftigen. [310]

# 9 References


[1] Deutsche Gesellschaft für Kristallwachstum und Kristallzüchtung e.V. (DGKK); *Kristalle - Schlüsselmaterialien für das 21. Jahrhundert*; **2019**; www.dgkk.de, info@dgkk.de.

[2] D. Segal; *Materials for the 21st Century*; 1st ed. (Oxford University Press, Oxford); **2017**; pp. 4, 53-54, 57-59, 61,64.

[3] W. Pape, M. Sengebusch; *Handwörterbuch der griechischen Sprache. Griechisch-deutsches Handwörterbuch (A-K)*; 3rd, 6th imprint (Vieweg & Sohn, Braunschweig); **1914**.

[4] F. Hoffmann; *Faszination Kristalle und Symmetrie*; 1st ed. (Springer Fachmedien Wiesbaden GmbH, Wiesbaden); **2016**; pp. 6-7, 40-42.

[5] W. Pfeifer; *Etymologisches Wörterbuch des Deutschen*; **1993** (digitized and revised version by W. Pfeifer in the Digital Dictionary of the German Language); Available from: https://www.dwds.de/wb/etymwb/Kristall [accessed on 08.09.2021].

[6] S. R. Wenham, M. A. Green; *Silicon solar cells*; Progress in Photovoltaics: Research and Applications; **1996**; 4 (1); 3-33; Available from: https://doi.org/10.1002/(SICI)1099-159X(199601/02)4:1<3::AID-PIP117>3.0.CO;2-S.

[7] B. Mukherjee, S. Simrock, J. Khachan, D. Rybka, R. Romaniuk; *Application of low-cost Gallium Arsenide light-emitting-diodes as kerma dosemeter and fluence monitor for high-energy neutrons*; Radiation Protection Dosimetry; **2007**; 126 (1-4); 256-260; Available from: https://academic.oup.com/rpd/article-abstract/126/1-4/256/1608065?redirectedFrom=fulltext.

[8] X. Duan, Y. Huang, Y. Cui, J. Wang, C. M. Lieber; *Indium phosphide nanowires as building blocks for nanoscale electronic and optoelectronic devices*; Nature; **2001**; 409 (6816); 66-69; Available from: https://doi.org/10.1038/35051047.

[9] A. Wang, J. Zhao, M. A. Green; *24% efficient silicon solar cells*; Applied Physics Letters; **1990**; 57 (6); 602-604; Available from: https://aip.scitation.org/doi/abs/10.1063/1.103610.

[10] W. Metaferia, K. L. Schulte, J. Simon, S. Johnston, A. J. Ptak; *Gallium arsenide solar cells grown at rates exceeding 300μm·h$^{-1}$ by hydride vapor phase epitaxy*; Nature Communications; **2019**; 10 (1); 3361; Available from: https://doi.org/10.1038/s41467-019-11341-3.

[11] E. Bauer, H. Poppa; *Recent advances in epitaxy*; Thin Solid Films; **1972**; 12 (1); 167-185; Available from: https://doi.org/10.1016/0040-6090(72)90412-9.

[12] K. Wang, Y. Gu, H. F. Zhou, L. Y. Zhang, C. Z. Kang, M. J. Wu, W. W. Pan, P. F. Lu, Q. Gong, S. M. Wang; *InPBi Single Crystals Grown by Molecular Beam Epitaxy*; Scientific Reports; **2014**; 4 (1); 5449; Available from: https://doi.org/10.1038/srep05449.

[13] J. Kwo, M. Hong, S. Nakahara; *Growth of rare-earth single crystals by molecular beam epitaxy: The epitaxial relationship between hcp rare earth and bcc niobium*; Applied Physics Letters; **1986**; 49 (6); 319-321; Available from: https://aip.scitation.org/doi/abs/10.1063/1.97155.

[14] H. Katsui, T. Goto; *Epitaxial growth of (104)- and (018)-oriented $LiCoO_2$ films on MgO single crystals prepared by chemical vapor deposition*; Surface and Coatings

Technology; **2013**; 218; 57-61; Available from: https://doi.org/10.1016/j.surfcoat.2012.12.027.

[15] M. Frondel; *Wettbewerb um Ressourcen – Rohstoffe als Trend oder Megatrend?*; editor: D. Bierbaum; In: *So investiert die Welt: Globale Trends in der Vermögensanlage*; 1st ed. (Betriebswirtschaftlicher Verlag Dr. Th. Gabler, GWV Fachverlage GmbH, 2008); **2008**; p. 62.

[16] K. Rave; *Windenergie – die treibende Kraft*; editor: J. Böttcher; In: *Handbuch Windenergie: Onshore-Projekte: Realisierung, Finanzierung, Recht und Technik*; 2nd ed. (De Gruyter Oldenbourg); **2019**; p. 1.

[17] W. Zhang, G. E. Eperon, H. J. Snaith; *Metal halide perovskites for energy applications*; Nature Energy; **2016**; 1 (6); 16048; Available from: https://doi.org/10.1038/nenergy.2016.48.

[18] E. Mosconi, T. Etienne, F. De Angelis, F. Maddalena, P. P. Boix, C. X. Yu, N. Mathews, C. Soci, S. Mhaisalkar, W. Tress; *First-Principles Modeling of Organohalide Thin Films and Interfaces/ Maximum Efficiency and Open-Circuit Voltage of Perovskite Solar Cells/ Charge Transport in Organometal Halide Perovskites*; editor: N.-G. Park, M. Grätzel, T. Miyasaka; In: *Organic-Inorganic Halide Perovskite Photovoltaics - From Fundamentals to Device Architectures*; 1st ed. (Springer International Publishing AG Switzerland); **2016**; pp. V-VI/ 19-20/ 53/ 203, 206, 218.

[19] B. P. Rand, J. Genoe, P. Heremans, J. Poortmans; *Solar cells utilizing small molecular weight organic semiconductors*; Progress in Photovoltaics: Research and Applications; **2007**; 15 (8); 659-676; Available from: https://doi.org/10.1002/pip.788.

[20] H. Dong, C. Wang, W. Hu; *High performance organic semiconductors for field-effect transistors*; Chemical Communications; **2010**; 46 (29); 5211-5222; Available from: http://dx.doi.org/10.1039/C0CC00947D.

[21] D. Weber; *$CH_3NH_3PbX_3$, ein Pb(II)-System mit kubischer Perowskitstruktur / $CH_3NH_3PbX_3$, a Pb(II)-System with Cubic Perovskite Structure*; Zeitschrift für Naturforschung B; **1978**; 33 (12); 1443-1445; Available from: https://www.degruyter.com/document/doi/10.1515/znb-1978-1214/html.

[22] A. Poglitsch, D. Weber; *Dynamic disorder in methylammoniumtrihalogenoplumbates (II) observed by millimeter-wave spectroscopy*; The Journal of Chemical Physics; **1987**; 87 (11); 6373-6378; Available from: https://aip.scitation.org/doi/abs/10.1063/1.453467.

[23] J. Höcker, F. Brust, M. Armer, V. Dyakonov; *A temperature-reduced method for the rapid growth of hybrid perovskite single crystals with primary alcohols*; CrystEngComm; **2021**; 23 (11); 2202-2207; Available from: http://dx.doi.org/10.1039/D0CE01759K.

[24] Y. Chen, S. Liu, N. Zhou, N. Li, H. Zhou, L.-D. Sun, C.-H. Yan; *An overview of rare earth coupled lead halide perovskite and its application in photovoltaics and light emitting devices*; Progress in Materials Science; **2021**; 120; 100737; Available from: https://doi.org/10.1016/j.pmatsci.2020.100737.

[25] Z. Bai, H. Zhong; *Halide perovskite quantum dots: potential candidates for display technology*; Science Bulletin; **2015**; 60 (18); 1622-1624; Available from: https://doi.org/10.1007/s11434-015-0884-y.

[26] J. Höcker, M. Ozcan, S. Hammer, M. Fischer, B. Bichler, M. Armer, P. Rieder, V. Drach, J. Pflaum, B. Nickel, V. Dyakonov; *Seed crystal free growth of high-quality double cation – double halide perovskite single crystals for optoelectronic applications*; Journal of Materials Chemistry C; **2020**; 8 (24); 8275-8283; Available from: http://dx.doi.org/10.1039/D0TC01617A.

[27] G. Rose; *De novis quibusdam fossilibus quae in montibus Uraliis inveniuntur*; **1839** (digitized by MünchnerDigitalisierungszentrum Digitale Bibliothek); Available from:

https://www.digitale-sammlungen.de/de/view/bsb10978561?page=,1 [accessed on 07.09.2021].

[28] G. Rose; *Ueber einige neue Mineralien des Urals*; Journal für Praktische Chemie; **1840**; 19 (1); 459-468; Available from: https://doi.org/10.1002/prac.18400190179.

[29] A. R. Chakhmouradian, P. M. Woodward; *Celebrating 175 years of perovskite research: a tribute to Roger H. Mitchell*; Physics and Chemistry of Minerals; **2014**; 41 (6); 387-391; Available from: https://doi.org/10.1007/s00269-014-0678-9.

[30] D. Weber; *$CH_3NH_3SnBr_xI_{3-x}$ (x = 0-3), ein Sn(II)-System mit kubischer Perowskitstruktur / $CH_3NH_3SnBr_xI_{3-x}$ (x = 0-3), a Sn(II)-System with Cubic Perovskite Structure*; Zeitschrift für Naturforschung B; **1978**; 33; Available from: https://www.degruyter.com/document/doi/10.1515/znb-1978-0809/pdf.

[31] M. Daub, H. Hillebrecht; *Synthesis, Single-Crystal Structure and Characterization of $(CH_3NH_3)_2Pb(SCN)_2I_2$*; Angewandte Chemie International Edition; **2015**; 54 (38); 11016-11017; Available from: https://doi.org/10.1002/anie.201506449.

[32] M. T. Weller, O. J. Weber, J. M. Frost, A. Walsh; *Cubic Perovskite Structure of Black Formamidinium Lead Iodide, $\alpha$-$[HC(NH_2)_2]PbI_3$, at 298 K*; The Journal of Physical Chemistry Letters; **2015**; 6 (16); 3209-3212; Available from: https://doi.org/10.1021/acs.jpclett.5b01432.

[33] M. T. Anderson, K. B. Greenwood, G. A. Taylor, K. R. Poeppelmeier; *B-cation arrangements in double perovskites*; Progress in Solid State Chemistry; **1993**; 22 (3); 197-233; Available from: https://doi.org/10.1016/0079-6786(93)90004-B.

[34] A. H. Slavney, T. Hu, A. M. Lindenberg, H. I. Karunadasa; *A Bismuth-Halide Double Perovskite with Long Carrier Recombination Lifetime for Photovoltaic Applications*; Journal of the American Chemical Society; **2016**; 138 (7); 2138-2141; Available from: https://doi.org/10.1021/jacs.5b13294.

[35] M. Armer, J. Höcker, C. Büchner, S. Häfele, P. Dörflinger, M. Sirtl, K. Tvingstedt, T. Bein, V. Dyakonov; *Influence of crystallisation on structural and optical properties of lead-free $Cs_2AgBiBr_6$ perovskite crystals*; CrystEngComm; **2021**; 23 (39); 6848-6854; Available from: http://dx.doi.org/10.1039/D1CE00844G.

[36] W. Pan, H. Wu, J. Luo, Z. Deng, C. Ge, C. Chen, X. Jiang, W.-J. Yin, G. Niu, L. Zhu, L. Yin, Y. Zhou, Q. Xie, X. Ke, M. Sui, J. Tang; *$Cs_2AgBiBr_6$ single-crystal X-ray detectors with a low detection limit*; Nature Photonics; **2017**; 11 (11); 726-732; Available from: https://doi.org/10.1038/s41566-017-0012-4.

[37] E. Meyer, D. Mutukwa, N. Zingwe, R. Taziwa; *Lead-Free Halide Double Perovskites: A Review of the Structural, Optical, and Stability Properties as Well as Their Viability to Replace Lead Halide Perovskites*; Metals; **2018**; 8 (9); 667; Available from: https://doi.org/10.3390/met8090667.

[38] S. Tao, I. Schmidt, G. Brocks, J. Jiang, I. Tranca, K. Meerholz, S. Olthof; *Absolute energy level positions in tin- and lead-based halide perovskites*; Nature Communications; **2019**; 10 (1); 2560; Available from: https://doi.org/10.1038/s41467-019-10468-7.

[39] D. Ricciarelli, D. Meggiolaro, F. Ambrosio, F. De Angelis; *Instability of Tin Iodide Perovskites: Bulk p-Doping versus Surface Tin Oxidation*; ACS Energy Letters; **2020**; 5 (9); 2787-2795; Available from: https://doi.org/10.1021/acsenergylett.0c01174.

[40] H. Yao, F. Zhou, Z. Li, Z. Ci, L. Ding, Z. Jin; *Strategies for Improving the Stability of Tin-Based Perovskite ($ASnX_3$) Solar Cells*; Advanced Science; **2020**; 7 (10); 1903540; Available from: https://doi.org/10.1002/advs.201903540.

[41] Y. M. Lee, J. Park, B. D. Yu, S. Hong, M.-C. Jung, M. Nakamura; *Surface Instability of Sn-Based Hybrid Perovskite Thin Film, $CH_3NH_3SnI_3$: The Origin of Its Material*

*Instability*; The Journal of Physical Chemistry Letters; **2018**; 9 (9); 2293-2297; Available from: https://doi.org/10.1021/acs.jpclett.8b00494.

[42] W. Gao, C. Ran, J. Xi, B. Jiao, W. Zhang, M. Wu, X. Hou, Z. Wu; *High-Quality $Cs_2AgBiBr_6$ Double Perovskite Film for Lead-Free Inverted Planar Heterojunction Solar Cells with 2.2% Efficiency*; ChemPhysChem; **2018**; 19 (14); 1696-1700; Available from: https://doi.org/10.1002/cphc.201800346.

[43] R. L. Z. Hoye, L. Eyre, F. Wei, F. Brivio, A. Sadhanala, S. Sun, W. Li, K. H. L. Zhang, J. L. MacManus-Driscoll, P. D. Bristowe, R. H. Friend, A. K. Cheetham, F. Deschler; *Fundamental Carrier Lifetime Exceeding 1μs in $Cs_2AgBiBr_6$ Double Perovskite*; Advanced Materials Interfaces; **2018**; 5 (15); 1800464; Available from: https://doi.org/10.1002/admi.201800464.

[44] N. K. Tailor, M. Abdi-Jalebi, V. Gupta, H. Hu, M. I. Dar, G. Li, S. Satapathi; *Recent progress in morphology optimization in perovskite solar cell*; Journal of Materials Chemistry A; **2020**; 8 (41); 21356-21386; Available from: http://dx.doi.org/10.1039/D0TA00143K.

[45] J. Chung, S. S. Shin, K. Hwang, G. Kim, K. W. Kim, D. S. Lee, W. Kim, B. S. Ma, Y.-K. Kim, T.-S. Kim, J. Seo; *Record-efficiency flexible perovskite solar cell and module enabled by a porous-planar structure as an electron transport layer*; Energy & Environmental Science; **2020**; 13 (12); 4854-4861; Available from: http://dx.doi.org/10.1039/D0EE02164D.

[46] H. Zhu, Z. Shen, L. Pan, J. Han, F. T. Eickemeyer, Y. Ren, X. Li, S. Wang, H. Liu, X. Dong, S. M. Zakeeruddin, A. Hagfeldt, Y. Liu, M. Grätzel; *Low-Cost Dopant Additive-Free Hole-Transporting Material for a Robust Perovskite Solar Cell with Efficiency Exceeding 21%*; ACS Energy Letters; **2021**; 6 (1); 208-215; Available from: https://doi.org/10.1021/acsenergylett.0c02210.

[47] M. Saliba, J.-P. Correa-Baena, C. M. Wolff, M. Stolterfoht, N. Phung, S. Albrecht, D. Neher, A. Abate; *How to make over 20% efficient perovskite solar cells in regular (n-i-p) and inverted (p-i-n) architectures*; Chemistry of Materials; **2018**; Available from: https://doi.org/10.1021/acs.chemmater.8b00136.

[48] W. Shockley, H. J. Queisser; *Detailed Balance Limit of Efficiency of p-n Junction Solar Cells*; Journal of Applied Physics; **1961**; 32 (3); 510-519; Available from: https://aip.scitation.org/doi/abs/10.1063/1.1736034.

[49] W. E. I. Sha, X. Ren, L. Chen, W. C. H. Choy; *The efficiency limit of $CH_3NH_3PbI_3$ perovskite solar cells*; Applied Physics Letters; **2015**; 106 (22); 221104; Available from: https://aip.scitation.org/doi/abs/10.1063/1.4922150.

[50] W. Demtröder; *Experimentalphysik 3 - Atome, Moleküle und Festkörper*; 4th ed. (Springer-Verlag Berlin, Heidelberg, New York); **2010**; pp. 14-15, 253-256, 261, 263, 403-416, 423-427.

[51] H. Van Swygenhoven; *Polycrystalline materials. Grain boundaries and dislocations*; Science; **2002**; 296 (5565); 66-67; Available from: https://www.science.org/doi/abs/10.1126/science.1071040.

[52] C. R. M. Grovenor; *Grain boundaries in semiconductors*; Journal of Physics C: Solid State Physics; **1985**; 18 (21); 4079-4119; Available from: http://dx.doi.org/10.1088/0022-3719/18/21/008.

[53] J.-W. Lee, S.-H. Bae, N. De Marco, Y.-T. Hsieh, Z. Dai, Y. Yang; *The role of grain boundaries in perovskite solar cells*; Materials Today Energy; **2018**; 7; 149-160; Available from: https://doi.org/10.1016/j.mtener.2017.07.014.

[54] A.-F. Castro-Méndez, J. Hidalgo, J.-P. Correa-Baena; *The Role of Grain Boundaries in Perovskite Solar Cells*; Advanced Energy Materials; **2019**; 9 (38); 1901489; Available from: https://doi.org/10.1002/aenm.201901489.

[55] Y. Liu, X. Ren, J. Zhang, Z. Yang, D. Yang, F. Yu, J. Sun, C. Zhao, Z. Yao, B. Wang, Q. Wei, F. Xiao, H. Fan, H. Deng, L. Deng, S. F. J. S. C. C. Liu; *120 mm single-crystalline perovskite and wafers: towards viable applications*; **2017**; 60 (10); 1367-1376; Available from: https://doi.org/10.1007/s11426-017-9081-3.

[56] Y. Liu, Z. Yang, S. Liu; *Recent Progress in Single-Crystalline Perovskite Research Including Crystal Preparation, Property Evaluation, and Applications*; Advanced Science; **2018**; 5 (1); 1700471; Available from: https://onlinelibrary.wiley.com/doi/abs/10.1002/advs.201700471.

[57] J. Ding, Q. Yan; *Progress in organic-inorganic hybrid halide perovskite single crystal: growth techniques and applications*; Science China Materials; **2017**; 60 (11); 1063-1078; Available from: https://doi.org/10.1007/s40843-017-9039-8.

[58] Y. Dang, D. Ju, L. Wang, X. Tao; *Recent progress in the synthesis of hybrid halide perovskite single crystals*; CrystEngComm; **2016**; 18 (24); 4476-4484; Available from: http://dx.doi.org/10.1039/C6CE00655H.

[59] Y. Dang, Y. Liu, Y. Sun, D. Yuan, X. Liu, W. Lu, G. Liu, H. Xia, X. Tao; *Bulk crystal growth of hybrid perovskite material $CH_3NH_3PbI_3$*; CrystEngComm; **2015**; 17 (3); 665-670; Available from: https://doi.org/10.1039/C4CE02106A.

[60] R. Gupta, T. B. Korukonda, S. K. Gupta, B. P. Dhamaniya, P. Chhillar, R. Datt, P. Vashishtha, G. Gupta, V. Gupta, R. Srivastava, S. Pathak; *Room temperature synthesis of perovskite ($MAPbI_3$) single crystal by anti-solvent assisted inverse temperature crystallization method*; Journal of Crystal Growth; **2020**; 537; 125598; Available from: https://doi.org/10.1016/j.jcrysgro.2020.125598.

[61] F. Yao, J. Peng, R. Li, W. Li, P. Gui, B. Li, C. Liu, C. Tao, Q. Lin, G. Fang; *Room-temperature liquid diffused separation induced crystallization for high-quality perovskite single crystals*; Nature Communications; **2020**; 11 (1); 1194; Available from: https://doi.org/10.1038/s41467-020-15037-x.

[62] M. I. Saidaminov, A. L. Abdelhady, B. Murali, E. Alarousu, V. M. Burlakov, W. Peng, I. Dursun, L. Wang, Y. He, G. Maculan, A. Goriely, T. Wu, O. F. Mohammed, O. M. Bakr; *High-quality bulk hybrid perovskite single crystals within minutes by inverse temperature crystallization*; Nature Communications; **2015**; 6; 7586; Available from: https://doi.org/10.1038/ncomms8586.

[63] G. Maculan, A. D. Sheikh, A. L. Abdelhady, M. I. Saidaminov, M. A. Haque, B. Murali, E. Alarousu, O. F. Mohammed, T. Wu, O. M. Bakr; *$CH_3NH_3PbCl_3$ Single Crystals: Inverse Temperature Crystallization and Visible-Blind UV-Photodetector*; The Journal of Physical Chemistry Letters; **2015**; 6 (19); 3781-3786; Available from: https://doi.org/10.1021/acs.jpclett.5b01666.

[64] M. I. Saidaminov, A. L. Abdelhady, G. Maculan, O. M. Bakr; *Retrograde solubility of formamidinium and methylammonium lead halide perovskites enabling rapid single crystal growth*; Chemical Communications; **2015**; 51 (100); 17658-17661; Available from: http://dx.doi.org/10.1039/C5CC06916E.

[65] H. Kim, H. R. Byun, M. S. Jeong; *Synthesis and Characterization of Multiple-Cation $Rb(MAFA)PbI_3$ Perovskite Single Crystals*; Scientific Reports; **2019**; 9 (1); 2022; Available from: https://doi.org/10.1038/s41598-019-38947-3.

[66] W. Borchardt-Ott, H. Sowa; *Kristallographie - Eine Einführung für Studierende der Naturwissenschaften*; 9th ed. (Springer-Verlag, Berlin, Heidelberg); **2018**; pp. 11-19, 25, 33-37.

[67] R. Gross, A. Marx; *Festkörper-Physik*; 2nd ed. (Walter de Gruyter GmbH, Berlin, Boston); **2014**; pp. 3-6, 10-11, 14-21.

[68] E. Schweda; *Jander/Blasius Anorganische Chemie I Theoretische Grundlagen und Qualitative Analyse*; 18th ed. (S. Hirzel Verlag, Stuttgart); **2016**; pp. 44-49.

[69] Z. Fan, K. Sun, J. Wang; *Perovskites for photovoltaics: a combined review of organic–inorganic halide perovskites and ferroelectric oxide perovskites*; Journal of Materials Chemistry A; **2015**; 3 (37); 18809-18828; Available from: http://dx.doi.org/10.1039/C5TA04235F.

[70] T. J. Jacobsson, M. Pazoki, A. Hagfeldt, T. Edvinsson; *Goldschmidt's Rules and Strontium Replacement in Lead Halogen Perovskite Solar Cells: Theory and Preliminary Experiments on $CH_3NH_3SrI_3$*; The Journal of Physical Chemistry C; **2015**; 119 (46); 25673-25683; Available from: https://doi.org/10.1021/acs.jpcc.5b06436.

[71] C. Li, X. Lu, W. Ding, L. Feng, Y. Gao, Z. Guo; *Formability of $ABX_3$ (X = F, Cl, Br, I) halide perovskites*; Acta Crystallographica Section B; **2008**; 64 (6); 702-707; Available from: https://doi.org/10.1107/S0108768108032734.

[72] G. Kieslich, S. Sun, A. K. Cheetham; *Solid-state principles applied to organic–inorganic perovskites: new tricks for an old dog*; Chemical Science; **2014**; 5 (12); 4712-4715; Available from: http://dx.doi.org/10.1039/C4SC02211D.

[73] G. Kieslich, S. Sun, A. K. Cheetham; *An extended Tolerance Factor approach for organic–inorganic perovskites*; Chemical Science; **2015**; 6 (6); 3430-3433; Available from: http://dx.doi.org/10.1039/C5SC00961H.

[74] S. Li, C. Zhang, J.-J. Song, X. Xie, J.-Q. Meng, S. Xu; *Metal Halide Perovskite Single Crystals: From Growth Process to Application*; Crystals; **2018**; 8 (5); 220; Available from: https://www.mdpi.com/2073-4352/8/5/220.

[75] N. K. Kumawat, A. Dey, A. Kumar, S. P. Gopinathan, K. L. Narasimhan, D. Kabra; *Band Gap Tuning of $CH_3NH_3Pb(Br_{1-x}Cl_x)_3$ Hybrid Perovskite for Blue Electroluminescence*; ACS Applied Materials & Interfaces; **2015**; 7 (24); 13119-13124; Available from: https://doi.org/10.1021/acsami.5b02159.

[76] X. Zhang, F. Li, R. Zheng; *Growth and optimization of hybrid perovskite single crystals for optoelectronics/electronics and sensing*; Journal of Materials Chemistry C; **2020**; 8 (40); 13918-13952; Available from: http://dx.doi.org/10.1039/D0TC00473A.

[77] R. Babu, L. Giribabu, S. P. Singh; *Recent Advances in Halide-Based Perovskite Crystals and Their Optoelectronic Applications*; Crystal Growth & Design; **2018**; 18 (4); 2645-2664; Available from: https://doi.org/10.1021/acs.cgd.7b01767.

[78] S. A. Kulkarni, T. Baikie, P. P. Boix, N. Yantara, N. Mathews, S. Mhaisalkar; *Band-gap tuning of lead halide perovskites using a sequential deposition process*; Journal of Materials Chemistry A; **2014**; 2 (24); 9221-9225; Available from: http://dx.doi.org/10.1039/C4TA00435C.

[79] M. Saliba, T. Matsui, J.-Y. Seo, K. Domanski, J.-P. Correa-Baena, M. K. Nazeeruddin, S. M. Zakeeruddin, W. Tress, A. Abate, A. Hagfeldt, M. Gratzel; *Cesium-containing triple cation perovskite solar cells: improved stability, reproducibility and high efficiency*; Energy & Environmental Science; **2016**; 9 (6); 1989-1997; Available from: http://dx.doi.org/10.1039/C5EE03874J.

[80] L.-Q. Xie, L. Chen, Z.-A. Nan, H.-X. Lin, T. Wang, D.-P. Zhan, J.-W. Yan, B.-W. Mao, Z.-Q. Tian; *Understanding the Cubic Phase Stabilization and Crystallization Kinetics in Mixed Cations and Halides Perovskite Single Crystals*; Journal of the American Chemical Society; **2017**; 139 (9); 3320-3323; Available from: https://doi.org/10.1021/jacs.6b12432.

[81] L. Chen, Y.-Y. Tan, Z.-X. Chen, T. Wang, S. Hu, Z.-A. Nan, L.-Q. Xie, Y. Hui, J.-X. Huang, C. Zhan, S.-H. Wang, J.-Z. Zhou, J.-W. Yan, B.-W. Mao, Z.-Q. Tian; *Toward Long-Term Stability: Single-Crystal Alloys of Cesium-Containing Mixed Cation and Mixed Halide Perovskite*; Journal of the American Chemical Society; **2019**; 141 (4); 1665-1671; Available from: https://doi.org/10.1021/jacs.8b11610.

[82] P. S. Whitfield, N. Herron, W. E. Guise, K. Page, Y. Q. Cheng, I. Milas, M. K. Crawford; *Structures, Phase Transitions and Tricritical Behavior of the Hybrid Perovskite Methyl Ammonium Lead Iodide*; Scientific Reports; **2016**; 6 (1); 35685; Available from: https://doi.org/10.1038/srep35685.

[83] A. A. Zhumekenov, M. I. Saidaminov, M. A. Haque, E. Alarousu, S. P. Sarmah, B. Murali, I. Dursun, X.-H. Miao, A. L. Abdelhady, T. Wu, O. F. Mohammed, O. M. Bakr; *Formamidinium Lead Halide Perovskite Crystals with Unprecedented Long Carrier Dynamics and Diffusion Length*; ACS Energy Letters; **2016**; 1 (1); 32-37; Available from: https://doi.org/10.1021/acsenergylett.6b00002.

[84] C. Witt, A. Schmid, N. Leupold, M. Schultz, J. Höcker, A. Baumann, R. Moos, F. Panzer; *Impact of Pressure and Temperature on the Compaction Dynamics and Layer Properties of Powder-Pressed Methylammonium Lead Halide Thick Films*; ACS Applied Electronic Materials; **2020**; 2 (8); 2619-2628; Available from: https://doi.org/10.1021/acsaelm.0c00493.

[85] W. Wang, J. Su, L. Zhang, Y. Lei, D. Wang, D. Lu, Y. Bai; *Growth of mixed-halide perovskite single crystals*; CrystEngComm; **2018**; 20 (12); 1635-1643; Available from: http://dx.doi.org/10.1039/C7CE01691C.

[86] K. Momma, F. Izumi; *VESTA 3 for three-dimensional visualization of crystal, volumetric and morphology data*; Journal of Applied Crystallography; **2011**; 44 (6); 1272-1276; Available from: https://doi.org/10.1107/S0021889811038970.

[87] Y. Zhang, M. Lyu, T. Qiu, E. Han, I. K. Kim, M.-C. Jung, Y. H. Ng, J.-H. Yun, L. Wang; *Halide Perovskite Single Crystals: Optoelectronic Applications and Strategical Approaches*; Energies; **2020**; 13 (16); 4250; Available from: https://www.mdpi.com/1996-1073/13/16/4250.

[88] G. W. A. Milne; *Software Review of ChemBioDraw 12.0*; Journal of Chemical Information and Modeling; **2010**; 50 (11); 2053-2053; Available from: https://doi.org/10.1021/ci100385n.

[89] V. M. Goldschmidt; *Die Gesetze der Krystallochemie*; Naturwissenschaften; **1926**; 14 (21); 477-485; Available from: https://doi.org/10.1007/BF01507527.

[90] R. D. Shannon, C. T. Prewitt; *Effective ionic radii in oxides and fluorides*; Acta Crystallographica Section B; **1969**; 25 (5); 925-946; Available from: https://doi.org/10.1107/S0567740869003220.

[91] R. D. Shannon; *Revised effective ionic radii and systematic studies of interatomic distances in halides and chalcogenides*; Acta Crystallographica Section A; **1976**; 32 (5); 751-767; Available from: https://doi.org/10.1107/S0567739476001551.

[92] J. Hulliger; *Chemistry and Crystal Growth*; Angewandte Chemie International Edition in English; **1994**; 33 (2); 143-162; Available from: https://doi.org/10.1002/anie.199401431.

[93] J. M. Kadro, K. Nonomura, D. Gachet, M. Grätzel, A. Hagfeldt; *Facile route to freestanding $CH_3NH_3PbI_3$ crystals using inverse solubility*; Scientific Reports; **2015**; 5 (1); 11654; Available from: https://doi.org/10.1038/srep11654.

[94] I. N. Stranski, L. Krastanow; *Zur Theorie der orientierten Ausscheidung von Ionenkristallen aufeinander*; Monatshefte für Chemie und verwandte Teile anderer Wissenschaften; **1937**; 71 (1); 351-364; Available from: https://doi.org/10.1007/BF01798103.

[95] G. Wedler, H.-J. Freund; *Lehrbuch der Physikalischen Chemie*; 6th ed. (Wiley-VCH Verlag GmbH & Co. KGaA, Weinheim); **2012**; pp. 635-636, 1010-1011.

[96] P. K. Nayak, D. T. Moore, B. Wenger, S. Nayak, A. A. Haghighirad, A. Fineberg, N. K. Noel, O. G. Reid, G. Rumbles, P. Kukura, K. A. Vincent, H. J. Snaith; *Mechanism for rapid growth of organic–inorganic halide perovskite crystals*; Nature

Communications; **2016**; 7 (1); 13303; Available from: https://doi.org/10.1038/ncomms13303.

[97] Y. Leng; *Materials Characterization - Introduction to Microscopic and Spectroscopic Methods*; 2nd ed. (Wiley-VCH Verlag GmbH & Co. KGaA, Weinheim); **2013**; pp. 47-50, 52-53, 62-67, 191-196.

[98] L. Spieß, G. Teichert, R. Schwarzer, H. Behnken, C. Genzel; *Moderne Röntgenbeugung - Röntgendiffraktometrie für Materialwissenschaftler, Physiker und Chemiker*; 2nd ed. (Vieweg+Teubner Verlag, Springer Fachmedien Wiesbaden GmbH, Wiesbaden); **2009**; pp. 90-91.

[99] V. Drach; *Einführung in die Physik der Funktionswerkstoffe*; University of Würzburg; **2020**, University Lecture.

[100] A. L. Abdelhady, M. I. Saidaminov, B. Murali, V. Adinolfi, O. Voznyy, K. Katsiev, E. Alarousu, R. Comin, I. Dursun, L. Sinatra, E. H. Sargent, O. F. Mohammed, O. M. Bakr; *Heterovalent Dopant Incorporation for Bandgap and Type Engineering of Perovskite Crystals*; The Journal of Physical Chemistry Letters; **2016**; 7 (2); 295-301; Available from: https://doi.org/10.1021/acs.jpclett.5b02681.

[101] P. Schmidt; *Interpretation of small-angle scattering curves proportional to a negative power of the scattering vector*; Journal of Applied Crystallography; **1982**; 15 (5); 567-569; Available from: https://doi.org/10.1107/S002188988201259X.

[102] W. Kleber, H.-J. Bautsch, J. Bohm, I. Kleber; *Einführung in die Kristallographie*; 13th ed. (VEB Verlag Technik, Berlin); **1977**; pp. 360-361.

[103] M. Mantler; *Fundamental Parameter Equations for Bulk Materials*; editor: B. Beckhoff, B. Kanngießer, N. Langhoff, R. Wedell, H. Wolff; In: *Handbook of Practical X-Ray Fluorescence Analysis*; 1st ed. (Springer-Verlag, Berlin, Heidelberg, New York); **2006**; pp. 316-317.

[104] J. Kirz, D. Attwood, B. Henke, M. Howells, K. Kennedy, K. Kim, J. Kortright, R. Perera, P. Pianetta, J. Riordan, J. Scofield, G. Stradling, A. Thompson, J. Underwood, D. Vaughan, G. Williams, H. Winick; *Center for X-ray Optics and Advanced Light Source - X-ray Data Booklet*; 3rd ed. (Lawrence Berkeley Laboratory, University of California, Berkeley); **2009**; pp. 9-14.

[105] D. Abou-Ras, T. Kirchartz, U. Rau; *Advanced Characterization Techniques for Thin Film Solar Cells*; 1st ed. (Wiley-VCH Verlag GmbH & Co. KGaA, Weinheim); **2011**; pp. 305-307.

[106] V-650 UV-VIS Spectrophotometer - A high resolution instrument for today's laboratory; JASCO Deutschland GmbH; Available from: https://www.jasco.de/en/content/V-650/~nm.13~nc.407/V-650-UV-VIS-Spectrophotometer.html [accessed on 01.09.2021].

[107] M. Bass, E. W. Van Stryland, D. R. Williams, W. L. Wolfe; *Handbook of Optics - Devices, Measurements, & Properties*; 2nd ed. (McGrwa-Hill, Inc., United States of America); (Subchapters, 25.3-25.5, 25.8); **1995**; pp. 894-895, 899.

[108] B. D. Viezbicke, S. Patel, B. E. Davis, D. P. Birnie III; *Evaluation of the Tauc method for optical absorption edge determination: ZnO thin films as a model system*; physica status solidi (b); **2015**; 252 (8); 1700-1710; Available from: https://doi.org/10.1002/pssb.201552007.

[109] J. Tauc, R. Grigorovici, A. Vancu; *Optical Properties and Electronic Structure of Amorphous Germanium*; physica status solidi (b); **1966**; 15 (2); 627-637; Available from: https://doi.org/10.1002/pssb.19660150224.

[110] J. Tauc; *Absorption edge and internal electric fields in amorphous semiconductors*; Materials Research Bulletin; **1970**; 5 (8); 721-729; Available from: https://doi.org/10.1016/0025-5408(70)90112-1.

[111] J. H. Noh, S. H. Im, J. H. Heo, T. N. Mandal, S. I. Seok; *Chemical Management for Colorful, Efficient, and Stable Inorganic–Organic Hybrid Nanostructured Solar Cells*; Nano Letters; **2013**; 13 (4); 1764-1769; Available from: https://doi.org/10.1021/nl400349b.

[112] E. A. Davis, N. F. Mott; *Conduction in non-crystalline systems V. Conductivity, optical absorption and photoconductivity in amorphous semiconductors*; The Philosophical Magazine: A Journal of Theoretical Experimental and Applied Physics; **1970**; 22 (179); 0903-0922; Available from: https://doi.org/10.1080/14786437008221061.

[113] X. Li, H. Zhu, J. Wei, K. Wang, E. Xu, Z. Li, D. Wu; *Determination of band gaps of self-assembled carbon nanotube films using Tauc/Davis–Mott model*; Applied Physics A; **2009**; 97 (2); 341-344; Available from: https://doi.org/10.1007/s00339-009-5330-z.

[114] S. M. Sze; *Semiconductor devices, physics and technology*; W. Zobrist, S. Russell, editors; 2nd ed. (John Wiley & Sons, New York); **1985/2002**; pp. 311, 538.

[115] J. Huang, Y. Shao, Q. Dong; *Organometal Trihalide Perovskite Single Crystals: A Next Wave of Materials for 25% Efficiency Photovoltaics and Applications Beyond?*; The Journal of Physical Chemistry Letters; **2015**; 6 (16); 3218-3227; Available from: https://doi.org/10.1021/acs.jpclett.5b01419.

[116] L. Sun, W. Li, W. Zhu, Z. Chen; *Single-crystal perovskite detectors: development and perspectives*; Journal of Materials Chemistry C; **2020**; 8 (34); 11664-11674; Available from: http://dx.doi.org/10.1039/D0TC02944K.

[117] J. Gao, Q. Liang, G. Li, T. Ji, Y. Liu, M. Fan, Y. Hao, S. Liu, Y. Wu, Y. Cui; *Single-crystalline lead halide perovskite wafers for high performance photodetectors*; Journal of Materials Chemistry C; **2019**; 7 (27); 8357-8363; Available from: http://dx.doi.org/10.1039/C9TC01309A.

[118] Q. Chen, N. De Marco, Y. Yang, T.-B. Song, C.-C. Chen, H. Zhao, Z. Hong, H. Zhou, Y. Yang; *Under the spotlight: The organic–inorganic hybrid halide perovskite for optoelectronic applications*; Nano Today; **2015**; 10 (3); 355-396; Available from: https://doi.org/10.1016/j.nantod.2015.04.009.

[119] J. Li, J. Dagar, O. Shargaieva, M. A. Flatken, H. Köbler, M. Fenske, C. Schultz, B. Stegemann, J. Just, D. M. Többens, A. Abate, R. Munir, E. Unger; *20.8% Slot-Die Coated $MAPbI_3$ Perovskite Solar Cells by Optimal DMSO-Content and Age of 2-ME Based Precursor Inks*; Advanced Energy Materials; **2021**; 11 (10); 2003460; Available from: https://doi.org/10.1002/aenm.202003460.

[120] K. Miyano, N. Tripathi, M. Yanagida, Y. Shirai; *Lead Halide Perovskite Photovoltaic as a Model p–i–n Diode*; Accounts of Chemical Research; **2016**; 49 (2); 303-310; Available from: https://doi.org/10.1021/acs.accounts.5b00436.

[121] J. Wu, J. Shi, Y. Li, H. Li, H. Wu, Y. Luo, D. Li, Q. Meng; *Quantifying the Interface Defect for the Stability Origin of Perovskite Solar Cells*; Advanced Energy Materials; **2019**; 9 (37); 1901352; Available from: https://doi.org/10.1002/aenm.201901352.

[122] Y. Liu, Y. Zhang, Z. Yang, D. Yang, X. Ren, L. Pang, S. Liu; *Thinness- and Shape-Controlled Growth for Ultrathin Single-Crystalline Perovskite Wafers for Mass Production of Superior Photoelectronic Devices*; Advanced Materials; **2016**; 28 (41); 9204-9209; Available from: https://doi.org/10.1002/adma.201601995.

[123] J. Feng, X. Yan, Y. Liu, H. Gao, Y. Wu, B. Su, L. Jiang; *Crystallographically Aligned Perovskite Structures for High-Performance Polarization-Sensitive Photodetectors*; Advanced Materials; **2017**; 29 (16); 1605993; Available from: https://doi.org/10.1002/adma.201605993.

[124] J. Ding, L. Jing, X. Cheng, Y. Zhao, S. Du, X. Zhan, H. Cui; *Design Growth of $MAPbI_3$ Single Crystal with (220) Facets Exposed and Its Superior Optoelectronic Properties*;

The Journal of Physical Chemistry Letters; **2018**; 9 (1); 216-221; Available from: https://doi.org/10.1021/acs.jpclett.7b03020.

[125] Y. Liu, J. Sun, Z. Yang, D. Yang, X. Ren, H. Xu, Z. Yang, S. Liu; *20-mm-Large Single-Crystalline Formamidinium-Perovskite Wafer for Mass Production of Integrated Photodetectors*; Advanced Optical Materials; **2016**; 4 (11); 1829-1837; Available from: https://doi.org/10.1002/adom.201600327.

[126] H. Fang, Q. Li, J. Ding, N. Li, H. Tian, L. Zhang, T. Ren, J. Dai, L. Wang, Q. Yan; *A self-powered organolead halide perovskite single crystal photodetector driven by a DVD-based triboelectric nanogenerator*; Journal of Materials Chemistry C; **2016**; 4 (3); 630-636; Available from: http://dx.doi.org/10.1039/C5TC03342J.

[127] V. Gonzalez-Pedro, E. J. Juarez-Perez, W.-S. Arsyad, E. M. Barea, F. Fabregat-Santiago, I. Mora-Sero, J. Bisquert; *General Working Principles of $CH_3NH_3PbX_3$ Perovskite Solar Cells*; Nano Letters; **2014**; 14 (2); 888-893; Available from: https://doi.org/10.1021/nl404252e.

[128] I. Mora-Seró; *How Do Perovskite Solar Cells Work?*; Joule; **2018**; 2 (4); 585-587; Available from: https://doi.org/10.1016/j.joule.2018.03.020.

[129] Y. Wang, Y. Zhang, P. Zhang, W. Zhang; *High intrinsic carrier mobility and photon absorption in the perovskite $CH_3NH_3PbI_3$*; Physical Chemistry Chemical Physics; **2015**; 17 (17); 11516-11520; Available from: http://dx.doi.org/10.1039/C5CP00448A.

[130] Q. Lin, A. Armin, R. C. R. Nagiri, P. L. Burn, P. Meredith; *Electro-optics of perovskite solar cells*; Nature Photonics; **2015**; 9 (2); 106-112; Available from: https://doi.org/10.1038/nphoton.2014.284.

[131] J. Höcker, D. Kiermasch, P. Rieder, K. Tvingstedt, A. Baumann, V. Dyakonov; *Efficient Solution Processed $CH_3NH_3PbI_3$ Perovskite Solar Cells with PolyTPD Hole Transport Layer*; Zeitschrift für Naturforschung A; **2019**; 74 (8); 665-672; Available from: https://doi.org/10.1515/zna-2019-0127.

[132] E. Edri, S. Kirmayer, S. Mukhopadhyay, K. Gartsman, G. Hodes, D. Cahen; *Elucidating the charge carrier separation and working mechanism of $CH_3NH_3PbI_{3-x}Cl_x$ perovskite solar cells*; Nature Communications; **2014**; 5 (1); 3461; Available from: https://doi.org/10.1038/ncomms4461.

[133] S. D. Stranks, G. E. Eperon, G. Grancini, C. Menelaou, M. J. Alcocer, T. Leijtens, L. M. Herz, A. Petrozza, H. J. Snaith; *Electron-hole diffusion lengths exceeding 1 micrometer in an organometal trihalide perovskite absorber*; Science; **2013**; 342 (6156); 341-344; Available from: https://www.science.org/lookup/doi/10.1126/science.1243982.

[134] M. Schwoerer, H. C. Wolf; *Organische Molekulare Festkörper - Einführung in die Physik von π-Systemen*; 1st (Wiley-VCH Verlag GmbH & Co. KGaA, Weinheim); **2005**; pp. 359-361.

[135] K. Tvingstedt, L. Gil-Escrig, C. Momblona, P. Rieder, D. Kiermasch, M. Sessolo, A. Baumann, H. J. Bolink, V. Dyakonov; *Removing Leakage and Surface Recombination in Planar Perovskite Solar Cells*; ACS Energy Letters; **2017**; 2 (2); 424-430; Available from: http://dx.doi.org/10.1021/acsenergylett.6b00719.

[136] A. D. Dhass, E. Natarajan, L. Ponnusamy; *Influence of shunt resistance on the performance of solar photovoltaic cell*; International Conference on Emerging Trends in Electrical Engineering and Energy Management (ICETEEEM); **2012**; 382-386; Available from: https://ieeexplore.ieee.org/document/6494522.

[137] D. Shi, V. Adinolfi, R. Comin, M. Yuan, E. Alarousu, A. Buin, Y. Chen, S. Hoogland, A. Rothenberger, K. Katsiev, Y. Losovyj, X. Zhang, P. A. Dowben, O. F. Mohammed, E. H. Sargent, O. M. Bakr; *Low trap-state density and long carrier diffusion in*

*organolead trihalide perovskite single crystals*; **2015**; 347 (6221); 519-522; Available from: https://www.science.org/doi/abs/10.1126/science.aaa2725.

[138] M. Bari, H. Wu, A. A. Bokov, R. F. Ali, H. N. Tailor, B. D. Gates, Z.-G. Ye; *Room-temperature synthesis, growth mechanisms and opto-electronic properties of organic–inorganic halide perovskite $CH_3NH_3PbX_3$ (X=I, Br, and Cl) single crystals*; CrystEngComm; **2021**; 23 (18); 3326-3339; Available from: http://dx.doi.org/10.1039/D0CE01690J.

[139] D. N. Dirin, I. Cherniukh, S. Yakunin, Y. Shynkarenko, M. V. Kovalenko; *Solution-Grown $CsPbBr_3$ Perovskite Single Crystals for Photon Detection*; Chemistry of Materials; **2016**; 28 (23); 8470-8474; Available from: https://doi.org/10.1021/acs.chemmater.6b04298.

[140] R. G. Niemann, A. G. Kontos, D. Palles, E. I. Kamitsos, A. Kaltzoglou, F. Brivio, P. Falaras, P. J. Cameron; *Halogen Effects on Ordering and Bonding of $CH_3NH_3^+$ in $CH_3NH_3PbX_3$ (X = Cl, Br, I) Hybrid Perovskites: A Vibrational Spectroscopic Study*; The Journal of Physical Chemistry C; **2016**; 120 (5); 2509-2519; Available from: https://doi.org/10.1021/acs.jpcc.5b11256.

[141] N. K. Kumawat, A. Dey, K. L. Narasimhan, D. Kabra; *Near Infrared to Visible Electroluminescent Diodes Based on Organometallic Halide Perovskites: Structural and Optical Investigation*; ACS Photonics; **2015**; 2 (3); 349-354; Available from: https://doi.org/10.1021/acsphotonics.5b00018.

[142] Y. Li, Y. Zhang, Z. Zhao, L. Zhi, X. Cao, Y. Jia, F. Lin, L. Zhang, X. Cui, J. Wei; *In Situ Investigation of the Growth of Methylammonium Lead Halide ($MAPbI_{3-x}Br_x$) Perovskite from Microdroplets*; Crystal Growth & Design; **2018**; 18 (6); 3458-3464; Available from: https://doi.org/10.1021/acs.cgd.8b00181.

[143] T. Jeon, S. J. Kim, J. Yoon, J. Byun, H. R. Hong, T.-W. Lee, J.-S. Kim, B. Shin, S. O. Kim; *Hybrid Perovskites: Effective Crystal Growth for Optoelectronic Applications*; Advanced Energy Materials; **2017**; 7 (19); 1602596; Available from: https://doi.org/10.1002/aenm.201602596.

[144] T. Zhang, M. Yang, E. E. Benson, Z. Li, J. van de Lagemaat, J. M. Luther, Y. Yan, K. Zhu, Y. Zhao; *A facile solvothermal growth of single crystal mixed halide perovskite $CH_3NH_3Pb(Br_{1-x}Cl_x)_3$*; Chemical Communications; **2015**; 51 (37); 7820-7823; Available from: http://dx.doi.org/10.1039/C5CC01835H.

[145] B. Murali, M. I. Saidaminov, A. L. Abdelhady, W. Peng, J. Liu, J. Pan, O. M. Bakr, O. F. Mohammed; *Robust and air-stable sandwiched organo-lead halide perovskites for photodetector applications*; Journal of Materials Chemistry C; **2016**; 4 (13); 2545-2552; Available from: http://dx.doi.org/10.1039/C6TC00610H.

[146] H. Wang, D. H. Kim; *Perovskite-based photodetectors: materials and devices*; Chemical Society Reviews; **2017**; 46 (17); 5204-5236; Available from: http://dx.doi.org/10.1039/C6CS00896H.

[147] Y.-H. Kim, H. Cho, J. H. Heo, T.-S. Kim, N. Myoung, C.-L. Lee, S. H. Im, T.-W. Lee; *Multicolored Organic/Inorganic Hybrid Perovskite Light-Emitting Diodes*; Advanced Materials; **2015**; 27 (7); 1248-1254; Available from: https://doi.org/10.1002/adma.201403751.

[148] Y. Zhou, F. Wang, H.-H. Fang, M. A. Loi, F.-Y. Xie, N. Zhao, C.-P. Wong; *Distribution of bromine in mixed iodide–bromide organolead perovskites and its impact on photovoltaic performance*; Journal of Materials Chemistry A; **2016**; 4 (41); 16191-16197; Available from: http://dx.doi.org/10.1039/C6TA07647E.

[149] Z. Chen, B. Turedi, A. Y. Alsalloum, C. Yang, X. Zheng, I. Gereige, A. AlSaggaf, O. F. Mohammed, O. M. Bakr; *Single-Crystal $MAPbI_3$ Perovskite Solar Cells Exceeding*

*21% Power Conversion Efficiency*; ACS Energy Letters; **2019**; 4 (6); 1258-1259; Available from: https://doi.org/10.1021/acsenergylett.9b00847.

[150] H.-S. Rao, B.-X. Chen, X.-D. Wang, D.-B. Kuang, C.-Y. Su; *A micron-scale laminar $MAPbBr_3$ single crystal for an efficient and stable perovskite solar cell*; Chemical Communications; **2017**; 53 (37); 5163-5166; Available from: http://dx.doi.org/10.1039/C7CC02447A.

[151] Y. Zhang, Y. Liu, Y. Li, Z. Yang, S. Liu; *Perovskite $CH_3NH_3Pb(Br_xI_{1-x})_3$ single crystals with controlled composition for fine-tuned bandgap towards optimized optoelectronic applications*; Journal of Materials Chemistry C; **2016**; 4 (39); 9172-9178; Available from: http://dx.doi.org/10.1039/C6TC03592B.

[152] Y. Fang, Q. Dong, Y. Shao, Y. Yuan, J. Huang; *Highly narrowband perovskite single-crystal photodetectors enabled by surface-charge recombination*; Nature Photonics; **2015**; 9; 679; Available from: http://dx.doi.org/10.1038/nphoton.2015.156.

[153] S. Amari, J.-M. Verilhac, E. Gros D'Aillon, A. Ibanez, J. Zaccaro; *Optimization of the Growth Conditions for High Quality $CH_3NH_3PbBr_3$ Hybrid Perovskite Single Crystals*; Crystal Growth & Design; **2020**; 20 (3); 1665-1672; Available from: https://doi.org/10.1021/acs.cgd.9b01429.

[154] Y. Liu, Y. Zhang, X. Zhu, J. Feng, I. Spanopoulos, W. Ke, Y. He, X. Ren, Z. Yang, F. Xiao, K. Zhao, M. Kanatzidis, S. Liu; *Triple-Cation and Mixed-Halide Perovskite Single Crystal for High-Performance X-ray Imaging*; Advanced Materials; **2021**; 33 (8); 2006010; Available from: https://doi.org/10.1002/adma.202006010.

[155] P. Nandi, C. Giri, D. Swain, U. Manju, D. Topwal; *Room temperature growth of $CH_3NH_3PbCl_3$ single crystals by solvent evaporation method*; CrystEngComm; **2019**; 21 (4); 656-661; Available from: http://dx.doi.org/10.1039/C8CE01939H.

[156] W.-Q. Liao, Y. Zhang, C.-L. Hu, J.-G. Mao, H.-Y. Ye, P.-F. Li, S. D. Huang, R.-G. Xiong; *A lead-halide perovskite molecular ferroelectric semiconductor*; Nature Communications; **2015**; 6 (1); 7338; Available from: https://doi.org/10.1038/ncomms8338.

[157] Y. Tidhar, E. Edri, H. Weissman, D. Zohar, G. Hodes, D. Cahen, B. Rybtchinski, S. Kirmayer; *Crystallization of Methyl Ammonium Lead Halide Perovskites: Implications for Photovoltaic Applications*; Journal of the American Chemical Society; **2014**; 136 (38); 13249-13256; Available from: https://doi.org/10.1021/ja505556s.

[158] B. Spingler, S. Schnidrig, T. Todorova, F. Wild; *Some thoughts about the single crystal growth of small molecules*; CrystEngComm; **2012**; 14 (3); 751-757; Available from: http://dx.doi.org/10.1039/C1CE05624G.

[159] Y. Yang, Y. Yan, M. Yang, S. Choi, K. Zhu, J. M. Luther, M. C. Beard; *Low surface recombination velocity in solution-grown $CH_3NH_3PbBr_3$ perovskite single crystal*; Nature Communications; **2015**; 6 (1); 7961; Available from: https://doi.org/10.1038/ncomms8961.

[160] L. Zhang, Y. Liu, X. Ye, Q. Han, C. Ge, S. Cui, Q. Guo, X. Zheng, Z. Zhai, X. Tao; *Exploring Anisotropy on Oriented Wafers of $MAPbBr_3$ Crystals Grown by Controlled Antisolvent Diffusion*; Crystal Growth & Design; **2018**; 18 (11); 6652-6660; Available from: https://doi.org/10.1021/acs.cgd.8b00896.

[161] J. A. Young; *Dichloromethane*; Journal of Chemical Education; **2004**; 81; Available from: https://pubs.acs.org/doi/abs/10.1021/ed081p1415.

[162] Y. Zhang, F. Huang, Q. Mi; *Preferential Facet Growth of Methylammonium Lead Halide Single Crystals Promoted by Halide Coordination*; Chemistry Letters; **2016**; 45 (8); 1030-1032; Available from: https://www.journal.csj.jp/doi/abs/10.1246/cl.160419.

[163] H. R. Byun, D. Y. Park, H. M. Oh, G. Namkoong, M. S. Jeong; *Light Soaking Phenomena in Organic–Inorganic Mixed Halide Perovskite Single Crystals*; ACS

Photonics; **2017**; 4 (11); 2813-2820; Available from: https://doi.org/10.1021/acsphotonics.7b00797.

[164] D. Kim, J.-H. Yun, M. Lyu, J. Kim, S. Lim, J. S. Yun, L. Wang, J. Seidel; *Probing Facet-Dependent Surface Defects in $MAPbI_3$ Perovskite Single Crystals*; The Journal of Physical Chemistry C; **2019**; 123 (23); 14144-14151; Available from: https://doi.org/10.1021/acs.jpcc.9b00943.

[165] J. Zhang, K. Wang, Q. Yao, Y. Yuan, J. Ding, W. Zhang, H. Sun, C. Shang, C. Li, T. Zhou, S. Pang; *Carrier Diffusion and Recombination Anisotropy in the $MAPbI_3$ Single Crystal*; ACS Applied Materials & Interfaces; **2021**; 13 (25); 29827-29834; Available from: https://doi.org/10.1021/acsami.1c07056.

[166] K. Schötz, A. M. Askar, W. Peng, D. Seeberger, T. P. Gujar, M. Thelakkat, A. Köhler, S. Huettner, O. M. Bakr, K. Shankar, F. Panzer; *Double peak emission in lead halide perovskites by self-absorption*; Journal of Materials Chemistry C; **2020**; 8 (7); 2289-2300; Available from: http://dx.doi.org/10.1039/C9TC06251C.

[167] Y. Liu, Z. Yang, D. Cui, X. Ren, J. Sun, X. Liu, J. Zhang, Q. Wei, H. Fan, F. Yu, X. Zhang, C. Zhao, S. Liu; *Two-Inch-Sized Perovskite $CH_3NH_3PbX_3$ (X = Cl, Br, I) Crystals: Growth and Characterization*; Advanced Materials; **2015**; 27 (35); 5176-5183; Available from: https://doi.org/10.1002/adma.201502597.

[168] J. Yu, G. Liu, C. Chen, Y. Li, M. Xu, T. Wang, G. Zhao, L. Zhang; *Perovskite $CsPbBr_3$ crystals: growth and applications*; Journal of Materials Chemistry C; **2020**; 8 (19); 6326-6341; Available from: http://dx.doi.org/10.1039/D0TC00922A.

[169] M. E. Wieser, T. B. Coplen; *Atomic weights of the elements 2009 (IUPAC Technical Report)*; Pure and Applied Chemistry; **2010**; 83 (2); 359-396; Available from: https://doi.org/10.1351/PAC-REP-10-09-14.

[170] D. Shi, V. Adinolfi, R. Comin, M. Yuan, E. Alarousu, A. Buin, Y. Chen, S. Hoogland, A. Rothenberger, K. Katsiev, Y. Losovyj, X. Zhang, P. A. Dowben, O. F. Mohammed, E. H. Sargent, O. M. Bakr; *Low trap-state density and long carrier diffusion in organolead trihalide perovskite single crystals*; Science; **2015**; 347 (6221); 519-522; Available from: https://www.science.org/doi/full/10.1126/science.aaa2725.

[171] F. Chen, C. Xu, Q. Xu, Y. Zhu, Z. Zhu, W. Liu, X. Dong, F. Qin, Z. Shi; *Structure Evolution of $CH_3NH_3PbBr_3$ Single Crystal Grown in N,N-Dimethylformamide Solution*; Crystal Growth & Design; **2018**; 18 (5); 3132-3137; Available from: https://doi.org/10.1021/acs.cgd.8b00256.

[172] G. A. Elbaz, D. B. Straus, O. E. Semonin, T. D. Hull, D. W. Paley, P. Kim, J. S. Owen, C. R. Kagan, X. Roy; *Unbalanced Hole and Electron Diffusion in Lead Bromide Perovskites*; Nano Letters; **2017**; 17 (3); 1727-1732; Available from: https://doi.org/10.1021/acs.nanolett.6b05022.

[173] Q. Dong, Y. Fang, Y. Shao, P. Mulligan, J. Qiu, L. Cao, J. Huang; *Electron-hole diffusion lengths > 175 μm in solution-grown $CH_3NH_3PbI_3$ single crystals*; Science; **2015**; 347 (6225); 967-970; Available from: https://science.sciencemag.org/content/sci/347/6225/967.full.pdf.

[174] H. Zhou, Z. Nie, J. Yin, Y. Sun, H. Zhuo, D. Wang, D. Li, J. Dou, X. Zhang, T. Ma; *Antisolvent diffusion-induced growth, equilibrium behaviours in aqueous solution and optical properties of $CH_3NH_3PbI_3$ single crystals for photovoltaic applications*; RSC Advances; **2015**; 5 (104); 85344-85349; Available from: http://dx.doi.org/10.1039/C5RA17579H.

[175] G. E. Eperon, S. D. Stranks, C. Menelaou, M. B. Johnston, L. M. Herz, H. J. Snaith; *Formamidinium lead trihalide: a broadly tunable perovskite for efficient planar heterojunction solar cells*; Energy & Environmental Science; **2014**; 7 (3); 982-988; Available from: http://dx.doi.org/10.1039/C3EE43822H.

[176] S. X. Tao, X. Cao, P. A. Bobbert; *Accurate and efficient band gap predictions of metal halide perovskites using the DFT-1/2 method: GW accuracy with DFT expense*; Scientific Reports; **2017**; 7 (1); 14386; Available from: https://doi.org/10.1038/s41598-017-14435-4.

[177] D. L. Proffit, H. W. Jang, S. Lee, C. T. Nelson, X. Q. Pan, M. S. Rzchowski, C. B. Eom; *Influence of symmetry mismatch on heteroepitaxial growth of perovskite thin films*; Applied Physics Letters; **2008**; 93 (11); 111912; Available from: https://aip.scitation.org/doi/abs/10.1063/1.2979237.

[178] S. Luo, W. A. Daoud; *Crystal Structure Formation of $CH_3NH_3PbI_{3-x}Cl_x$ Perovskite*; Materials; **2016**; 9 (3); 123; Available from: https://www.mdpi.com/1996-1944/9/3/123.

[179] L. Vegard; *Die Konstitution der Mischkristalle und die Raumfüllung der Atome*; Zeitschrift für Physik; **1921**; 5 (1); 17-26; Available from: https://doi.org/10.1007/BF01349680.

[180] X. Cheng, L. Jing, Y. Zhao, S. Du, J. Ding, T. Zhou; *Crystal orientation-dependent optoelectronic properties of $MAPbCl_3$ single crystals*; Journal of Materials Chemistry C; **2018**; 6 (6); 1579-1586; Available from: http://dx.doi.org/10.1039/C7TC05156E.

[181] J. Li, Z. Han, Y. Gu, D. Yu, J. Liu, D. Hu, X. Xu, H. Zeng; *Perovskite Single Crystals: Synthesis, Optoelectronic Properties, and Application*; Advanced Functional Materials; **2021**; 31 (11); 2008684; Available from: https://doi.org/10.1002/adfm.202008684.

[182] N. J. Jeon, J. H. Noh, W. S. Yang, Y. C. Kim, S. Ryu, J. Seo, S. I. Seok; *Compositional engineering of perovskite materials for high-performance solar cells*; Nature; **2015**; 517 (7535); 476-480; Available from: https://doi.org/10.1038/nature14133.

[183] N.-G. Park; *Organometal Perovskite Light Absorbers Toward a 20% Efficiency Low-Cost Solid-State Mesoscopic Solar Cell*; The Journal of Physical Chemistry Letters; **2013**; 4 (15); 2423-2429; Available from: https://doi.org/10.1021/jz400892a.

[184] C. Wehrenfennig, G. E. Eperon, M. B. Johnston, H. J. Snaith, L. M. Herz; *High Charge Carrier Mobilities and Lifetimes in Organolead Trihalide Perovskites*; Advanced Materials; **2014**; 26 (10); 1584-1589; Available from: https://onlinelibrary.wiley.com/doi/abs/10.1002/adma.201305172.

[185] M. A. Green, A. Ho-Baillie, H. J. Snaith; *The emergence of perovskite solar cells*; Nature Photonics; **2014**; 8 (7); 506-514; Available from: https://doi.org/10.1038/nphoton.2014.134.

[186] X. Cheng, S. Yang, B. Cao, X. Tao, Z. Chen; *Single Crystal Perovskite Solar Cells: Development and Perspectives*; Advanced Functional Materials; **2020**; 30 (4); 1905021; Available from: https://onlinelibrary.wiley.com/doi/abs/10.1002/adfm.201905021.

[187] C. M. Sutter-Fella, Y. Li, M. Amani, J. W. Ager, F. M. Toma, E. Yablonovitch, I. D. Sharp, A. Javey; *High Photoluminescence Quantum Yield in Band Gap Tunable Bromide Containing Mixed Halide Perovskites*; Nano Letters; **2016**; 16 (1); 800-806; Available from: https://doi.org/10.1021/acs.nanolett.5b04884.

[188] L. M. Herz; *Charge-Carrier Mobilities in Metal Halide Perovskites: Fundamental Mechanisms and Limits*; ACS Energy Letters; **2017**; 2 (7); 1539-1548; Available from: http://dx.doi.org/10.1021/acsenergylett.7b00276.

[189] L. Zhao, K. M. Lee, K. Roh, S. U. Z. Khan, B. P. Rand; *Improved Outcoupling Efficiency and Stability of Perovskite Light-Emitting Diodes using Thin Emitting Layers*; **2019**; 31 (2); 1805836; Available from: https://onlinelibrary.wiley.com/doi/abs/10.1002/adma.201805836.

[190] C. Sun, Z. Gao, H. Liu, L. Wang, Y. Deng, P. Li, H. Li, Z.-H. Zhang, C. Fan, W. Bi; *One Stone, Two Birds: High-Efficiency Blue-Emitting Perovskite Nanocrystals for LED*

*and Security Ink Applications*; Chemistry of Materials; **2019**; 31 (14); 5116-5123; Available from: https://doi.org/10.1021/acs.chemmater.9b01010.

[191] B. R. Sutherland, E. H. Sargent; *Perovskite photonic sources*; Nature Photonics; **2016**; 10; 295; Available from: https://doi.org/10.1038/nphoton.2016.62.

[192] H. Dong, C. Zhang, X. Liu, J. Yao, Y. S. Zhao; *Materials chemistry and engineering in metal halide perovskite lasers*; Chemical Society Reviews; **2020**; 49 (3); 951-982; Available from: http://dx.doi.org/10.1039/C9CS00598F.

[193] L. Dou, Y. Yang, J. You, Z. Hong, W.-H. Chang, G. Li, Y. Yang; *Solution-processed hybrid perovskite photodetectors with high detectivity*; Nature Communications; **2014**; 5 (1); 5404; Available from: https://doi.org/10.1038/ncomms6404.

[194] Z. Chen, C. Li, A. A. Zhumekenov, X. Zheng, C. Yang, H. Yang, Y. He, B. Turedi, O. F. Mohammed, L. Shen, O. M. Bakr; *Solution-Processed Visible-Blind Ultraviolet Photodetectors with Nanosecond Response Time and High Detectivity*; Advanced Optical Materials; **2019**; 7 (19); 1900506; Available from: https://onlinelibrary.wiley.com/doi/abs/10.1002/adom.201900506.

[195] C. Bi, Q. Wang, Y. Shao, Y. Yuan, Z. Xiao, J. Huang; *Non-wetting surface-driven high-aspect-ratio crystalline grain growth for efficient hybrid perovskite solar cells*; Nature Communications; **2015**; 6; 7747; Available from: https://doi.org/10.1038/ncomms8747.

[196] C. Momblona, L. Gil-Escrig, E. Bandiello, E. M. Hutter, M. Sessolo, K. Lederer, J. Blochwitz-Nimoth, H. J. Bolink; *Efficient vacuum deposited p-i-n and n-i-p perovskite solar cells employing doped charge transport layers*; Energy & Environmental Science; **2016**; 9 (11); 3456-3463; Available from: http://dx.doi.org/10.1039/C6EE02100J.

[197] A. Y. Alsalloum, B. Turedi, X. Zheng, S. Mitra, A. A. Zhumekenov, K. J. Lee, P. Maity, I. Gereige, A. AlSaggaf, I. S. Roqan, O. F. Mohammed, O. M. Bakr; *Low-Temperature Crystallization Enables 21.9% Efficient Single-Crystal $MAPbI_3$ Inverted Perovskite Solar Cells*; ACS Energy Letters; **2020**; 5 (2); 657-662; Available from: https://doi.org/10.1021/acsenergylett.9b02787.

[198] H. Min, M. Kim, S.-U. Lee, H. Kim, G. Kim, K. Choi, J. H. Lee, S. I. Seok; *Efficient, stable solar cells by using inherent bandgap of α-phase formamidinium lead iodide*; Science; **2019**; 366 (6466); 749-753; Available from: https://science.sciencemag.org/content/sci/366/6466/749.full.pdf.

[199] M. Stolterfoht, C. M. Wolff, Y. Amir, A. Paulke, L. Perdigon-Toro, P. Caprioglio, D. Neher; *Approaching the fill factor Shockley-Queisser limit in stable, dopant-free triple cation perovskite solar cells*; Energy & Environmental Science; **2017**; 10 (6); 1530-1539; Available from: http://dx.doi.org/10.1039/C7EE00899F.

[200] T. Glaser, C. Müller, M. Sendner, C. Krekeler, O. E. Semonin, T. D. Hull, O. Yaffe, J. S. Owen, W. Kowalsky, A. Pucci, R. Lovrinčić; *Infrared Spectroscopic Study of Vibrational Modes in Methylammonium Lead Halide Perovskites*; The Journal of Physical Chemistry Letters; **2015**; 6 (15); 2913-2918; Available from: https://doi.org/10.1021/acs.jpclett.5b01309.

[201] P. Wang, J. Guan, D. T. K. Galeschuk, Y. Yao, C. F. He, S. Jiang, S. Zhang, Y. Liu, M. Jin, C. Jin, Y. Song; *Pressure-Induced Polymorphic, Optical, and Electronic Transitions of Formamidinium Lead Iodide Perovskite*; The Journal of Physical Chemistry Letters; **2017**; 8 (10); 2119-2125; Available from: https://doi.org/10.1021/acs.jpclett.7b00665.

[202] L. Chen, Y.-Y. Tan, Z.-X. Chen, T. Wang, S. Hu, Z.-A. Nan, L.-Q. Xie, Y. Hui, J.-X. Huang, C. Zhan, S.-H. Wang, J.-Z. Zhou, J.-W. Yan, B.-W. Mao, Z.-Q. Tian; *Toward Long-Term Stability: Single-Crystal Alloys of Cesium-Containing Mixed Cation and Mixed Halide Perovskite*; Journal of the American Chemical Society; **2019**; Available from: https://doi.org/10.1021/jacs.8b11610.

[203] G. P. Nagabhushana, R. Shivaramaiah, A. Navrotsky; *Direct calorimetric verification of thermodynamic instability of lead halide hybrid perovskites*; Proceedings of the National Academy of Sciences; **2016**; 113 (28); 7717-7721; Available from: https://www.pnas.org/content/pnas/113/28/7717.full.pdf.

[204] N.-G. Park; *Perovskite solar cells: an emerging photovoltaic technology*; Materials Today; **2015**; 18 (2); 65-72; Available from: https://doi.org/10.1016/j.mattod.2014.07.007.

[205] Z. Wang, Z. Shi, T. Li, Y. Chen, W. Huang; *Stability of Perovskite Solar Cells: A Prospective on the Substitution of the A Cation and X Anion*; Angewandte Chemie International Edition; **2017**; 56 (5); 1190-1212; Available from: https://onlinelibrary.wiley.com/doi/abs/10.1002/anie.201603694.

[206] Q. Han, S.-H. Bae, P. Sun, Y.-T. Hsieh, Y. Yang, Y. S. Rim, H. Zhao, Q. Chen, W. Shi, G. Li, Y. Yang; *Single Crystal Formamidinium Lead Iodide ($FAPbI_3$): Insight into the Structural, Optical, and Electrical Properties*; Advanced Materials; **2016**; 28 (11); 2253-2258; Available from: https://onlinelibrary.wiley.com/doi/abs/10.1002/adma.201505002.

[207] Y. Fang, H. Wei, Q. Dong, J. Huang; *Quantification of re-absorption and re-emission processes to determine photon recycling efficiency in perovskite single crystals*; Nature Communications; **2017**; 8; 14417; Available from: https://doi.org/10.1038/ncomms14417.

[208] Y.-C. Zhao, W.-K. Zhou, X. Zhou, K.-H. Liu, D.-P. Yu, Q. Zhao; *Quantification of light-enhanced ionic transport in lead iodide perovskite thin films and its solar cell applications*; Light: Science & Applications; **2017**; 6 (5); e16243-e16243; Available from: https://doi.org/10.1038/lsa.2016.243.

[209] J. Zhao, Y. Deng, H. Wei, X. Zheng, Z. Yu, Y. Shao, J. E. Shield, J. Huang; *Strained hybrid perovskite thin films and their impact on the intrinsic stability of perovskite solar cells*; Science Advances; **2017**; 3 (11); eaao5616; Available from: https://advances.sciencemag.org/content/advances/3/11/eaao5616.full.pdf.

[210] J. Cao, S. X. Tao, P. A. Bobbert, C.-P. Wong, N. Zhao; *Interstitial Occupancy by Extrinsic Alkali Cations in Perovskites and Its Impact on Ion Migration*; Advanced Materials; **2018**; 30 (26); 1707350; Available from: https://onlinelibrary.wiley.com/doi/abs/10.1002/adma.201707350.

[211] J. Xing, Q. Wang, Q. Dong, Y. Yuan, Y. Fang, J. Huang; *Ultrafast ion migration in hybrid perovskite polycrystalline thin films under light and suppression in single crystals*; Physical Chemistry Chemical Physics; **2016**; 18 (44); 30484-30490; Available from: http://dx.doi.org/10.1039/C6CP06496E.

[212] H. J. Snaith, A. Abate, J. M. Ball, G. E. Eperon, T. Leijtens, N. K. Noel, S. D. Stranks, J. T.-W. Wang, K. Wojciechowski, W. Zhang; *Anomalous Hysteresis in Perovskite Solar Cells*; The Journal of Physical Chemistry Letters; **2014**; 5 (9); 1511-1515; Available from: https://doi.org/10.1021/jz500113x.

[213] D.-H. Kang, N.-G. Park; *On the Current–Voltage Hysteresis in Perovskite Solar Cells: Dependence on Perovskite Composition and Methods to Remove Hysteresis*; Advanced Materials; **2019**; 31 (34); 1805214; Available from: https://onlinelibrary.wiley.com/doi/abs/10.1002/adma.201805214.

[214] P. Liu, W. Wang, S. Liu, H. Yang, Z. Shao; *Fundamental Understanding of Photocurrent Hysteresis in Perovskite Solar Cells*; Advanced Energy Materials; **2019**; 9 (13); 1803017; Available from: https://onlinelibrary.wiley.com/doi/abs/10.1002/aenm.201803017.

[215] E. A. Duijnstee, J. M. Ball, V. M. Le Corre, L. J. A. Koster, H. J. Snaith, J. Lim; *Toward Understanding Space-Charge Limited Current Measurements on Metal Halide*

*Perovskites*; ACS Energy Letters; **2020**; 5 (2); 376-384; Available from: https://doi.org/10.1021/acsenergylett.9b02720.

[216] M. Maeda, M. Hattori, A. Hotta, I. Suzuki; *Dielectric Studies on $CH_3NH_3PbX_3$ (X = Cl and Br) Single Cystals*; Journal of the Physical Society of Japan; **1997**; 66 (5); 1508-1511; Available from: https://doi.org/10.1143/JPSJ.66.1508.

[217] J.-W. Lee, S.-G. Kim, J.-M. Yang, Y. Yang, N.-G. Park; *Verification and mitigation of ion migration in perovskite solar cells*; APL Materials; **2019**; 7 (4); 041111; Available from: https://aip.scitation.org/doi/abs/10.1063/1.5085643.

[218] T.-Y. Yang, G. Gregori, N. Pellet, M. Grätzel, J. Maier; *The Significance of Ion Conduction in a Hybrid Organic–Inorganic Lead-Iodide-Based Perovskite Photosensitizer*; Angewandte Chemie International Edition; **2015**; 54 (27); 7905-7910; Available from: https://onlinelibrary.wiley.com/doi/abs/10.1002/anie.201500014.

[219] A. Francisco-López, B. Charles, M. I. Alonso, M. Garriga, M. Campoy-Quiles, M. T. Weller, A. R. Goñi; *Phase Diagram of Methylammonium/Formamidinium Lead Iodide Perovskite Solid Solutions from Temperature-Dependent Photoluminescence and Raman Spectroscopies*; The Journal of Physical Chemistry C; **2020**; 124 (6); 3448-3458; Available from: https://doi.org/10.1021/acs.jpcc.9b10185.

[220] F. Cordero, F. Craciun, F. Trequattrini, A. Generosi, B. Paci, A. M. Paoletti, G. Pennesi; *Stability of Cubic $FAPbI_3$ from X-ray Diffraction, Anelastic, and Dielectric Measurements*; The Journal of Physical Chemistry Letters; **2019**; 10 (10); 2463-2469; Available from: https://doi.org/10.1021/acs.jpclett.9b00896.

[221] A. D. Wright, C. Verdi, R. L. Milot, G. E. Eperon, M. A. Pérez-Osorio, H. J. Snaith, F. Giustino, M. B. Johnston, L. M. Herz; *Electron–phonon coupling in hybrid lead halide perovskites*; Nature Communications; **2016**; 7 (1); 11755; Available from: https://doi.org/10.1038/ncomms11755.

[222] W. Yu, F. Li, L. Yu, M. R. Niazi, Y. Zou, D. Corzo, A. Basu, C. Ma, S. Dey, M. L. Tietze, U. Buttner, X. Wang, Z. Wang, M. N. Hedhili, C. Guo, T. Wu, A. Amassian; *Single crystal hybrid perovskite field-effect transistors*; Nature Communications; **2018**; 9 (1); 5354; Available from: https://doi.org/10.1038/s41467-018-07706-9.

[223] J. Wang, S. P. Senanayak, J. Liu, Y. Hu, Y. Shi, Z. Li, C. Zhang, B. Yang, L. Jiang, D. Di, A. V. Ievlev, O. S. Ovchinnikova, T. Ding, H. Deng, L. Tang, Y. Guo, J. Wang, K. Xiao, D. Venkateshvaran, L. Jiang, D. Zhu, H. Sirringhaus; *Investigation of Electrode Electrochemical Reactions in $CH_3NH_3PbBr_3$ Perovskite Single-Crystal Field-Effect Transistors*; Advanced Materials; **2019**; 31 (35); 1902618; Available from: https://onlinelibrary.wiley.com/doi/abs/10.1002/adma.201902618.

[224] Y. Song, W. Bi, A. Wang, X. Liu, Y. Kang, Q. Dong; *Efficient lateral-structure perovskite single crystal solar cells with high operational stability*; Nature Communications; **2020**; 11 (1); 274; Available from: https://doi.org/10.1038/s41467-019-13998-2.

[225] B. Turedi, V. Yeddu, X. Zheng, D. Y. Kim, O. M. Bakr, M. I. Saidaminov; *Perovskite Single-Crystal Solar Cells: Going Forward*; ACS Energy Letters; **2021**; 6 (2); 631-642; Available from: https://doi.org/10.1021/acsenergylett.0c02573.

[226] J. Song, X. Feng, H. Li, W. Li, T. Lu, C. Guo, H. Zhang, H. Wei, B. Yang; *Facile Strategy for Facet Competition Management to Improve the Performance of Perovskite Single-Crystal X-ray Detectors*; The Journal of Physical Chemistry Letters; **2020**; 11 (9); 3529-3535; Available from: https://doi.org/10.1021/acs.jpclett.0c00770.

[227] X. Wang, Y. Li, Y. Xu, Y. Pan, C. Zhu, D. Zhu, Y. Wu, G. Li, Q. Zhang, Q. Li, X. Zhang, J. Wu, J. Chen, W. Lei; *Solution-Processed Halide Perovskite Single Crystals with Intrinsic Compositional Gradients for X-ray Detection*; Chemistry of Materials;

**2020**; 32 (12); 4973-4983; Available from: https://doi.org/10.1021/acs.chemmater.9b05000.

[228] X.-D. Wang, W.-G. Li, J.-F. Liao, D.-B. Kuang; *Recent Advances in Halide Perovskite Single-Crystal Thin Films: Fabrication Methods and Optoelectronic Applications*; Solar RRL; **2019**; 3 (4); 1800294; Available from: https://onlinelibrary.wiley.com/doi/abs/10.1002/solr.201800294.

[229] B. Gruber; *The relationship between reduced cells in a general Bravais lattice*; **1973**; 29 (4); 433-440; Available from: https://onlinelibrary.wiley.com/doi/abs/10.1107/S0567739473001063.

[230] W. H.; *Classifications of space groups, point groups and lattices*; International Tables for Crystallography; **2006**; A; 726-731; Available from: https://onlinelibrary.wiley.com/doi/abs/10.1107/97809553602060000515.

[231] Y. Liu, Z. Yang, S. Liu; *Recent Progress in Single-Crystalline Perovskite Research Including Crystal Preparation, Property Evaluation, and Applications*; **2018**; 5 (1); 1700471; Available from: https://doi.org/10.1002/advs.201700471.

[232] B. Murali, H. K. Kolli, J. Yin, R. Ketavath, O. M. Bakr, O. F. Mohammed; *Single Crystals: The Next Big Wave of Perovskite Optoelectronics*; ACS Materials Letters; **2020**; 2 (2); 184-214; Available from: https://doi.org/10.1021/acsmaterialslett.9b00290.

[233] Y. Liu, Q. Dong, Y. Fang, Y. Lin, Y. Deng, J. Huang; *Fast Growth of Thin $MAPbI_3$ Crystal Wafers on Aqueous Solution Surface for Efficient Lateral-Structure Perovskite Solar Cells*; Advanced Functional Materials; **2019**; 29 (47); 1807707; Available from: https://onlinelibrary.wiley.com/doi/abs/10.1002/adfm.201807707.

[234] E. L. Paul, H.-H. Tung, M. Midler; *Organic crystallization processes*; Powder Technology; **2005**; 150 (2); 133-143; Available from: https://doi.org/10.1016/j.powtec.2004.11.040.

[235] S. Teychené, I. Rodríguez-Ruiz, R. K. Ramamoorthy; *Reactive crystallization: From mixing to control of kinetics by additives*; Current Opinion in Colloid & Interface Science; **2020**; 46; 1-19; Available from: https://doi.org/10.1016/j.cocis.2020.01.003.

[236] N. Miyazaki; *26 - Thermal Stress and Dislocations in Bulk Crystal Growth*; editor: P. Rudolph; In: *Handbook of Crystal Growth (Second Edition)*; Boston; Elsevier; **2015**; pp. 1049-1092.

[237] C. Reichardt; *Solvatochromic Dyes as Solvent Polarity Indicators*; Chemical Reviews; **1994**; 94 (8); 2319-2358; Available from: https://doi.org/10.1021/cr00032a005.

[238] L. H. Hall, L. B. Kier, W. J. Murray; *Molecular connectivity II: Relationship to water solubility and boiling point*; Journal of Pharmaceutical Sciences; **1975**; 64 (12); 1974-1977; Available from: https://doi.org/10.1002/jps.2600641215.

[239] C. C. Stoumpos, C. D. Malliakas, M. G. Kanatzidis; *Semiconducting Tin and Lead Iodide Perovskites with Organic Cations: Phase Transitions, High Mobilities, and Near-Infrared Photoluminescent Properties*; Inorganic Chemistry; **2013**; 52 (15); 9019-9038; Available from: https://doi.org/10.1021/ic401215x.

[240] A. Kojima, K. Teshima, Y. Shirai, T. Miyasaka; *Organometal Halide Perovskites as Visible-Light Sensitizers for Photovoltaic Cells*; Journal of the American Chemical Society; **2009**; 131 (17); 6050-6051; Available from: https://doi.org/10.1021/ja809598r.

[241] C. Bi, Q. Wang, Y. Shao, Y. Yuan, Z. Xiao, J. Huang; *Non-wetting surface-driven high-aspect-ratio crystalline grain growth for efficient hybrid perovskite solar cells*; Nature Communications; **2015**; 6 (1); 7747; Available from: https://doi.org/10.1038/ncomms8747.

[242] R. Guo, B. Dahal, A. Thapa, Y. R. Poudel, Y. Liu, W. Li; *Ambient processed (110) preferred $MAPbI_3$ thin films for highly efficient perovskite solar cells*; Nanoscale

Advances; **2021**; 3 (7); 2056-2064; Available from: http://dx.doi.org/10.1039/D0NA01029D.

[243] J.-Y. Jeng, K.-C. Chen, T.-Y. Chiang, P.-Y. Lin, T.-D. Tsai, Y.-C. Chang, T.-F. Guo, P. Chen, T.-C. Wen, Y.-J. Hsu; *Nickel Oxide Electrode Interlayer in $CH_3NH_3PbI_3$ Perovskite/PCBM Planar-Heterojunction Hybrid Solar Cells*; Advanced Materials; **2014**; 26 (24); 4107-4113; Available from: http://dx.doi.org/10.1002/adma.201306217.

[244] J. Lee, H. Kang, G. Kim, H. Back, J. Kim, S. Hong, B. Park, E. Lee, K. Lee; *Achieving Large-Area Planar Perovskite Solar Cells by Introducing an Interfacial Compatibilizer*; Advanced Materials; **2017**; 29 (22); 1606363-n/a; Available from: http://dx.doi.org/10.1002/adma.201606363.

[245] K.-G. Lim, H.-B. Kim, J. Jeong, H. Kim, J. Y. Kim, T.-W. Lee; *Boosting the Power Conversion Efficiency of Perovskite Solar Cells Using Self-Organized Polymeric Hole Extraction Layers with High Work Function*; Advanced Materials; **2014**; 26 (37); 6461-6466; Available from: http://dx.doi.org/10.1002/adma.201401775.

[246] T. Liu, K. Chen, Q. Hu, R. Zhu, Q. Gong; *Inverted Perovskite Solar Cells: Progresses and Perspectives*; Advanced Energy Materials; **2016**; 6 (17); Available from: http://dx.doi.org/10.1002/aenm.201600457.

[247] W. C. M., Z. Fengshuo, P. Andreas, T. L. Perdigón, K. Norbert, N. Dieter; *Reduced Interface-Mediated Recombination for High Open-Circuit Voltages in $CH_3NH_3PbI_3$ Solar Cells*; Advanced Materials; **2017**; 29 (28); 1700159; Available from: https://onlinelibrary.wiley.com/doi/abs/10.1002/adma.201700159.

[248] S. Ryu, J. Seo, S. S. Shin, Y. C. Kim, N. J. Jeon, J. H. Noh, S. I. Seok; *Fabrication of metal-oxide-free $CH_3NH_3PbI_3$ perovskite solar cells processed at low temperature*; Journal of Materials Chemistry A; **2015**; 3 (7); 3271-3275; Available from: http://dx.doi.org/10.1039/C5TA00011D.

[249] C. Li, J. Hu, S. Wang, J. Ren, B. Chen, T. Pan, X. Niu, F. Hao; *Lattice Strain Relaxation and Grain Homogenization for Efficient Inverted $MAPbI_3$ Perovskite Solar Cells*; The Journal of Physical Chemistry Letters; **2021**; 12 (19); 4569-4575; Available from: https://doi.org/10.1021/acs.jpclett.1c01074.

[250] Y. Lu, Z. Si, H. Liu, Y. Ge, J. Hu, Z. Zhang, X. Mu, K. Selvakumar, M. Sui; *In $CH_3NH_3PbI_3$ Perovskite Film, the Surface Termination Layer Dominates the Moisture Degradation Pathway*; Chemistry – A European Journal; **2021**; 27 (11); 3729-3736; Available from: https://doi.org/10.1002/chem.202003121.

[251] Q. Wang, Q. Dong, T. Li, A. Gruverman, J. Huang; *Thin Insulating Tunneling Contacts for Efficient and Water-Resistant Perovskite Solar Cells*; Advanced Materials; **2016**; 28 (31); 6734-6739; Available from: http://dx.doi.org/10.1002/adma.201600969.

[252] Z. Xiao, C. Bi, Y. Shao, Q. Dong, Q. Wang, Y. Yuan, C. Wang, Y. Gao, J. Huang; *Efficient, high yield perovskite photovoltaic devices grown by interdiffusion of solution-processed precursor stacking layers*; Energy & Environmental Science; **2014**; 7 (8); 2619-2623; Available from: http://dx.doi.org/10.1039/C4EE01138D.

[253] A. Baumann, S. Väth, P. Rieder, M. C. Heiber, K. Tvingstedt, V. Dyakonov; *Identification of Trap States in Perovskite Solar Cells*; The Journal of Physical Chemistry Letters; **2015**; 6 (12); 2350-2354; Available from: http://dx.doi.org/10.1021/acs.jpclett.5b00953.

[254] M. Fischer, K. Tvingstedt, A. Baumann, V. Dyakonov; *Doping Profile in Planar Hybrid Perovskite Solar Cells Identifying Mobile Ions*; ACS Applied Energy Materials; **2018**; 1 (10); 5129-5134; Available from: https://doi.org/10.1021/acsaem.8b01119.

[255] J. Huang, Y. Yuan, Y. Shao, Y. Yan; *Understanding the physical properties of hybrid perovskites for photovoltaic applications*; Nature Reviews Materials; **2017**; 2; 17042; Available from: https://doi.org/10.1038/natrevmats.2017.42.

[256] P. Löper, M. Stuckelberger, B. Niesen, J. Werner, M. Filipič, S.-J. Moon, J.-H. Yum, M. Topič, S. De Wolf, C. Ballif; *Complex Refractive Index Spectra of $CH_3NH_3PbI_3$ Perovskite Thin Films Determined by Spectroscopic Ellipsometry and Spectrophotometry*; The Journal of Physical Chemistry Letters; **2015**; 6 (1); 66-71; Available from: http://dx.doi.org/10.1021/jz502471h.

[257] K. Tvingstedt, O. Malinkiewicz, A. Baumann, C. Deibel, H. J. Snaith, V. Dyakonov, H. J. Bolink; *Radiative efficiency of lead iodide based perovskite solar cells*; Sci Rep; **2014**; 4; 6071; Available from: https://www.ncbi.nlm.nih.gov/pubmed/25317958.

[258] Q. Chuanjiang, M. Toshinori, F. Takashi, P. W. J., A. Chihaya; *Degradation Mechanisms of Solution-Processed Planar Perovskite Solar Cells: Thermally Stimulated Current Measurement for Analysis of Carrier Traps*; Advanced Materials; **2016**; 28 (3); 466-471; Available from: https://onlinelibrary.wiley.com/doi/abs/10.1002/adma.201502610.

[259] O. Malinkiewicz, A. Yella, Y. H. Lee, G. M. Espallargas, M. Graetzel, M. K. Nazeeruddin, H. J. Bolink; *Perovskite solar cells employing organic charge-transport layers*; Nat Photon; **2014**; 8 (2); 128-132; Available from: http://dx.doi.org/10.1038/nphoton.2013.341.

[260] M. Mangrulkar, A. G. Boldyreva, S. A. Lipovskikh, P. A. Troshin, K. J. Stevenson; *Influence of hydrazinium iodide on the intrinsic photostability of $MAPbI_3$ thin films and solar cells*; Journal of Materials Research; **2021**; Available from: https://doi.org/10.1557/s43578-021-00158-w.

[261] L. A. Muscarella, E. M. Hutter, J. M. Frost, G. G. Grimaldi, J. Versluis, H. J. Bakker, B. Ehrler; *Accelerated Hot-Carrier Cooling in $MAPbI_3$ Perovskite by Pressure-Induced Lattice Compression*; The Journal of Physical Chemistry Letters; **2021**; 12 (17); 4118-4124; Available from: https://doi.org/10.1021/acs.jpclett.1c00676.

[262] *Best Research-Cell Efficiencies*; National Renewable Energy Laboratory (NREL); **2021**; Available from: https://www.nrel.gov/pv/assets/pdfs/cell-pv-eff-emergingpv.202001042.pdf [accessed on 07.09.2021].

[263] Q. Wang, C. Bi, J. Huang; *Doped hole transport layer for efficiency enhancement in planar heterojunction organolead trihalide perovskite solar cells*; Nano Energy; **2015**; 15; 275-280; Available from: https://doi.org/10.1016/j.nanoen.2015.04.029.

[264] W. Zhang, B. Zhao, Z. He, X. Zhao, H. Wang, S. Yang, H. Wu, Y. Cao; *High-efficiency ITO-free polymer solar cells using highly conductive PEDOT:PSS/surfactant bilayer transparent anodes*; Energy & Environmental Science; **2013**; 6 (6); 1956-1964; Available from: http://pubs.rsc.org/en/content/articlepdf/2013/ee/c3ee41077c.

[265] D. H. Sin, H. Ko, S. B. Jo, M. Kim, G. Y. Bae, K. Cho; *Decoupling Charge Transfer and Transport at Polymeric Hole Transport Layer in Perovskite Solar Cells*; ACS Applied Materials & Interfaces; **2016**; 8 (10); 6546-6553; Available from: http://dx.doi.org/10.1021/acsami.5b12023.

[266] Z. Yu, Y. Xia, D. Du, J. Ouyang; *PEDOT:PSS Films with Metallic Conductivity through a Treatment with Common Organic Solutions of Organic Salts and Their Application as a Transparent Electrode of Polymer Solar Cells*; ACS Applied Materials & Interfaces; **2016**; 8 (18); 11629-11638; Available from: http://dx.doi.org/10.1021/acsami.6b00317.

[267] O. Bubnova, Z. U. Khan, H. Wang, S. Braun, D. R. Evans, M. Fabretto, P. Hojati-Talemi, D. Dagnelund, J.-B. Arlin, Y. H. Geerts, S. Desbief, D. W. Breiby, J. W. Andreasen, R. Lazzaroni, W. M. Chen, I. Zozoulenko, M. Fahlman, P. J. Murphy, M. Berggren, X. Crispin; *Semi-metallic polymers*; Nat Mater; **2014**; 13 (2); 190-194; Available from: http://dx.doi.org/10.1038/nmat3824.

[268] Y. Hou, W. Chen, D. Baran, T. Stubhan, N. A. Luechinger, B. Hartmeier, M. Richter, J. Min, S. Chen, C. O. R. Quiroz, N. Li, H. Zhang, T. Heumueller, G. J. Matt, A. Osvet, K. Forberich, Z.-G. Zhang, Y. Li, B. Winter, P. Schweizer, E. Spiecker, C. J. Brabec; *Overcoming the Interface Losses in Planar Heterojunction Perovskite-Based Solar Cells*; Advanced Materials; **2016**; 28 (25); 5112-5120; Available from: http://dx.doi.org/10.1002/adma.201504168.

[269] Q. Xue, G. Chen, M. Liu, J. Xiao, Z. Chen, Z. Hu, X.-F. Jiang, B. Zhang, F. Huang, W. Yang, H.-L. Yip, Y. Cao; *Improving Film Formation and Photovoltage of Highly Efficient Inverted-Type Perovskite Solar Cells through the Incorporation of New Polymeric Hole Selective Layers*; Advanced Energy Materials; **2016**; 6 (5); 1502021-n/a; Available from: http://dx.doi.org/10.1002/aenm.201502021.

[270] D. Zhao, M. Sexton, H.-Y. Park, G. Baure, J. C. Nino, F. So; *High-Efficiency Solution-Processed Planar Perovskite Solar Cells with a Polymer Hole Transport Layer*; Advanced Energy Materials; **2015**; 5 (6); 1401855; Available from: https://doi.org/10.1002/aenm.201401855.

[271] R. S. Sprick, M. Hoyos, M. S. Wrackmeyer, A. V. Sheridan Parry, I. M. Grace, C. Lambert, O. Navarro, M. L. Turner; *Extended conjugation in poly(triarylamine)s: synthesis, structure and impact on field-effect mobility*; Journal of Materials Chemistry C; **2014**; 2 (32); 6520-6528; Available from: http://dx.doi.org/10.1039/C4TC00871E.

[272] O. Malinkiewicz, C. Roldán-Carmona, A. Soriano, E. Bandiello, L. Camacho, M. K. Nazeeruddin, H. J. Bolink; *Metal-Oxide-Free Methylammonium Lead Iodide Perovskite-Based Solar Cells: the Influence of Organic Charge Transport Layers*; Advanced Energy Materials; **2014**; 4 (15); 1400345; Available from: https://onlinelibrary.wiley.com/doi/abs/10.1002/aenm.201400345.

[273] X. Xu, C. Ma, Y. Cheng, Y.-M. Xie, X. Yi, B. Gautam, S. Chen, H.-W. Li, C.-S. Lee, F. So, S.-W. Tsang; *Ultraviolet-ozone surface modification for non-wetting hole transport materials based inverted planar perovskite solar cells with efficiency exceeding 18%*; Journal of Power Sources; **2017**; 360; 157-165; Available from: https://www.sciencedirect.com/science/article/abs/pii/S0378775317307851?via%3Dihub.

[274] Z. Xiao, Q. Dong, C. Bi, Y. Shao, Y. Yuan, J. Huang; *Solvent Annealing of Perovskite-Induced Crystal Growth for Photovoltaic-Device Efficiency Enhancement*; Advanced Materials; **2014**; 26 (37); 6503-6509; Available from: https://onlinelibrary.wiley.com/doi/abs/10.1002/adma.201401685.

[275] Y. Shao, Z. Xiao, C. Bi, Y. Yuan, J. Huang; *Origin and elimination of photocurrent hysteresis by fullerene passivation in $CH_3NH_3PbI_3$ planar heterojunction solar cells*; Nature Communications; **2014**; 5 (1); 5784; Available from: https://doi.org/10.1038/ncomms6784.

[276] Q. Wang, Y. Shao, Q. Dong, Z. Xiao, Y. Yuan, J. Huang; *Large fill-factor bilayer iodine perovskite solar cells fabricated by a low-temperature solution-process*; Energy & Environmental Science; **2014**; 7 (7); 2359-2365; Available from: http://dx.doi.org/10.1039/C4EE00233D.

[277] M. Vogel, S. Doka, C. Breyer, M. C. Lux-Steiner, K. Fostiropoulos; *On the function of a bathocuproine buffer layer in organic photovoltaic cells*; Applied Physics Letters; **2006**; 89 (16); 163501; Available from: https://aip.scitation.org/doi/abs/10.1063/1.2362624.

[278] J. H. Kim, S. T. Williams, N. Cho, C.-C. Chueh, A. K.-Y. Jen; *Enhanced Environmental Stability of Planar Heterojunction Perovskite Solar Cells Based on Blade-Coating*; Advanced Energy Materials; **2015**; 5 (4); 1401229; Available from: https://doi.org/10.1002/aenm.201401229.

[279] T. Leijtens, G. E. Eperon, N. K. Noel, S. N. Habisreutinger, A. Petrozza, H. J. Snaith; *Stability of Metal Halide Perovskite Solar Cells*; Advanced Energy Materials; **2015**; 5 (20); 1500963; Available from: https://doi.org/10.1002/aenm.201500963.

[280] M. Bag, L. A. Renna, R. Y. Adhikari, S. Karak, F. Liu, P. M. Lahti, T. P. Russell, M. T. Tuominen, D. Venkataraman; *Kinetics of Ion Transport in Perovskite Active Layers and Its Implications for Active Layer Stability*; Journal of the American Chemical Society; **2015**; 137 (40); 13130-13137; Available from: https://doi.org/10.1021/jacs.5b08535.

[281] X. Li, M. Ibrahim Dar, C. Yi, J. Luo, M. Tschumi, S. M. Zakeeruddin, M. K. Nazeeruddin, H. Han, M. Grätzel; *Improved performance and stability of perovskite solar cells by crystal crosslinking with alkylphosphonic acid ω-ammonium chlorides*; Nature Chemistry; **2015**; 7 (9); 703-711; Available from: https://doi.org/10.1038/nchem.2324.

[282] C. Zheng, O. Rubel; *Unraveling the Water Degradation Mechanism of $CH_3NH_3PbI_3$*; The Journal of Physical Chemistry C; **2019**; 123 (32); 19385-19394; Available from: https://doi.org/10.1021/acs.jpcc.9b05516.

[283] S. Svanström, A. García Fernández, T. Sloboda, T. J. Jacobsson, H. Rensmo, U. B. Cappel; *X-ray stability and degradation mechanism of lead halide perovskites and lead halides*; Physical Chemistry Chemical Physics; **2021**; Available from: http://dx.doi.org/10.1039/D1CP01443A.

[284] J.-Y. Jeng, Y.-F. Chiang, M.-H. Lee, S.-R. Peng, T.-F. Guo, P. Chen, T.-C. Wen; *$CH_3NH_3PbI_3$ Perovskite/Fullerene Planar-Heterojunction Hybrid Solar Cells*; Advanced Materials; **2013**; 25 (27); 3727-3732; Available from: https://doi.org/10.1002/adma.201301327.

[285] A. Dualeh, P. Gao, S. I. Seok, M. K. Nazeeruddin, M. Grätzel; *Thermal Behavior of Methylammonium Lead-Trihalide Perovskite Photovoltaic Light Harvesters*; Chemistry of Materials; **2014**; 26 (21); 6160-6164; Available from: https://doi.org/10.1021/cm502468k.

[286] J. Bisquert, E. J. Juarez-Perez; *The Causes of Degradation of Perovskite Solar Cells*; The Journal of Physical Chemistry Letters; **2019**; 10 (19); 5889-5891; Available from: https://doi.org/10.1021/acs.jpclett.9b00613.

[287] T. A. Berhe, W.-N. Su, C.-H. Chen, C.-J. Pan, J.-H. Cheng, H.-M. Chen, M.-C. Tsai, L.-Y. Chen, A. A. Dubale, B.-J. Hwang; *Organometal halide perovskite solar cells: degradation and stability*; Energy & Environmental Science; **2016**; 9 (2); 323-356; Available from: http://dx.doi.org/10.1039/C5EE02733K.

[288] A. Uddin, M. B. Upama, H. Yi, L. Duan; *Encapsulation of Organic and Perovskite Solar Cells: A Review*; Coatings; **2019**; 9 (2); 65; Available from: https://www.mdpi.com/2079-6412/9/2/65.

[289] H. Kim, J. Lee, B. Kim, H. R. Byun, S. H. Kim, H. M. Oh, S. Baik, M. S. Jeong; *Enhanced Stability of $MAPbI_3$ Perovskite Solar Cells using Poly(p-chloro-xylylene) Encapsulation*; Scientific Reports; **2019**; 9 (1); 15461; Available from: https://doi.org/10.1038/s41598-019-51945-9.

[290] M. Adnan, J. K. Lee; *All Sequential Dip-Coating Processed Perovskite Layers from an Aqueous Lead Precursor for High Efficiency Perovskite Solar Cells*; Scientific Reports; **2018**; 8 (1); 2168; Available from: https://doi.org/10.1038/s41598-018-20296-2.

[291] Y. Zhong, R. Munir, J. Li, M.-C. Tang, M. R. Niazi, D.-M. Smilgies, K. Zhao, A. Amassian; *Blade-Coated Hybrid Perovskite Solar Cells with Efficiency > 17%: An In Situ Investigation*; ACS Energy Letters; **2018**; 3 (5); 1078-1085; Available from: https://doi.org/10.1021/acsenergylett.8b00428.

[292] G. Vavra; *On the kinematics of zircon growth and its petrogenetic significance: a cathodoluminescence study*; Contributions to Mineralogy and Petrology; **1990**; 106 (1); 90-99; Available from: https://doi.org/10.1007/BF00306410.

[293] H. Seifert; *Das Problem der Kristalltracht und seine technische Bedeutung*; Chemie Ingenieur Technik; **1955**; 27 (3); 135-142; Available from: https://doi.org/10.1002/cite.330270304.

[294] A. S. Vaughan; *Etching and morphology of poly(vinylidene fluoride)*; Journal of Materials Science; **1993**; 28 (7); 1805-1813; Available from: https://doi.org/10.1007/BF00595749.

[295] T. Y. Makogon, R. Larsen, C. A. Knight, E. Dendy Sloan; *Melt growth of tetrahydrofuran clathrate hydrate and its inhibition: method and first results*; Journal of Crystal Growth; **1997**; 179 (1); 258-262; Available from: https://doi.org/10.1016/S0022-0248(97)00118-8.

[296] W. Franke; *Tracht and habit of synthetic minerals under hydrothermal conditions*; European Journal of Mineralogy; **1989**; 1; 557-566; Available from: https://www.schweizerbart.de/papers/ejm/detail/1/82509/Tracht_and_habit_of_synthetic_minerals_grown_under?af=crossref.

[297] B. Chen, M. Yang, S. Priya, K. Zhu; *Origin of J–V Hysteresis in Perovskite Solar Cells*; The Journal of Physical Chemistry Letters; **2016**; 7 (5); 905-917; Available from: https://doi.org/10.1021/acs.jpclett.6b00215.

[298] Y. Wu, H. Shen, D. Walter, D. Jacobs, T. Duong, J. Peng, L. Jiang, Y.-B. Cheng, K. Weber; *On the Origin of Hysteresis in Perovskite Solar Cells*; Advanced Functional Materials; **2016**; 26 (37); 6807-6813; Available from: https://doi.org/10.1002/adfm.201602231.

[299] A. Y. Alsalloum, B. Turedi, K. Almasabi, X. Zheng, R. Naphade, S. D. Stranks, O. F. Mohammed, O. M. Bakr; *22.8%-Efficient single-crystal mixed-cation inverted perovskite solar cells with a near-optimal bandgap*; Energy & Environmental Science; **2021**; 14 (4); 2263-2268; Available from: http://dx.doi.org/10.1039/D0EE03839C.

[300] J. Zhao, G. Kong, S. Chen, Q. Li, B. Huang, Z. Liu, X. San, Y. Wang, C. Wang, Y. Zhen, H. Wen, P. Gao, J. Li; *Single crystalline $CH_3NH_3PbI_3$ self-grown on FTO/$TiO_2$ substrate for high efficiency perovskite solar cells*; Science Bulletin; **2017**; 62 (17); 1173-1176; Available from: https://doi.org/10.1016/j.scib.2017.08.022.

[301] Y. Huang, Y. Zhang, J. Sun, X. Wang, J. Sun, Q. Chen, C. Pan, H. Zhou; *The Exploration of Carrier Behavior in the Inverted Mixed Perovskite Single-Crystal Solar Cells*; Advanced Materials Interfaces; **2018**; 5 (14); 1800224; Available from: https://doi.org/10.1002/admi.201800224.

[302] J. Schlipf, A. M. Askar, F. Pantle, B. D. Wiltshire, A. Sura, P. Schneider, L. Huber, K. Shankar, P. Müller-Buschbaum; *Top-Down Approaches Towards Single Crystal Perovskite Solar Cells*; Scientific Reports; **2018**; 8 (1); 4906; Available from: https://doi.org/10.1038/s41598-018-23211-x.

[303] J. Wu, F. Ye, W. Yang, Z. Xu, D. Luo, R. Su, Y. Zhang, R. Zhu, Q. Gong; *Perovskite Single-Crystal Microarrays for Efficient Photovoltaic Devices*; Chemistry of Materials; **2018**; 30 (14); 4590-4596; Available from: https://doi.org/10.1021/acs.chemmater.8b00945.

[304] H.-L. Yue, H.-H. Sung, F.-C. Chen; *Seeded Space-Limited Crystallization of $CH_3NH_3PbI_3$ Single-Crystal Plates for Perovskite Solar Cells*; Advanced Electronic Materials; **2018**; 4 (7); 1700655; Available from: https://doi.org/10.1002/aelm.201700655.

[305] W. Kong, S. Wang, F. Li, C. Zhao, J. Xing, Y. Zou, Z. Yu, C.-H. Lin, Y. Shan, Y. H. Lai, Q. Dong, T. Wu, W. Yu, C. Guo; *Ultrathin Perovskite Monocrystals Boost the*

*Solar Cell Performance*; Advanced Energy Materials; **2020**; 10 (34); 2000453; Available from: https://doi.org/10.1002/aenm.202000453.

[306] Y. Lei, Y. Chen, R. Zhang, Y. Li, Q. Yan, S. Lee, Y. Yu, H. Tsai, W. Choi, K. Wang, Y. Luo, Y. Gu, X. Zheng, C. Wang, C. Wang, H. Hu, Y. Li, B. Qi, M. Lin, Z. Zhang, S. A. Dayeh, M. Pharr, D. P. Fenning, Y.-H. Lo, J. Luo, K. Yang, J. Yoo, W. Nie, S. Xu; *A fabrication process for flexible single-crystal perovskite devices*; Nature; **2020**; 583 (7818); 790-795; Available from: https://doi.org/10.1038/s41586-020-2526-z.

[307] J. Park, Y. E. Bak, L. Lee, H. Choi, M. A. Khan, M. M. Sung; *Interdigitated Hierarchical Integration of an Efficient Lateral Perovskite Single-Crystal Solar Cell*; ChemSusChem; **2020**; 13 (7); 1882-1889; Available from: https://doi.org/10.1002/cssc.201903038.

[308] Z. Chen, Q. Dong, Y. Liu, C. Bao, Y. Fang, Y. Lin, S. Tang, Q. Wang, X. Xiao, Y. Bai, Y. Deng, J. Huang; *Thin single crystal perovskite solar cells to harvest below-bandgap light absorption*; Nature Communications; **2017**; 8 (1); 1890; Available from: https://doi.org/10.1038/s41467-017-02039-5.

[309] M. Stolterfoht, C. M. Wolff, J. A. Márquez, S. Zhang, C. J. Hages, D. Rothhardt, S. Albrecht, P. L. Burn, P. Meredith, T. Unold, D. Neher; *Visualization and suppression of interfacial recombination for high-efficiency large-area pin perovskite solar cells*; Nature Energy; **2018**; 3 (10); 847-854; Available from: https://doi.org/10.1038/s41560-018-0219-8.

[310] J. Höcker, V. Dyakonov; *E. Hybrid perovskite crystals: Growth, characterization and application*; editor: L. Schmidt-Mende, V. Dyakonov, S. Olthof; In: *Roadmap: Organic-inorganic hybrid perovskite semiconductors and devices*; APL Materials; **2021**; 9 (109202); 28-30; Available from: https://aip.scitation.org/doi/10.1063/5.0047616.

[311] S. Shrestha, G. J. Matt, A. Osvet, D. Niesner, R. Hock, C. J. Brabec; *Assessing Temperature Dependence of Drift Mobility in Methylammonium Lead Iodide Perovskite Single Crystals*; The Journal of Physical Chemistry C; **2018**; 122 (11); 5935-5939; Available from: https://doi.org/10.1021/acs.jpcc.8b00341.

[312] H. Wei, D. DeSantis, W. Wei, Y. Deng, D. Guo, T. J. Savenije, L. Cao, J. Huang; *Dopant compensation in alloyed $CH_3NH_3PbBr_{3-x}Cl_x$ perovskite single crystals for gamma-ray spectroscopy*; Nature Materials; **2017**; 16 (8); 826-833; Available from: https://doi.org/10.1038/nmat4927.

[313] Y. Liu, Y. Zhang, Z. Yang, J. Feng, Z. Xu, Q. Li, M. Hu, H. Ye, X. Zhang, M. Liu, K. Zhao, S. Liu; *Low-temperature-gradient crystallization for multi-inch high-quality perovskite single crystals for record performance photodetectors*; Materials Today; **2019**; 22; 67-75; Available from: https://doi.org/10.1016/j.mattod.2018.04.002.

[314] Z. Yuan, W. Huang, S. Ma, G. Ouyang, W. Hu, W. Zhang; *A high performance perovskite $CH_3NH_3PbCl_3$ single crystal photodetector: benefiting from an evolutionary preparation process*; Journal of Materials Chemistry C; **2019**; 7 (18); 5442-5450; Available from: http://dx.doi.org/10.1039/C9TC00892F.

[315] J. Song, Q. Cui, J. Li, J. Xu, Y. Wang, L. Xu, J. Xue, Y. Dong, T. Tian, H. Sun, H. Zeng; *Ultralarge All-Inorganic Perovskite Bulk Single Crystal for High-Performance Visible–Infrared Dual-Modal Photodetectors*; Advanced Optical Materials; **2017**; 5 (12); 1700157; Available from: https://doi.org/10.1002/adom.201700157.

[316] L. Ma, Z. Yan, X. Zhou, Y. Pi, Y. Du, J. Huang, K. Wang, K. Wu, C. Zhuang, X. Han; *A polymer controlled nucleation route towards the generalized growth of organic-inorganic perovskite single crystals*; Nature Communications; **2021**; 12 (1); 2023; Available from: https://doi.org/10.1038/s41467-021-22193-1.

[317] W. Wei, Y. Zhang, Q. Xu, H. Wei, Y. Fang, Q. Wang, Y. Deng, T. Li, A. Gruverman, L. Cao, J. Huang; *Monolithic integration of hybrid perovskite single crystals with heterogenous substrate for highly sensitive X-ray imaging*; Nature Photonics; **2017**; 11 (5); 315-321; Available from: https://doi.org/10.1038/nphoton.2017.43.

# 10 Appendix

## A XRF, EDX, and XRD Data of the $MAPb(Cl_{1-x}Br_x)_3$ and $MAPb(Br_{1-y}I_y)_3$ Perovskite Crystals and Powders

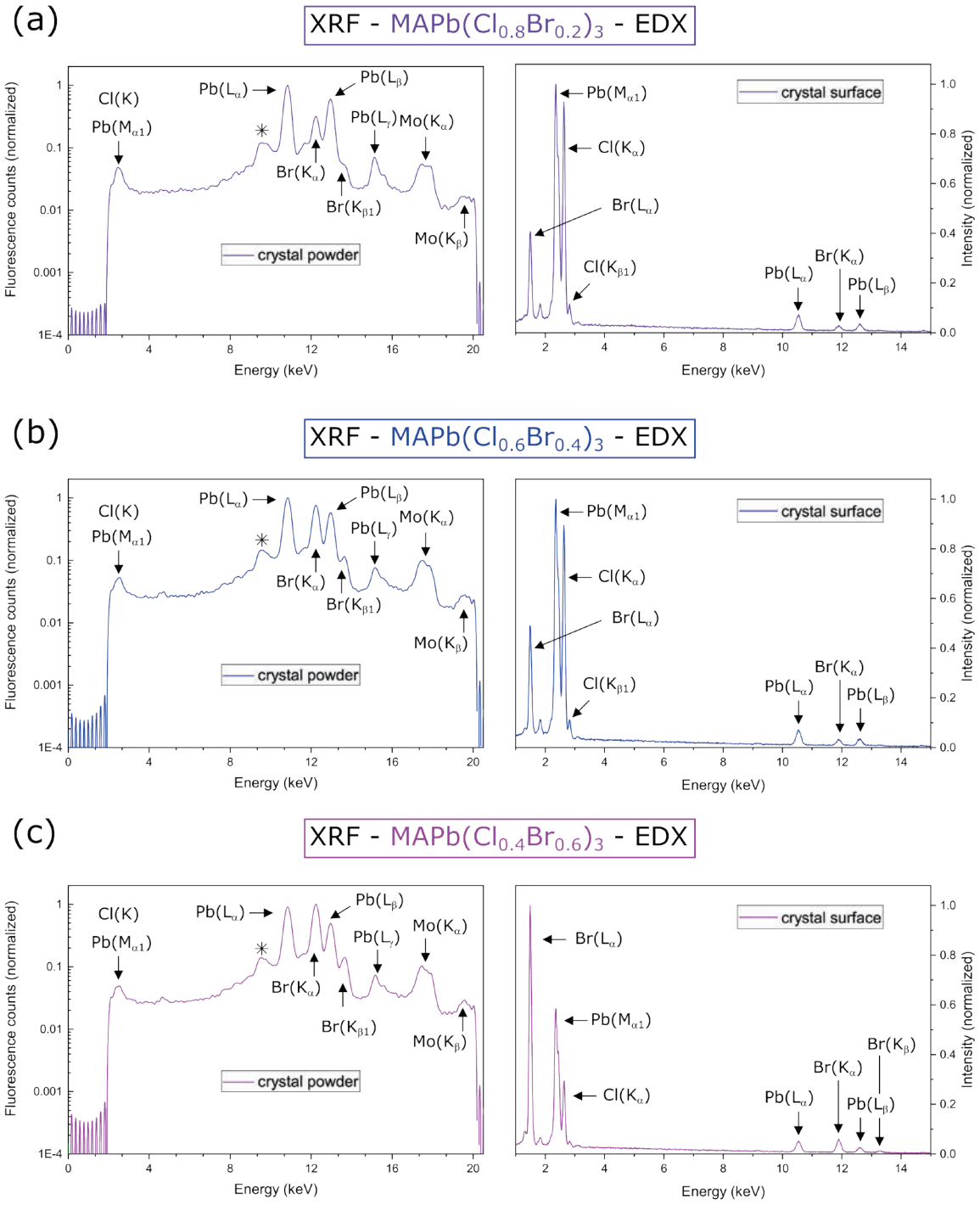


**Figure A1.** (a) – (d) XRF and EDX measurements of the double-halide $MAPb(Cl_{1-x}Br_x)_3$ (y = 0.2, 0.4, 0.6 and 0.8) perovskites. The asterisks (*) in the XRF spectra can be assigned to the sample holder.

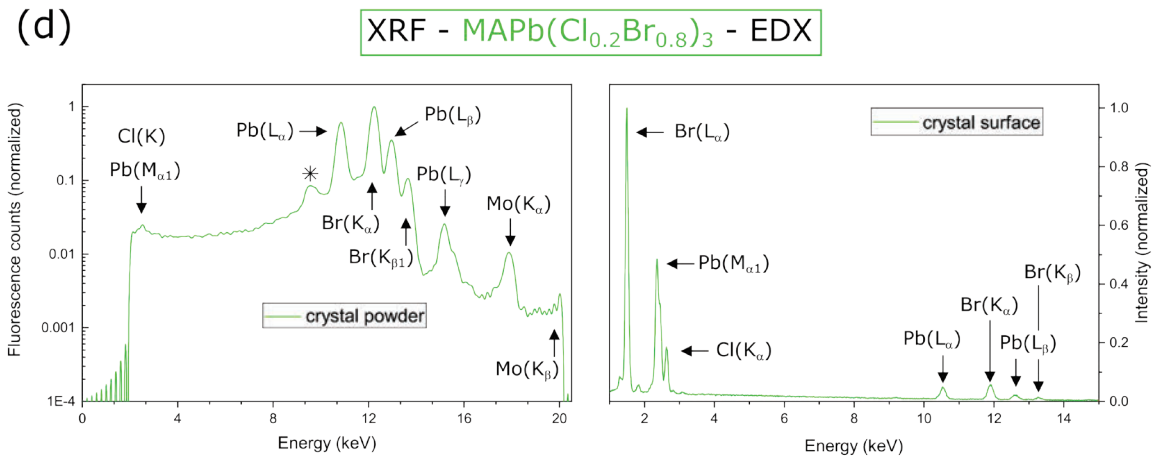


**Figure A1.** (continued).

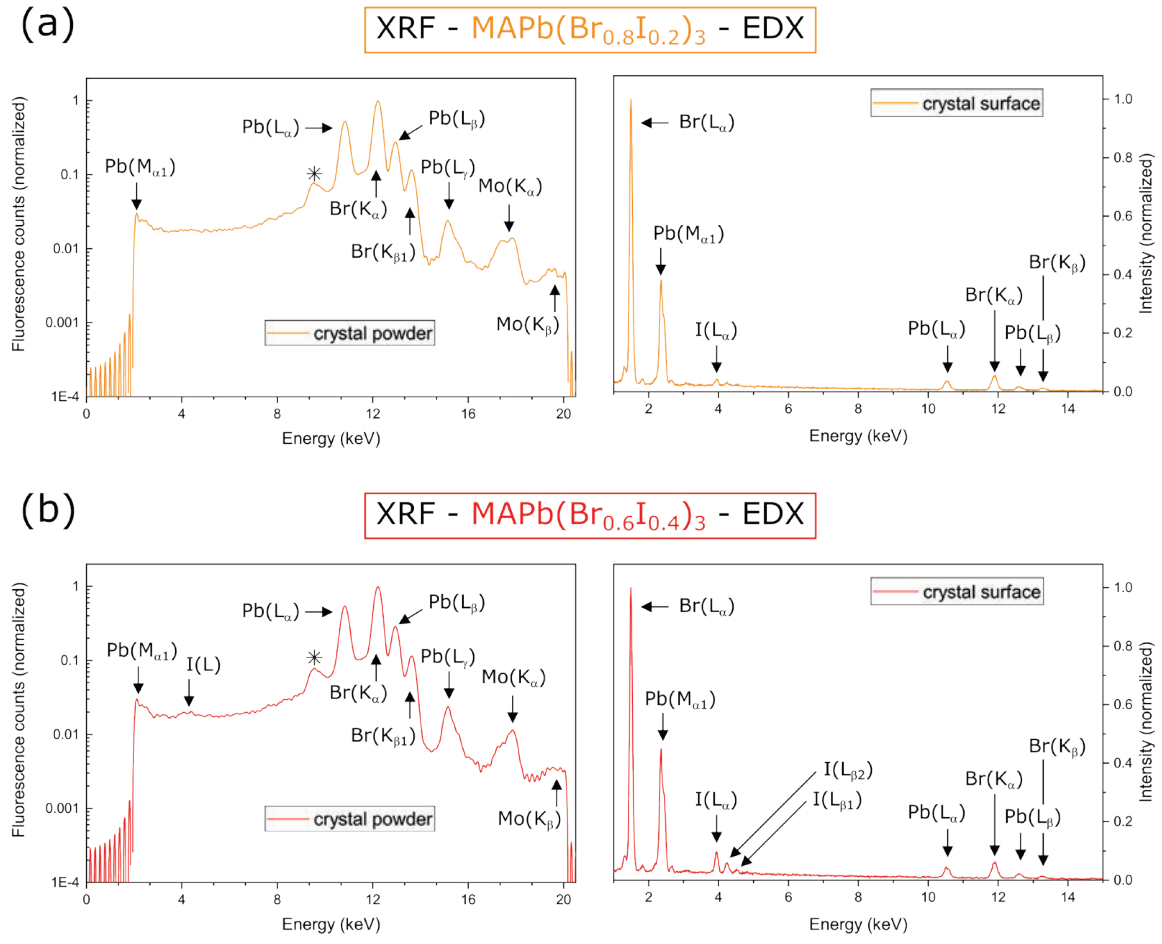


**Figure A2.** XRF and EDX measurements of the double-halide $MAPb(Br_{1-y}I_y)_3$ (y = 0.2, 0.4, 0.6, 0.8 and 0.9) perovskites. The asterisks (*) in the XRF spectra can be assigned to the sample holder.

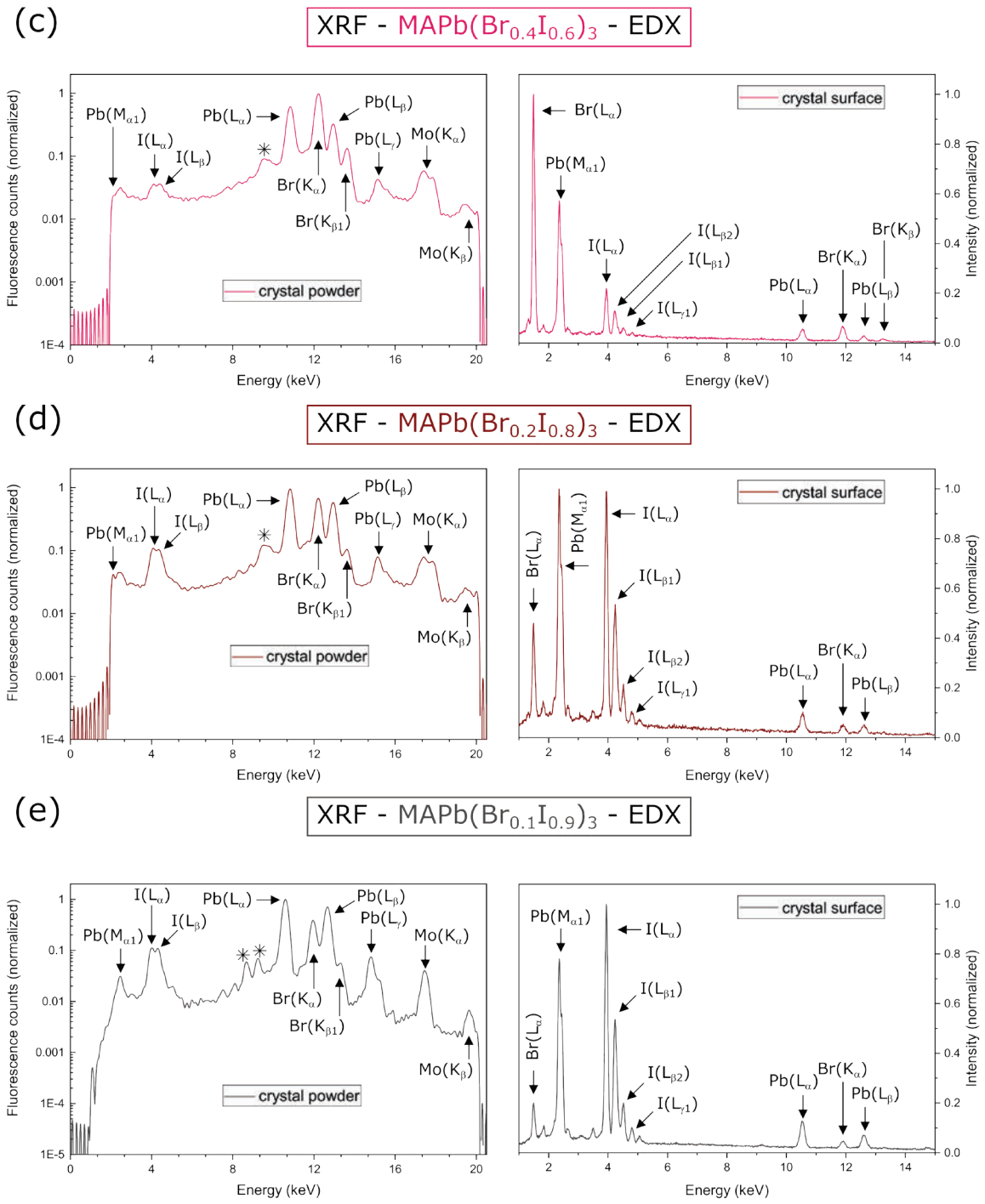


**Figure A2.** (continued).

**Table A1.** Theoretical mass fractions for the elements carbon (C), hydrogen (H), nitrogen (N), lead (Pb), chlorine (Cl), bromine (Br), and iodine (I) to determine the stoichiometric ratios of the methylammonium lead trihalide perovskites.

| Stoichiometry | C [%] | H [%] | N [%] | Pb [%] | Cl [%] | Br [%] | I [%] |
|---|---|---|---|---|---|---|---|
| $MAPbCl_3$ | 3.48 | 1.75 | 4.05 | 59.95 | 30.77 | - | - |
| $MAPb(Cl_{0.8}Br_{0.2})_3$ | 3.23 | 1.62 | 3.76 | 55.66 | 22.86 | 12.88 | - |
| $MAPb(Cl_{0.6}Br_{0.4})_3$ | 3.01 | 1.52 | 3.51 | 51.93 | 16.00 | 24.03 | - |
| $MAPb(Cl_{0.4}Br_{0.6})_3$ | 2.82 | 1.42 | 3.29 | 48.68 | 10.00 | 33.79 | - |
| $MAPb(Cl_{0.2}Br_{0.8})_3$ | 2.66 | 1.34 | 3.10 | 45.81 | 4.70 | 42.40 | - |
| $MAPbBr_3$ | 2.51 | 1.26 | 2.92 | 43.26 | - | 50.05 | - |
| $MAPb(Br_{0.8}I_{0.2})_3$ | 2.37 | 1.19 | 2.76 | 40.85 | - | 37.81 | 15.01 |
| $MAPb(Br_{0.6}I_{0.4})_3$ | 2.24 | 1.13 | 2.62 | 38.70 | - | 26.87 | 28.44 |
| $MAPb(Br_{0.4}I_{0.6})_3$ | 2.13 | 1.07 | 2.49 | 36.77 | - | 17.01 | 40.53 |
| $MAPb(Br_{0.2}I_{0.8})_3$ | 2.03 | 1.02 | 2.37 | 35.01 | - | 8.10 | 51.47 |
| $MAPb(Br_{0.1}I_{0.9})_3$ | 1.98 | 1.00 | 2.31 | 34.20 | - | 3.96 | 56.55 |
| $MAPbI_3$ | 1.94 | 0.98 | 2.26 | 33.42 | - | - | 61.41 |

**Table A2.** Evaluation of the XRD fitting data to determine the lattice plane ($d_{hkl}$) and the lattice constant (a) of the $MAPbCl_3$ crystal powder.

| Number | Fitting data 2θ (°) | Fitting data q ($Å^{-1}$) | Miller indices (hkl) | $d_{hkl}$ (Å) | a (Å) |
|---|---|---|---|---|---|
| 1 | 15.5558 | 1.10392 | 100 | 5.69172 | 5.69172 |
| 2 | 22.075 | 1.56167 | 110 | 4.02337 | 5.6899 |
| 3 | 27.0934 | 1.91068 | 111 | 3.28845 | 5.69577 |
| 4 | 31.4168 | 2.20844 | 200 | 2.84507 | 5.69015 |
| 5 | 35.2538 | 2.47009 | 210 | 2.54371 | 5.68791 |
| 6 | 38.7408 | 2.70547 | 211 | 2.3224 | 5.6887 |
| 7 | 45.0403 | 3.1242 | 220 | 2.01113 | 5.68834 |
| 8 | 47.9315 | 3.3133 | 221 | 1.89635 | 5.68906 |
| 9 | 47.9315 | 3.3133 | 300 | 1.89635 | 5.68906 |
| 10 | 50.7273 | 3.49415 | 310 | 1.7982 | 5.6864 |
| 11 | 53.404 | 3.66536 | 311 | 1.71421 | 5.68539 |
| 12 | 55.9626 | 3.82714 | 222 | 1.64175 | 5.68718 |
| 13 | 58.4722 | 3.98396 | 320 | 1.57712 | 5.68638 |

**Table A3.** Evaluation of the XRD fitting data to determine the lattice plane ($d_{hkl}$) and the lattice constant (a) of the $MAPbBr_3$ crystal powder. Reproduced from Ref. [26] with permission from the Royal Society of Chemistry.

| Number | Fitting data 2θ (°) | Fitting data q ($Å^{-1}$) | Miller indices (hkl) | $d_{hkl}$ (Å) | a (Å) |
|---|---|---|---|---|---|
| 1 | 14.8925 | 1.05712 | 100 | 5.9437 | 5.9437 |
| 2 | 21.1091 | 1.49413 | 110 | 4.20524 | 5.9471 |
| 3 | 25.972 | 1.83299 | 111 | 3.42784 | 5.93719 |
| 4 | 30.0793 | 2.11664 | 200 | 2.96847 | 5.93694 |
| 5 | 33.7207 | 2.36586 | 210 | 2.65577 | 5.93849 |
| 6 | 37.0536 | 2.59188 | 211 | 2.42418 | 5.93801 |
| 7 | 43.0706 | 2.99423 | 220 | 2.09843 | 5.93526 |
| 8 | 45.8421 | 3.17685 | 221 | 1.9778 | 5.93341 |
| 9 | 45.8421 | 3.17685 | 300 | 1.9778 | 5.93341 |
| 10 | 48.4668 | 3.34808 | 310 | 1.87665 | 5.93449 |
| 11 | 53.4439 | 3.66789 | 222 | 1.71302 | 5.93409 |
| 12 | 55.8065 | 3.81732 | 320 | 1.64597 | 5.93462 |
| 13 | 58.1461 | 3.96369 | 321 | 1.58519 | 5.93122 |

**Table A4.** Evaluation of the XRD fitting data to determine the lattice plane ($d_{hkl}$) and the lattice constants (a/c) of the $MAPbI_3$ crystal powder.

| Number | Fitting data 2θ (°) | Fitting data q ($Å^{-1}$) | Miller indices (hkl) | $d_{hkl}$ (Å) | a/c (Å) |
|---|---|---|---|---|---|
| 1 | 14.0011 | 0.99417 | 002 | 6.32005 | c = 12.64009 |
| 2 | 14.0011 | 0.99417 | 110 | 6.32005 | a = 8.93789 |
| 3 | 19.8789 | 1.40796 | 200 | 4.46261 | 8.92523 |
| 4 | 24.4012 | 1.72386 | 211 | 3.64483 | 8.92797 |
| 5 | 28.0575 | 1.97733 | 004 | 3.17761 | 12.71043 |
| 6 | 28.362 | 1.99835 | 220 | 3.14418 | 8.89309 |
| 7 | 30.8298 | 2.16819 | 114 | 2.89789 | 12.29472 |
| 8 | 31.5439 | 2.21715 | 310 | 2.8339 | 8.96158 |
| 9 | 31.7856 | 2.2337 | 310 | 2.8129 | 8.89517 |
| 10 | 40.3438 | 2.81285 | 400 | 2.23375 | 8.93498 |
| 11 | 42.4954 | 2.95611 | 006 | 2.12549 | 12.75296 |
| 12 | 42.7187 | 2.97092 | 411 | 2.1149 | 8.97275 |
| 13 | 42.9673 | 2.98739 | 330 | 2.10324 | 8.92327 |
| 14 | 45.6284 | 3.16283 | 116 | 1.98657 | 12.24603 |
| 15 | 47.3202 | 3.27349 | 206 | 1.91941 | 12.13944 |
| 16 | 50.1059 | 3.45413 | 422 | 1.81903 | 8.91141 |
| 17 | 51.9782 | 3.57441 | 431 | 1.75783 | 8.96319 |
| 18 | 52.3969 | 3.60117 | 510 | 1.74476 | 8.89657 |
| 19 | 54.4851 | 3.73394 | 217 | 1.68272 | 12.36543 |
| 20 | 58.1327 | 3.96286 | 008 | 1.58552 | 12.68415 |
| 21 | 58.7547 | 4.0015 | 440 | 1.57021 | 8.88244 |

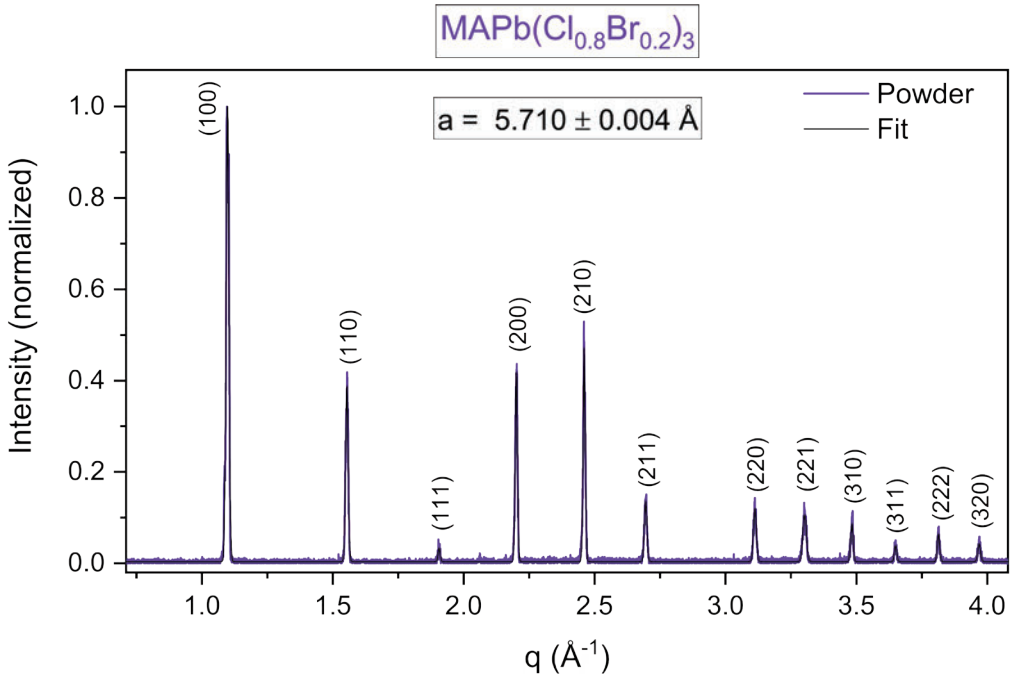


**Figure A3.** XRD pattern of the MAPb($Cl_{0.8}Br_{0.2}$)$_3$ crystal powder. The evaluation of the fit resulted in a lattice constant of a = 5.710 Å. The crystal structure is simple cubic.

**Table A5.** Evaluation of the XRD fitting data to determine the lattice plane ($d_{hkl}$) and the lattice constant (a) of the MAPb($Cl_{0.8}Br_{0.2}$)$_3$ crystal powder.

| Number | Fitting data 2θ (°) | Fitting data q (Å$^{-1}$) | Miller indices (hkl) | $d_{hkl}$ (Å) | a (Å) |
|---|---|---|---|---|---|
| 1 | 15.479 | 1.0985 | 100 | 5.71979 | 5.71979 |
| 2 | 21.9682 | 1.55421 | 110 | 4.04269 | 5.71722 |
| 3 | 27.0354 | 1.90667 | 111 | 3.29538 | 5.70776 |
| 4 | 31.3095 | 2.20109 | 200 | 2.85458 | 5.70916 |
| 5 | 35.109 | 2.46026 | 210 | 2.55387 | 5.71063 |
| 6 | 38.5818 | 2.69479 | 211 | 2.33161 | 5.71125 |
| 7 | 44.8553 | 3.11204 | 220 | 2.019 | 5.71058 |
| 8 | 47.762 | 3.30227 | 221 | 1.90269 | 5.70806 |
| 9 | 50.5464 | 3.48251 | 310 | 1.80421 | 5.70541 |
| 10 | 53.1674 | 3.6503 | 311 | 1.72128 | 5.70883 |
| 11 | 55.7382 | 3.81302 | 222 | 1.64782 | 5.70823 |
| 12 | 58.2301 | 3.96892 | 320 | 1.5831 | 5.70794 |

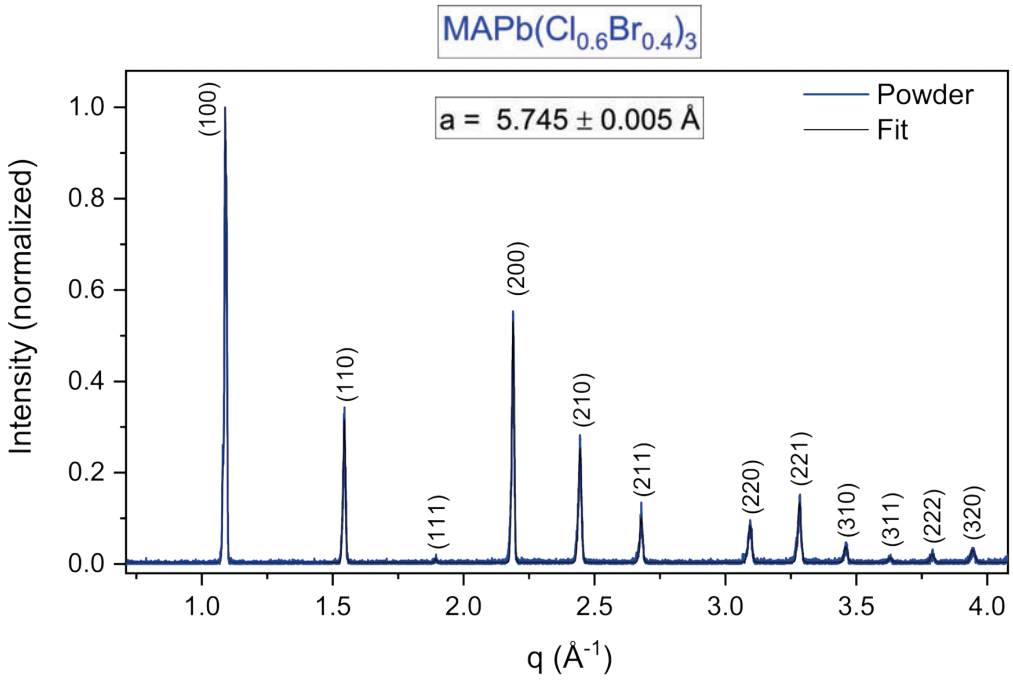


**Figure A4.** XRD pattern of the $MAPb(Cl_{0.6}Br_{0.4})_3$ crystal powder. The evaluation of the fit resulted in a lattice constant of a = 5.745 Å. The crystal structure is simple cubic.

**Table A6.** Evaluation of the XRD fitting data to determine the lattice plane ($d_{hkl}$) and the lattice constant (a) of the $MAPb(Cl_{0.6}Br_{0.4})_3$ crystal powder.

| Number | Fitting data 2θ (°) | Fitting data q (Å$^{-1}$) | Miller indices (hkl) | $d_{hkl}$ (Å) | a (Å) |
|---|---|---|---|---|---|
| 1 | 15.3777 | 1.09135 | 100 | 5.75724 | 5.75724 |
| 2 | 21.8324 | 1.54472 | 110 | 4.06753 | 5.75235 |
| 3 | 26.8633 | 1.89475 | 111 | 3.3161 | 5.74365 |
| 4 | 31.1349 | 2.18912 | 200 | 2.87019 | 5.74038 |
| 5 | 34.8815 | 2.44482 | 210 | 2.57 | 5.7467 |
| 6 | 38.342 | 2.67867 | 211 | 2.34564 | 5.74561 |
| 7 | 44.5865 | 3.09434 | 220 | 2.03054 | 5.74324 |
| 8 | 47.4756 | 3.28362 | 300 | 1.91349 | 5.74048 |
| 9 | 47.4756 | 3.28362 | 221 | 1.91349 | 5.74048 |
| 10 | 50.215 | 3.46117 | 310 | 1.81534 | 5.7406 |
| 11 | 52.8378 | 3.62931 | 311 | 1.73124 | 5.74186 |
| 12 | 55.3775 | 3.79031 | 222 | 1.6577 | 5.74244 |
| 13 | 57.8172 | 3.94321 | 320 | 1.59342 | 5.74515 |

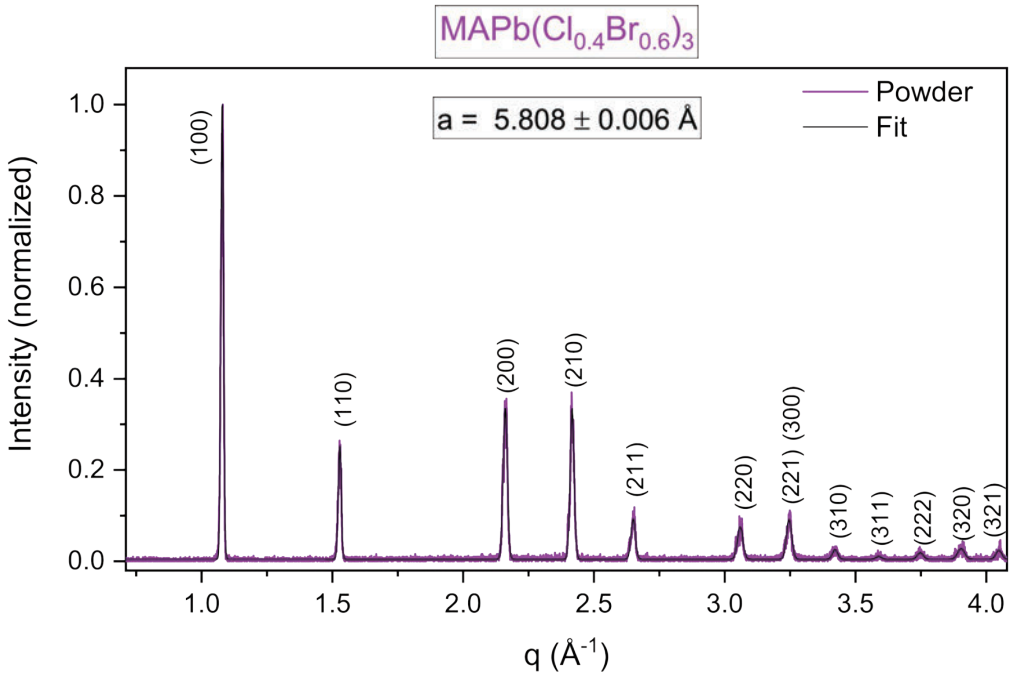


**Figure A5.** XRD pattern of the $MAPb(Cl_{0.4}Br_{0.6})_3$ crystal powder. The evaluation of the fit resulted in a lattice constant of a = 5.808 Å. The crystal structure is simple cubic.

**Table A7.** Evaluation of the XRD fitting data to determine the lattice plane ($d_{hkl}$) and the lattice constant (a) of the $MAPb(Cl_{0.4}Br_{0.6})_3$ crystal powder.

| Number | Fitting data 2θ (°) | Fitting data q ($Å^{-1}$) | Miller indices (hkl) | $d_{hkl}$ (Å) | a (Å) |
|---|---|---|---|---|---|
| 1 | 15.2063 | 1.07926 | 100 | 5.82174 | 5.82174 |
| 2 | 21.5977 | 1.52831 | 110 | 4.11119 | 5.81411 |
| 3 | 30.7349 | 2.16168 | 200 | 2.90663 | 5.81325 |
| 4 | 34.4694 | 2.41681 | 210 | 2.59978 | 5.81329 |
| 5 | 37.9349 | 2.65128 | 211 | 2.36987 | 5.80496 |
| 6 | 44.0913 | 3.0617 | 220 | 2.05219 | 5.80447 |
| 7 | 46.9292 | 3.24798 | 221 | 1.93449 | 5.80347 |
| 8 | 46.9292 | 3.24798 | 300 | 1.93449 | 5.80347 |
| 9 | 49.6123 | 3.42227 | 310 | 1.83597 | 5.80584 |
| 10 | 52.234 | 3.59076 | 311 | 1.74982 | 5.80349 |
| 11 | 54.6779 | 3.74614 | 222 | 1.67724 | 5.81014 |
| 12 | 57.1666 | 3.90261 | 320 | 1.61 | 5.80492 |
| 13 | 59.545 | 4.05043 | 321 | 1.55124 | 5.80421 |

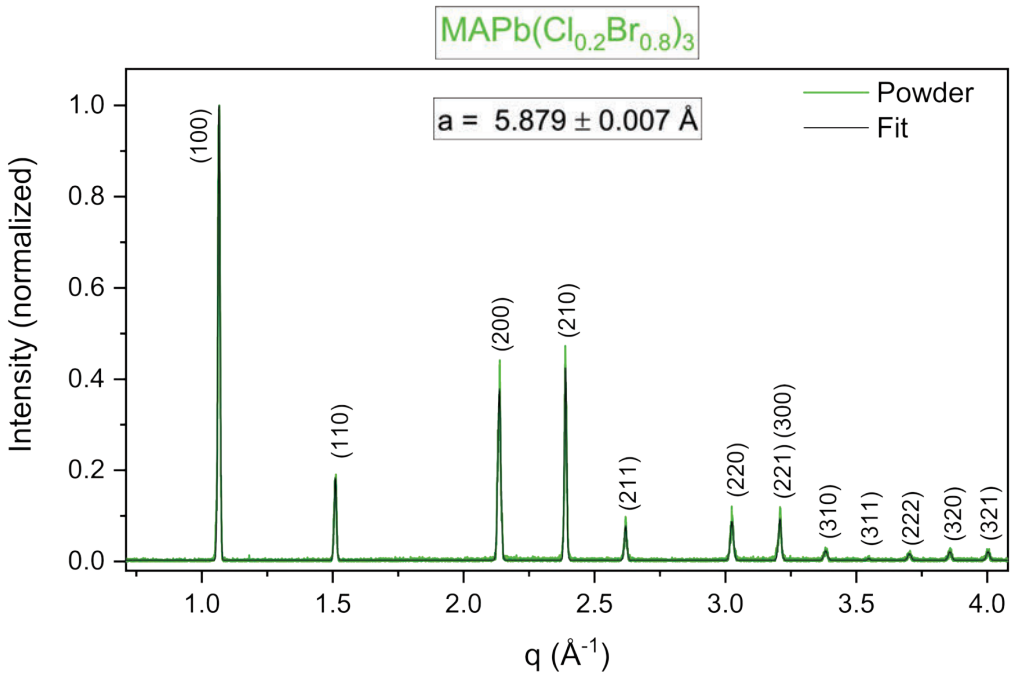


**Figure A6.** XRD pattern of the $MAPb(Cl_{0.2}Br_{0.8})_3$ crystal powder. The evaluation of the fit resulted in a lattice constant of a = 5.879 Å. The crystal structure is simple cubic.

**Table A8.** Evaluation of the XRD fitting data to determine the lattice plane ($d_{hkl}$) and the lattice constant (a) of the $MAPb(Cl_{0.2}Br_{0.8})_3$ crystal powder.

| Number | Fitting data 2θ (°) | Fitting data q (Å$^{-1}$) | Miller indices (hkl) | $d_{hkl}$ (Å) | a (Å) |
|---|---|---|---|---|---|
| 1 | 15.0149 | 1.06576 | 100 | 5.89552 | 5.89552 |
| 2 | 21.3366 | 1.51005 | 110 | 4.16091 | 5.88442 |
| 3 | 30.3654 | 2.1363 | 200 | 2.94115 | 5.88229 |
| 4 | 34.0631 | 2.38918 | 210 | 2.62986 | 5.88054 |
| 5 | 37.4481 | 2.61849 | 211 | 2.39955 | 5.87767 |
| 6 | 43.5295 | 3.02459 | 220 | 2.07737 | 5.87568 |
| 7 | 46.316 | 3.20789 | 221 | 1.95866 | 5.87599 |
| 8 | 46.316 | 3.20789 | 300 | 1.95866 | 5.87599 |
| 9 | 49.0214 | 3.38404 | 310 | 1.85671 | 5.87143 |
| 10 | 51.5156 | 3.54478 | 311 | 1.77252 | 5.87878 |
| 11 | 53.995 | 3.70289 | 222 | 1.69683 | 5.878 |
| 12 | 56.4617 | 3.85847 | 320 | 1.62841 | 5.87132 |
| 13 | 58.7831 | 4.00326 | 321 | 1.56952 | 5.87259 |

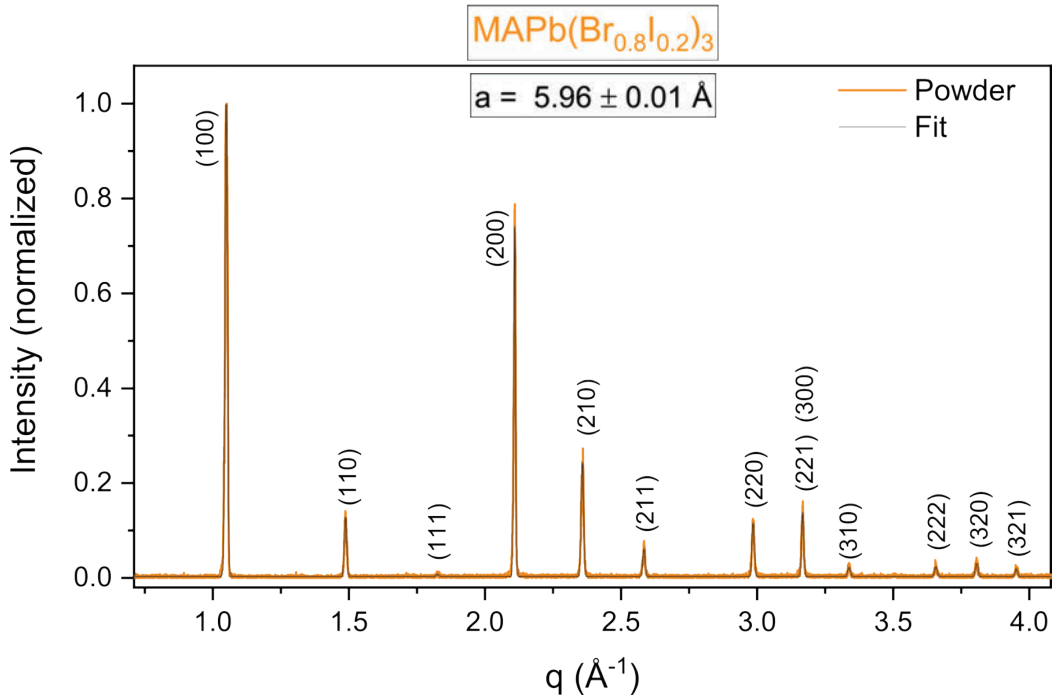


**Figure A7.** XRD pattern of the $MAPb(Br_{0.8}I_{0.2})_3$ crystal powder. The evaluation of the fit resulted in a lattice constant of a = 5.96 Å. The crystal structure is simple cubic.

**Table A9.** Evaluation of the XRD fitting data to determine the lattice plane ($d_{hkl}$) and the lattice constant (a) of the $MAPb(Br_{0.8}I_{0.2})_3$ crystal powder.

| Number | Fitting data 2θ (°) | Fitting data q ($Å^{-1}$) | Miller indices (hkl) | $d_{hkl}$ (Å) | a (Å) |
|---|---|---|---|---|---|
| 1 | 14.7935 | 1.05013 | 100 | 5.98325 | 5.98325 |
| 2 | 21.0179 | 1.48775 | 110 | 4.22328 | 5.97262 |
| 3 | 25.8478 | 1.82437 | 111 | 3.44403 | 5.96523 |
| 4 | 29.9728 | 2.10932 | 200 | 2.97877 | 5.95754 |
| 5 | 33.6095 | 2.35828 | 210 | 2.6643 | 5.95756 |
| 6 | 36.9421 | 2.58435 | 211 | 2.43124 | 5.95531 |
| 7 | 42.9337 | 2.98516 | 220 | 2.1048 | 5.95328 |
| 8 | 45.6904 | 3.1669 | 221 | 1.98402 | 5.95205 |
| 9 | 45.6904 | 3.1669 | 300 | 1.98402 | 5.95205 |
| 10 | 48.2809 | 3.33601 | 310 | 1.88344 | 5.95596 |
| 11 | 53.2547 | 3.65586 | 222 | 1.71866 | 5.95362 |
| 12 | 55.6126 | 3.80512 | 320 | 1.65125 | 5.95365 |
| 13 | 57.9709 | 3.95279 | 321 | 1.58956 | 5.94758 |

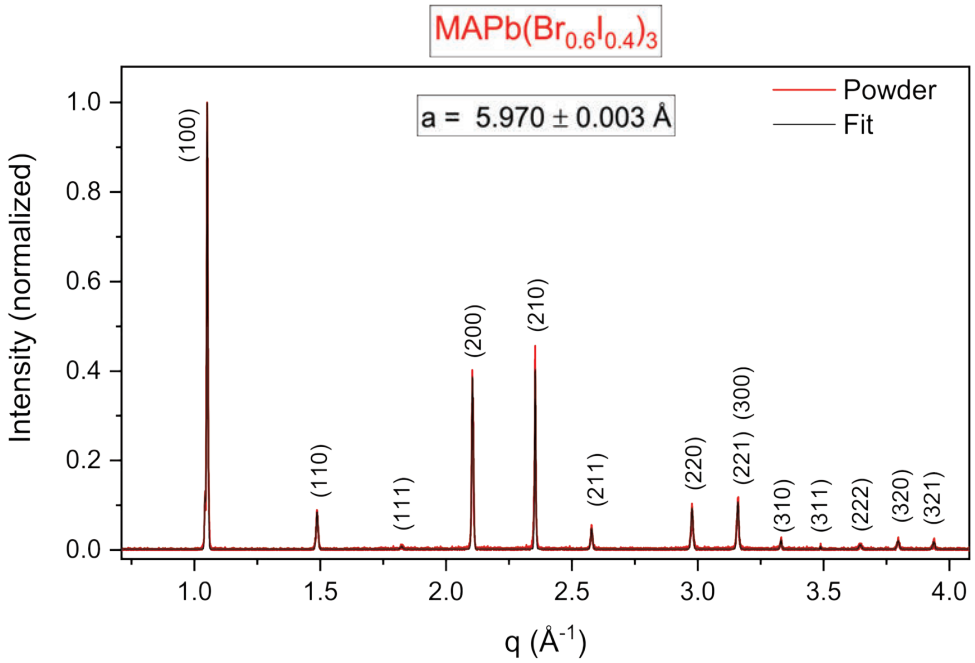


**Figure A8.** XRD pattern of the $MAPb(Br_{0.6}I_{0.4})_3$ crystal powder. The evaluation of the fit resulted in a lattice constant of a = 5.97 Å. The crystal structure is simple cubic.

**Table A10.** Evaluation of the XRD fitting data to determine the lattice plane ($d_{hkl}$) and the lattice constant (a) of the $MAPb(Br_{0.6}I_{0.4})_3$ crystal powder.

| Number | Fitting data 2θ (°) | Fitting data q ($Å^{-1}$) | Miller indices (hkl) | $d_{hkl}$ (Å) | a (Å) |
|---|---|---|---|---|---|
| 1 | 14.8096 | 1.05127 | 100 | 6.02281 | 5.97678 |
| 2 | 21.0201 | 1.4879 | 110 | 5.97678 | 5.972 |
| 3 | 25.8393 | 1.82378 | 111 | 4.22284 | 5.96716 |
| 4 | 29.9128 | 2.10519 | 200 | 3.44514 | 5.96922 |
| 5 | 33.5475 | 2.35406 | 210 | 2.98461 | 5.96826 |
| 6 | 36.8527 | 2.57831 | 211 | 2.66909 | 5.96925 |
| 7 | 42.8125 | 2.97713 | 220 | 2.43694 | 5.96934 |
| 8 | 45.5759 | 3.15939 | 221 | 2.11048 | 5.9662 |
| 9 | 45.5759 | 3.15939 | 300 | 1.98873 | 5.9662 |
| 10 | 48.2088 | 3.33133 | 310 | 1.98873 | 5.96434 |
| 11 | 50.6294 | 3.48786 | 311 | 1.88609 | 5.97472 |
| 12 | 53.0882 | 3.64526 | 222 | 1.80145 | 5.97093 |
| 13 | 55.4691 | 3.79608 | 320 | 1.72366 | 5.96783 |
| 14 | 57.7297 | 3.93776 | 321 | 1.65518 | 5.97028 |

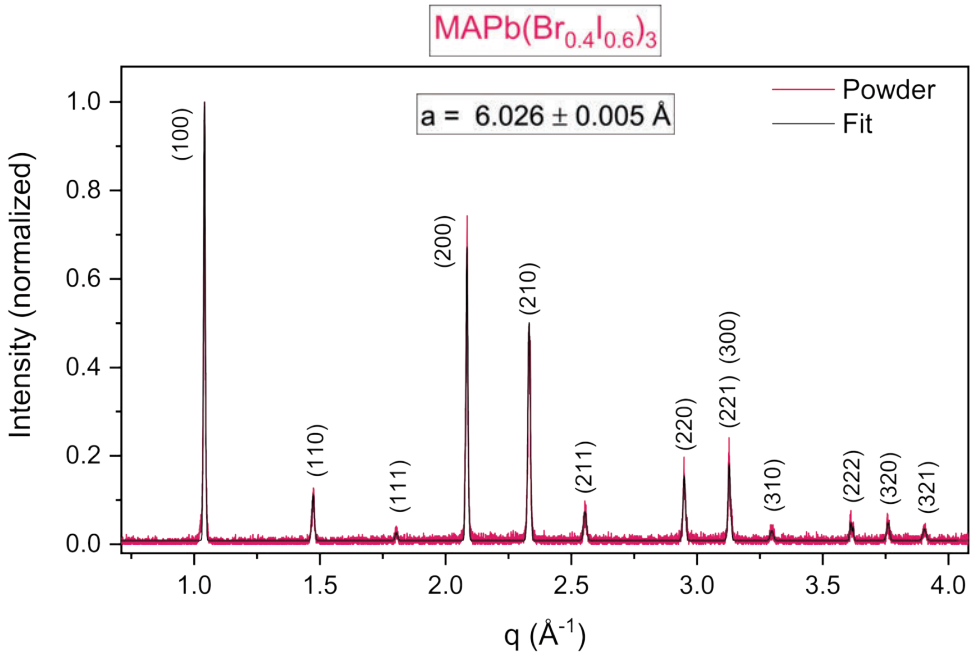


**Figure A9.** XRD pattern of the $MAPb(Br_{0.4}I_{0.6})_3$ crystal powder. The evaluation of the fit resulted in a lattice constant of a = 6.026 Å. The crystal structure is simple cubic.

**Table A11.** Evaluation of the XRD fitting data to determine the lattice plane ($d_{hkl}$) and the lattice constant (a) of the $MAPb(Br_{0.4}I_{0.6})_3$ crystal powder.

| Number | Fitting data 2θ (°) | Fitting data q ($Å^{-1}$) | Miller indices (hkl) | $d_{hkl}$ (Å) | a (Å) |
|---|---|---|---|---|---|
| 1 | 14.6649 | 1.04105 | 100 | 6.03543 | 6.03543 |
| 2 | 20.8122 | 1.47335 | 110 | 4.26455 | 6.03099 |
| 3 | 25.5708 | 1.80515 | 111 | 3.4807 | 6.02876 |
| 4 | 29.6142 | 2.08465 | 200 | 3.01402 | 6.02804 |
| 5 | 33.2283 | 2.33229 | 210 | 2.69399 | 6.02395 |
| 6 | 36.4993 | 2.55443 | 211 | 2.45972 | 6.02505 |
| 7 | 42.3864 | 2.94887 | 220 | 2.13071 | 6.02655 |
| 8 | 45.0923 | 3.12762 | 221 | 2.00893 | 6.0268 |
| 9 | 45.0923 | 3.12762 | 300 | 2.00893 | 6.0268 |
| 10 | 47.689 | 3.29752 | 310 | 1.90543 | 6.02549 |
| 11 | 52.6824 | 3.6194 | 222 | 1.73598 | 6.0136 |
| 12 | 54.8568 | 3.75745 | 320 | 1.6722 | 6.02919 |
| 13 | 57.1898 | 3.90406 | 321 | 1.6094 | 6.02182 |
| 14 | 14.6649 | 1.04105 | 100 | 6.03543 | 6.03543 |

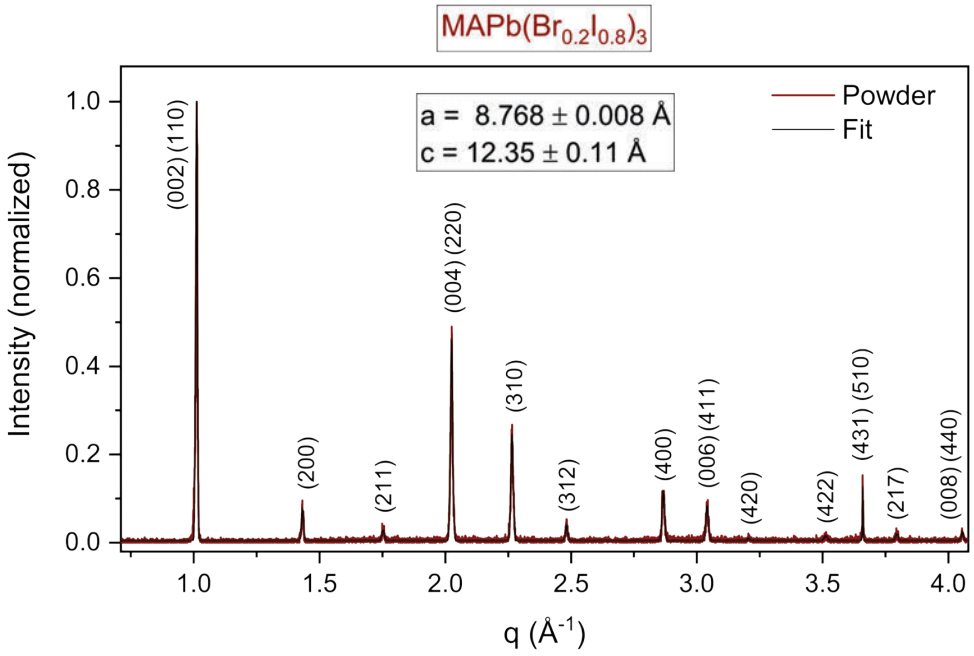


**Figure A10.** XRD pattern of the $MAPb(Br_{0.2}I_{0.8})_3$ crystal powder. The evaluation of the fit resulted in the lattice constants a = 8.768 Å and c = 12.35 Å. The crystal structure is body-centred tetragonal.

**Table A12.** Evaluation of the XRD fitting data to determine the lattice plane ($d_{hkl}$) and the lattice constants (a/c) of the $MAPb(Br_{0.2}I_{0.8})_3$ crystal powder.

| Number | Fitting data 2θ (°) | Fitting data q (Å$^{-1}$) | Miller indices (hkl) | $d_{hkl}$ (Å) | a/c (Å) |
|---|---|---|---|---|---|
| 1 | 14.2524 | 1.01192 | 002 | 6.20917 | c = 12.41834 |
| 2 | 14.2524 | 1.01192 | 110 | 6.20917 | a = 8.78109 |
| 3 | 20.2382 | 1.43315 | 200 | 4.38419 | 8.76838 |
| 4 | 24.808 | 1.75216 | 211 | 3.58597 | 8.78381 |
| 5 | 28.7518 | 2.02524 | 004 | 3.10243 | 12.40974 |
| 6 | 28.7518 | 2.02524 | 220 | 3.10243 | 8.77501 |
| 7 | 32.2481 | 2.26535 | 310 | 2.77361 | 8.77091 |
| 8 | 35.4226 | 2.48153 | 312 | 2.53198 | 9.47379 |
| 9 | 41.1433 | 2.8662 | 400 | 2.19217 | 8.76867 |
| 10 | 43.7743 | 3.04077 | 006 | 2.06631 | 12.39789 |
| 11 | 43.7743 | 3.04077 | 411 | 2.06631 | 8.76663 |
| 12 | 46.2643 | 3.20451 | 420 | 1.96073 | 8.76866 |
| 13 | 51.0062 | 3.51208 | 422 | 1.78902 | 8.76437 |
| 14 | 53.3085 | 3.65928 | 431 | 1.71705 | 8.75529 |
| 15 | 53.3085 | 3.65928 | 510 | 1.71705 | 8.75529 |
| 16 | 55.4158 | 3.79272 | 217 | 1.65664 | 12.1738 |
| 17 | 59.6019 | 4.05394 | 008 | 1.5499 | 12.39916 |
| 18 | 59.6019 | 4.05394 | 440 | 1.5499 | 8.76753 |

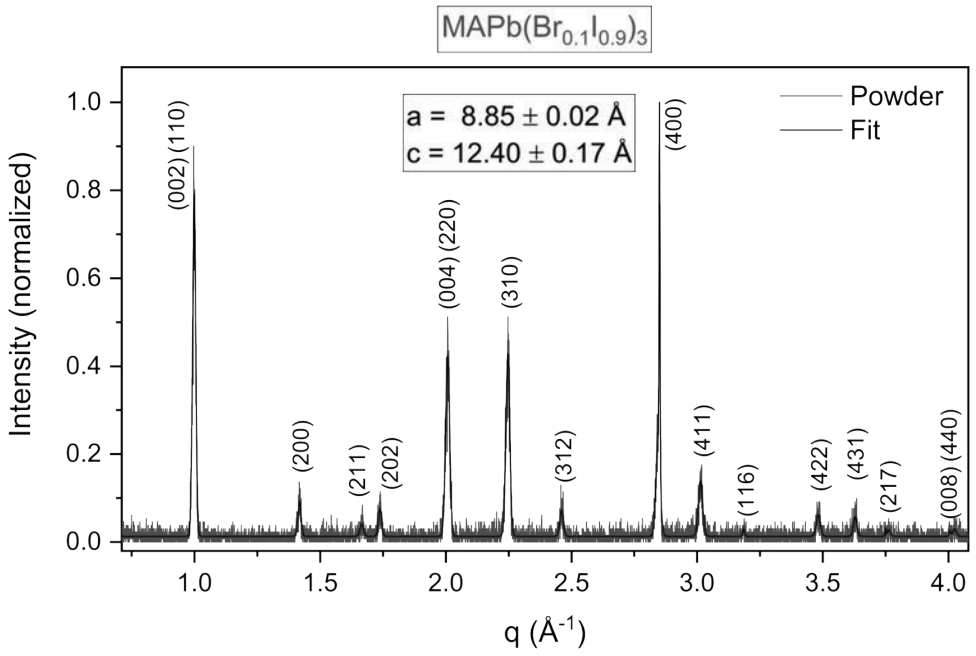


**Figure A11.** XRD pattern of the $MAPb(Br_{0.1}I_{0.9})_3$ crystal powder. The evaluation of the fit resulted in the lattice constants a = 8.85 Å and c = 12.40 Å. The crystal structure is body-centred tetragonal.

**Table A13.** Evaluation of the XRD fitting data to determine the lattice plane ($d_{hkl}$) and the lattice constants (a/c) of the $MAPb(Br_{0.1}I_{0.9})_3$ crystal powder.

| Number | Fitting data 2θ (°) | Fitting data q ($Å^{-1}$) | Miller indices (hkl) | $d_{hkl}$ (Å) | a/c (Å) |
|---|---|---|---|---|---|
| 1 | 14.0698 | 0.99902 | 002 | 6.28934 | c = 12.57868 |
| 2 | 14.0698 | 0.99902 | 110 | 6.28934 | a = 8.89447 |
| 3 | 20.0191 | 1.41779 | 200 | 4.43168 | 8.86335 |
| 4 | 24.6024 | 1.73786 | 211 | 3.61547 | 8.85607 |
| 5 | 28.4924 | 2.00735 | 004 | 3.13009 | 12.52035 |
| 6 | 28.4924 | 2.00735 | 220 | 3.13009 | 8.85322 |
| 7 | 31.9769 | 2.2468 | 310 | 2.79651 | 8.84333 |
| 8 | 40.7992 | 2.84325 | 400 | 2.20986 | 8.83943 |
| 9 | 43.3587 | 3.0133 | 411 | 2.08515 | 8.84655 |
| 10 | 45.9253 | 3.1823 | 116 | 1.97441 | 12.1711 |
| 11 | 50.528 | 3.48133 | 422 | 1.80482 | 8.84179 |
| 12 | 52.8235 | 3.62839 | 431 | 1.73167 | 8.82983 |
| 13 | 54.7799 | 3.75259 | 217 | 1.67436 | 12.30399 |
| 14 | 54.9652 | 3.76429 | 217 | 1.66915 | 12.26573 |
| 15 | 58.852 | 4.00753 | 008 | 1.56784 | 12.54275 |
| 16 | 59.1607 | 4.02666 | 440 | 1.5604 | 8.82694 |

# B Characterisation of the FAMA, CsFAMA, and $FAPbI_3$ Crystals

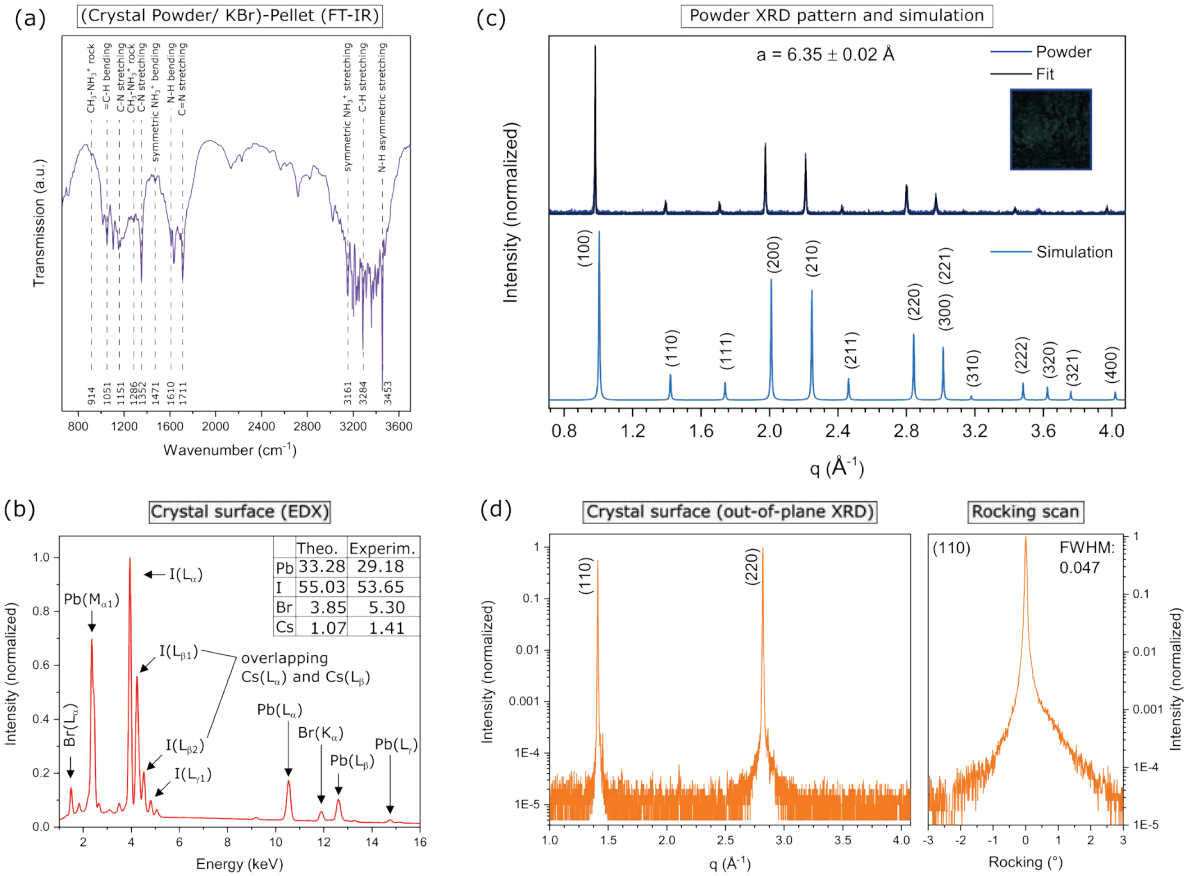


**Figure B1.** (a) FT-IR measurement of the $(FAPbI_3)_{0.9}(MAPbBr_3)_{0.05}(CsPbBr_3)_{0.05}$ crystal powder to prove the incorporation of the organic cations $CH_3NH_3^+$ and $CH_5N_2^+$. (b) EDX measurements of the crystal surface to quantify the elements caesium (Cs), lead (Pb), iodine (I), and bromine (Br). (c) PXRD pattern and the corresponding simulation revealed a simple cubic crystal structure with a lattice constant of a = 6.35±0.02 Å. Furthermore, the image of the measured crystal powder is shown as inset. The PXRD simulation of the perovskite were made by using the crystallographic data from Ref. [81]. (d) Out-of-plane XRD measurement of the crystal surface with corresponding rocking curve. Both measurements are an indication of a high quality of the crystal surface.

**Table B1.** Evaluation of the XRD fitting data to determine the lattice plane ($d_{hkl}$) and the lattice constant (a) of the $(FAPbI_3)_{0.9}(MAPbBr_3)_{0.05}(CsPbBr_3)_{0.05}$ crystal powder.

| Number | Fitting data 2θ (°) | Fitting data q ($Å^{-1}$) | Miller indices (hkl) | $d_{hkl}$ (Å) | a (Å) |
|---|---|---|---|---|---|
| 1 | 13.8198 | 0.98136 | 100 | 6.40255 | 6.40255 |
| 2 | 19.6658 | 1.39302 | 110 | 4.51049 | 6.37879 |
| 3 | 24.1853 | 1.70884 | 111 | 3.67687 | 6.36853 |
| 4 | 28.0353 | 1.9758 | 200 | 3.18007 | 6.36015 |
| 5 | 31.4572 | 2.21121 | 210 | 2.84151 | 6.35382 |
| 6 | 34.5572 | 2.42278 | 211 | 2.59338 | 6.35245 |
| 7 | 40.1648 | 2.80088 | 220 | 2.24329 | 6.34497 |
| 8 | 42.7345 | 2.97196 | 300 | 2.11415 | 6.34246 |
| 9 | 45.1643 | 3.13236 | 310 | 2.0059 | 6.3432 |
| 10 | 49.7969 | 3.4342 | 222 | 1.82959 | 6.3379 |
| 11 | 51.9926 | 3.57533 | 320 | 1.75737 | 6.3363 |
| 12 | 58.2718 | 3.97151 | 400 | 1.58206 | 6.32826 |

**Table B2.** Evaluation of the XRF measurements, presented by energies of principal K-, L-, and M-shell emission lines of bromine, iodine, and lead. Reproduced from Ref. [26] with permission from the Royal Society of Chemistry.

| Emission line | | Theory (keV) [104] | Experimental data[11] (keV) | |
|---|---|---|---|---|
| | | | Powder | Surface |
| Bromine | $K\alpha_1$ | 11.92 | 12.0 | 12.0 |
| | $K\alpha_2$ | 11.88 | | |
| | $K\beta_1$ | 13.29 | 13.3 | 13.3 |
| | $L\alpha_1$ | 1.48 | | |
| | $L\alpha_2$ | 1.48 | | |
| | $L\beta_1$ | 1.53 | | |
| | | | | |
| Iodine | $K\alpha_1$ | 28.61 | | |
| | $K\alpha_2$ | 28.32 | | |
| | $K\beta_1$ | 32.29 | | |
| | $L\alpha_1$ | 3.94 | 4.0 | 4.0 |
| | $L\alpha_2$ | 3.93 | | |
| | $L\beta_1$ | 4.22 | 4.3 | 4.3 |
| | $L\beta_2$ | 4.51 | | 4.6 |
| | $L\gamma_1$ | 4.80 | 5.0 | 5.0 |
| | | | | |
| Lead | $K\alpha_1$ | 74.97 | | |
| | $K\alpha_2$ | 72.80 | | |
| | $K\beta_1$ | 84.94 | | |
| | $L\alpha_1$ | 10.55 | 10.6 | 10.6 |
| | $L\alpha_2$ | 10.45 | | |
| | $L\beta_1$ | 12.61 | 12.7 | 12.7 |
| | $L\beta_2$ | 12.62 | | |
| | $L\gamma_1$ | 14.76 | 14.8 | 14.8 |
| | $M\alpha_1$ | 2.35 | 2.4 | 2.4 |

[11] The collected data were determined by the peak maximum and have an accuracy of ± 0.1 keV.

**Table B3.** Evaluation of the XRD fitting data of the $(FAPbI_3)_{0.9}(MAPbBr_3)_{0.1}$ crystal powder to determine the lattice plane ($d_{hkl}$) and the lattice constant (a). Reproduced from Ref. [26] with permission from the Royal Society of Chemistry.

| Number | Fitting data 2θ (°) | Fitting data q ($Å^{-1}$) | Miller indices (hkl) | $d_{hkl}$ (Å) | a (Å) |
|---|---|---|---|---|---|
| 1 | 13.9551 | 0.9909 | 100 | 6.341 | 6.341 |
| 2 | 19.784 | 1.4013 | 110 | 4.484 | 6.341 |
| 3 | 24.2955 | 1.7165 | 111 | 3.661 | 6.340 |
| 4 | 28.1466 | 1.9833 | 200 | 3.168 | 6.336 |
| 5 | 31.5755 | 2.2193 | 210 | 2.831 | 6.331 |
| 6 | 34.6886 | 2.4317 | 211 | 2.584 | 6.329 |
| 7 | 40.2579 | 2.8071 | 220 | 2.238 | 6.331 |
| 8 | 42.8218 | 2.9778 | 221 | 2.110 | 6.330 |
| 9 | 45.3157 | 3.1421 | 310 | 1.600 | 6.323 |
| 10 | 49.845 | 3.4373 | 222 | 1.828 | 6.332 |
| 11 | 52.0703 | 3.5803 | 320 | 1.755 | 6.328 |
| 12 | 54.2264 | 3.7176 | 321 | 1.690 | 6.324 |
| 13 | 58.1938 | 3.9667 | 400 | 1.584 | 6.336 |

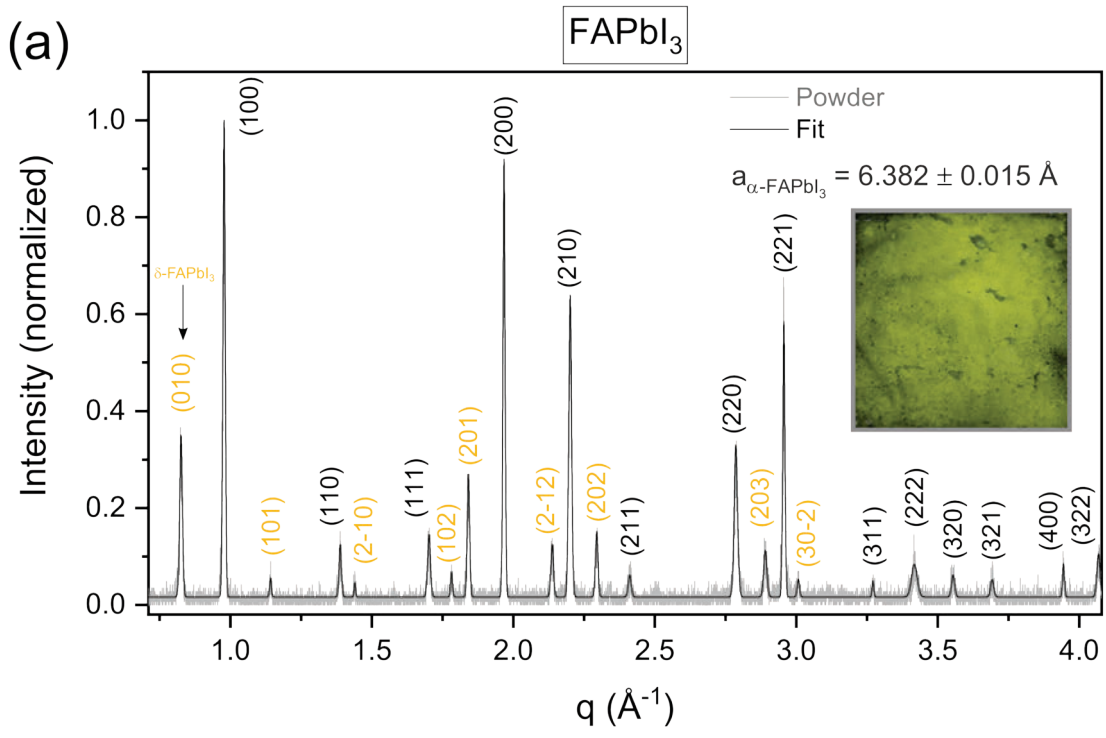


**Figure B2.** (a) Measured XRD pattern of the $FAPbI_3$ crystal powder with associated fit. In addition, the $FAPbI_3$ crystal powder is shown. (b) Simulated XRD patterns of the α- and δ-phase of $FAPbI_3$. Furthermore, the images of a decomposed $FAbI_3$ crystal (yellow) and a freshly prepared (black) $FAPbI_3$ crystal are shown. The simulations are taken from Ref. [32] and Ref. [83]. Reproduced from Ref. [26] with permission from the Royal Society of Chemistry.

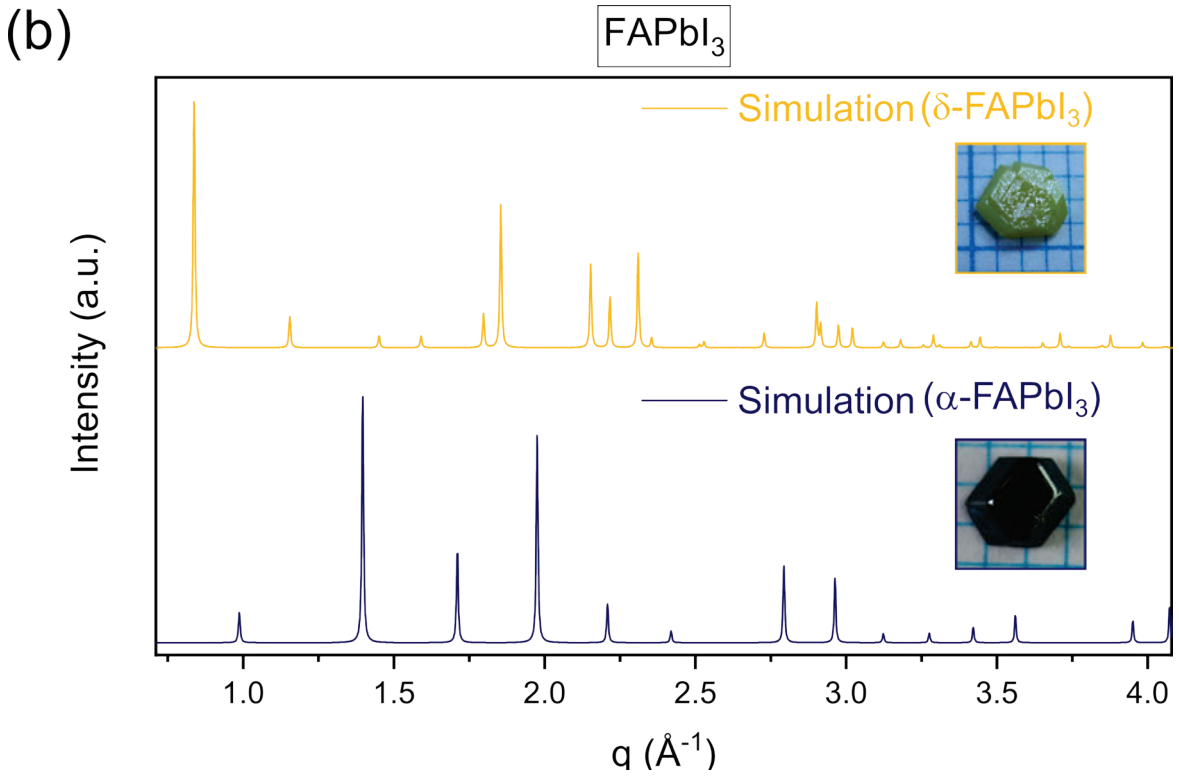


**Figure B2.** (continued).

**Table B4.** Evaluation of the XRD fitting data to determine the lattice plane ($d_{hkl}$) and the lattice constant (a) of the $FAPbI_3$ crystal powder. Reproduced from Ref. [26] with permission from the Royal Society of Chemistry.

| Number | Fitting data 2θ (°) | Fitting data q ($Å^{-1}$) | Miller indices (hkl) | $d_{hkl}$ (Å) | a (Å) |
|---|---|---|---|---|---|
| 1 | 13.7755 | 0.9782 | 100 | 6.423 | 6.423 |
| 2 | 19.6015 | 1.3885 | 110 | 4.5251 | 6.400 |
| 3 | 24.0876 | 1.7020 | 111 | 3.6916 | 6.394 |
| 4 | 27.912 | 1.9673 | 200 | 3.1938 | 6.388 |
| 5 | 31.3069 | 2.2009 | 210 | 2.8548 | 6.384 |
| 6 | 34.3908 | 2.4115 | 211 | 2.6055 | 6.382 |
| 7 | 39.9483 | 2.7864 | 220 | 2.2549 | 6.378 |
| 8 | 42.4932 | 2.9560 | 221 | 2.1256 | 6.377 |
| 9 | 47.2756 | 3.2706 | 310 | 1.9211 | 6.372 |
| 10 | 49.5341 | 3.4172 | 222 | 1.8387 | 6.369 |
| 11 | 51.6576 | 3.5539 | 320 | 1.7680 | 6.375 |
| 12 | 53.8246 | 3.6921 | 321 | 1.7018 | 6.368 |
| 13 | 57.8294 | 3.9440 | 400 | 1.5931 | 6.372 |
| 14 | 59.821 | 4.0675 | 322 | 1.5447 | 6.369 |

# C EDX Measurements of the RITC Crystals

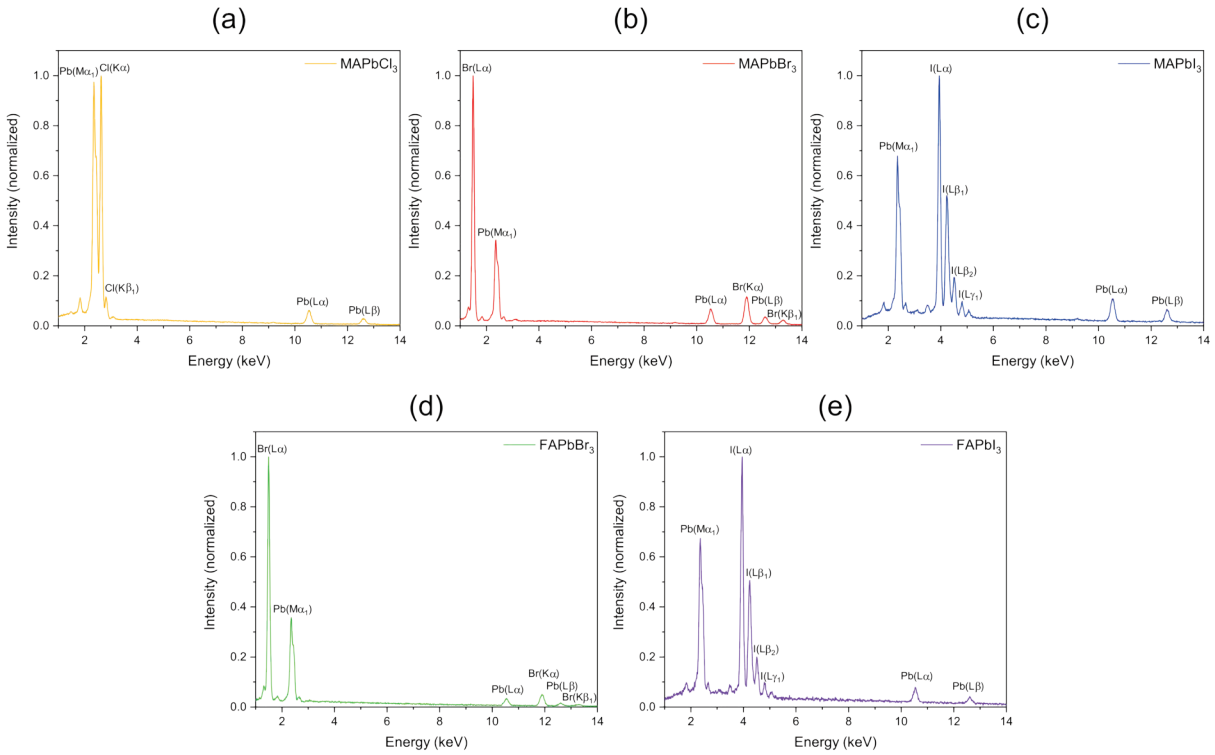


**Figure C1.** EDX spectra of the (a) $MAPbCl_3$, (b) $MAPbBr_3$, (c) $MAPbI_3$, (d) $FAPbBr_3$, and (e) $FAPbI_3$ crystal surfaces to identify the elements chlorine (Cl), bromine (Br), iodine (I), and lead (Pb). Based on their characteristic emission lines, the elements could be precisely assigned. Reproduced from Ref. [23] with permission from the Royal Society of Chemistry.

# 11 List of Abbreviations

| **Perovskite terms** | |
|---|---|
| OLTP | organolead trihalide perovskite |
| MLTP | methylammonium lead trihalide perovskite |
| $CaTiO_3$ | calcium titanate |
| $MAPbCl_3$ | methylammonium lead trichloride |
| $MAPbBr_3$ | methylammonium lead tribromide |
| $MAPbI_3$ | methylammonium lead triiodide |
| $FAPbBr_3$ | formamidinium lead tribromide |
| $FAPbI_3$ | formamidinium lead triiodide |
| $CsPbBr_3$ | caesium lead tribromide |
| $MASnBr_3$ | methylammonium tin tribromide |
| $MASnI_3$ | methylammonium tin triiodide |
| $Cs_2AgBiBr_6$ | caesium silver bismuth bromide |
| **Elements, salts and further materials** | |
| H | hydrogen |
| C | carbon |
| N | nitrogen |
| Cl | chlorine |
| Br | bromine |
| I | iodine |
| Pb | lead |
| Si | silicon |
| Cu | copper |
| Mo | molybdenum |
| Bi | bismuth |
| Au | gold |
| $MA^+$/ $CH_3NH_3^+$ | methylammonium cation |
| $FA^+$/ $CH_5N_2^+$ | formamidinium cation |
| $PbCl_2$ | lead chloride |
| $PbBr_2$ | lead bromide |
| $PbI_2$ | lead iodide |
| MACl | methylammonium chloride |
| MABr | methylammonium bromide |
| MAI | methylammonium iodide |
| FABr | formamidinium bromide |
| FAI | formamidinium iodide |
| CsBr | caesium bromide |
| $C_2H_3NaO_2$ | sodium acetate |
| $KAl(SO_4)_2 \cdot 12\ H_2O$ | potassium aluminium sulphate/ alum |
| KBr | potassium bromide |
| NaCl | sodium chloride |
| PTFE | polytetrafluoroethylene |
| LDPE | low density polyethylene |
| NaOH | sodium hydroxide |
| $NaBH_4$ | sodium borohydride |

| | |
|---|---|
| PEDOT:PSS | poly(3,4-ethylenedioxythiophene) polystyrene sulfonate |
| PolyTPD | poly[*N*,*N*'-bis(4-butilphenyl)-*N*,*N*'-bis(phenyl)-benzidine] |
| PTAA | poly[bis(4-phenyl)(2,4,6-trimethylphenyl)amine] |
| PFN | poly[(9,9-bis(3-(*N,N*-dimethylamino)propyl)-2,7-fluorene)-*alt*-2,7-(9,9-dioctylfluorene)] |
| $PC_{61}BM$ | [6,6]-phenyl-C61-butyric acid methyl ester |
| BCP | 2,9-dimethyl-4,7-diphenyl-1,10-phenatroline |
| LiF | lithium fluoride |
| ITO | indium doped tin oxide |
| **Solvents** | |
| DMF | *N*,*N*-dimethylformamide |
| GBL | γ-butyrolactone |
| DMSO | dimethylsulfoxide |
| DCM/ $CH_2Cl_2$ | dichloromethane |
| $CHCl_3$ | chloroform |
| DCB | 1,2-dichlorobenzene |
| $H_2O$ | water |
| TMS | tetramethylsilane |
| **Methods and techniques** | |
| XRD | X-ray diffraction |
| PXRD | powder X-ray diffraction |
| XRF | X-ray fluorescence |
| EDX | energy-dispersive X-ray spectroscopy |
| PL | photoluminescence |
| UV-VIS/NIR | ultraviolet-visible/ near-infrared |
| FT-IR | Fourier-transform infrared spectroscopy |
| SEM | scanning electron microscope |
| EA | elemental analysis |
| ICP-OES | inductively coupled plasma optical emission spectrometry |
| MPPT | maximum power point tracking |
| AVC | antisolvent vapour-assistant crystallisation |
| ITC | inverse temperature crystallisation |
| A-ITC | alcohol-induced inverse temperature crystallisation |
| RITC | reactive inverse temperature crystallisation |
| RC | reactive crystallisation |
| RTC | room temperature crystallisation |
| RFCM | re-fill crystallisation method |
| **Crystallographic aspects** | |
| sc | simple cubic |
| fcc | face-centred cubic |
| bcc | body-centred cubic |
| (hkl) | Miller indices |
| **Others** | |
| HTL | hole transport layer |
| ETL | electron transport layer |
| VB | valence band |
| HOMO | highest occupied molecular orbital |
| LUMO | lowest unoccupied molecular orbital |

# 12 List of Symbols

| Symbol | Meaning | Unit |
|---|---|---|
| $\vec{G}$ | reciprocal lattice vector | |
| $\delta_{ij}$ | Kronecker delta | |
| t | Goldschmidt tolerance factor | |
| r | radius | [m] |
| ω | nucleation rate | |
| K´ | arbitrary constant | |
| λ | wavelength | [nm] |
| $d_{hkl}$ | lattice plane distance | [Å] |
| θ | Bragg angle | [°] |
| a/ b/ c | lattice constant | [Å] |
| α/ β/ γ | angle | [°] |
| q | scattering vector | [$Å^{-1}$] |
| FWHM | full width at a half maximum | [°] |
| T | transmittance | |
| R | reflectance | |
| A | absorptance | |
| Abs | absorbance | |
| $E_{AE}$ | absorption edge | [eV] |
| $E_g$ | band gap | [eV] |
| α | absorption coefficient | [$cm^{-1}$] |
| c | speed of light | [$m \cdot s^{-1}$] |
| h | Planck's constant | [J·s] |
| ν | photon frequency | [Hz] |
| K | proportionality constant | |
| i | intensity | |
| d | thickness | [m] |
| I | current | [A] |
| J | current density | [$mA \cdot cm^{-2}$] |
| $E_e$ | irradiance | [$mW \cdot cm^{-2}$] |
| $A_X$ | active area | [$m^2$] |
| $R_{ph}$ | photoresponsivity | [$A \cdot W^{-1}$] |
| $L_D$ | charge carrier diffusion length | [m] |
| $V_{OC}$ | open-circuit voltage | [V] |
| $I_{SC}$ | short-circuit current | [A] |
| $J_{SC}$ | short-circuit current density | [$mA \cdot cm^{-2}$] |
| FF | fill factor | [%] |
| PCE | power conversion efficiency | [%] |
| P | electrical power | [W] |
| $R_{Shunt}$ | shunt resistance | [Ω] |
| $R_{Series}$ | series resistance | [$\Omega \cdot cm^{-2}$] |
| RT | room temperature | [°C] |
| T | temperature | [°C or K] |
| V | volume | [l] |

| | | |
|---|---|---|
| Bp | boiling point | [°C] |
| $A_r$ | relative atomic mass | [u] |
| $\sigma$ | electrical conductivity | $[S \cdot m^{-1}]$ |
| $\varepsilon_r$ | dielectric constant | |
| $\varepsilon_0$ | vacuum permittivity | $[(A \cdot s) \cdot (V \cdot m)^{-1}]$ |
| $C_p$ | capacitance | [F] |
| $G_p$ | electrical conductance | $[\Omega^{-1}]$ |
| $R_p$ | electrical resistance | [Ω] |
| $E_a$ | activation energy | [eV] |
| $E_T$ | molar electronic transition energy | $[kcal \cdot mol^{-1}]$ |
| $N_A$ | Avogadro constant | $[mol^{-1}]$ |
| $c_m$ | molar concentration | $[mol \cdot l^{-1}]$ |
| $\rho_i$ | mass concentration | $[g \cdot l^{-1}]$ |
| M | mass fraction | |

# List of Publications

## Refereed Articles

- J. Höcker, D. Kiermasch, P. Rieder, K. Tvingstedt, A. Baumann, and V. Dyakonov, *Efficient solution processed $CH_3NH_3PbI_3$ perovskite solar cells with polyTPD hole transport layer*, Zeitschrift für Naturforschung A, 2019 (74, 665-672), https://doi.org/10.1515/zna-2019-0127.

- J. Höcker, M. Ozcan, S. Hammer, M. Fischer, B. Bichler, M. Armer, P. Rieder, V. Drach, J. Pflaum, B. Nickel, and V. Dyakonov, *Seed Crystal Free Growth of High-quality Double Cation – Double Halide Perovskite Single Crystals for Optoelectronic Applications*, Journal of Chemistry C, 2020 (8, 8275-8283), https://doi.org/10.1039/D0TC01617A.

- C. Witt, A. Schmid, N. Leupold, M. Schultz, J. Höcker, A. Baumann, R. Moss, and F. Panzer, *Impact of Pressure and Temperature on the Compaction Dynamics and Layer Properties of Powder-Pressed Methylammonium Lead Halide Thick Films*, ACS Applied Electronic Materials, 2020 (2, 8, 2619-2628), https://doi.org/10.1021/acsaelm.0c00493.

- J. Höcker, F. Brust, M. Armer, and V. Dyakonov, *A temperature-reduced method for the rapid growth of hybrid perovskite single crystals with primary alcohols*, CrystEngComm, 2021 (23, 2202-2207), https://doi.org/10.1039/D0CE01759K.

- J. Höcker and V. Dyakonov, *Hybrid perovskite crystals: Growth, characterization and application*, which is a section of the paper *Roadmap: Organic-inorganic hybrid perovskite semiconductors and devices*, APL Materials, 2021 (9, 109202), https://aip.scitation.org/doi/10.1063/5.0047616.

- M. Armer, J. Höcker (shared first author), C. Büchner, S. Häfele, P. Dörflinger, M. Sirtl, K. Tvingstedt, T. Bein, and V. Dyakonov, *Influence of crystallisation on structural and optical properties of lead-free $Cs_2AgBiBr_6$ perovskite crystals*, CrystEngComm, 2021 (23, 6848-6854), https://doi.org/10.1039/D1CE00844G.

- A. Trifonov, S. Grisard, A. Kosarev, I. Akimov, D. Yakovlev, J. Höcker, V. Dyakonov, and M. Bayer, *Photon echo polarimetry of excitons and biexcitons in a $CH_3NH_3PbI_3$ perovskite single crystal*, ACS Photonics, 2022 (9, 2, 621-629), https://doi.org/10.1021/acsphotonics.1c01603.

- E. Kirstein, D. Yakovlev, M. Glazov, E. Zhukov, D. Kudlacik, I. Kalitukha, V. Sapega, G. Dimitriev, M. Semina, M. Nestoklon, E. Ivchenko, D. Dirin, O. Nazarenko, M. Kovalenko, A. Baumann, J. Höcker, V. Dyakonov, and M. Bayer, *The Landé factors of electrons and holes in lead halide perovskites: universal dependence on the band gap*, (submitted).

# Contributed Talks and Poster Presentations

- DPG Frühjahrstagung 2018 (Talk): J. Höcker, D. Kiermasch, P. Rieder, K. Tvingstedt, A. Baumann, and V. Dyakonov, *The influence of solvent engineering on the fundamental functionality of organolead triiodide perovskite solar cells*.

- DPG Frühjahrstagung 2019 (Poster): J. Höcker, M. Armer, V. Drach, F. Brust, S. Braxmeier, V. Dyakonov, and A. Baumann, *Investigation of organic/inorganic lead tribromide single crystals by liquid growth methods*.

- Attendance at the Online School on Fundamentals of Emerging Solar Cells (PV School) 2021 with successful completion of the final aptitude test.

- OrgMatPerPV conference 2021 (E-Poster): J. Höcker, D. Kiermasch, P. Rieder, K. Tvingstedt, A. Baumann, and V. Dyakonov, *The polymer polyTPD as hole transport layer for efficient solution processed $MAPbI_3$ perovskite solar cells* (winner of the "Best E-Poster prize" from Solar RRL).

- HOPV conference 2021 (E-Poster): J. Höcker, P. Rieder, and V. Dyakonov, *High-quality $MAPbI_3$ crystal wafers and crystal "films" for optoelectronic applications*.

- SolTech conference 2021 (Talk): J. Höcker, M. Armer, P. Dörflinger, V. Schmid, M. Fischer, and V. Dyakonov, *Perovskite Crystals and Films: Fabrication, Characterisation, and Photovoltaic Applications*.

# Transparency Table

The above-mentioned publications were partly used for the preparation of this thesis. The following table gives an overview of the used text passages and figures with the corresponding page numbers. The use of the publications was permitted by the respective journals that hold the copyright of the publications. Furthermore, each chapter in which parts of publications are used is marked with a corresponding footnote. In addition, text passages and figures are marked with the references of the respective publication. Furthermore, references that come after the end of a sentence always refer to the complete paragraph in a chapter.

| Publication | Figure and text material used | Dissertation |
|---|---|---|
| [35] | Fig. S1 and figure caption reproduced. | pp. 17 – 18 |
| [310] | Fig. 19 and figure caption reproduced/ text reproduced and modified from Subchapter III. Fabrication – E. | pp. 41, 46, 88, 101 – 108 |
| [26] | Whole manuscript reproduced, except Fig. 4, Fig. S7, Fig. S8, Fig. S9a, and the related text description. | pp. 45, 51 – 65, 139, 150 – 152 |
| [23] | Whole manuscript reproduced. | pp. 67 – 78, 153 |
| [131] | Whole manuscript in a modified version reproduced, except Table S1, Fig. S4 and the related text description. | pp. 79 – 85 |

# Danksagung

Ich möchte mich bei Allen bedanken, die mich während meines Promotionsstudiums begleitet und unterstützt haben.

- Als allererstes möchte ich mich bei Prof. Dr. Vladimir Dyakonov bedanken, bei dem ich schon meine Bachelorarbeit, meine Projektarbeit sowie meine Masterarbeit anfertigen durfte. Zudem ermöglichte er mir die Anfertigung meiner Doktorarbeit an seinem Lehrstuhl im Rahmen der GSST. Für seine wissenschaftliche Aufsicht, Rat und Hilfestellung im Hinblick auf Projekte, Publikationen und Vorträge gebührt ihm mein besonderer Dank.
- Ein weiterer besonderer Dank gilt meiner Kollegin und Laborpartnerin Melina Armer, für die vielen Stunden in denen wir uns unterhalten, gefachsimpelt und Probleme besprochen haben. Zudem vielen Dank für die Durchsicht meiner Arbeit.
- Herzlichen Dank auch an Philipp Rieder, der mir seit dem Masterstudium in den unterschiedlichsten wissenschaftlichen Bereichen weitergeholfen hat.
- Dr. Volker Drach hat mich seit Beginn des Studiums in Vorlesungen und im Praktikum begleitet. Zudem hat er mich in verschieden Messtechniken während meiner Promotion eingewiesen. Bis zum Ende meiner Doktorarbeit konnte ich ihn immer um wissenschaftlichen Rat fragen. Zudem durfte ich mit ihm das Praktikum „Physikalische Technologien der Material-Synthese und – Charakterisierung“ betreuen. Für all das gebührt im großer Dank.
- Zudem möchte ich mich bei unserem Röntgenmeister Dr. Sebastian Hammer bedanken. Von ihm habe ich die hohe Kunst des Röntgens an unserem Lehrstuhlgerät gelernt und mich von seinem Röntgen-Enthusiasmus mitreißen lassen.
- Mein Dank an André Thiem-Riebe darf selbstverständlich nicht fehlen, der mir bei den Umsetzungen meiner Ideen in Bezug auf technische Bauteile, sowie bei Fragen in Bezug auf das Labor stets weiterhalf.
- Bedanken möchte ich mich auch bei Diep Phan für die administrativen Tätigkeiten, wie die Abgabe meiner Lieferscheine, Rechnungen und vieles mehr.
- Weiterhin möchte ich mich auch bei unseren Mitgliedern der Perowskite-Gruppe bedanken, insbesondere hier bei Mathias Fischer für seine Impedanz-Messungen an meinen Kristallen. Dank gilt auch allen Mitgliedern des Lehrstuhls und ihre Fragen an mich, wenn ich im Lehrstuhl-Seminar einen Vortrag gehalten habe.
- Besonderer Dank gilt auch meinen Projektpartnern Prof. Dr. Jens Pflaum von der Universität Würzburg, Christina Witt und Dr. Fabian Panzer von der Universität Bayreuth, Mehmet Ozcan und PD Dr. Bert Nickel von der LMU München, sowie Erik Kirstein, Dr. Artur Trifonov und Prof. Dr. Dmitri Yakovlev von der TU Dortmund.
- Bedanken möchte ich mich auch bei Stephan Braxmeier, Philipp Potsch, Clara Scheuring, Dr. MariaCarla Arduini und Dr. Jochen Manara vom ZAE-Bayern für die EDX, SEM und FT-IR Messungen. Für die ICP-OES Messungen möchte ich mich bei Dr. Bärbel Graser, Johannes Vogel und Simon Englert von der Firma CLG Chemische Labor Dr. Graser KG bedanken. Die Elementaranalyse-Messungen verdanke ich Liselotte Michels und Sabine Timmroth vom Anorganischen Institut der Universität Würzburg. Mein Dank gilt zudem Jonathan Landeck für seine Glasbläserarbeiten.
- Bedanken möchte ich mich ebenfalls bei Dr. Stephan Schröder-Köhne für die administrativen Tätigkeiten in Bezug auf die GSST. Schließlich möchte ich mich auch bei Prof. Dr. Robert Luxenhofer und Prof. Dr. Jürgen Hartmann für die Betreuung im Rahmen der GSST bedanken.

# Affidavit

I hereby confirm that my thesis entitled

**High-quality Organolead Trihalide Perovskite Crystals: Growth, Characterisation, and Photovoltaic Applications**

is the result of my own work. I did not receive any help or support from commercial consultants. All sources and/or materials applied are listed and specified in the thesis.

Furthermore, I confirm that this thesis has not yet been submitted as part of another examination process neither in identical nor in similar form.

Würzburg, 18.10.2021

Julian Höcker